Degradation and other Phenomena in Hydrogenated Amorphous Silicon Thin Films and Solar Cells

by

Ricardo Rüther BE, MSc

This thesis is submitted in fulfilment of the requirement for the degree of

Doctor of Philosophy

of

The University of Western Australia

Department of Electrical & Electronic Engineering

The University of Western Australia

1995

Pai e Mãe, ouro de mina (Djavan)

To my parents Maria Olivia and Rudi

Preface

The research described in this thesis was undertaken in the Department of Electrical & Electronic Engineering at The University of Western Australia, where most of the experimental work was carried out. Some of the experiments described were carried out in the Lucas Heights Research Laboratories at the Australian Nuclear Science and Technology Organisation (ANSTO) in New South Wales, as part of an Australian Institute of Nuclear Science and Engineering (AINSE) Postgraduate Research Award which I was awarded.

The work described is original and was carried out by myself except where the specific contributions of other persons are acknowledged. Reference to the work published by other individuals has extensively been made throughout this thesis, and was always cited in the usual manner.

Ricardo Rüther

April 1995

Acknowledgments

It is not very often that one has the opportunity to publicly express gratitude to individuals and institutions from which assistance, advice and support were received. I take this moment to acknowledge with many thanks all the help I have been given throughout these last four years.

To my supervisor, Dr. John Livingstone, for giving me the opportunity to work in such an interesting research field, and for continuous and complete support through all these years while we have been working in this exciting research topic.

Efficient library services are an essential element for any one undertaking the kind of work described in this thesis. I would like to thank Ritva Matero, Will Hamilton and all of the staff at the University FIZ-library, for their dedication and willing help in keeping me informed about what is going on in the field of amorphous silicon solar cells and other related topics. With the help of that team I can be sure that I have read most of the relevant publications regarding the work this thesis deals with.

To Dr. Nick Dytlewski and the Applications of Nuclear Physics team at the Australian Nuclear Science and Technology Organisation (ANSTO) in New South Wales, for the expertise, patience and interest in my research project. The support of Dr. David Cohen is also gratefully acknowledged.

I also wish to acknowledge with thanks Ian Muirhead and Telecom Australia Research Laboratories (TELSTRA Corporation) for access and permission to use their raw data

on amorphous silicon solar modules, and the Western Australian Regional Office, Bureau of Meteorology, for meteorological data.

It is for me an honour to thank the Australian Institute of Nuclear Science and Engineering (AINSE) for granting me an AINSE-Postgraduate Research Award for a project associated with this programme. This allowed all the work done at ANSTO to be carried out without financial restraints, and also made it possible for me to collaborate readily with the researchers there.

The award of a PhD scholarship by the Brazilian Research Council (CNPq-Brasil) has made it possible for me to spend these last four years here in Perth very comfortably, and to concentrate full-time on my research project. I thus acknowledge the Ministry of Education of Brazil for the privilege of being sent here to carry out this project.

Abstract

Hydrogenated amorphous silicon thin films and solar cells constitute a most interesting research topic, which attracts widespread interest both because of the prospects of producing low-cost photovoltaic cells, and because of the striking and complex mechanisms of light-induced degradation. Amorphous silicon is an attractive choice of photovoltaic material because it can be easily fabricated as a thin film in processes that are simultaneously low-energy intensive, inherently avoid the demands required by crystal perfection and consume a minimum of raw materials. The basic objective of this research project was a twofold investigation into degradation mechanisms and related phenomena:

(i) From a materials point of view: The deposition and characteristics of amorphous silicon thin films, with emphasis on the study of H-Si bonding configurations. The effects of temperature on the amorphous network both during and after deposition were also investigated

(ii) From a device point of view: The effects of operating temperature and spectral response on the performance of amorphous silicon solar modules

Intrinsic-type hydrogenated amorphous silicon thin films were fabricated by a reactive-sputtering technique under various deposition conditions. An *in situ* treatment of in-chamber annealing (ICA) was developed, which allowed a higher degree of control over H-Si bonding configurations in the films. In-chamber annealing in either vacuum or in a hydrogen atmosphere resulted in an increase of the silicon monohydride bonding type (generally regarded as the optimal bonding structure,

although there is some controversy on the matter), the hydrogen treatment having shown to be more effective. Mono-to-higher hydride ratios obtained with this *in situ* treatment were considerably higher than for samples not in-chamber annealed. A review of the literature shows that only films sputtered at much higher power densities than the ones presented here have been found to present comparable bonding configurations. However, the high energy bombardment which occurs at these higher power densities produces stress and increases the deep gap states density.

Films were characterised by Fourier transform infrared (FTIR) spectroscopy, for H-Si bonding configurations and total bonded hydrogen content, and by elastic recoil detection analysis (ERDA) and Rutherford backscattering (RBS) for hydrogen profiling and total concentration. Surface morphology characterisation was carried out using scanning electron microscopy (SEM). Treatment at various in-chamber annealing temperatures under hydrogen atmospheres showed that an optimum temperature exists in the narrow ~ 240 - 260 °C region. This, along with the substrate temperature, was found to be crucial in obtaining a-Si:H with optimised bonding configurations. Further, post-deposition thermal annealing at temperatures ranging from 200 to 600 °C showed that hydride clustering takes place at temperatures as low as 200 °C. Also, concomitant film thickness reduction pointed to film densification on annealing. This latter effect was especially strong for films with a higher hydrogen concentration and for films fabricated under non-optimal in-chamber annealing conditions.

On the second part of this study, commercial p-i-n amorphous silicon solar modules were light-soaked at different operating cell temperatures, under a solar simulator calibrated to the AM 1.0 spectrum and 100 $mW.cm^{-2}$ irradiation intensity. Variations in output degradation between sets exposed simultaneously to the same spectrum, but with a 50 °C cell temperature difference, indicated that thermal annealing might not be the major contributor to the so-called seasonal effect as is generally believed. Under

outdoor conditions, the seasonal effect describes an improvement in a-Si normalised performance during the summer, contrary to what happens with crystalline silicon photovoltaics, which perform better in winter because of lower operating temperatures. This effect has been widely attributed to the higher operating temperatures occurring in summer months, which appear to induce some degree of thermal annealing. This low-temperature thermal annealing then offsets the light-induced degradation known as the Staebler-Wronski effect (SWE), common in amorphous silicon solar cells. The reason for this belief is that the SWE is a reversible process, which can be reversed by thermal annealing, and the a-Si solar module outdoor efficiency trends follow the same trend of ambient temperature. One other possible cause for the seasonal effect in a-Si photovoltaic devices that has been speculated upon, is the effect of solar irradiation spectral content. Using a spectroradiometer, the solar spectral distribution in Perth, Australia, was measured in the summer and winter solstices, and spring and autumn equinoxes. A marked shift in the terrestrial solar spectral content was identified, which could be qualitatively correlated to amorphous silicon solar cells spectral response. Winter spectra are shifted to the red end of the spectrum, and a-Si solar cells, due to their higher bandgap, are heavily blue biased. As a consequence, the total useful solar radiation for this kind of cell is somewhat reduced in winter. The qualitative results presented in this work point out to a considerable contribution of spectral effects to the seasonal effect, and they appear to be more pronounced than the thermal annealing contribution.

In this framework, amorphous silicon thin film *materials* and solar cell *devices* are presented, along with degradation mechanisms, temperature effects and spectral response aspects.

Contents

Chapter 3: Amorphous Silicon Solar Cells

Chapter 4: Preparation of Amorphous Silicon

Chapter 5: Characterisation Techniques

Chapter 6: Materials and Methods

Chapter 7: The Role of Substrate Temperature and In-Chamber Annealing in H-Si Bonding Configurations and H Content in a-Si:H Thin Films

Chapter 1

Introduction

Amorphous silicon is a major solar cell material, and represents the fastest growing segment of the photovoltaic (PV) market [1]. This material was first reported in 1969 by Chittick *et al.* [2]; amorphous silicon solar cells were first investigated in 1974 and reported in 1976 by Carlson and Wronski [3], and they were first introduced as a commercial product in 1980 [4].

1.1 Why is a-Si a Good Choice of Photovoltaic Material?

Amorphous silicon is an attractive PV material because of its unusual optoelectronic properties, which are well suited for solar cell applications. Hydrogenated amorphous silicon (a-Si:H or simply a-Si) and its related alloy thin films are among the most promising technologies for the low-cost production of PV solar cells for terrestrial applications. Due to this material's properties, which in many aspects contrast with those of its crystalline bulk counterpart, a-Si solar cells are at present the most economic choice in many niche applications. In the last decade amorphous silicon has attracted a great deal of attention and has held out many promises, some of which have not yet been fully achieved, and there is some speculation on whether or not they ever will. What is undeniable, however, and does not come as a surprise, is the fact that today amorphous silicon is, among the PV technologies commercially available, the one which presents the fastest growth. The reasons for that include:

- The techniques used to produce a-Si allow the deposition of thin films on inexpensive substrate materials such as plastics, stainless steel and glass

- Processing temperatures are typically below 300 °C compared to 600 to 1400 °C for crystalline silicon (c-Si) processing, so that the total energy consumed in the deposition process is quite low (actually, the electric power density employed in industrial a-Si deposition is comparable to the intensity of terrestrial sunlight, on the order of 1kW per m^2 of film surface)

- Because thin film solar cells can be deposited on a variety of substrates, amorphous silicon solar panels can be made flexible, unbreakable and lightweight

- The use of a substrate means that only as much of the costly high purity silicon as is necessary to absorb sunlight is needed. a-Si solar cells use films which are typically less than 0.5 µm thick (a-Si is a more efficient absorber of light than a crystalline film of the same thickness), while c-Si cell thickness is usually 200 - 400 µm for a number of physical and technological reasons

- The technology for a-Si solar cell production allows for large area solar modules (of the order of a square metre) to be monolithically manufactured using low-cost automated methods. Moreover, because thin films can be deposited on curved surfaces as well as on flat areas, there is a series of applications suited to this technology, including roofing tiles and automobile sunroofs, both being currently commercially produced

- Because it is more aesthetically appealing than its crystalline counterpart, in some applications amorphous silicon is favoured for cosmetic reasons. Furthermore, there is the possibility of fabricating semi-transparent, see-through PV modules which now start to be incorporated into building roofs and façades

- Large-scale production costs for a-Si are already low and still dropping, and cost estimates for economies-of-scale volumes of less than US$ 1 per watt are possible today [5]

- The optical absorption properties of a-Si can be changed slightly by varying its hydrogen content, and they can be changed greatly by alloying it with carbon or nitrogen (to achieve bandgaps as high as 3.0 eV) and germanium (to reduce the bandgap to as low as 1.0 eV) [6]. Being able to control the absorption spectrum by alloying opens the opportunity for spectral splitting in high efficiency multijunction cells, and also to tailoring a solar cell's spectral response to suit any particular application

- Multijunction, two-terminal large-area solar modules employing a-Si alloys have already reached 10% stabilised efficiency [7], and might eventually reach stabilised efficiencies of at least 18% [8]

In small-scale applications and consumer products, single-junction amorphous silicon solar cells have already achieved a considerable market penetration (in fact, in room-light applications, basically due to their spectral response, a-Si solar cells are more efficient than c-Si cells). Amorphous silicon-based alloy multijunction thin film solar cells and modules are now emerging as a cost effective alternative to conventional crystalline silicon photovoltaics. For future large-scale bulk power applications,

considerable research efforts are being directed worldwide towards solving the still remaining problem of light-induced degradation and reduced efficiency. Progress in this direction is being achieved as a result of a variety of innovations in the design, materials and structure of the cells. Even though the fabrication of efficient and stable solar cells involves much more than the optimisation of the a-Si:H material, considerable progress is likely to eventuate from an improved understanding of the fundamental mechanism and characteristics of the constituent materials, the most important of which being the a-Si:H intrinsic (i-type) layer of p-i-n solar cells.

The performance of amorphous silicon-based solar cells is limited by light-induced degradation and also by their narrower spectral response (due to the material's wider bandgap) and a short carrier lifetime as compared to crystalline silicon solar cells. During the past 15 years, since the development and marketing of the first commercial a-Si:H solar cells, the technology has evolved considerably. Despite the light-induced degradation, known as the Staebler-Wronski effect (SWE) [9], still present even in the best quality solar cells, amorphous silicon solar cells are being manufactured in large area modules for outdoor applications (the largest area modules manufactured to date being 2.5 x 5 foot). Recently, amorphous silicon-based alloys have led to photovoltaic modules of a one square foot commercial type with 10.2% stabilised efficiency [7]. Reaching the 10% figure becomes quite significant when such efficiency is combined with mass production processes of suitable size (in the 50 - 100 MW/year/machine range). It becomes then possible for the first time for solar energy to economically compete with conventional fossil fuels and nuclear energy at approximately 7 US cents/kWh [10,11]. Encouraging as these figures might be, however, it must be emphasised that worldwide commercial solar cell and module production today is still below 100 MW/year total, which includes all photovoltaic technologies.

Even though the technology which has received the most attention in the application of amorphous silicon materials is the photovoltaic solar cell, a-Si has been successfully

used in a variety of other applications, including liquid crystal displays, scanner arrays (FAX machines), photoreceptors (photocopy machines, laser printers), position sensitive detectors, and thin film transistors among others.

1.2 The Problem of Light-Induced Degradation, its Reversibility and Implications

Although light-induced degradation is generally regarded as the most serious problem limiting the widespread use of amorphous silicon-based solar cells in outdoor applications, little is understood about the nature or origin of this degradation. Research on light-induced degradation has been ongoing since the discovery of the effect, usually referred to as the Staebler-Wronski effect (SWE) [9], and the literature on the subject is abundant. One of the most exciting aspects in the physics of hydrogenated amorphous silicon is its metastability. It is now generally accepted that these metastable changes are kinetically allowed by the diffusive motion of the bonded hydrogen within the amorphous network [12,13]. As Catalano pointed out [14], evidence continues to build that weak hydrogen bonds are responsible for the light induced effect. Although one may, therefore, be inclined to consider the effect intrinsic, further work is needed to fully understand the process.

Worldwide effort in the reduction or elimination of the light-induced degradation has been addressing amorphous silicon ***devices*** and ***alloy materials***, the former research being mostly empirical (and the most successful so far). The recent production of more stable amorphous silicon solar cells has been achieved both by circumvention of the Staebler-Wronski effect through better cell design (mainly the layer thickness reduction versus efficiency trade-off and the multijunction design approach), and a more basic research in a-Si:H thin film materials, attempting to overcome or minimise the light-induced degradation. While most of the improvements in the stabilised efficiency

of present devices are due to design considerations, more stable material is also being produced as the understanding of the mechanisms underlying the effect improves. Current efforts in overcoming the amorphous silicon ***material*** stability problem focus on understanding the effect of hydrogen content and bonding configurations and determining how other material properties (microstructure, impurities, etc.) and preparation variables influence stability [15]. Although the microscopic mechanism of the light-induced metastable changes is not thoroughly understood, hydrogen motion is apparently involved in the formation of light-induced defects [16-18]. The motion of hydrogen, its bonding configurations and bonding stability in the silicon network are believed to play a major role in the Staebler-Wronski effect. As hydrogen diffuses it can change the bonding configurations of the silicon network. Thus, a detailed knowledge of H-Si bond stability and hydrogen evolution is of fundamental interest if a more stable amorphous silicon material is to eventuate. Moreover, the quality of high bandgap amorphous silicon carbon alloys (a-SiC:H), required for advanced solar cell designs, is believed to be limited by preferential H bonding to carbon [19]. The mechanisms of hydrogen incorporation in a-Si:H are, therefore, of both scientific and technological interest.

The light-induced degradation in the electrical properties of amorphous silicon is a reversible effect, and the material's original properties can be fully restored by low temperature (150 - 200 °C) annealing in the dark for a few hours. Even though thermal annealing of defects is a highly temperature dependent process, some degree of recovery can be observed even at temperatures as low as 50 - 70 °C, typical of a-Si solar modules operated outdoors in many sunny and warm climates. This forms part of an effect that was only noticed fairly recently, after monitoring amorphous silicon modules in the field for several months, and which is sometimes referred to as the *seasonal effect*. Quite to the contrary to what happens with crystalline silicon solar modules in the field, a-Si modules perform better in summer than in winter. The reasons for this behaviour are complex and can be summarised as follows:

- Photovoltaic modules of either kind of silicon technology (amorphous or crystalline) present a negative temperature coefficient in output power (T_{coeff}). This T_{coeff} ranges from -0.5 to -0.8 %/°C for c-Si and from -0.1 to -0.3 %/°C for a-Si [20]. From this consideration alone, it would be expected for both kinds of solar cells to drop in efficiency during summer months, the effect being more prominent in c-Si than in a-Si

- Because the efficiency of a-Si solar modules can be restored by thermal annealing, the higher operating temperatures associated with summer month conditions (higher irradiance levels, as well as higher ambient temperatures) point to a better performance in that period

- There are considerable shifts in the terrestrial solar spectrum from winter to summer, particularly significant in the blue or shorter wavelength end of the spectrum. Mainly because of their wider bandgap, a-Si solar modules present a considerably narrower spectral response than c-Si modules, and the most marked seasonal changes in the terrestrial spectral content lie exactly within the range of a-Si's spectral response. Basically, for amorphous silicon there is less "collectable" radiation in winter than it is during summer, so that a better performance should be expected during summer months

The overall effect for the different silicon PV technologies is that a-Si performs better in summer, while c-Si solar cells perform better during the winter.

1.3 Outline of the thesis

Based on the above considerations, the work described in the present thesis deals with two aspects of the amorphous silicon technology, namely:

(i) The hydrogenated amorphous silicon intrinsic-type (i-type) thin film material, its production, characterisation, H-Si bonding configurations and the effects of temperature on the amorphous network. Most of the work described in this part (chapters 7 to 10) aims at improving the understanding of the role of hydrogen in the amorphous network and on how to control the way hydrogen atoms bond to silicon atoms in the random network

(ii) Commercial-type amorphous silicon solar modules, their degradation behaviour, temperature effects and spectral response characteristics. The work described in this second part (chapter 11) being focussed on the seasonal effect

The correlation between those two aspects emerges from the role temperature plays both during a-Si material preparation (H-Si network formation, which is believed to be directly related to the Staebler-Wronski effect) and during a-Si device operation and light-induced degradation (temperature effects on device output and thermal annealing recovery respectively). In this sense, the thesis is divided into two main blocks of information and experimental work, being one part devoted to *amorphous silicon thin film materials* and the other to *amorphous silicon thin film solar cells and modules*, with spectral effects included in the second part as a necessary element for a complete picture of the above mentioned seasonal effect.

Chapter 2

Amorphous Silicon Thin Films

2.1 Historical Background

Hydrogenated amorphous silicon was first deposited in the late 1960s. Amorphous silicon without hydrogen, however, was already known and studied and was prepared by thermal evaporation or by sputtering. Because the unhydrogenated material presented a very high defect density, which prevented doping, photoconductivity and other desired semiconductor characteristics, a-Si was not regarded as a promising semiconductor material in those early days. After Chittick, Alexander and Stirling [2] first prepared a-Si:H, using glow discharge decomposition of silane gas as a deposition technique, it was demonstrated that the presence of hydrogen resulted in reduced conduction via defect states (implying a low defect density), and increased conduction due to impurities [2,21]. Also, although not recognised as such at that time, the infrared vibrations of silicon-hydrogen bonds were observed, as well as some metastable phenomena which are now being extensively studied [22]. The promise of this new method of making amorphous silicon was recognised by Spear [23], whose research showed that the material has good electrical transport properties with a fairly high carrier mobility and strong photoconductivity [24,25]. What definitively introduced a-Si:H as a new material with useful technological applications, was the report in 1975 of substitutional n-type or p-type doping by the addition of phosphine or diborane to the deposition gas [26]. It was Lewis *et al.* [27], however, who recognised that it was the

presence of hydrogen in the amorphous network that was essential. They introduced hydrogen into their sputtering system and obtained a material with low defect density, useful for electronic devices. The hydrogen caused a similar improvement in the material properties as was found for glow discharge a-Si:H, with a high photoconductivity, low defect density and doping [22]. Soon thereafter it was confirmed that the glow discharge material also contained hydrogen [28].

2.2 Hydrogenated Amorphous Silicon (a-Si:H)

In amorphous silicon deposition, although higher electron temperatures exist in the plasma, the deposition onto virtually cold substrates results in very short-range ordering in the structure, which is not necessarily of tetrahedral form [2]. It has been regarded as a derivative of crystalline silicon, in which the lack of structural order simply degrades the electronic properties. If this were absolutely true this material would be of very little interest. The disordered atomic structure and the presence of hydrogen result in new phenomena, which are markedly different from those in crystalline semiconductors. The structural disorder results in the localised band tail states characteristic of amorphous materials, with consequences in the optical transport and recombination properties, while the presence of hydrogen results in unique defect, doping and metastability effects [22]. The exact nature of the energy bands in a-Si:H is not agreed upon, but some basic features are well accepted. It is agreed that there exist conduction and valence bands separated by a region of very low density of states (DOS). This region of very low DOS can be thought of as a pseudogap and is usually referred to as the energy gap for a-Si:H. The absence of long-range order smears out sharp features characteristic of the electronic DOS for crystalline silicon, and fluctuations in short-range order lead to tailing of electronic states into the gap. The greater the local disorder, the farther the tail states are induced into the gap. It is also agreed that dangling bonds introduce defect states near the centre of the gap.

Fig 2.1 shows a schematic description of the density of states distribution for amorphous silicon. The disorder at the band edges leads to the localised band tail states that extend from the conduction and valence bands into the energy gap of the material. The width of these tails depends on the degree of disorder and bonding character of the state [22]. The separation in energy between the delocalised states of the valence and conduction bands is called the mobility gap.

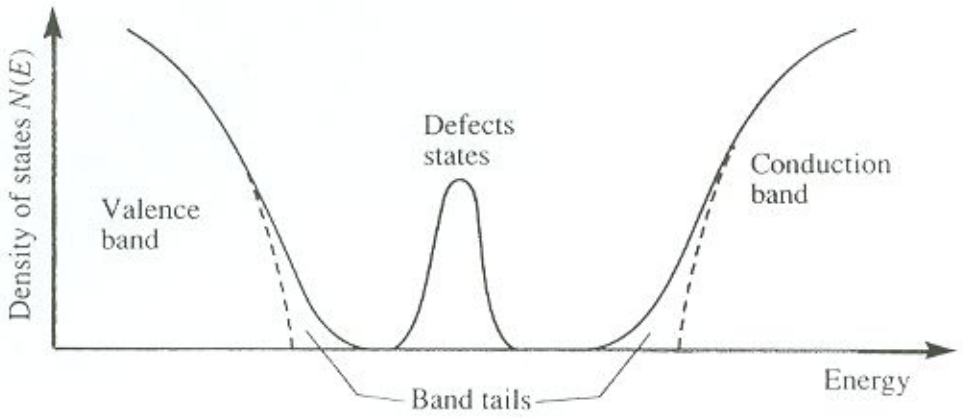

Figure 2.1: Schematic representation of the density of states distribution for a-Si:H, showing the bands, the band tails, and the defect states in the band gap. The dashed curves are the equivalent density of states in c-Si. [22].

The size of the band gap increases with increasing hydrogen incorporation in amorphous silicon [29,30]. This has been speculated to be the result of either decreasing the number of band tail states or of Si-H alloying [31]. Cody *et al.* [32] believe that the addition of hydrogen allows the amorphous structure to relax to a structure more like that of crystalline silicon. Thus, there would be less deviation in local order and less tail states caused by local disorder. Albers [31], however, believes this to be unlikely, since the process could give at most an energy gap equal to that of crystalline silicon (corresponding to the case of no disorder). The indirect gap of c-Si is 1.12 eV, while the

energy gaps observed in a-Si:H range from 1.4 to 2.0 eV. It should be noted that c-Si does have a direct gap of 3.4 eV which is larger than the gaps observed in a-Si:H [31]. However, this gap would only be observed in a-Si:H if momentum conservation rules made the indirect transition impossible. Since momentum conservation rules are relaxed in a-Si:H, it seems improbable that the direct gap would be the one observed in amorphous silicon [31]. Therefore, a Si-H alloying effect seems like a more plausible explanation for the observed increase in the energy gap.

For solar cells and other applications, what is essential is not the amorphous nature of a-Si:H, but rather the fact that it is a thin film which can be processed at low temperatures and over large areas. Moreover, the lack of long-range order or crystalline structure actually makes amorphous silicon a more efficient absorber of light than a crystalline film of the same thickness [33]. The structural differences between the amorphous and crystalline material are such that a-Si has a melting temperature about 250 K lower than that of c-Si [12]. Amorphous silicon, either hydrogenated or non-hydrogenated, is a metastable material which is thermodynamically unstable with respect to the crystalline form. The excess energy in a-Si stems from the reactive precursor molecules adsorbed at the growth surface. Figure 2.2 below illustrates the hierarchy of structural, configurational and electronic equilibria in a-Si:H.

Amorphous semiconductors, however, are not completely disordered. The covalent bonds between the silicon atoms are much the same as in crystalline silicon, with the same number of neighbours and the same average bond lengths and bond angles. The amorphous material has the same short-range order as the crystal, but lacks the long-range order. The first few nearest neighbour distances are separately distinguished, but the correlation between atom pairs loses structure after a few interatomic spacings. A real crystal contains defects such as vacancies, interstitials and dislocations. The continuous random network may also contain defects, but the definition of a defect has to be modified. Any atom which is out of place in a crystal is a defect, the simplest of

such kind being vacancies and interstitials. The only specific structural feature of a random network is the coordination of an atom to its neighbour. Thus the elementary defect of an amorphous semiconductor is the coordination defect, when an atom has too many or too few bonds. The ability of the disordered network to adapt to any atomic coordination allows an isolated coordination defect, which is not possible in a crystal [22].

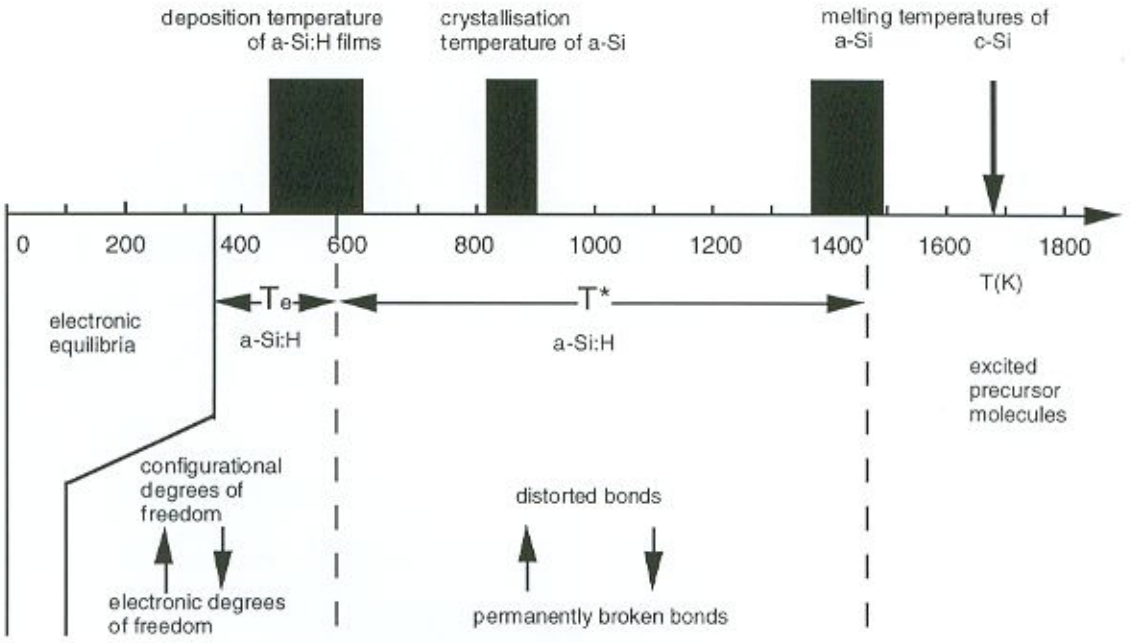

Figure 2.2: Hierarchy of structural, configurational and electronic equilibria in a-Si:H . Adapted from [12].

2.3 Hydrogen in Amorphous Silicon

Dangling bonds (coordination defects) are an inevitable consequence of the nonperiodic nature of amorphous silicon. In unhydrogenated amorphous silicon the network presents a high bonding disorder, because a fourfold coordinated network is overconstrained [34]. The incorporation of hydrogen to satisfy these silicon dangling

bonds and reduce disorder is responsible for the satisfactory electrical transport and optical properties of a-Si:H, and it is actually the incorporation of hydrogen in the disordered network which renders this material suitable for photovoltaic applications. Indeed, the high density of defects present in earlier evaporated and sputtered a-Si (unhydrogenated) films led to the belief that amorphous semiconductor films could not be doped. As mentioned above, the success in valence control of amorphous silicon by Spear and Le Comber [26] was the result of hydrogenation, and the role of hydrogen in reducing gap states in tetrahedral semiconductors was revealed in studies on sputtered amorphous films [27]. The incorporation of hydrogen into a-Si leads to a relatively low density of defect states ($< 10^{17}$ cm^{-3} [35]), thereby facilitating doping of the material in either type. Intrinsic a-Si:H behaves as slightly n-type because the electron mobility is greater than that of holes. In the hydrogenated material, hydrogen interacts with the silicon network and optimises the local bonding configurations; it saturates the dangling bonds and modifies the whole network; both the concentration and incorporation of this element affect the film properties. It is well established that states in the centre of the energy gap are due to dangling bonds; hydrogen can compensate dangling bonds, which is also possible by using fluorine. Another function that H plays, however, and that cannot be achieved by using F (possibly because of the high strength of the F-Si bond), is to reduce the tail states, whose origin is not well understood [36]. Although the dangling bond density in a-Si with no hydrogen is ~ 10^{19} cm^{-3}, and therefore much lower than the actual H content of a-Si:H (~ 10^{21} cm^{-3}), a large number of dangling bonds ($\geq 10^{15}$ cm^{-3}) remain unsaturated even in high quality films [37]. Thus, it can be concluded that only a small fraction of incorporated hydrogen eliminates potential dangling bonds and most of them bond to other sites. Most probably, hydrogen incorporation itself involves bond breaking to release strain in the construction of a Continuous Random Network (CRN) and then termination of the reconstructed dangling bonds, and creates local inhomogeneities such as voids or microvoids [37,38]. However, it is generally agreed that hydrogen also plays a negative role by introducing sites which are unstable under exposure to light. In terms of bonding configurations, it

is believed that a special requirement for a-Si:H solar cells is the need for the proper incorporation of hydrogen in the amorphous network. It is generally agreed [14,39,40], although there is still some controversy on the issue [41], that hydrogen should be present in the monohydride or Si-H bond form, rather than in the SiH_2, or SiH_3 and $(SiH_2)_n$ configurations. However, Beldi *et al.* [42] and Zellama *et al.* [43] reported films containing significant proportions of polyhydride groups with photovoltaic properties comparable to those of optimised standard films. Moreover, Toneva *et al.* [44] showed that a certain amount of dihydride (SiH_2) bonds is needed in order to relax the internal strains in the material. Also controversial is the effect of hydrogen concentration on stability. Morin *et al.* [45] have found that in the particular group of samples presented in their study there was not possible to deduce that enhanced stability would result from a reduction in the hydrogen content or the optical gap as was found by Wagner *et al.* [46]. Regarding light-induced degradation, if we accept the model in which weakly bonded hydrogen (WBH) plays a vital role in metastability, then we should attempt to produce a-Si:H material with a maximum of tightly bonded hydrogen (TBH) or, conversely, a minimum of WBH.

2.3.1 Si-H Bonding Configurations in a-Si:H

Infrared (IR) spectroscopy is commonly used to identify Si-H bonds in amorphous silicon. Generally, identifying the IR absorption peaks involves various degrees of uncertainty. In general, the procedure for assigning a bonding configuration to a particular absorption peak is to look up literature or handbook values for the vibration frequency of the counterpart in the gas phase, and then to consider the frequency shift due to the solid environment and the inductive effect [19,47] of near neighbour atoms. Usually several possibilities exist and to single out the correct one is difficult. In the particular case of a-Si:H, the analysis of infrared spectra indicates the bonded hydrogen content and the bonding configurations from the integrated intensities of distinct

absorption regions to which Si-H bonds are assigned. Table 2.1 below shows the assignments most commonly reported in the literature for the infrared vibrational modes of Si-H bonds in a-Si:H. Some disagreement still exists concerning the assignment of such modes, mostly for samples having a high hydrogen content, and particularly for multihydrogen-silicon-related modes [48].

Absorption bands may be considered as arising from vibrations involving bond-length changes (*stretching vibrations*) or vibrations involving bond-angle changes (deformation) of the group (*bending, rocking,* and *wagging vibrations*). Each of these may in some cases be considered as arising from symmetric or asymmetric vibrations [49]. The vibration bands due to stretching occur at higher frequencies than those due to deformation, because more energy is required to stretch the group than to deform it due to the bonding force directly opposing the change.

Table 2.1: Infrared vibrational frequencies for SiH_x (x = 1, 2, 3) [50-52].

	Mode (cm^{-1})		
Group	Stretching	Bending	Wagging/Rocking
SiH	2000	----------	630-650
SiH_2	2090	875 - 880	630-650
$(SiH_2)_n$	2090-2100	890, 845	630-650
SiH_3	2140	905, 860	630-650

The reasons for the continuing debate on Si-H infrared assignments are related to the physical properties of a-Si:H [50]. Due to the absence of long-range periodicity in the amorphous network, as well as to the presence of defect sites and the absence of model compounds that are hydrogen-rich, the assignment of the H-Si-related IR bands has been more difficult than originally envisaged for a binary alloy [53]. The IR modes may be affected by film morphology (*i.e.*, the presence of columnar morphology) [54], microstructure properties (*i.e.* the presence of microvoids, with atomic dimensions) [55], and the presence of polymer $(SiH_2)_n$ species [56]. The early assignments of the SiH_2 vibrational frequencies were first questioned by Freeman and Paul [51], in an analysis of integrated absorption data which showed that two types of modes existed in the 2090-2140 cm^{-1} region. Paul [48] then proposed that these would be due to a monohydride species in two different environments. The lack of a clear correspondence between the oscillator strengths of the ~ 2100 cm^{-1} stretch vibration and the SiH_2 bending band mode at ~ 900 cm^{-1} pointed to a contribution of SiH groups also to the ~ 2100 cm^{-1} band [53,57]. It was argued that monohydride species give rise to stretch modes at ~ 2000 and ~ 2100 cm^{-1} depending on their structural environment. The work of Shanks *et al.* [55], using a comparison of integrated absorption, and Reimer [58], using nuclear magnetic resonance (NMR) data, led to the assignment of two types of Si-H modes, one due to a clustered phase and the other to a distributed phase (fig. 2.3 below).

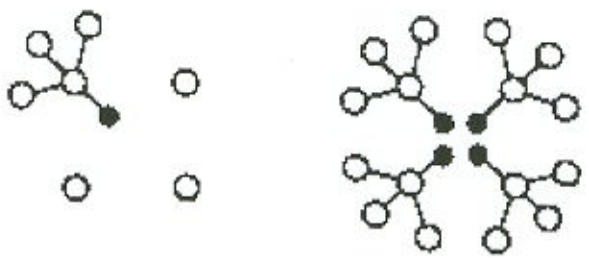

Figure 2.3: Schematic representation of Si-H distribution in a-Si:H films, showing the distributed and clustered monohydride phases. Open circles denote Si atoms; closed circles are H atoms [55,59].

According to Street [60] in a-Si:H films typically 3 - 4 at.% of hydrogen is in the diluted, distributed phase, and the remainder (5 - 10 at.%) is clustered. Matsuda *et al.* [61] have reported the preparation of a-Si:H films by the PECVD method using a xenon-silane gas mixture with no significant degradation after 10^4 minutes of light-exposure. The network structure of these films has been reported to be inhomogeneous, with the presence of microvoids and clustered hydrogen.

It has been shown that the frequency of the Si-H stretching vibrations in a-Si:H can vary from 1985 to 2010 cm^{-1} as the hydrogen concentration in the film is raised from 1 to 18 at.%. This frequency shift can be described quantitatively by the induction model [62], according to which the vibration frequency depends on both the local surroundings of the Si-H bond and the average composition of the material.

Zou *et al.* [63] have calculated that the Si-H stretching frequencies shift up from 1940 to 2145 cm^{-1} as the Si-H bond configurations change from lower to higher hydrides (SiH, SiH_2, $(SiH_2)_n$, and SiH_3). They have demonstrated that the doublets between 850 and 900 cm^{-1} result from the SiH_3 configuration. For the SiH_3 configuration, the calculated degenerate asymmetric stretching frequency was shown to be 2145 cm^{-1}, the bending frequency 906 cm^{-1}, the wagging frequency 853 cm^{-3}. The last two frequencies are very near to the doublets 907 and 862 cm^{-1} observed by experiments [63]. Lucovsky *et al.* [64] found that the absorption at 2140 cm^{-1} occurred simultaneously with that of the high frequency doublets (907 and 862 cm^{-1}) indicating that these doublets are probably related with the SiH_3 configuration.

2.4 The Staebler-Wronski Effect (SWE) in a-Si:H Thin Films

One of the most exciting aspects in the physics of hydrogenated amorphous silicon is its metastability. Metastable defect formation in a-Si:H is a most interesting phenomenon,

and is also of significant technological importance. The dominant electronic defect in a-Si:H thin films is the broken or "dangling" Si bond. The density of these dangling bonds is not a constant determined during growth, but increases after prolonged electron-hole pair recombination events up to an apparent saturation [65-66], and decreases upon annealing to a lower limit. These changes, which were first noticed as a degradation in the conductivity of this material upon light-soaking [9], are known as the "Staebler-Wronski effect" (SWE), and are metastable and fully reversible. In this context, two aspects are of interest. The local relaxations involved in metastability have some relation with the details of a-Si:H microstructure, which is affected by the growth process; and, hydrogen motion is apparently involved in these relaxations since the kinetics of defect annealing are very similar to those of bulk hydrogen diffusion [13]. Even though it is now generally accepted that these metastable changes are kinetically allowed by the diffusive motion of the bonded hydrogen within the amorphous network [12], defect annealing and hydrogen transport may as well be separate processes, both depending on the same network relaxation mechanism and may, therefore, exhibit similar kinetics [67]. But as Catalano pointed out [14], evidence continues to build that weak hydrogen bonds are responsible for the light-induced effect. Although one may, therefore, be inclined to consider the Staebler-Wronski effect intrinsic, further work is needed to fully understand the process. Thus, there are several motivations for understanding the mechanisms of H incorporation and details of a-Si:H growth. By understanding the a-Si network formation process it is hoped to learn how to produce material with improved electronic quality. Current efforts in overcoming the amorphous silicon stability problem focus on reducing the hydrogen content and determining how other material properties (microstructure, impurities, etc.) and preparation variables influence stability [15].

Many different models have been proposed to explain the electronic instability of a-Si:H [68-69], and it is widely accepted that the increased defect density after light-soaking is due to the mechanism of weak bond-dangling bond conversion, induced

by optically excited carriers [70]. From a thermodynamic point of view, dangling bond formation in amorphous silicon is an exothermic reaction with negative entropy and free energy changes [71]. Thus, since dangling bond creation reduces entropy, the lowest energy or equilibrium state is with the weak bonds split into dangling bonds. In crystalline materials, on the contrary, defects increase the entropy of the system. Weak hydrogen-silicon bonds (WHB) appear to be a function of deposition conditions and a reduction in WHB could conceivably result in a material with a low equilibrium dangling bond density at the illumination levels encountered in an operating solar cell [71]. Greim *et al.* [72] have illustrated the possible role of hydrogen in the Staebler-Wronski effect as follows: during illumination the photogenerated electron-hole pairs contribute to free hydrogen from Si-H bonds in H-clusters, thus creating dangling bond traps that act as recombination centres for the photogenerated carriers. The H atoms diffusing from interstitial sites to interstitial sites can create more traps by breaking stretched Si-Si bonds (Si-Si + H => Si-H + Si). This interpretation is consistent with the fact that the SWE is more pronounced in films with a high H concentration [73], where more of the loosely bound hydrogen is available. Ovshinsky [11] is also convinced that the SWE is intimately tied to weak bond formation, and that the answer to this effect lies in stronger and more tetrahedrally bonded configurations and more dense materials.

The a-Si:H network and its defect structure appear to be the result of an equilibrium process that is upset by a variety of causes, including illumination, thermal and electron-beam exposure and carrier injection [74-75]. Time constants for re-equilibration are in the minute range at 200 °C for intrinsic-type material, but due to an activation energy of 1-1.5 eV [76], thermally induced relaxation can be extremely slow at room temperature. In equilibrium, the defect density is determined by the Fermi level position, *i.e.* by the occupancy of localised states; because the amorphous network is not entirely rigid, electronic energy changes can induce configurational changes, which include transitions from bonded to broken configurations.

Among the many microscopic models that have been proposed for the observed metastability in a-Si:H, the weak-bond breaking model by Stutzmann [77], suggesting rupture of strained Si-Si bonds and conversion into dangling bonds; the internal conversion model by Adler [78], proposing conversion of neutral into charged defects; and the impurity model by Redfield and Bube [79], relating structural instability to extrinsic impurities, are the most frequently cited. However, there has remained considerable uncertainty as to the microscopic processes of defect formation, the precursor states for induced defects, the formation mechanisms, about the saturation level of defects and the stoichiometry dependence of the instability [76]. Each of these models seems to be able to describe the main observations of a-Si:H metastability from which they derived. No model, however, offers a complete description of all the aspects involved in the light-induced degradation of amorphous silicon thin films and solar cells. Nevertheless, they all agree in many points which include:

(i) Creation of dangling bonds

(ii) Possible involvement of hydrogen either directly, by the formation of unstable hydrogen sites, or indirectly, by the stabilisation of defects

(iii) The film stability might be improved beyond today's device quality materials

Control over the hydrogen bonding configurations and reduction of the number of weak bonds appears to be, therefore, one of the most important targets in the attempts to overcome, or at least minimise, the Staebler-Wronski effect.

2.5 Hydrogen and Metastability in a-Si:H

The phenomenon of metastability in a-Si:H is closely related to the defect equilibrium properties. Some external excitation (illumination, charge, current flow, energetic

particles, *etc.*) induces defects which are subsequently removed by annealing. The metastable defects anneal at 150 - 200 °C, which is the temperature at which equilibration occurs in a few minutes, immediately suggesting a connection between metastability and defect equilibration. Annealing is simply the restoration of thermal equilibrium which is disturbed by the external excitation. The annealing kinetics of the light-induced defects is such that several hours at 130 °C are needed to anneal the defects completely, but only a few minutes at 200 °C. Annealing is the process of relaxation to the equilibrium state with a low defect density. The association of the relaxation kinetics with the hydrogen diffusion rate is regarded as evidence that the defect creation process is the result of hydrogen motion [22].

Stradins and Fritzsche [80] have very recently shown by subgap absorption and steady state photoconductivity measurements that metastable defects can be induced by light with appreciable efficiency at 4.2 K. This means that defect creation by recombination of photocarriers proceeds without thermal activation. This in turn suggests that a very local atomic motion, presumably of hydrogen, is sufficient to stabilise the pair of dangling bond defects created in the recombination process. The key for understanding the metastability problem in amorphous silicon is most probably related to a more detailed knowledge of hydrogen bonding configurations, hydrogen motion and hydrogen bonding stability mechanisms. The diversity of results reported for a-Si:H prepared by various techniques and deposition conditions indicate that a complete understanding of the physics of this amorphous material is far from being realised. In contrast to what was found by Wagner *et al.* [46], Morin and co-workers [45] have found that it was not possible to conclude that improved stability would result from a reduction in the hydrogen content in a-Si:H films. Hydrogen and metastability in a-Si:H remain a most exciting research topic and considerable research efforts are continuously being focused on their many aspects, not only because the solution or minimisation of the light-induced degradation problem is of a high technological importance, but also

because amorphous silicon provides an ideal system in which to study the physics of amorphous semiconductors.

2.6 Atomic Hydrogen and Hydrogen Plasma Treatments

Hydrogen can partially penetrate the silicon network. The stable bonding configurations are the Si-H bonds and unstrained Si-Si bonds which are too strongly bonded to be broken by hydrogen. Highly strained Si-Si bonds have energies close enough to the chemical potential of the hydrogen that they are broken and either remain as Si-H bonds or are reconstructed into stronger Si-Si bonds [22,34]. There is experimental evidence that bonded hydrogen in the a-Si:H film can be removed by reaction with hydrogen from a plasma [81,82]. These reactions produce the silicon dangling bonds which may bond to each other or incorporate another hydrogen. Similarly, weak Si-Si bonds are broken by hydrogen and may be reformed as different stronger bonds. All these reactions change the hydrogen content and modify the local structural order of the silicon network. An *et al.* [83] showed, for films prepared by PECVD, that by alternating a-Si:H growth with exposure to atomic H generated by a tungsten filament heated in H_2 it is possible to convert weak Si-Si bonds to Si-H bonds in the top ~ 200 Å of the film. It is believed that this is made possible as the H chemical potential in the film is raised [34].

The ideal structure and bonding of hydrogen in amorphous silicon and its role in determining the material's photovoltaic properties is still, as previously mentioned, a matter of debate. Thus a higher degree of control over Si-H bonding configurations in the deposition of a-Si:H is desirable. Techniques such as hydrogen plasma treatment, strong hydrogen or helium dilution of silane gas, and ion-gun chemical vapour deposition (CVD), can be used to fabricate a device-quality a-Si:H i-layer with a wide bandgap which cannot be achieved by conventional plasma enhanced chemical vapour

deposition (PECVD) preparation conditions [84]. That is because the higher deposition temperatures involved in producing device-quality PECVD films incur in low hydrogen concentrations and the associated narrower bandgaps. Deposition and post-deposition techniques have to be developed in which films can be prepared at optimum deposition temperatures and hydrogen contents and bonding configurations can still be tailored in order to obtain the desired bandgap and structure. Also, techniques using atomic hydrogen obtained from the thermal decomposition of molecular H_2 with a hot filament should be preferred, so that the potentially damaging effects due to direct hydrogen plasma exposure (i.e. energetic particle impact) are avoided.

2.6.1 Technological Consequences

Hydrogen treatment methods using either atomic H or a hydrogen plasma have been recently applied to the deposition of amorphous silicon thin films with excellent results. In what the authors called "alternately repeating deposition and hydrogen plasma treatment method (ADHT)", Tanaka *et al.* [85] have grown films in which the optical bandgap of the a-Si material was increased by hydrogen plasma treatment. They produced wide optical bandgap and the highly photoconductive a-Si:H films without carbon, to be used as the window layer in p-i-n amorphous silicon solar cells. The conversion efficiency of solar cells with this ADHT film was almost the same as that using an a-SiC:H buffer layer. Using this method, the use of inverted carbon graded a-SiC:H layers and the technological process complications involved can be avoided.

Wide bandgap a-Si:H is of particular interest to improve the open circuit voltage (V_{oc}) and the conversion efficiency of amorphous silicon solar cells. The film quality of wide bandgap a-Si:H has marked influence on the output characteristics of multijunction solar cells [86]. To increase the optical gap of a-Si:H, one of the methods used is alloying with elements such as carbon, oxygen or nitrogen. This, however, distorts the

amorphous silicon network, often resulting in the degradation of film properties, and it would thus be preferable to broaden the bandgap without alloying. The optical bandgap of pure a-Si:H is almost entirely determined by the bonded hydrogen content (C_H) of the film [87], and when it is prepared by the RF plasma chemical vapour deposition (plasma-CVD) technique, C_H is most effectively controlled by the substrate temperature (Ts) during deposition [88]. Wide bandgap a-Si:H films with a large amount of hydrogen are usually obtained at Ts $\leq$ 100°C, which often results in poor film properties (low photoconductivity, high defect density, *etc.*). It is known that hydrogen atoms can also be incorporated into a-Si:H after film deposition, by exposing the film to a hydrogen plasma for example. In earlier studies about post-hydrogenation [89-91], interest was focused mainly on the termination of dangling bonds in relatively defective a-Si:H or a-Si films. More recently, Okamoto *et al.* [87] have reported about the effect of additional hydrogen intentionally incorporated into device quality a-Si:H with a moderate bonded hydrogen content (C_H ~10 - 15 at.%).

Narrow bandgap a-Si:H is also of technological interest to be used as a bottom layer in multijunction a-Si based solar cells, and a-SiGe:H has been used to that effect [92]. One problem with the deposition of Si alloys containing Ge for example is that higher deposition temperatures are required, which increase H evolution [11] and degrade film quality. Therefore, hydrogen treatment of a-SiGe:H alloys might prove beneficial in the control of hydrogen content and bonding configurations.

Chapter 3

Amorphous Silicon Solar Cells

A variety of applications of a-Si:H have been proposed or are under development; almost all of them depend on the ability to deposit a-Si:H over large areas. Photovoltaic solar energy conversion was the original major application proposed for a-Si:H, and is the largest in production to date [3,4]. The first devices had an efficiency of only 2 - 3 % [3] and since then there has been a remarkable increase in the efficiency of the cells. Conversion efficiency increased roughly 1 % per year, to a present value of around 14 % [7,11]. Innovations in the design, materials and structure of the amorphous silicon solar cell were responsible for these vast improvements in the efficiency figures. Because the sensitivity of a-Si devices peaks at shorter wavelengths as compared to that of c-Si solar cells, there is a much better match to the spectrum of fluorescent light. The a-Si solar cell is thus ideal for indoor applications, and its use in consumer products has allowed an important niche market to flourish [4]. Moreover, because many such products require rather high voltages to drive their circuits, the possibility of integrated-type, monolithic structures possible in the a-Si technology constitute an attractive low-cost alternative.

This chapter highlights the most important characteristics and properties of amorphous silicon solar cell devices. A sidelight is included to introduce the topic of seasonal shifts

in device performance and variations in the terrestrial solar spectral content, which will be further discussed in chapter 11.

3.1 Low-Cost Solar Cells

The optical absorption coefficient of a-Si:H is more than an order of magnitude larger than that of single crystal silicon [93] at the maximum solar photon-energy region near 500 nm. Calculations of the optimum thickness of solar photovoltaic active region for various solar cell materials indicate that only ~ 0.5 μm is necessary for the active layer of a-Si solar cells [94]. This represents the thinnest of all solar cell materials under consideration, and is less than 1/500 of the material thickness usually used in single-crystalline silicon solar cells [95]. Consequently, it represents not only a resource saving, but also an energy saving solar cell material as well. Furthermore, the fact that amorphous silicon can be deposited onto any foreign substrate material without the constraints of lattice periodicity represents a major advantage for practical applications. This non-epitaxial deposition is well suited for mass production of large-area, low-cost solar cells.

3.2 Device Configuration

The first amorphous silicon solar cell was presented by Carlson and Wronski in 1976 [3], in a glass / p-i-n device configuration, with a conversion efficiency of 2.4 % in AM 1.0 sunlight. In 1977, Carlson [96] presented a 5.5 % efficient solar cell with a Pt / a-Si:H Schottky barrier configuration, which then appeared to offer the best promise of approaching the estimated efficiency limit of ~ 15 %. One year later, Okamoto *et al.* [97] reported 4.5 % efficiency with a p-i-n on stainless steel (SS) structure. Even though both Schottky barrier and Metal-Insulator-Semiconductor (MIS)

solar cells were produced and demonstrated in the early stages of amorphous silicon solar cell technology development, most a-Si photovoltaic devices presently produced in both industrial and laboratory scales are based on the p-i-n (or n-i-p) junction design. The p-i-n structure and its variations is schematically shown in figure 3.1 below, and it has been recognised as having several advantages over other design structures, not only on performance and stability, but also in reproducibility, scaling up to large-area cells and automation of the manufacturing processes [98]. The primary substrates on which amorphous silicon solar cells are formed are glass and stainless steel, as well as flexible polymers to a lesser extent.

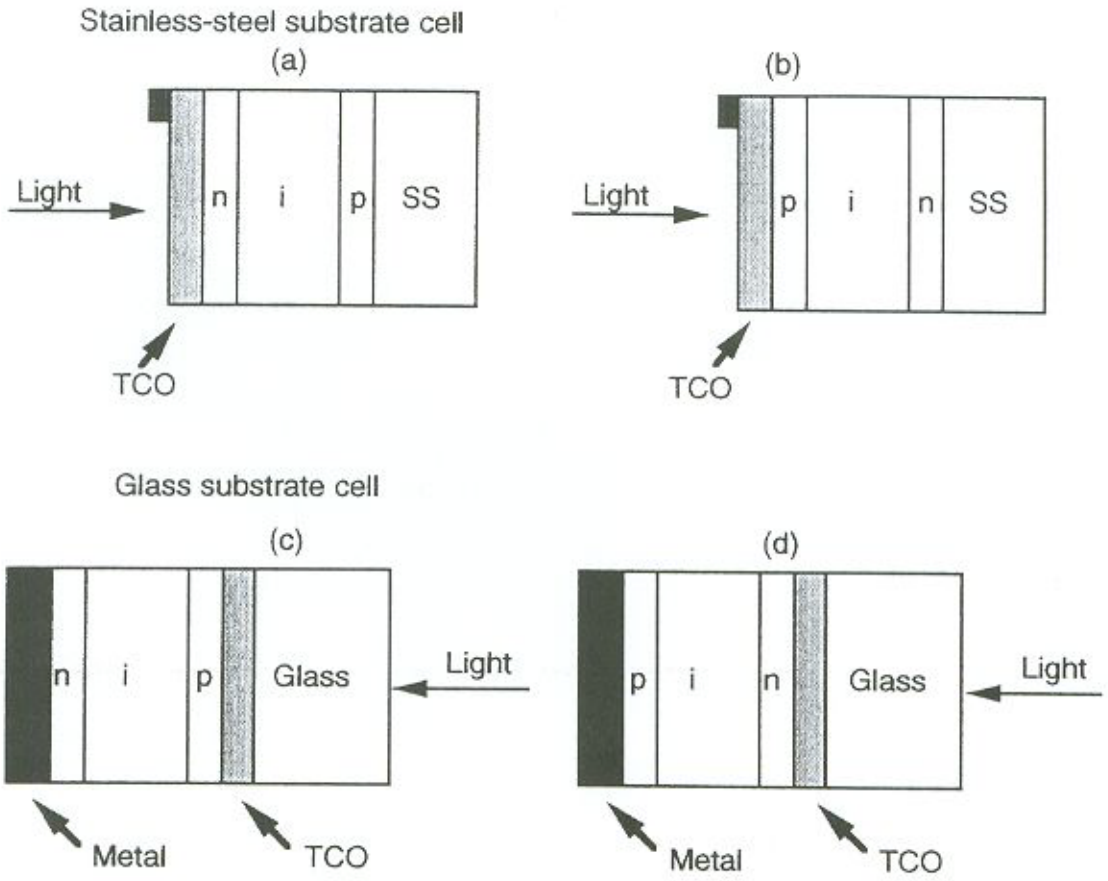

Figure 3.1: Schematic structures for p-i-n type amorphous silicon solar cells. (a) TCO / n-i-p / SS; (b) TCO / p-i-n / SS; (c) Glass / TCO / p-i-n / Metal; and (d) Glass / TCO / n-i-p / Metal. Dimensions are not to scale.

Because of the relatively lower current densities generated by amorphous silicon solar cells compared to their crystalline silicon counterparts, current collection can in most cases be effectively performed without the need of a metal grid, and a transparent conductive oxide (TCO) is commonly used to that effect. Indium tin oxide (ITO), tin oxide (SnO_2) and zinc oxide (ZnO) are widely used because of their low sheet resistivity and high transparency in the visible region. High growth temperatures and a degradation of optical properties in hydrogen plasma limit the applications of tin oxide films. Zinc oxide has recently gained great attention as a TCO because of both high stability in hydrogen plasma and low growth temperature, as well as a lower sheet resistance than that of SnO_2 [99].

A basic difference between the photovoltaic mechanisms of silicon single crystal p-n junctions and amorphous silicon p-i-n junctions is caused by the very short diffusion length and very high absorption coefficient of amorphous silicon [100]. In the p-i-n a-Si solar cell, there exists a high electric field in the carrier generation region. Doped a-Si:H has a very high defect density, and a correspondingly small charge collection and narrow depletion width [101]. The doped layers therefore primarily provide the electrical junction, and are made as thin as possible. The p- and n-layers establish the open circuit voltage (V_{oc}); the thicker undoped (i-type) layer has a high charge collection because of its low defect density and collects the photocurrent. The internal electric field in the i-layer varies very sharply as function of both the midgap state density and induced space charge distributions [102]. In this device configuration, the p- and n-layers provide the built-in potential of the junction, but contribute very little to the collection of carriers. Therefore, the doped layers need to be no more than the width of the depletion layer to establish the junction, and any additional unnecessary thickness reduces the charge collection by absorbing incident light. In order to increase the collection efficiency, the undoped layer should be as thick as possible to absorb the maximum flux of photons,

but should not be thicker than the depletion width if collection efficiency is to be maximised [22].

The maximum theoretical V_{oc} of a solar cell is set by its built-in voltage. For amorphous silicon p-i-n cells the Fermi levels in the p- and n- contact regions lie on the order of 0.4 and 0.2 eV from their respective band edges (the Fermi levels in the p-region is ~ 0.4 eV above the valence band and in the n-region it is ~ 0.2 eV below the conduction band, resulting in a built-in voltage ($V_{built\text{-}in}$) of Egap - 0.6 eV $\simeq$ 1.1 eV)[103]. The conversion efficiency of solar cells is limited by optical and electrical factors. Optical losses depend on the match of the solar spectrum with the optical absorption coefficient of the active material and also on the reflectivity at the different interfaces of the device. These losses limit the maximum value of I_{sc}. The electrical losses depend on transport mechanisms which affect the fill factor (FF) and V_{oc} as previously mentioned.

In amorphous silicon, a high internal electric field gives rise to a large drift current. For that reason, associated with the fact that in this material the diffusion length is very short, the behaviour in this kind of solar cell can be referred to as drift-type photovoltaic effect. In fact, the drift current is almost four orders of magnitude larger than the diffusion current [104].

The maximum theoretical efficiency of single-junction cells is estimated to be about 14 - 15 % [22], but that of multijunction cells is around 24 % [105]. Present single-junction cells are about 80 - 90 % of the theoretical efficiency. A single junction solar cell is a compromise between the high V_{oc} of a material with a large bandgap and the high charge collection over a wide portion of the solar spectrum from a material with low bandgap. As previously pointed out, the bandgap in a-Si:H can be tailored within a wide range, either by alloying with other elements or by varying the hydrogen content.

3.2.1 p-i-n and n-i-p Junctions

The photovoltaic performance of p-i-n and n-i-p-based solar cells is strongly dependent on the photovoltaic properties of the a-Si:H film and cell construction parameters, such as the thickness of each a-Si:H layer and the amount of doping of the p- and n- layers. There is also a dependence on the order of deposition of the p-, i- and n-layers [98]. It has been shown that the photovoltaic performance of ITO / n-i-p / SS cells is superior to that of ITO / p-i-n / SS cells (figure 3.1 (a) and (b) respectively) [106]. However, for glass-substrate cells, a Glass / ITO / p-i-n / Metal structure has been commonly adopted because of its better cell performance compared with that of a Glass / ITO / n-i-p / Metal structure (figure 3.1 (c) and (d) respectively). The difference in conversion efficiency between the two types of SS-substrate cells is due to the type of dopant in the doped layer deposited prior to i-layer deposition; which is also the case in glass-substrate cells [98]. Cells which have the i-layer deposited on the boron-doped p-layer, have junction properties more suitable for solar cells than those that are deposited on the n-type layer. It has been pointed out that the i-layer of the p-i-n structure contains a certain amount of phosphorus or boron that is incorporated from the pre-deposited doped layer [107].

3.2.2 Multijunction and Tandem a-Si-Based Solar Cells

Multiple junction solar cells are more efficient photovoltaic converters than single-junction devices. By combining blue and red-sensitive solar cells, high energy photons are absorbed in a higher bandgap semiconductor with a resultant higher voltage output, and the lower energy part of the solar spectrum is absorbed by introducing a lower bandgap semiconductor junction as a bottom cell. The spectral response region is thus broadened with this design approach. Multijunction and stacked (tandem) solar cells were originally proposed for crystalline semiconductor devices [108], but theoretical

estimates have not been realised. This is partly because of the difficulty in developing high quality material for the low bandgap junctions, and also due to mismatches in lattice constants between higher and lower bandgap materials. From a theoretical point of view, the tandem-type solar cell can be considered as the most efficient method of conversion of sunlight into electricity. The basic idea is to split the solar spectrum into multiple regions and to assign each spectral region to a particular semiconductor material, or, in the case of a-Si, to a particular a-Si bandgap junction. Thus, the energy loss due to the difference hν - Egap (hν being the photon energy) is minimised.

The higher efficiency expected in a tandem-type solar cell compared to a conventional single-junction device is not only the result of a broadened spectral response region, but also due to a higher V_{oc} in the tandem solar cell. V_{oc} is in this case the sum of the V_{oc} of each junction in the cell, and the energy loss due to hν - Egap is divided in each junction for the respective spectral region [108]. Moreover, amorphous semiconductors have a relatively large elasticity in the lattice constant, so that in tandem-type structures the lattice strain is lower than in crystalline materials. Triple junctions of a-SiC:H (1.85 eV) / a-Si:H (1.70 eV) / a-SiGe:H (1.38 eV); a-Si:H (1.75 eV) / a-Si:H (1.75 eV) / a-SiGe:H (1.38 eV) [109,110], and tandem a-Si:H (same bandgap = 1.75 eV) [111] solar cells using both glass and stainless steel substrates have been prepared in the laboratory level and start now to be incorporated into production lines [112]. Figure 3.2 shows the schematic representation of a three-stacked solar cell device deposited on a stainless steel substrate.

The most rewarding aspect of using the multijunction design approach in a-Si solar cells however, is related to the circumvention of the light-induced degradation effect. Multijunction a-Si solar cells present much thinner i-layers than single-junction devices. Decreasing the thickness of the i-layer increases the strength of the internal

electric field so that the photogenerated carriers are swept out of the active layer before they can recombine or be trapped and give rise to metastable defect centres. Multijunction amorphous silicon solar cells are thus more stable to light-induced effects than their single-junction counterparts. Another reason for their better stability is that the lower junctions of a multijunction solar cell do not receive as much light as a single-junction cell would, and thus degrade more slowly.

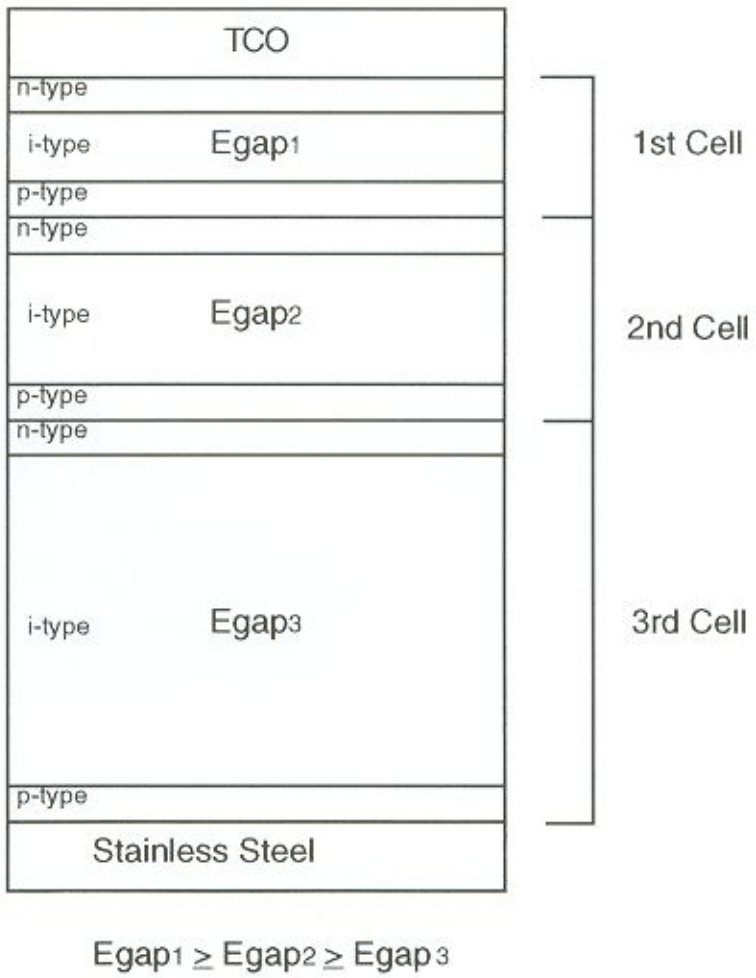

Figure 3.2: Schematic representation of multijunction/tandem-type amorphous silicon-based solar cells deposited on a stainless steel substrate

3.3 Spectral Response Characteristics

In "conventional" (crystalline Si) solar cells, the response at short wavelengths (also referred to as blue response) is poor due to the deep junction employed; the effect is also augmented by the absorption in the antireflective coating [113]. At long wavelengths, the spectral response is determined by the diffusion length in the cell material (for a fixed bandgap). In the amorphous silicon solar cell, the active material's bandgap and its high optical absorption coefficient is what ultimately determines the device's spectral response characteristics. The optical absorption coefficient of a-Si:H is more than an order of magnitude larger than that of crystalline silicon over most of the visible light range [114], resulting in a considerably high quantum efficiency at shorter wavelengths for the amorphous cells. A higher bandgap as compared to that of its crystalline counterpart, however, limits the spectral response in the long wavelength region to less than 800 nm for a single-junction, 1.75 eV bandgap material a-Si solar cell. Figure 3.3 shows the measured quantum efficiencies for selected solar cell types. Single-junction amorphous silicon solar cells present an excellent collection efficiency in the visible region of the solar spectrum (with response better than 5 % in the 360 - 790 nm region for a 1.75 eV bandgap material [115]). In multijunction-type a-Si solar cells, due to the lower bandgap a-Si-based alloys used in the bottom cell, spectral response is extended into the infrared region (with response better than 5 % in the 360 - 900 nm region for a triple-junction 1.75 / 1.75 / 1.35 eV, two-terminal solar cell [115]). Crystalline Si solar cells, in contrast, have a response better than 5 % in the 380 - 1180 nm region (Egap = 1.12 eV) [115].

Due to a relatively high bandgap and high optical absorption coefficient at shorter wavelengths, amorphous silicon-based solar cells are heavily blue-biased compared to crystalline silicon cells. The consequences of these differences in spectral response characteristics will be further analysed in the discussion on the seasonal effect in a-Si:H solar modules under outdoor conditions, to be presented in chapter 11.

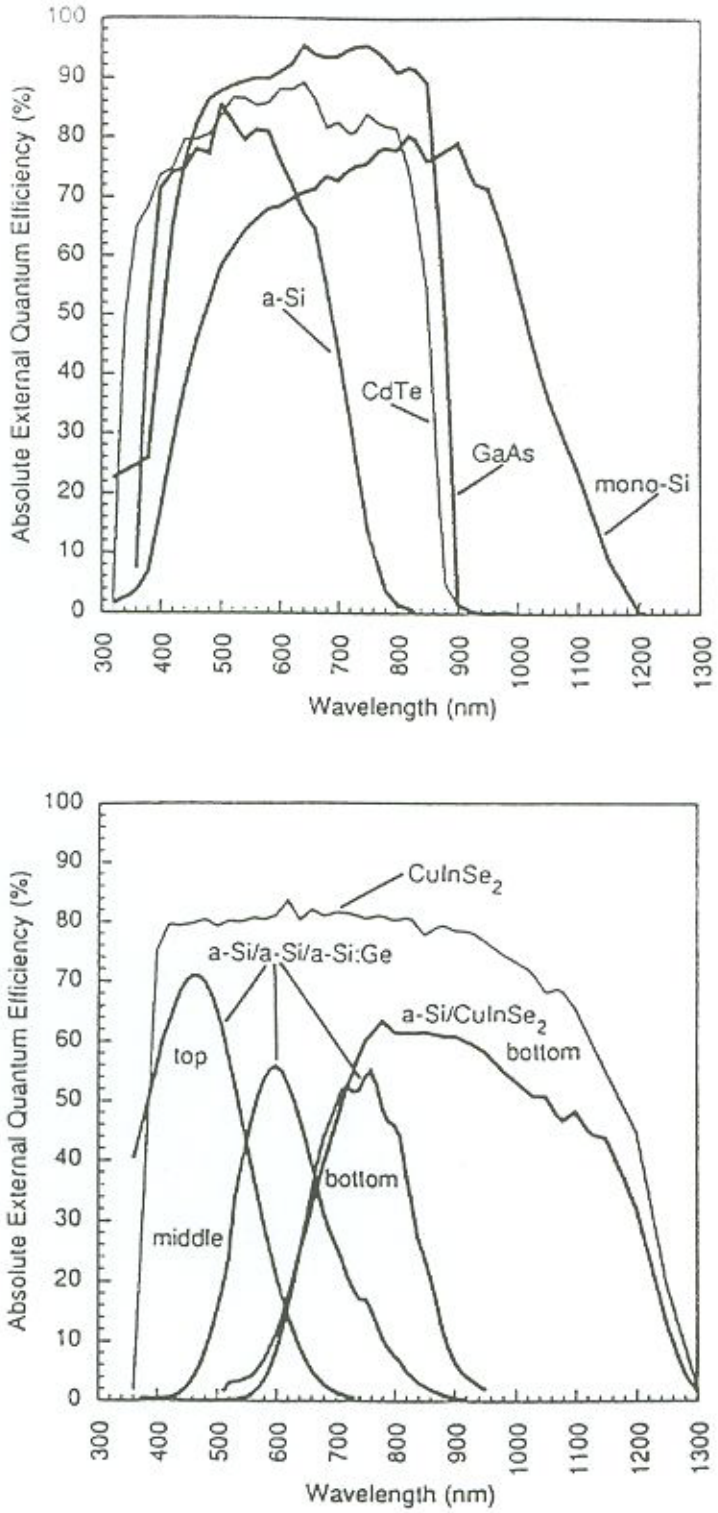

Figure 3.3: Measured quantum efficiencies for commercial-type single crystalline Si, and laboratory-type a-Si:H, CdTe and GaAs, a-Si:H / a-Si:H / a-SiGe:H three-junction tandem, $CuInSe_2$, and the bottom cell in a four-terminal tandem made of a-Si:H mechanically stacked on $CuInSe_2$. From [115].

3.4 Terrestrial Solar Spectral Content and Seasonal Shifts

The intensity of sunlight per unit area reaching the earth's surface at solar noon is usually referred to as "1 Sun intensity", which corresponds to 100 $mW.cm^{-2}$. This is the *total* energy content of the solar spectrum reaching the planet's surface after being "filtered" by the atmosphere. Before atmospheric attenuation, extraterrestrial radiation presents a very broad spectral distribution, with ~ 7 % in the ultraviolet region (< 380 nm), ~ 47 % in the visible range (380 - 780 nm) and ~ 46 % in the infrared region (780 - ∞) [116]. The solar radiation received at the surface of the earth, however, is subject to variations due to *atmospheric scattering* by air molecules, water vapour and dust, and also to *atmospheric absorption* by ozone, water and carbon dioxide. Since the amount of air molecules, water vapour, dust, ozone and carbon dioxide all depend on both the site location and time of the year, neither the total solar energy received nor its spectral content can be regarded as constants.

The ratio of the optical thickness of the atmosphere through which solar radiation passes to the optical thickness it would pass through if the sun were at the zenith position is defined as the *air mass* (AM). At sea level AM = 1 when the sun is at the zenith, and AM = 2 when the zenith angle is $\theta_Z = 60°$. For zenith angles from 0° to 70° at sea level, $AM = (\cos \theta_Z)^{-1}$ [116]. For higher zenith angles, the effect of the earth's curvature becomes significant and must be taken into account. From summer to winter, due to increased zenith angles, there is an increase in midday air mass from 1.0 to 1.4 [117], which results in a shift of the terrestrial solar spectral distribution towards longer wavelengths. Figure 3.4 shows the spectral distribution of solar radiation for various air masses.

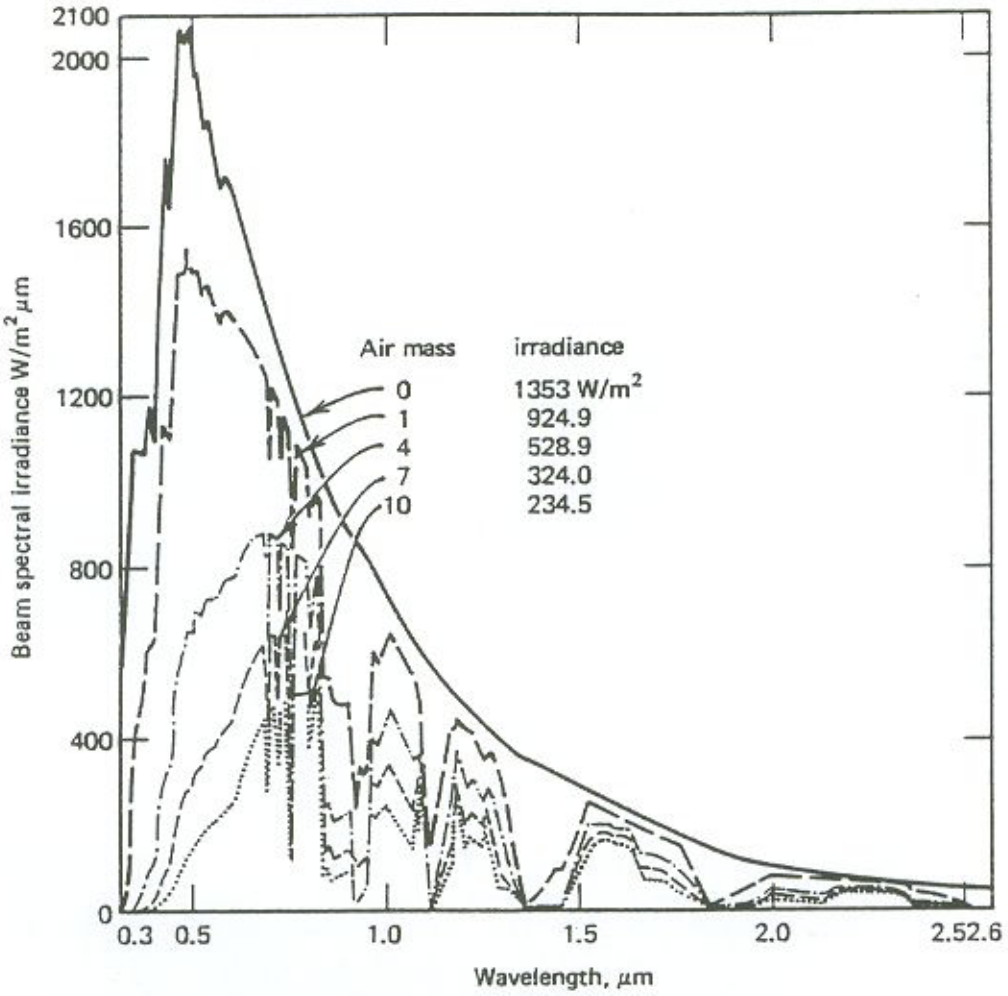

Figure 3.4: Spectral distribution of direct solar radiation for various air masses, assuming a very clear atmosphere. From [116].

3.5 The Staebler-Wronski Effect in a-Si Solar Cells

In the Staebler-Wronski effect, a-Si:H shows an increase in the number of defects after long-time light illumination (light-soaking). Illumination with hν > Egap generates defects in the material which cause various device-related properties (i.e. transport and recombination) to deteriorate. These defects are associated with localised states in the band gap of the material which manifest themselves in a number of ways, the most

important being that they reduce the lifetime of excess carriers by accelerating their recombination process, thus reducing the conversion efficiency of amorphous silicon solar cells. The number of defects eventually saturates under intense illumination and the sample can almost be annealed to its original state. The induced defects, thought to be threefold-coordinated Si atoms (dangling bonds), play an important role in the recombination process. The defect density in the i-layer is increased, which in turn causes a higher space charge and more compensation of the internal electric field so that recombination of photogenerated carriers increases and their collection decreases.

The single-junction p-i-n a-Si:H solar cell in fact consists of two cells, a p-i front cell and an i-n back cell in tandem. This results in a high electric field in both the front and the back parts of the i-layer, but a very low electric field in the middle part. The carrier collection efficiency, and hence the fill factor, depend on these field profiles [118]. Because in a-Si:H the major transport mechanism is due to a field-aided diffusion (the drift-type photovoltaic effect previously mentioned), the range of holes and electrons is the critical parameter determining transport, and for carriers to be efficiently collected the range must be much larger than the distance to be covered. In as-deposited or annealed-state a-Si:H this condition is usually met, and the range is of the order of 5 μm [118], which is much larger than the distance to be travelled, usually 0.5 μm or less. However, with light-induced degradation the midgap defect density increases significantly, leading to a marked reduction in the electric field in the middle of the device. Also, the increase in the defect density causes a severe decrease in the range of the carriers, making it comparable to the thickness of the i-layer, with a consequent reduction in the quantum efficiency of red photons, which reduces the fill factor.

In the early a-Si:H solar cells, the SWE caused the conversion efficiency to drop by as much as 40 %; present generation of commercial-type solar cells, however, are expected to degrade only ~ 10 % after the first 1000 hours under sunlight exposure (approximately 1 year outdoors in many Northern hemisphere sites) and stabilise after

that. The general features of the degradation vary; the amount of degradation depends on the film quality and the initial conversion efficiency. In terms of the photovoltaic performance, *i.e.* I-V characteristics, the SWE manifests itself as a strong degradation in fill factor (FF) and short circuit current (I_{sc}), as well as a decrease in the open circuit voltage (V_{oc}) to a lesser extent. Also, being a consequence of recombination events, the SWE depends on the load condition of the solar cell; the open circuit condition is therefore the worst case load for stability performance studies.

3.6 Thermal Annealing of the Staebler-Wronski Effect

Thermal annealing of a-Si:H solar cells at ~ 150 °C for a few hours in the dark usually restores the original output parameters. In the field, under outdoor conditions, solar modules are exposed to different ambient and operating cell temperatures during the year. This has led to the observation of an unusual phenomenon in the operation of this kind of solar cell outdoors. The effect of self-annealing, *i.e.* the ability of the a-Si:H solar cell to recover, at least partially, from the SWE during the warmer conditions of summer months, has been widely reported in the literature lately [119-121]. If the annealing process which restores initial cell efficiencies involves bond breaking as it was mentioned in section 2.4, then it should be strongly temperature dependent. The annealing energy, which has a distribution energy centred at ~ 1.05 eV [122] has been shown to lead to annealing times in the order of 1 hour at 150 °C and around 1000 hours at 50 °C in the dark to anneal completely the light-induced defects in amorphous silicon films. For this reason, the self-annealing or thermal annealing effect is not likely to be the main or even the sole contributor to the reported efficiency recoveries as generally believed [119-121]. Section 3.7 will present further aspects about the seasonal effect in a-Si photovoltaics. Figure 3.5 shows the strong temperature dependence of the thermal annealing process, according to Hata and Wagner's calculations [122] for defects with an annealing energy of 1.05 eV.

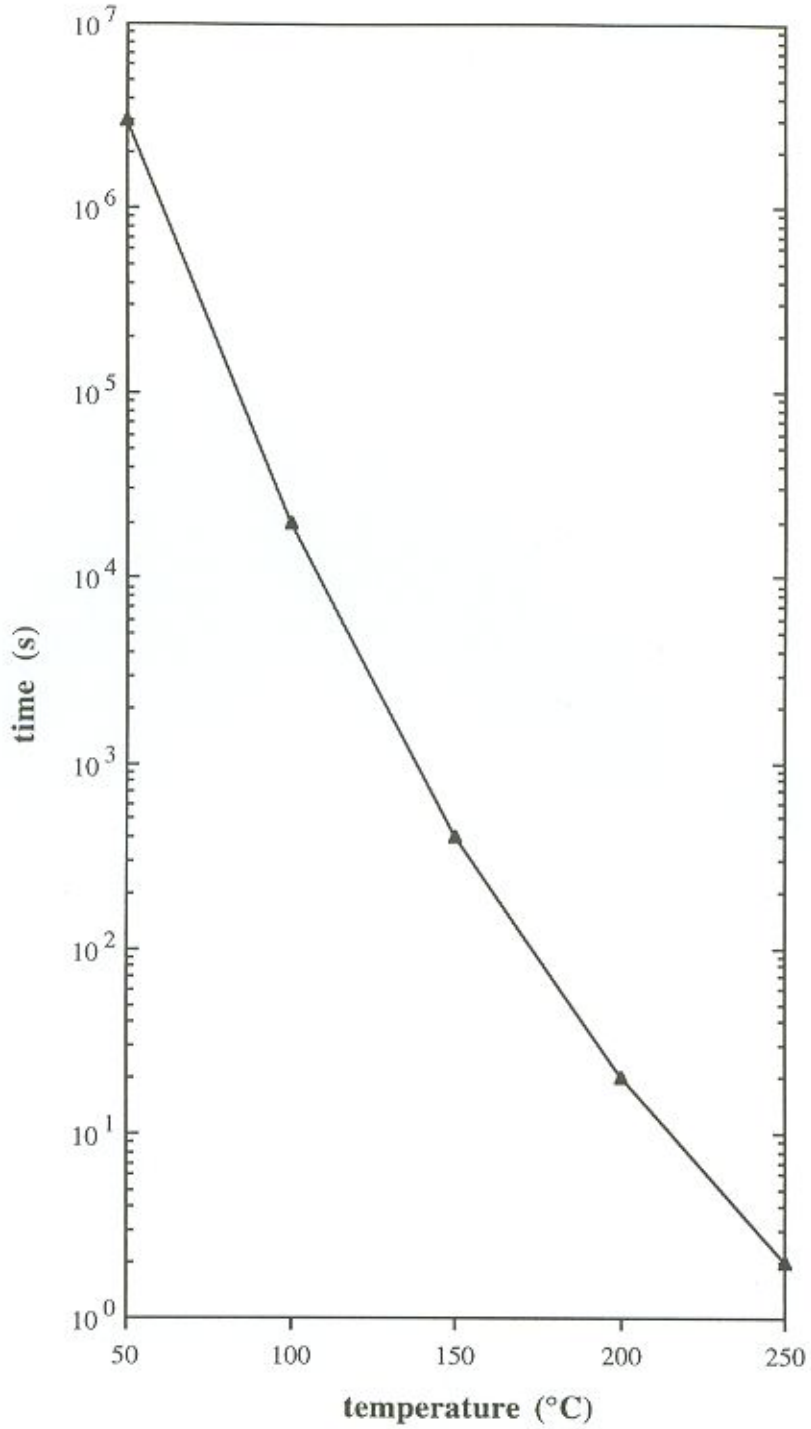

Figure 3.5: Estimated defect annealing time for the a-Si:H thermal annealing temperature dependence, for defects with an annealing energy of 1.05 eV at different temperatures. Data from [122].

3.7 Seasonal Effect in a-Si:H Solar Modules under Outdoor Conditions

Amorphous silicon solar modules exposed to outdoor conditions exhibit, over a long-time scale, an efficiency pattern which improves during summer months and decreases in winter time. The variations are usually attributed to two main mechanisms: (i) thermal annealing effects enhanced by summer month temperatures, which might partly offset the efficiency decrease caused by the reversible light-induced changes in the amorphous silicon material, the Staebler-Wronski effect; and (ii) seasonal spectral variations in the solar radiation reaching the earth's surface, which are quite marked in the wavelength region in which amorphous silicon solar cells respond.

There is still debate over this matter; the first mechanism however, is usually regarded as being dominant and many investigators do not even mention the latter effect [119-121,123]. The seasonal effect describes the output efficiency pattern in a long-time scale. Output power decreases during winter months and recovers during summer time. In relation to initial values, Ragot *et al.* [124] report that the maximal power ranges from 71 % in winter to 83 % in summer for their testing site in southern France. This periodic evolution in module efficiency in an annual basis has been widely reported in the literature [115,124-126] and it can be correlated with the evolution of the ambient temperature, what has led to the belief that a partial recovery (thermal annealing) of the Staebler-Wronski effect during summer months is the major cause of the increased efficiency.

Figure 3.6 below shows the evolution of the maximum power (P_{max}) over a 4.5 years period, where the oscillation illustrates the seasonal effect. The figure also shows the variation in the ambient temperature during the same period.

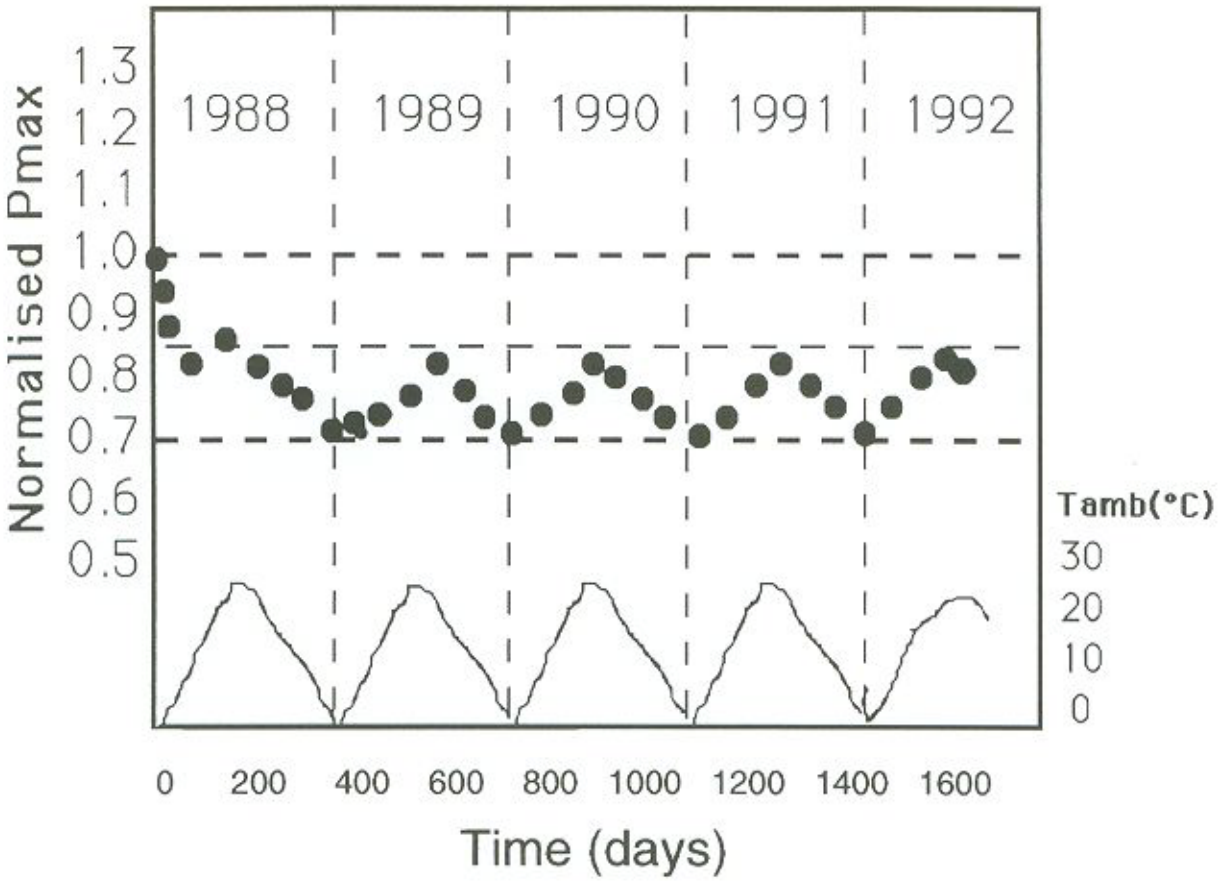

Figure 3.6: Normalised evolution of the maximum power (Pmax) with exposure time showing the seasonal effect on amorphous silicon solar modules over a 4.5 years period outdoors. Adapted from [124]. Also shown is the variation in the mean ambient temperature during the same period.

Solar spectrum variations during the year are considerable, especially in the response range of amorphous silicon alloys and other higher bandgap materials. For these materials spectral effects become an issue since their response range falls in the region of the solar spectrum where most changes between winter and summer occur, as was pointed out in sections 3.3 and 3.4. Light-induced annealing of defects [127-130] might also be present, and if so the effect will also be more prominent during summer months, when days are longer and irradiation levels are higher due to lower air mass values caused by lower zenith angles.

Compared to crystalline silicon PV the amorphous silicon material presents some contrasting characteristics, which have to be considered in outdoor applications. The temperature coefficient in output power is in the order of - 0.1 to - 0.3 %/°C for amorphous, while it ranges from - 0.5 to - 0.8 %/°C for single crystal silicon solar cells [20], resulting in reduced power loss at high temperatures for the amorphous cells. Spectral response, being a function of the material's bandgap, is much narrower for amorphous silicon, ranging from around 360 to 780 nm (for E_{gap} = 1.75 eV), while the crystalline silicon response ranges from about 380 to 1180 nm (E_{gap} = 1.12 eV). Adding to these characteristics the Staebler-Wronski effect, the general picture for outdoor applications is that, for a given site outdoors, amorphous silicon PV perform better in summer, while crystalline silicon PV perform better in winter.

Chapter 4

Preparation of Amorphous Silicon

4.1 Introduction

Amorphous silicon thin films have been prepared by a variety of methods, including evaporation, ion plating, arc discharge, corona discharge, ion implantation, glow discharge (including all its various configurations) and sputtering [35]. Glow discharge decomposition of silane gas (SiH_4) and reactive sputtering from a Si target in a mixture of inert gas and H_2 are the most widely used methods for depositing hydrogenated amorphous silicon. The extensive investigation of the glow discharge Plasma Enhanced Chemical Vapour Deposition (PECVD) process and of the resulting films rapidly led to material with the lowest structural and compositional inhomogeneities [131], and for that reason the PECVD process has attracted considerably more attention. Moreover, the initial failures in producing good quality a-Si:H films by sputtering techniques (early work suggested that sputtered a-Si:H films were inferior in their electronic properties to those produced by the glow discharge method) partially shifted the interests away from this method for the production of solar cells. In terms of the Staebler-Wronski effect, no differences concerning the defect creation and saturation could be found between high quality glow discharge and sputter-produced a-Si:H films, the latter containing extremely few oxygen impurities [132]. Reactive sputtering has many advantages as a deposition process. Among these, one can cite the ability to uncouple the two source materials, Si and H, and independently optimise the role that

each plays; avoid toxic gases like silane and phosphine; and a lesser degree of contamination from O_2 and N_2 [35]. Sputtering is in principle an attractive method for the preparation of amorphous silicon films owing to the ease of depositing large area, uniform films. Defect densities as low as 10^{15} $cm^{-3}.eV^{-1}$, which are comparable to state-of-the-art glow discharge produced films, have been measured [14]. Alloys of tetrahedral amorphous materials are preparation dependent, and as a consequence, a large variety of a-Si:H materials can be produced considering the various choices of above mentioned deposition techniques and also the deposition parameters within each of these techniques. In the continuing global effort to produce more stable amorphous silicon solar cells each of these techniques plays an important role in the drive to elucidate and eventually eliminate or minimise the Staebler-Wronski effect.

Since the work carried out on amorphous silicon thin films described in this thesis was conducted on RF reactive sputter-deposited samples, we shall briefly describe the most-widely used PECVD technique, and then concentrate on the sputtering process.

4.2 Plasma Enhanced Chemical Vapour Deposition (PECVD)

In the PECVD technique a gas such as silane (SiH_4) is directed through the chamber and an electrical discharge is then used to ionise the silane. Before initiating the discharge, the low pressure SiH_4 is a poor conductor of electricity. If the voltage across the two parallel metal plates in the chamber is large enough, electrons will flow from the cathode to the anode, being accelerated in the electric field between these electrodes. Some of these high energy electrons may collide with neutral SiH_4 molecules, ionising them. A plasma is a collection of atoms and molecules, some ionised, and because electrons and ions can of course drift under an electric field, plasmas conduct electricity. The plasma initiates the reduction of SiH_4 to SiH_3, SiH_2,

SiH or Si radicals, which then impinge on the substrate, warmed by Joule heating. A thermally-assisted surface reaction follows, which helps in the ejection of most of the hydrogen species. This requires that the growth radical simultaneously find two or three Si atoms suited for bonding [33]. In order to maintain a high surface mobility of the growth species and avoid the formation of polymeric chains, the growing surface has to be kept at reasonably high temperatures. Alternatively, "hitting" the growing surface with hydrogen ions during growth can raise the effective temperature of the surface and achieve the same results. As a consequence, paradoxical as it may seem, films grown in plasmas where the silane is diluted with hydrogen can actually result in less hydrogen being incorporated in the film.

The kinetics underlying film growth from non-equilibrium glow discharge reactive plasmas have not yet been well understood, and a better understanding of the growth kinetics of a-Si:H from SiH_4 glow discharge plasma is yet to be properly described, in order to control the deposition process as well as the properties of the resulting films [133].

4.3 Reactive Sputtering

In the preparation of a-Si:H by sputtering, or more accurately "reactive sputtering" techniques, the source of silicon is a solid silicon target that is bombarded by ~ 1 keV ions (usually argon). Silicon atoms are thus sputtered and transported through the plasma to a heated substrate. Hydrogen is added in controlled amounts to the sputtering gas, is atomised and reacts with the sputtered silicon. The process is "reactive" since H_2 dissociates and is ionised in the plasma, producing Si-H bonds on the target, chamber, and substrate surfaces [134].

In a recent review, Abelson [66] has summarised the present knowledge concerning the growth of a-Si:H by reactive sputtering as follows:

> Silicon arrives at the growing surface in the form of ~ 90 % atomic Si and ~ 8 % SiH sputtered from the target surface; an additional ~ 2 % arrives as radicals from the plasma decomposition of silane (when sputtering from a c-Si target in a H containing atmosphere, silane gas is manufactured by wall reactions, and then decomposed by electron impact in the plasma, presumably into SiH_2 + 2H [66]. The Si and SiH stick near their point of impact. Translational energy and/or bombardment by noble gas ions is necessary to densify and smooth the growing film. Atomic H is produced by electron impact dissociation of H_2 in the plasma volume. The total H flux increases linearly with the hydrogen partial pressure in the discharge, and is 2-3 times the silicon flux under typical conditions. Fast atomic H arise from the acceleration, neutralisation and reflection of H_2^+ ions at the sputtering target. About half of the arriving H flux reacts with the growing film surface, either by incorporating into a-Si:H or abstracting a bonded H to produce H_2. Ar^+ ions also fall from the plasma to substrate potential. The flux of H arriving as fast neutrals is large, especially at higher H_2 pressures; these H can penetrate below the physical surface, and displace bonded H through momentum-transfer collisions. The translationally fast H penetrate over 50 Å into the surface of growing a-Si:H. These H transfer enough momentum to displace 50 to 75 % of the existing H from Si-H bonds. Both the incident and released H may be re-captured onto Si-H bonds. And finally wall production and plasma dissociation of SiH_4 contributes significant quantities of H to the growth process.

Figure 4.1 shows schematically the growth fluxes reaching the a-Si:H surface during reactive sputter deposition.

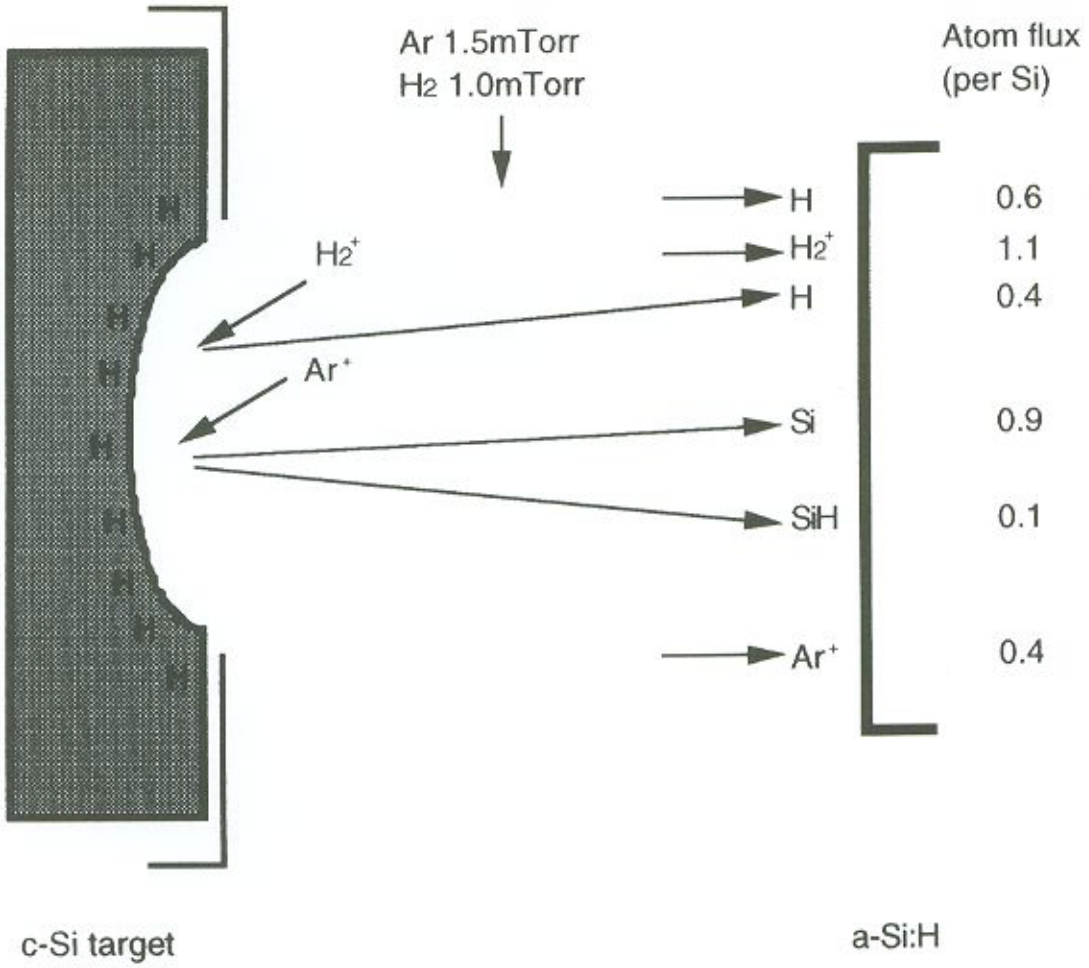

Figure 4.1: Growth fluxes reaching the a-Si:H surface during reactive sputter deposition. Adapted from [66,134].

The technology of reactive sputtering has inherently a series of advantages as a deposition process. The most important of these is the ability to uncouple the two source components, Si and H, and independently optimise the role each plays in the

formation of the random network and the consequent optoelectronic properties. In the glow discharge decomposition of silane techniques this type of control is not possible, because the source components are initially chemically bonded in the feed gas. Moreover, sputtered films are in general mechanically strong, with good film-substrate adhesion, and the process is easily scalable [131]. From a fundamental study of hydrogen incorporation point of view, the reactive-sputtering offers two key advantages. One is that the low working pressure (~10^{-3} Torr) largely eliminates gas-phase chemistry, so that plasma diagnostics and kinetic interpretation are greatly simplified; the other advantage is that, as previously mentioned, the hydrogen content of the film can be varied from zero to a saturation value that is deposition-conditions dependent by changing the hydrogen partial pressure in the discharge. In PECVD by contrast, the growth flux is dominated by the $Si\text{-}H_3$ radical, with a fixed 3:1 excess of hydrogen, and the total bonded hydrogen content is primarily determined by the substrate temperature T_s [134].

One of the selecting factors in the choice of an industrial a-Si:H deposition method is the deposition rate; its increase over a few $Å.s^{-1}$ can lead to material quality degradation. The technique of reactive magnetron sputtering, in which a magnetic coil is placed in the cathode plate underneath the target, in order to increase deposition rates, has been successfully employed in the deposition of a-Si:H at rates as high as 18 $Å.s^{-1}$ with an electronic quality equivalent to state-of-the-art a-Si:H material [135,136].

Plasma processes are quite complex and interdependent since they are out-of-equilibrium systems. During growth, the a-Si:H surface is exposed to neutrals, ions, electrons and photons [137]. All these may affect surface chemistry and the resulting film properties. Plasma analysis in the glow discharge decomposition of silane has been extensively investigated by means of various techniques such as mass analysis and optical spectroscopy. The mechanism of the sputtering of a silicon target by a hydrogen plasma, however, has not been clarified yet because of the difficulties in the direct

observation of plasma-Si target interactions [138]. The reaction of hydrogen plasma with silicon target depends on a series of experimental parameters including plasma density, target temperature and hydrogen partial pressure [138]. The reactive sputtering growth flux consists mostly of energetic silicon (~ 10 eV) and hydrogen (< 1 to ~ 250 eV) atoms [66]. This is vastly different than PECVD in terms of the sticking probability and interaction depth of the precursors.

4.4 Doping

Doping in the glow discharge processes can be achieved by adding either phosphine or diborane to silane to produce n- or p-type a-Si:H respectively [2]. In the case of sputtering, the doping impurities can be incorporated into the solid target or be supplied from the gas phase in addition to the inert gas and hydrogen mixture. The P and B atoms are mostly incorporated in the growing amorphous film as threefold-coordinated structures (P_3 and B_3), which are electrically inactive [139]. Thermodynamic equilibrium within the film during growth determines the fraction of fourfold-coordinated, electrically active dopants (P_4 and B_4) which varies with doping level and is typically $(P_4) / (P_3) \leq 10^{-2}$ [139]. Despite the low doping efficiency, the conductivity is enhanced by several orders of magnitude compared with undoped a-Si:H and is accompanied by a large shift in the Fermi level [140].

Chapter 5

Characterisation Techniques

5.1 Fourier Transform Infrared Spectroscopy

5.1.1 Introduction

Lying between the visible and the microwave regions of the electromagnetic spectrum, the infrared region is commonly divided into near-infrared (13300 - 4000 cm^{-1} or 0.75 - 2.5 μm), mid-infrared (4000 - 400 cm^{-1} or 2.5 - 25 μm), and far-infrared (400 - 10 cm^{-1} or 25 - 1000 μm). The mid-infrared, also called fundamental region, is the area of the spectrum most useful for analytical spectroscopy and is where all the information regarding a-Si:H is available. The term *frequency* is often used when referring to infrared spectra peak positions, when the actual measurement being given is in wavenumbers. Since frequency is proportional to wavenumber, this is a widely accepted practice.

Infrared (IR) vibrational spectroscopy is a rather powerful analytical technique and throughout this study has been extensively applied to identify different local atomic configurations (SiH, SiH_2, SiH_3, $(SiH)_n$ $(SiH_2)_n$) through their characteristic vibrational frequencies. Moreover, total bonded hydrogen content of a-Si:H films was also routinely determined by calculating the integrated absorption of H-Si peaks. Furthermore, the IR technique was also used to describe changes in the hydrogen

incorporation following the evolution of hydrogen via thermal annealing cycles at different temperatures.

5.1.2 Fourier Transform Infrared Spectroscopy Fundamentals

The theory of IR spectroscopy states that a molecule may absorb infrared radiation of the appropriate frequency to excite it from one vibrational or rotational level to another [141]. When a beam of infrared energy passes through a sample, the energy at certain frequencies is absorbed by the sample, and a plot of energy absorbed versus frequency is the sample's absorption spectrum, which is characteristic of the particular molecule and its molecular motions.

The development of Fourier transform infrared (FTIR) spectroscopy techniques began with the invention of the two-beam interferometer by A. A. Michelson [142] more than a century ago. Figure 5.1 shows the simplest form of the Michelson interferometer, the main component of an FTIR spectrometer.

In the Michelson interferometer, a beam of radiation can be divided into two paths and the two beams can then be recombined after a path difference has been introduced, thereby creating a condition under which *interference* between the beams can occur. The interferometer contains a fixed mirror, a movable mirror, and a beamsplitter, where a beam of radiation from an external source can be partially reflected to the fixed mirror and partially transmitted to the moving mirror. The two beams are reflected by these mirrors back to the beamsplitter, where they recombine. The intensity variations of the beam emerging from the interferometer can be measured as a function of path difference by a detector, and generate a continuous electrical signal called an *interferogram.*

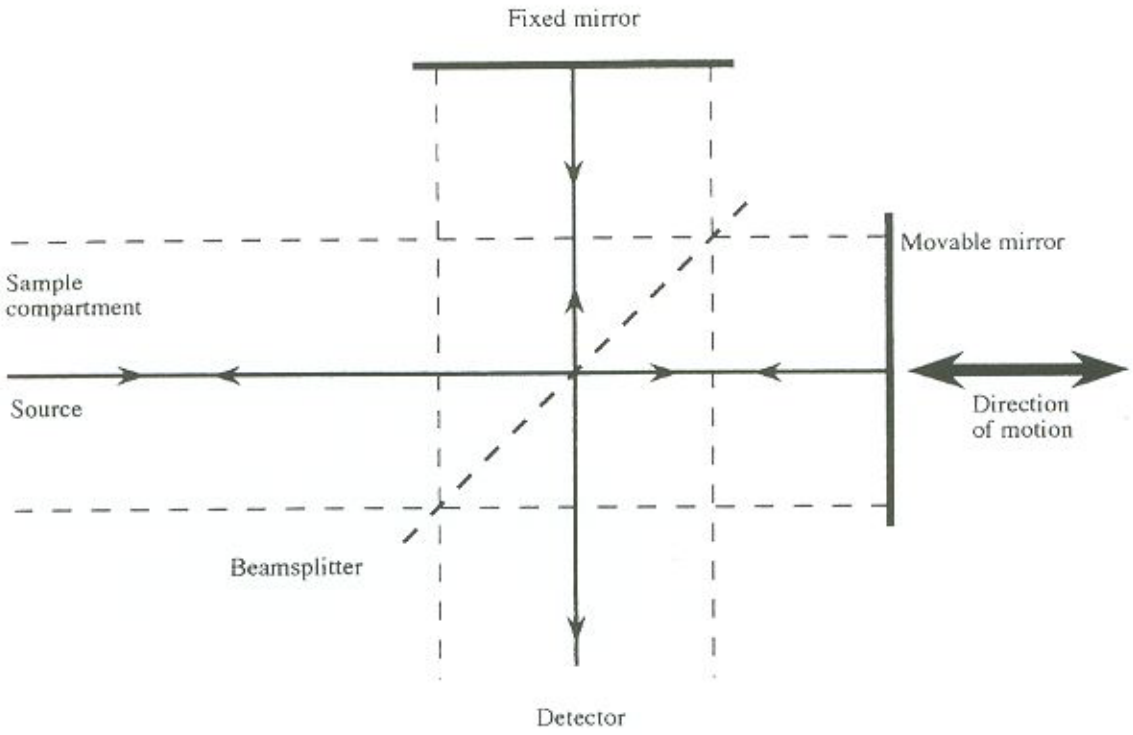

Figure 5.1: Schematic representation of a Michelson interferometer. The median ray is shown by the solid line, and the extremes of the collimated beam are shown by the broken lines.

The moving mirror is driven at a constant velocity by a computer-controlled linear motor, to provide the varying optical path difference. A HeNe laser generates a reference signal which enables the spectrometer electronics to sample the interferogram at precise intervals, generating a digital signal. The interferogram is then converted into a single-beam spectrum by a Fourier transform. The procedure in FTIR instruments is to first collect the spectrum of the source (single-beam background spectrum) and store it on disk. The sample is then inserted in the sample compartment and the single-beam spectrum of the source, modified by the sample, is collected and ratioed with the single-beam background spectrum to obtain the desired transmission spectrum.

In FTIR spectroscopy there exists a quantitative relationship amongst signal-to-noise ratio (the ratio of the amplitude of a spectral band at any point to the amplitude of the noise at that same point), resolution (the smallest frequency or wavelength separation for which two distinct spectral lines of equal intensity can be distinguished), and measurement time. This relationship is such that the signal-to-noise of a spectrum measured at a given resolution is proportional to the square root of the measurement time [141]. The signal-to-noise ratio of a spectrum is also related to the resolution. For a given number of scans it increases as the resolution decreases. These trading rules will be further considered in following sections.

5.1.3 Determination of the Hydrogen Concentration (C_H) in a-Si:H Films by IR Spectroscopy

Since hydrogen is such an important constituent of a-Si:H thin films, means to determine its concentration and also its bonding configurations in the amorphous network in a fast and non-destructive way are highly desirable. The hydrogen concentration of a-Si:H films can be determined from their infrared spectra. Brodsky, Cardona and Cuomo [52] have identified, by comparing the infrared spectra of a-Si:H and silane, disilane, higher silanes and halogen silanes, the three IR vibrational modes (stretching, bending and wagging/rocking) mentioned in section 2.3.1. The ~ 640 cm^{-1} bond wagging (rocking) mode is believed to result from silicon bonded to hydrogen in any configuration in a-Si:H, and the total bonded hydrogen concentration in a-Si:H films can thus be determined from the integration of that IR peak. Moreover, the wagging band centred around 640 cm^{-1} has been shown to be proportional to the H content with the same proportionality constant whatever the H content and the film microstructure [55].

The atomic density of bonded hydrogen atoms in a-Si:H films (N_H) is given by [55]

$$N_H = A_{wag} \cdot I_{wag} \tag{5.1}$$

and

$$Iwag = \int [\alpha(\omega)/\omega]\, d\omega \tag{5.2}$$

where $A_{wag} = 1.6 \times 10^{19}$ cm^{-2} is the proportionality constant determined experimentally [143,144], α is the absorption coefficient, and ω is the wavenumber, in cm^{-1}. The integral (I_{wag} or I_{640}) corresponds to the integrated intensity under the particular IR absorption mode, in this case the ~ 640 cm^{-1} peak. The hydrogen atomic concentrations (C_H), usually shown as atomic percentages, are calculated from the ratio between N_H and the atomic density of silicon (i.e. the H mole fraction $N_H / (N_{Si} + N_H)$), $N_{Si} = 5 \times 10^{22}$ cm^{-3} [41,55,145]

$$C_H = N_H / (5 \times 10^{22}) \cdot 100\ \% \tag{5.3}$$

The analysis of infrared absorption spectra allows not only to determine the bonded hydrogen content from the integrated intensity of the wagging band, but also to obtain information on the hydrogen bonding configurations from the intensities of the stretching and bending bands that occur in the 2000 - 2100 cm^{-1} and 800 - 900 cm^{-1} range respectively. Moreover, film oxygen and nitrogen concentrations can be obtained from the related bands located in the 700 - 1200 cm^{-1} region. Furthermore, the amount of hydrogen bonded in some sort of microstructure can be estimated from the integrated band intensities of the IR-stretching modes centred at ~ 2000 cm^{-1} (monohydride bonding configuration, I_{2000}) and ~ 2100 cm^{-1} (polyhydride bonding and clustered

monohydrides on internal surface of microvoids, I_{2100}), in terms of the parameter R [146] defined as:

$$R = I_{2100} / (I_{2000} + I_{2100}) \qquad (5.4)$$

The prefactor A_{wag} in equation 5.1 has been determined by Shanks *et al.* [55], who determined this proportionality constant for the various vibrational modes (A_{wag} for the wagging, A_{bend} for the bending, and $A_{stretch}$ for the stretching band) by comparing the integrated intensities of the various peaks to the total hydrogen concentration determined by nuclear reaction analysis. Table 5.1 lists the constant "A" for the various Si-H infrared vibrational modes.

Table 5.1: The proportionality constant "A" between the integrated infrared absorption and the hydrogen concentration [55].

Wavenumber (cm^{-1})	~ 640	~ 840 - 890	~ 2000	~ 2100	~ 2100
Mode	Wag	Bend	Stretch	Stretch	Stretch
Bonding	Si-H $Si-H_2$ $(Si-H_2)n$ $Si-H_3$	$Si-H_2$ $(Si-H_2)n$	Si-H (isolated)	Si-H (cluster)	$Si-H_2$ $(Si-H_2)n$ $Si-H_3$
Proportionality constant (cm^{-2})	A_{wag} $1.6x10^{19}$	A_{bend} $2x10^{20}$	$A_{stretch}$ $2.2x10^{19}$	$A_{stretch}$ $1.7x10^{20}$	$A_{stretch}$ $9.1x10^{19}$

It should be emphasised that Shanks *et al.* [55] found the value of A_{wag} to be almost independent of preparation conditions and total hydrogen concentration. However, the values of A_{bend} and $A_{stretch}$ were found to vary with preparation conditions and hydrogen concentration, and therefore the concentration of hydrogen in a-Si:H films as determined from the bending and/or stretching bands should be viewed with caution. In this study, the integrated intensity of the stretching bands (usually denoted as I_{2000} and I_{2100}) was found to lead to large variations as compared to the wagging band peak (I_{640}) when used to estimate C_H. We therefore avoided using the stretching band integrated intensities except to compare the evolution of H and variations in bonding configuration distributions in a same sample during thermal annealing studies.

5.1.3.1 Correction to C_H for Film Thickness < 1μm

Intrinsic layers in typical p-i-n amorphous silicon solar cells usually have a thickness (d) of less than 0.5 μm. In the characterisation of this material, however, film thicknesses in the order of 1 μm are required for some of the characterisation techniques, including electrical conductivity measurements and infrared analysis. In the determination of the hydrogen concentration (C_H) in a-Si:H thin films by the method just described, and which is universally accepted, Maley and Szafranek [147] have recently shown that when the film thickness is less than ~ 1 μm this technique systematically overestimates the hydrogen content. A simple method to correct C_H has been presented by them. According to Maley [148], in most cases it is possible to correct the results from the widely used Brodsky, Cardona and Cuomo (BCC) [52] method so that they are accurate to within 10 %. Infrared transmission spectra are influenced by coherent reflections unless the films are deposited on roughened c-Si surfaces; for the range of optical constants appropriate for a-Si:H on c-Si this overestimate in the absorption coefficient (from which C_H is estimated) is only a

function of the film thickness [147]. The error is found to be independent of the hydrogen concentration and is as large as 80 % in the limit d -> 0. This indicates that previously reported experimental evidence for the dependence of C_H on d [149] was probably an analytical artefact.

The errors in the BCC method have been found to be primarily a function of the optical path length, *i.e.*, the product of frequency and film thickness. The errors also depend on the film refractive index and absorption coefficient, although to a lesser extent. For a-Si:H with $C_H \leq 30$ at.%, the absorption spectra determined by the BCC method can be corrected using an empirically determined correction factor

$$\alpha_{corr} = \alpha_{BCC} / (1.72 - K\omega d) \qquad \text{for } d < 1\mu m \qquad (5.5)$$

where K = 0.0011, ω is the peak frequency in cm^{-1}, and d is in μm. The correction is applicable for ωd values for which the denominator is larger than 1 [145,147]. Equation 5.5 assumes that the film refractive index (n) is between ~ 3.2 and 3.7, and the correction factor needs to be modified if the range of n is significantly different [148,150]. This is important for silicon-germanium and silicon-carbon alloys and even a-Si:H with high C_H and poor microstructure.

5.2 Scanning Electron Microscopy (SEM)

The scanning electron microscope (SEM) is a powerful tool in surface analysis. It offers improved resolution as compared to the optical microscope, due to the small wavelength associated with the electron beam. Also, due to a smaller effective aperture, depth of field is larger.

The interaction of an electron beam in the 1-100 keV range with a solid results in a variety of emissions from this solid. All of these can be analysed to reveal a series of detailed and varied information on the material. In SEM the most relevant species resultant of those interactions are the secondary electrons and the backscattered electrons. Figure 5.2 shows a schematic diagram of a SEM. The electron gun, which is the source of electron emission, consists of a simple hairpin-shaped tungsten (W) or lanthanum hexaboride (LaB_6) filament (cathode).

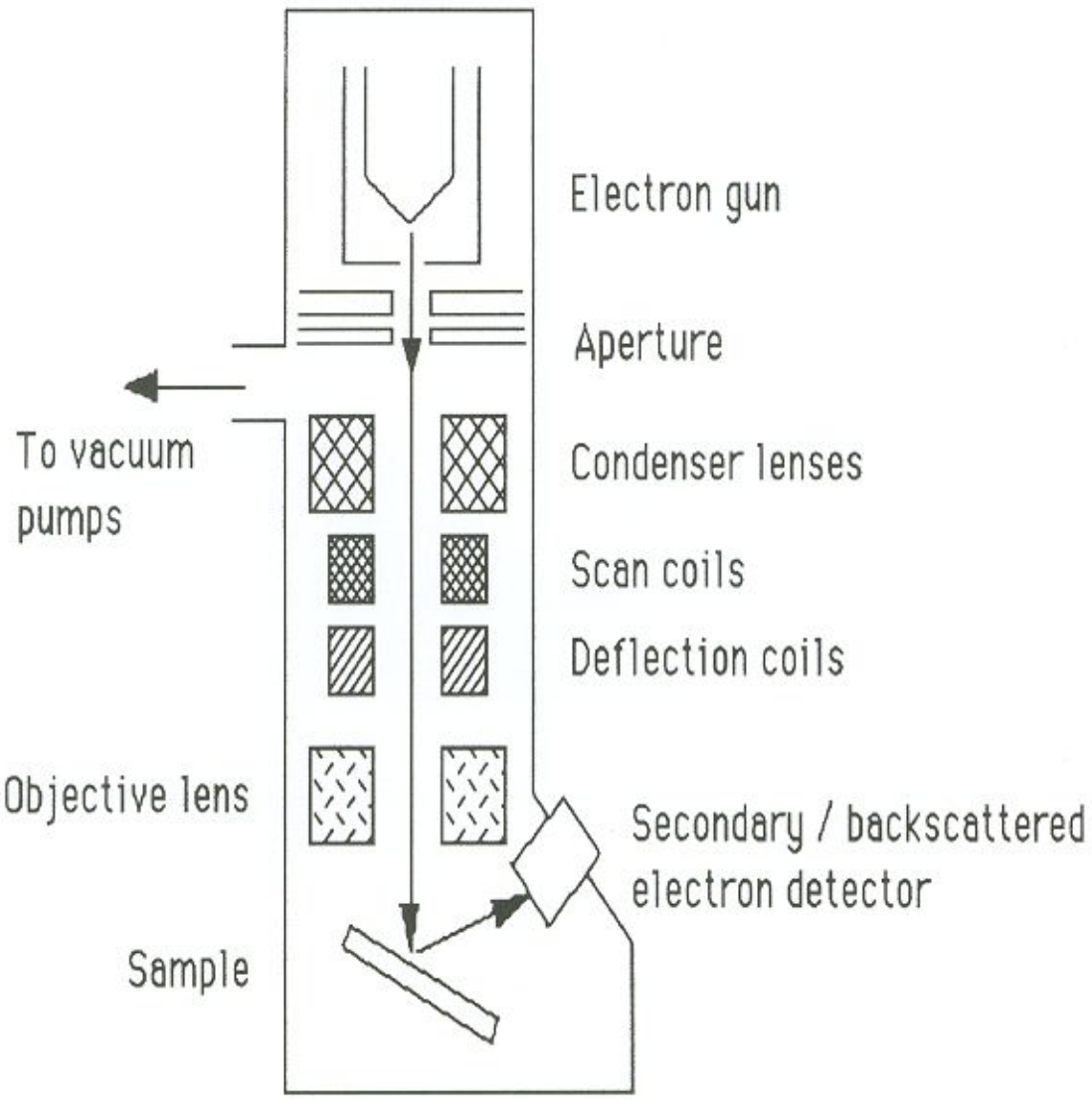

Figure 5.2: Schematic diagram of the basic components of a scanning electron microscope (SEM) used in image analysis.

The electrons, generated at the filament by thermionic emission, are attracted to the anode and pass through a hole in the centre of that electrode. They are then confined to a small diameter beam by using a combination of magnetic and electric coil lenses to finally impinge on the sample. The resultant electron beam-solid interactions are collected by a detector to modulate the intensity of an electron beam in a cathode ray tube (CRT). Because the scanning of the CRT ray beam is synchronised with the raster pattern of the SEM electron beam over the selected portion of the specimen surface, an image of the specific specimen signal is observed.

5.3 Elastic Recoil Detection Analysis (ERDA) and Rutherford Backscattering (RBS)

When energetic ion beams are incident on a sample, they suffer a wide range of interactions. Any one of these interactions can be made the basis of an analysis technique simply by observing that type of interaction and designing the detection system to exclude, as far as possible, the others [151]. Ion beam analysis has been demonstrated to be a powerful technique for sensitive measurements of the atomic composition and impurity concentrations in the near-surface (~ 1 - 2 μm) regions of solids [152]. One of the most commonly used techniques is Rutherford backscattering (RBS), where light ions such as H or He with energies of ~ 1 - 3 MeV are incident on the sample under investigation and ions backscattered at some well-defined angle are detected. Analysis of the energy distribution of the backscattered ions yields the near-surface depth distribution of atomic species with masses greater than that of the projectile beam [153]. Hydrogen (^{1}H) is the most difficult atomic species to profile. Because of its light mass, RBS cannot be used. The determination of the concentration of hydrogen in solids, either in the bulk or on the surface, is a very difficult analytical task not only due to the low mass, but also because of the shallow electronic structure of this element [154]. Until recently, for depth profiling of hydrogen concentration,

nuclear reaction analysis (NRA) using $^{1}H(^{19}F,\alpha\gamma)^{16}O$ and $^{1}H(^{15}N,\alpha\gamma)^{12}C$ reactions was commonly applied [155]. Instead of nuclear reactions, L'Ecuyer *et al.* [156] have proposed the use of the elastic recoil detection analysis (ERDA), a fast and non-destructive technique for determining the depth distribution of light elements in heavy materials. The principal advantages of this technique are its high sensitivity in quantitative analysis and in the determination of surface profiles. It makes use of both high cross section for recoil scattering and of the regular dependence of the energy of the scattered particle on the mass of the target atom [157]. The principle behind ERDA is similar to ion backscattering. In both cases an elastic scattering event is essential. However, instead of analysing the incident ions scattered from target atoms, in the case of ERDA, the light nuclei recoiling after being hit by a heavier ion are detected [158]. While L'Ecuyer *et al.* used a ^{35}Cl beam at 30 MeV to detect Li in a target, Doyle and Peercy [153] adapted the forward-scattering ERDA technique for accurate measurements of ^{1}H depth distributions in the near-surface region of solids using a ^{4}He beam from a 2.5 MeV Van de Graaff accelerator. The most widely used form of depth profiling is ERDA, because it only requires a ^{4}He ion beam at low (~ 2 MeV) energies, available on the many Van de Graaff accelerators around the world. The other reactions previously used for NRA ($^{1}H(^{19}F,\alpha\gamma)^{16}O$ and $^{1}H(^{15}N,\alpha\gamma)^{12}C$) require much higher energies, only available on Tandem accelerators, which are not so common [159].

The principle of the method is depicted schematically in figure 5.3. A ^{4}He ion beam of energy E_0 is incident on a solid target at an angle α with respect to the surface. When a light nucleus is recoiled by an incident heavier ion, it recoils at a scattering angle θ with an energy

$$E_2 = kE_1 \qquad (5.6)$$

where E1 is the energy of a particle just before the collision, and k is the kinematic factor given by

$$k = (4M_1M_2 / M_1 + M_2) * \cos^2\theta \qquad (5.7)$$

M_1 and M_2 being respectively the mass of the incident ion and the target atom.

Due to conservation of energy and momentum, $k = 0$ for $\theta \geq 90°$, the recoiled atoms are scattered only in the forward direction. In order to stop the large flux of elastically scattered incident ions from also being detected, it is necessary to mount a stopper foil as an absorber in front of the detector. Since the absorber should be thick enough to stop the scattered ions, the recoils with mass higher than M_1 will also be stopped. Due to their lower stopping power the lighter recoils can pass the stopper foil. The energy of detected recoils will then be

$$E_f(x) = E_2(x) - \delta E_a (E_2) \qquad (5.8)$$

with

$E_2(x)$ = energy of the recoils coming out of the target,

x = collision depth,

δE_a = energy loss in the stopper foil

The energy E_2 can be calculated taking into account that the energy loss of the incident beam along its trajectory is equal to x /sin α, the energy transfer to the recoiled atom is kE_1, and finally the energy loss of the recoiled atom while traversing the exit path is x / sin $(\theta - \alpha)$. If the stopping powers S_1 and S_2 for incident and outgoing particles respectively are assumed constant, E_2 can be written as

$$E_2 = kE_0 - \{S\}\, x \qquad (5.9)$$

where

$$\{S\} = (kS_1 / \sin\alpha) + (S_2 / \sin(\theta - \alpha)) \qquad (5.10)$$

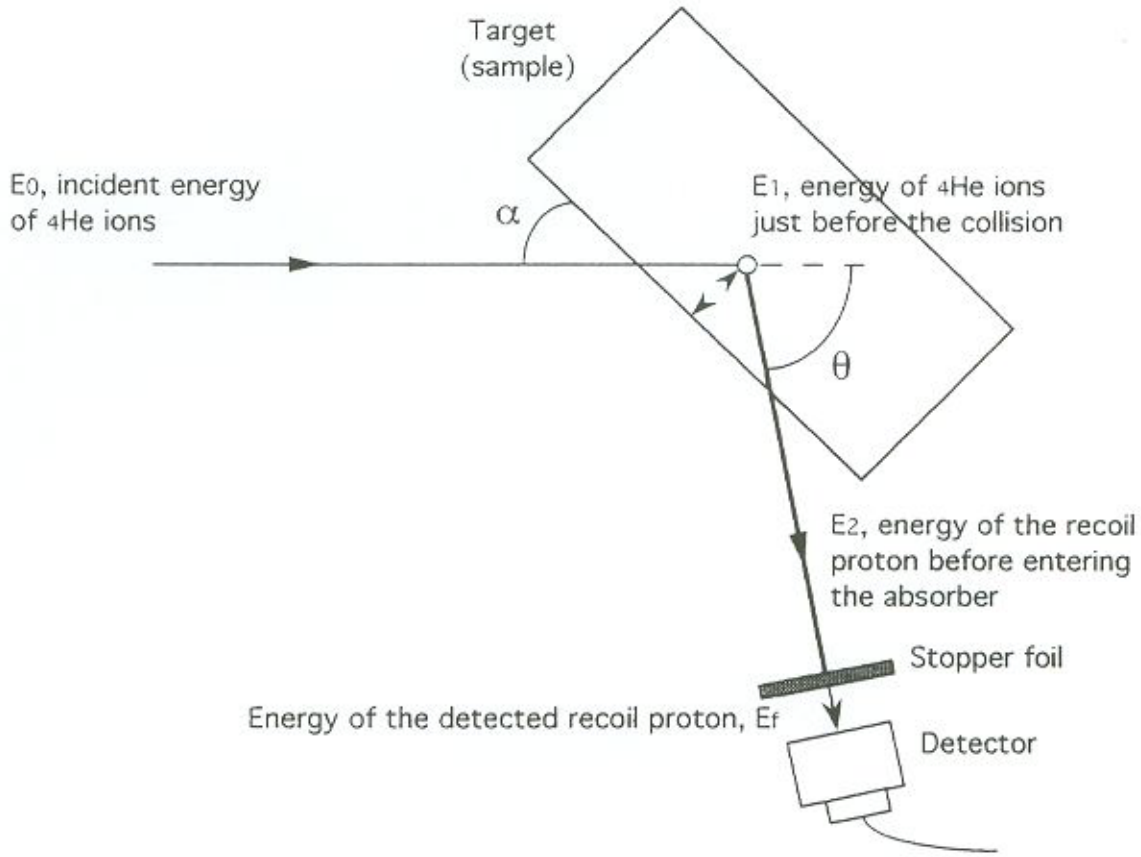

Figure 5.3 Schematic representation of the experimental arrangement for profiling hydrogen in solids using the ERDA technique.

If energy spread effects are neglected, the ideal energy spectrum $n(E_f)$ of the detected recoils is given by

$$n(E_d)\, dE_f = I\Omega\sigma(E_1)\, C(x)\, dx \qquad (5.11)$$

with

I = number of incident particles

Ω = solid angle of detection

$\sigma(E)$ = elastic scattering cross-section

$C(x)$ = concentration profile of hydrogen

At incident energies below several MeV the recoil cross section is purely Rutherford and is given by

$$d\sigma(E)/d\Omega = ((Z_1 Z_2 e^2 (M_1 + M_2)) / (2M_2 E_1))^2 * (1 / \cos^3\theta) \qquad (5.12)$$

where Z_1 and Z_2 are the atomic numbers of the incident and recoiled atoms, respectively.

In order to cross check the depth scaling of ERDA measurements, a backscattering spectrum obtained for the same sample as that to be used as a reference standard can be used. By performing complementary measurements with ERDA and RBS for samples of different thickness an accurate depth scale for ERDA can be obtained.

The hydrogen concentration $C(x)$ can be obtained from the spectrum height according to eq. (5.11). However, the most accurate way to obtain an absolute value of $C(x)$ is to use a reference standard. Although in practical analyses of a simple solid like in a-Si:H the qualitative features are obtainable by inspecting $Y(E)$ versus the energy spectrum, it is preferable to process the data and convert the energy scale into a depth scale and the yield into atomic concentration [160]. A number of computer programs have been

developed to perform this type of calculation by various authors [160-164]. In this work RUMP-type [161] computer codes were used to simulate hydrogen depth profiles of a-Si:H films.

5.4 Spectroradiometry

Optical radiation reaching the earth's surface is commonly taken to cover the wavelength region from 200 nm (in the ultraviolet) to 10600 nm (in the infrared) [165]. These limits are set on the short-wavelength end by atmospheric absorption, and on the long-wavelength end by definition, since the term "light" is then substituted by the term "heat". In practical terms, however, there is almost no interest in measuring light over this entire range, and most instrumentation is designed to cover a portion of it. Moreover, each application has its own signal level range as well as its own wavelength range. Spectral analysis of the sun is important in the development of solar cells, particularly for the amorphous silicon-based technology where solar cell spectral sensitivity can be tailored to match the time- and site-dependent solar spectral content. For this purpose, the use of a spectroradiometer is by far the most accurate measure of the sunlight's energy content.

A typical spectroradiometer has a silicon detector, cosine spatial response input optics and a digital readout with a six or seven-decade dynamic range [165]. The spectral range of a silicon detector is typically 300 nm to 1100 nm, though the use of UV-enhanced silicon with a shallower junction can take that down to 200 nm. A typical silicon-based system can read down to 10^{-9} W.cm^{-2}.nm from 400 nm to 1000 nm; a photomultiplier can increase the sensitivity by 10000 but over a smaller wavelength range. Scattered light rejection approaches 1000:1 for a single monochromator, and 1000000:1 for a double monochromator [165]. Low scatter becomes important for UV spectral measurements of light sources with large amounts of near-UV and visible

irradiance as is the case of the sun. The use of a photomultiplier is essential in spectral measurements of sunlight in the short-wavelength region, because, as the sharp cut-off in the short-wavelength region in figure 3.4 qualitatively shows, solar spectral irradiance levels change by a factor of ten million from 280 nm to 320 nm.

Chapter 6

Materials and Methods

6.1 Amorphous Silicon Thin Films

This section describes the materials and methods used in a series of experiments involving intrinsic-type amorphous silicon thin films.

6.1.1 Substrate Preparation

For infrared transmission measurements, a-Si:H thin films were deposited on the polished side of single-side-polished mono-crystalline silicon (c-Si) 1 x 2 cm^2 chips cut from (100), high resistivity wafers. Crystalline silicon substrates were usually used not only because of their excellent infrared transparency, but also because the index of refraction of crystal silicon matches better the index of refraction of a-Si than most other infrared transmitting materials available [52]. Thus, the interference fringes from multiple reflections within the film were also minimised. Langford *et al.* [166] have shown that for single-polished crystalline silicon substrates, the spectrum is unchanged for deposition on the rough or polished side, and is identical to that on a double-polished substrate, so that it is unnecessary to buy the more expensive double-polished substrates for infrared analysis. For film thickness measurements made

with a stylus-type profilometer, samples were deposited on sodalime glass substrates. SEM, ERDA and RBS measurements were usually carried out on the same samples (deposited on c-Si substrates) used for infrared spectroscopy measurements.

6.1.2 Substrate Cleaning

In semiconductor technology in general, and in thin film deposition in particular, substrate cleaning represents a critical step and must not be overlooked. Amorphous silicon thin films have been observed to be under considerable stress [167,168], and if not strongly bonded to the substrate they might peel off. Substrate cleaning plays an important role in the adhesion, morphology and structure of a-Si:H grown on c-Si by sputtering techniques [169]. In the present work, as already mentioned, substrates used for amorphous silicon deposition were crystalline silicon 1 x 2 cm^2 chips, for FTIR, SEM, ERDA, and RBS analysis; and sodalime glass (microscope slides), for the routine thickness measurements. Cleaning procedures were as follows:

1) Ultrasonic wash in Decon90 (a commercial soda-based cleaning solution) solution (Decon90 : distilled-deionised (DD) water = 1:50 by volume) for 10 minutes

2) Rinse in DD water 5 times

3) Boil in trichloroethylene for 5 minutes

4) Rinse in DD water

5) Boil in acetone for 5 minutes

6) Rinse in DD water

7) Boil in isopropyl alcohol for 5 minutes

8) Rinse in DD water

9) Chemical etching in diluted HF solution (HF : DD water = 1:5 by volume) for 30 seconds

10) Rinse in DD water

11) Blow dry with nitrogen gas

While steps 1) to 8) were carried out to degrease and clean the substrates, the HF dip step 9) was used to strip off the native silicon oxide on the surface. Step 9) was only used for the crystalline silicon substrates. Recently, Yang and Abelson [169] compared four different cleaning procedures and their effects on film adhesion and surface morphology. They concluded that the diluted HF chemical etch (very similar to the procedure presented above) was the simplest and most effective method.

6.1.3 Thin Film Deposition

A variety of intrinsic-type (i-type) a-Si:H thin films were deposited by the reactive sputtering technique. The RF sputtering apparatus is shown schematically in figure 6.1. The cathode target was a nominally intrinsic high purity (microelectronic purity) cast polycrystalline silicon 6 inch diameter, 0.250 inch thick disk. This lower "J" shaped, water-cooled electrode was connected to an RF generator (13.56 MHz) which generated the RF plasma, in a conventional vacuum system capable of providing initial pressures around 10^{-7} Torr in the 20 litres chamber. The sputter region was determined by a 4.5 inch diameter grounded shield. The substrates used [1 x 2 cm^2 (100) c-Si and 2 x 3 cm^2 glass chips] and masks were mounted on the heated and grounded upper electrode (stainless steel substrate holder). Typically, 3 to 4 c-Si substrates (to allow for FTIR, ERDA and SEM studies as well as for repeatability purposes) and 1 glass substrate were co-deposited in each deposition run. The radiant heater consisted of a tungsten heating element, which served the dual purpose of heating the substrates and also providing a hot filament in which atomic hydrogen could be obtained from the

molecular hydrogen (H_2) introduced in the reactor for the in-chamber annealing in hydrogen treatment to be further detailed.

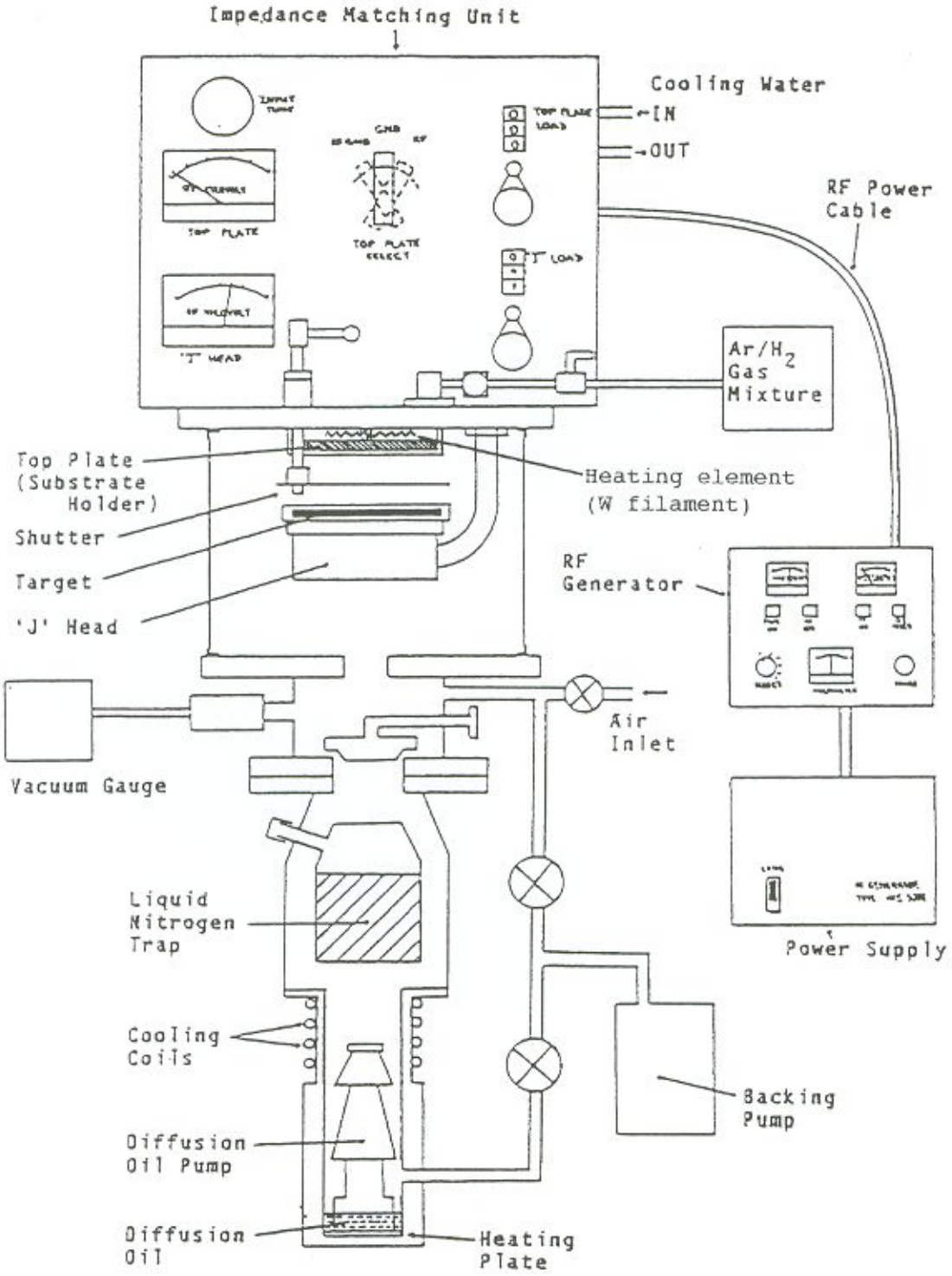

Figure 6.1: RF sputtering deposition system used for the deposition of a-Si:H thin films, showing the reactor chamber, vacuum system, control panel and RF generator unit.

A low thermal mass thermocouple, attached to the substrate holder and in contact with the deposition side of the substrate, was used to control the deposition or substrate temperature (T_s). The distance between electrodes (target-substrate distance) was 5 cm. Films were deposited with substrate temperatures ranging from 150 to 300 °C. Before sputtering, the chamber was evacuated to a base vacuum below 10^{-6} Torr. The sputtering mixture was obtained by adjusting the argon (ultra high purity Ar) and hydrogen (ultra high purity H_2) flows through calibrated rotameters to the desired Ar : H_2 ratio. In order to minimise oxygen and nitrogen contamination, the sputtering gases passed through a sequence of gas purifiers and oxygen traps, which were incorporated in the gas lines. Table 6.1 summarises the range in deposition conditions used in the preparation of amorphous silicon thin films presented in this thesis.

Table 6.1: Typical deposition conditions for i-type a-Si:H thin films using the reactive sputtering method

RF frequency	13.56 MHz
RF power density	300 - 400 $mW.cm^{-2}$
"J" electrode potential	1000 V
Pressure	1 - 4 x 10^{-3} Torr
Source gases	Argon (Ar, ultra-high purity grade)
	Hydrogen (H_2, ultra-high purity grade)
Ar:H_2 ratio	4:1 - 3:1
Deposition rate	~ 0.7 - 1.1 $Å.s^{-1}$
Presputter time	30 min
Deposition time	90 - 180 min
Deposition temperature (T_s)	150 - 300 °C
Film thickness	0.30 - 1.10 µm

In order to avoid cross contamination with dopant impurities, the reactor used to deposit intrinsic-type a-Si:H was not exposed to dopant gases, being an i-type-film dedicated deposition station. Dopant gases have a tendency to adsorb on the chamber walls and then desorb and contaminate later runs. Also, after deposition and before turning off the RF power, the shutter was closed to avoid any powder produced at plasma extinction to reach the surface, which would result in the formation of macroscopic defects [137].

6.1.4 The In-Chamber Annealing (ICA) Treatment

The parameter ranges for high quality a-Si:H growth are usually very limited, making if difficult for hydrogen to be incorporated in a well-controlled manner [170]. The introduction of hydrogen into the amorphous network by various methods after deposition is likely to be more controllable. The high diffusivity of hydrogen at temperatures in the order of 200 °C, the strong temperature dependence of defect creation and annealing in a-Si:H, and the possibility to convert weak Si-Si bonds to Si-H bonds as the chemical potential in the film is raised [34], led us to propose an *in situ* in-chamber annealing (ICA) treatment for a-Si:H thin films [171,172]. In this treatment, samples are annealed, just after deposition and before reaching room temperature, in the same reactor chamber in which they were deposited, in either vacuum or a hydrogen atmosphere, at temperatures slightly below the deposition temperature (T_S). A tungsten heating element used to maintain the substrate temperature (T_S) at the typical 200 °C < T_S < 300 °C range also served the purpose of acting as a hot filament where the hydrogen gas (H_2) was dissociated into atomic hydrogen. The filament was mounted behind the substrate holder, and etching was thus minimised. With this treatment, a higher degree of control over the Si-H bonding configurations in sputter-deposited a-Si:H thin films was expected to be attained. Very recently, An *et al.* [83] have studied the modification of a-Si:H by thermally generated atomic hydrogen in PECVD grown films, reporting considerable Si-Si to Si-H bond conversion rates. In

most of the following experiments related to i-type a-Si:H thin films to be described in this thesis, the in-chamber annealing treatment will be further detailed and discussed. Table 6.2 shows typical in-chamber annealing conditions for the samples presented in this study.

Table 6.2: Typical in-chamber annealing conditions for i-type a-Si:H thin films

In-chamber annealing temperature	T_{ICA} = 210 - 285 °C
In-chamber annealing time	120 min
In-chamber annealing atmosphere	1) Vacuum (10^{-6} Torr) 2) Ar:H_2 mixture (4:1), hot W filament 3) Ar:H_2 plasma (4:1), hot W filament

6.1.5 After Deposition

The thermal history of samples can critically affect their structure and defect properties [75]. It is therefore important to specify the way in which the samples are cooled down from the deposition temperature (T_s = 150 - 300 °C) to room temperature. Typically, after deposition was completed and, when applicable, in-chamber annealing was terminated by turning off the substrate heater and closing the source gas flow, the chamber was pumped down to $\leq 10^{-6}$ Torr. Samples were then allowed to cool radiatively in vacuum. Figure 6.2 shows the temperature versus cool-down time measured by a thermocouple placed next to the substrates on the stainless steel substrate-holder. The radiative cool-down rate in the glass-transition temperature of

defects (~ 200 °C), where the defect subsystem of the material is most sensitive to cool-down [75], was ~ 2 °C.min^{-1}.

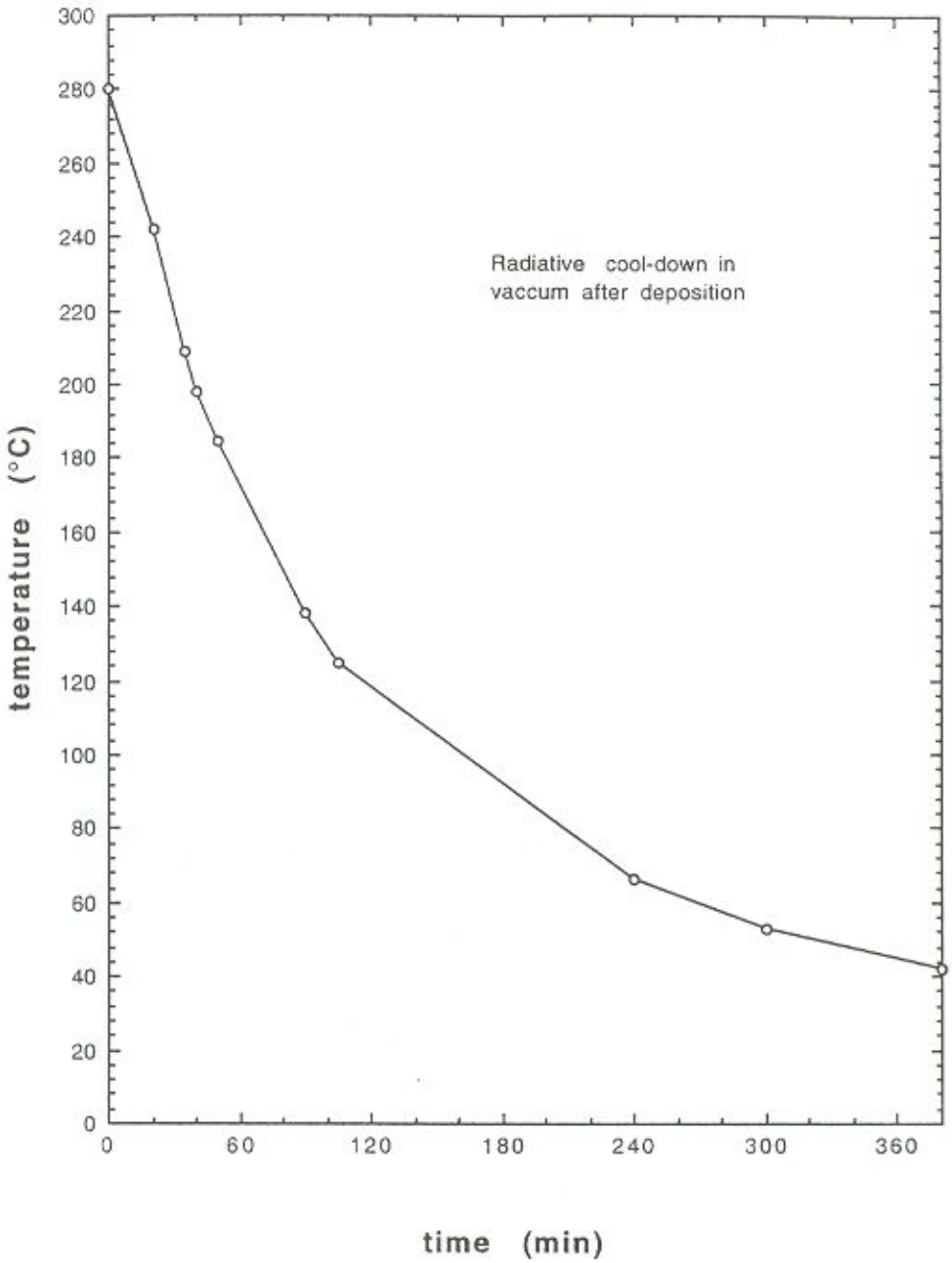

Figure 6.2: Evolution of the substrate temperature (cool-down in vacuum curve) after film growth.

After reaching room temperature, samples were unloaded from the reactor chamber and infrared spectra (FTIR) were immediately taken from a-Si:H films deposited on

polished c-Si substrates. Film thickness was also checked by means of a stylus displacement-type surfometer (Planar Products Type SF101) for samples deposited on glass substrates. A step of the same thickness as the film was formed by masking part of the glass substrate before sputtering and the height of this step was measured after deposition with the stylus surfometer. Figure 6.3 shows a schematic depiction of the technique. For SEM surface morphology analysis, samples were mounted on appropriate holders and carbon and gold coated. ERDA measurements were performed on the same samples used for FTIR analysis to avoid sample-to-sample variations and making use of the nondestructive character of both techniques. The following sections describe details on each of the above mentioned characterisation techniques.

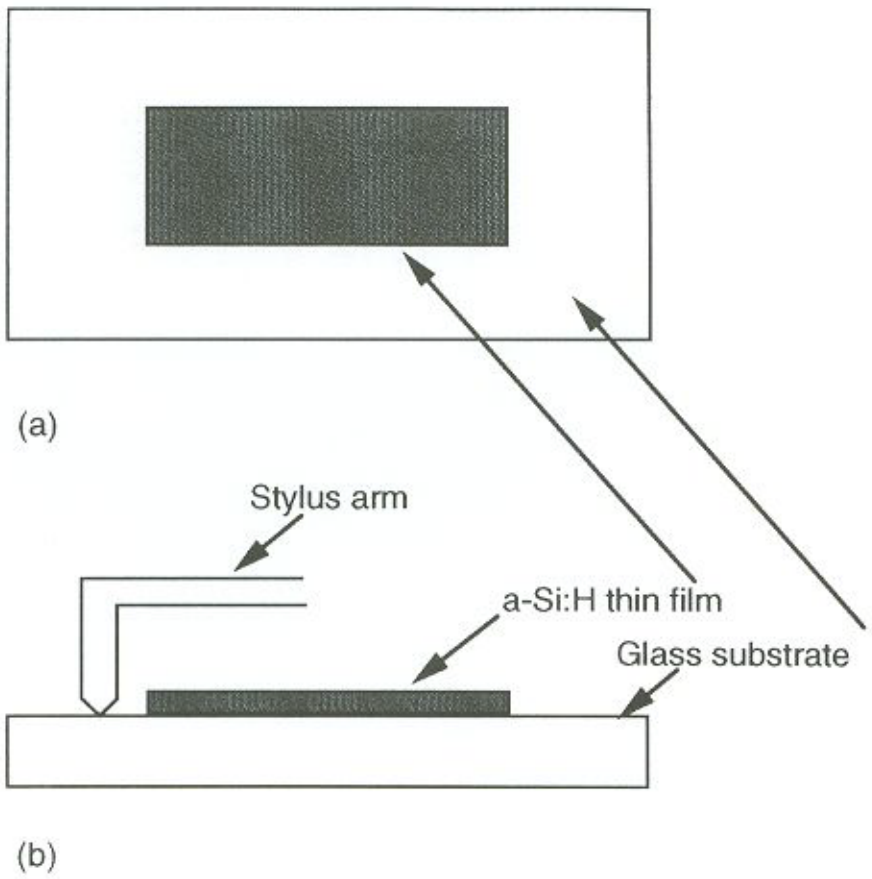

Figure 6.3: Schematic representation of mechanical thickness measurements; (a) top view showing film + substrate, and (b) lateral view showing film + substrate and stylus arm.

6.1.6 Infrared Spectroscopy (FTIR) Measurements

6.1.6.1 Sample Spectra Collection

For most of the infrared spectroscopy measurements, a BioRad (Digilab) model FTS-7 Fourier transform infrared spectrometer was used. In some cases a model FTS-40 equipped with a liquid nitrogen-cooled cadmium mercury telluride (CMT) detector was used. Both spectrometers comprise an optical system connected to a dedicated data station (Digilab 3200) system, where single-beam spectra, converted from interferograms by Fourier transformation, are computed. Like most of the modern FTIR spectrometers, these instruments have a single beam, and sample spectra are obtained by first collecting the spectrum of the source (single-beam background spectrum), and storing it on disk. The sample is then placed on an appropriate sample holder, which is then inserted in the attachment in the instrument's sample compartment. The single-beam spectrum of the source, modified by the sample, is then collected and ratioed with the single-beam background spectrum to obtain the desired spectrum, which can be displayed as either a % transmittance or absorbance spectrum. Thin a-Si:H films are not free-standing films and have thus to be deposited onto a substrate. Because of that, two spectra, one for a bare c-Si substrate and the other for the a-Si:H film deposited on a c-Si substrate (both cut from the same c-Si wafer to minimise interference fringe background from the substrate due to thickness variations), were always obtained and stored on disk. Finally, the sample spectrum for the a-Si:H thin film was obtained by subtracting the former from the latter.

Infrared spectra were collected in the 4400 - 400 cm^{-1} region, and analyses were performed with the software supplied with the instrument. When the resolution is decreased, the signal-to-noise ratio increases, while the time for one scan decreases [141]. At a resolution of 8 cm^{-1}, spectral features start disappearing, so a resolution

of 4 cm^{-1} was used. After 16 scans, very small differences were noticed in the improvement of the signal-to-noise ratio unless several scans were added. Therefore a value of 16 scans was selected for the experiments.

6.1.6.2 Spectral Baseline Correction, Peak Deconvolution and Bandfitting into Component Peaks

Baseline correction is used to flatten the baseline of an absorbance spectrum with a curved or sloping baseline. Two-point baseline correction is an essential operation when quantifying the integrated intensity of a particular infrared peak, and care should be taken when choosing the points, since their misplacement can be a considerable source of error. Figure 6.4 shows the raw spectrum of an a-Si:H thin film (after subtraction of the c-Si substrate spectrum), where the dashed line is the assumed approximate baseline. When examining the IR spectra of amorphous or polycrystalline solids, a property easily recognised is the nonstandard appearance of the spectral plots. This effect is mainly due to optical properties of the films [173]. Some of the causes are:

(i) Interference patterns can sometimes be superimposed in the spectra

(ii) Some spectra have sloping baselines, with positive or negative slopes

(iii) Scattering losses can cause nonabsorbing regions to have higher absorbance values

For those reasons is that baseline correction is always a necessary step in the analysis of infrared spectra in thin solid films, and for this purpose it is accepted that, for intervals smaller than 1000 cm^{-1}, the baseline can be approximated by a straight line [173,174].

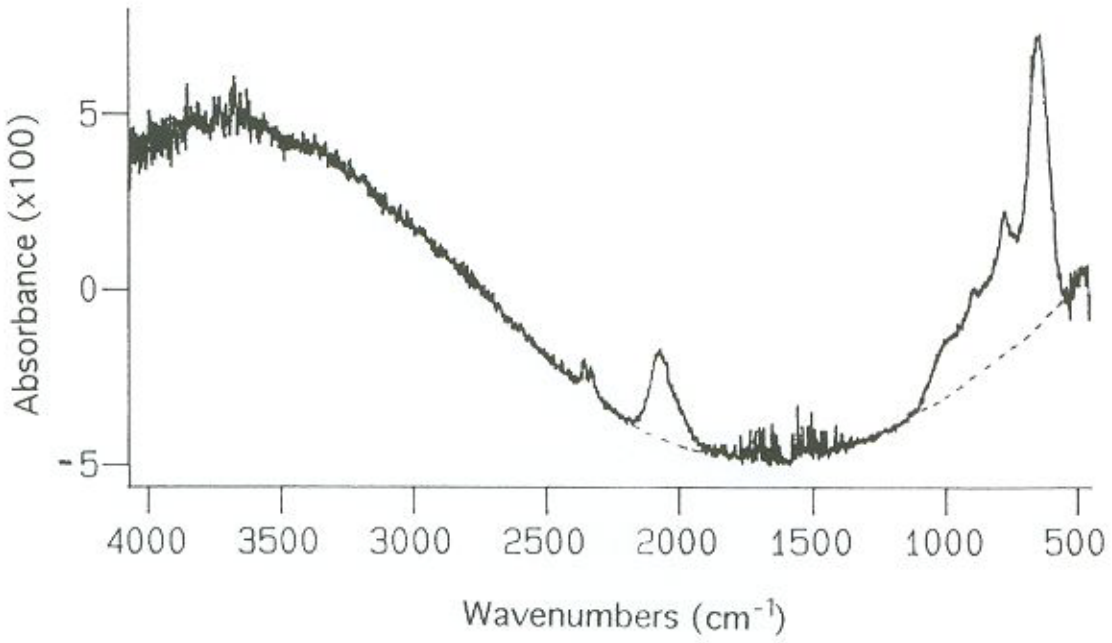

Figure 6.4: Typical raw IR spectrum of an a-Si:H thin film (after subtraction of the crystalline silicon substrate spectrum). The dashed line is the approximate baseline assumed for baseline correction.

Baseline correction can also be performed on the whole area of interest of a particular a-Si:H infrared spectrum, *i.e.* from ~ 2300 to 450 cm^{-1}, in which case the spectrum will look like the example shown in figure 6.5. It should be stressed that for quantification purposes, as is the case in the determination of hydrogen concentrations in a-Si:H thin films using the infrared technique, the two-point baseline correction procedure should be preferred for its higher degree of accuracy.

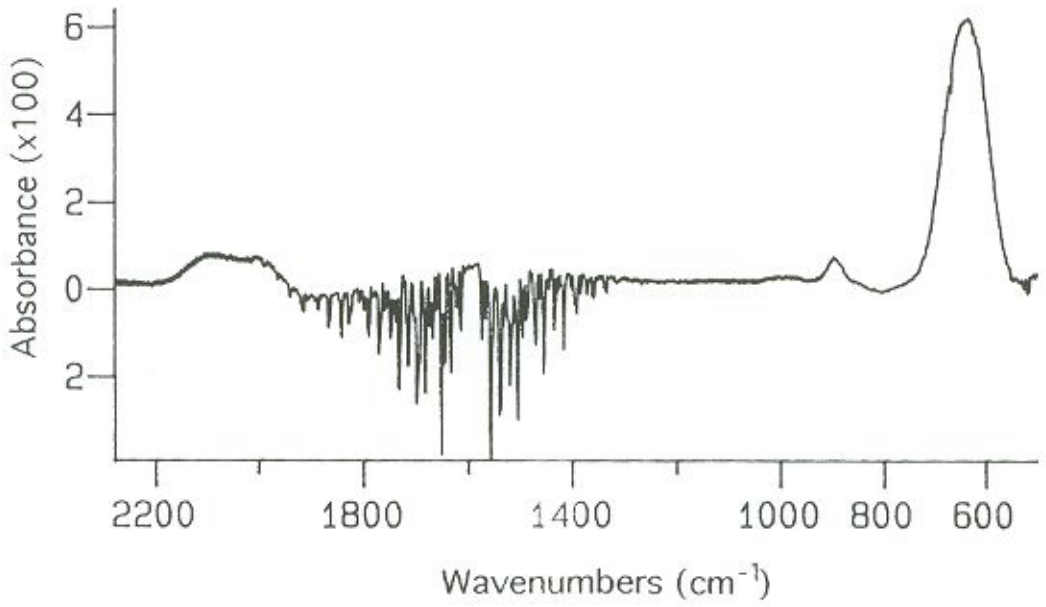

Figure 6.5: IR absorption spectrum of an a-Si:H thin film after baseline correction in the 2300 to 450 cm^{-1} region.

Infrared vibrational spectra of a-Si:H thin films usually contain peaks due to modes which vibrate very close to one another, resulting in overlapping (convoluted) peaks which cannot be individually resolved from the original band profile. Deconvolution attempts to enhance the apparent resolution of overlapping peaks where the limiting resolution is the natural width of the bands, not the resolution with which the spectrum was collected. Figure 6.6 shows an example of peak deconvolution for the H-Si infrared stretching band (2200 - 1900 cm^{-1} region), where the ~ 2100 and ~ 2000 cm^{-1} peaks have been deconvoluted.

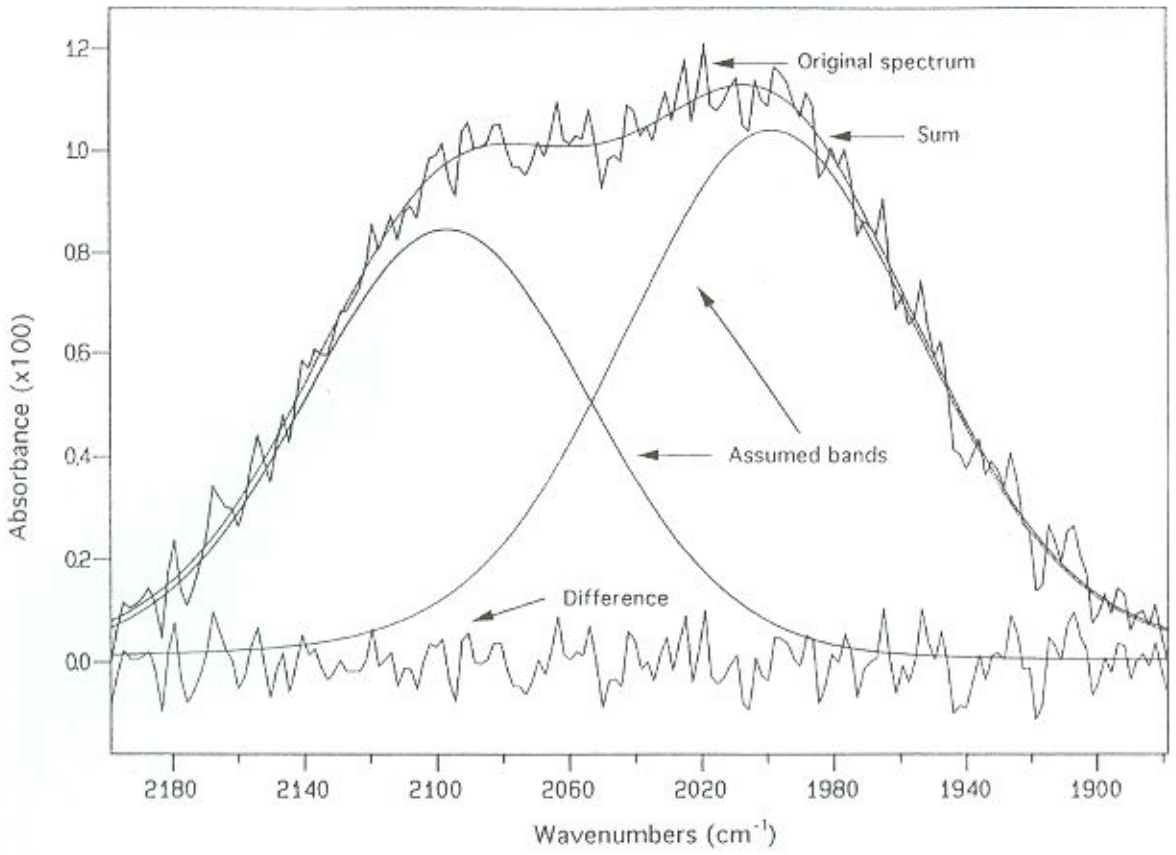

Figure 6.6: Deconvolution of the infrared stretching band of an a-Si:H thin film into its component peaks, showing the original spectrum, the two assumed component peaks (centred at ~ 2100 and ~ 2000 cm^{-1}), the sum of these component peaks, and the difference between the original spectrum and the assumed peaks.

Bandfitting is the mathematical operation whereby a sum of Gaussian or Lorentzian lineshapes are fitted to an unknown band profile. An initial estimate to the underlying lines of a band profile is usually done manually by adding bands and changing their initial parameters [position, height, half-width (full width at half maximum - FWHM) and % Gaussian] in order to obtain the lowest Root Mean Square (RMS) deviation between the raw input spectrum and the best estimate. After that an automatic optimisation process is usually selected. The Nelder-Mead optimisation method is presently the recommended choice [175]. It is a version of the Downhill Simplex

algorithm and is fairly robust. Typically, it will start out with a detailed investigation of the parameters which takes many steps and then follow with a set of trial movements which come rapidly but usually yield little or no improvement (this is done in order to locate a productive avenue for optimisation). Finally, it will gradually improve the fit. Figure 6.7 exemplifies the bandfitting procedure for an a-Si:H thin film slightly contaminated with nitrogen and oxygen (bands at ~ 670, 790, 980 and 1080 cm^{-1}) and includes a series of Si-H peaks (bending and wagging bands) as well as Si-N and Si-O peaks.

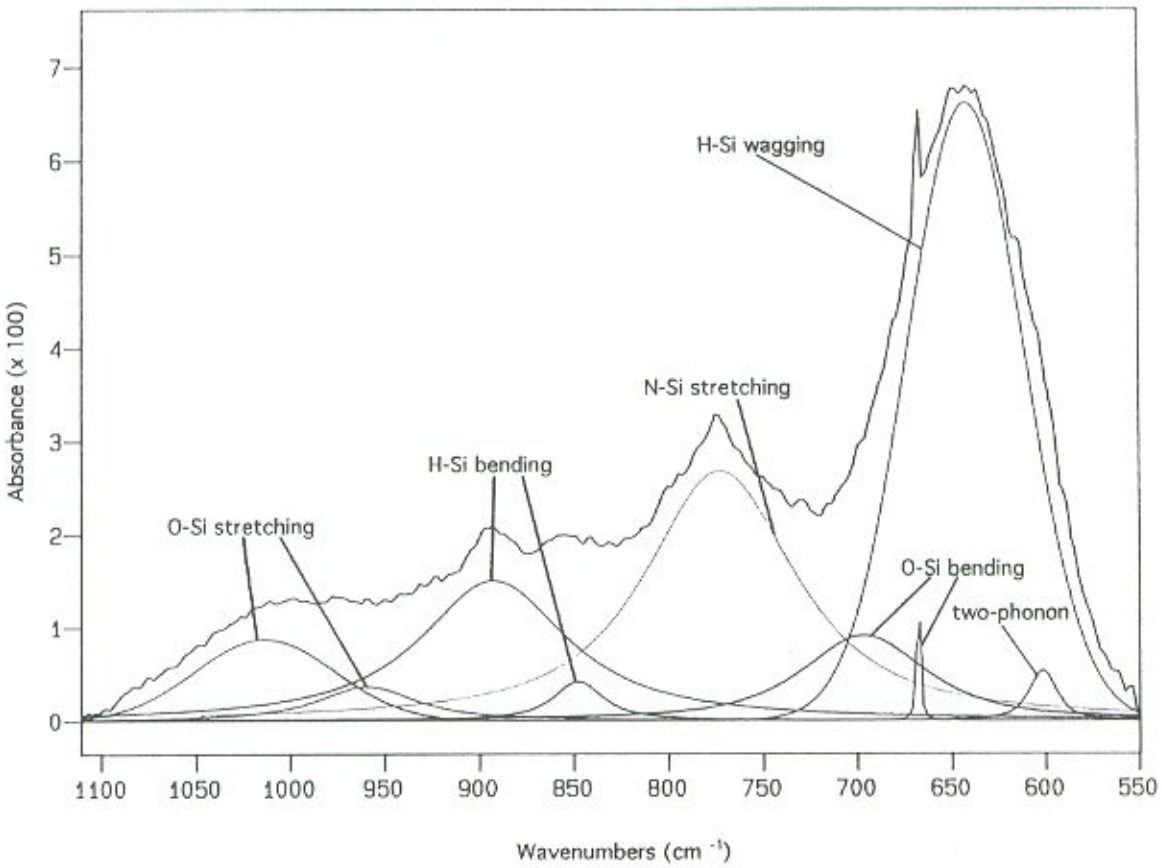

Figure 6.7: Example of a deconvoluted and bandfitted portion of the infrared spectrum (1100 to 550 cm^{-1}) of an a-Si:H thin film, showing Si-H peaks (bending and wagging bands) as well as some additional peaks due to Si-N and Si-O.

6.1.6.3 Si-H Infrared Data Analysis

For the infrared data analysis of a-Si:H thin films described in this thesis, vibrational peaks in the stretching, bending and wagging mode regions of the infrared spectrum were quantified using the procedures previously described. In general, the Si-H stretching band was deconvoluted into two Gaussians centred at ~ 2000 and ~ 2100 cm^{-1}. For the bending band, in the cases where it was present at all, deconvolution resulted in peaks centred at ~ 845, 875 and 890 cm^{-1} with some additional peaks assigned to carbon, oxygen and nitrogen contamination occasionally occurring at ~ 690, 770 to 790, 960 to 980 and 1020 to 1100 cm^{-1}. In the wagging band, the ~ 640 cm^{-1} Si-H peak was used to determine the film's total bonded hydrogen concentration as described in section 5.1.3. An additional feature, vibrating at ~ 600 cm^{-1} and showing a small absorption was also present in some samples. It is usually assigned to two-phonon absorption in the crystalline silicon substrate [144] (see figure 6.7). In all cases, peak centre and integrated intensity (equation 5.2 in section 5.1.3) was the most relevant information to be used in infrared data analysis of a-Si:H thin films. Peak height, full-width at half maximum (FWHM) and percent Gaussian were always recorded as complementary information. The peak centre position (in wavenumbers) is used to ascertain to which bond configuration a particular peak corresponds, and also to verify frequency shifts associated with thermal annealing experiments which lead in some cases to bond switching. The integrated intensity gives information on the abundance of a particular species and was used to quantify all bond types occurring in the amorphous silicon network.

6.1.7 Scanning Electron Microscopy (SEM) Analysis of a-Si:H

Scanning electron microscopy (SEM) studies were carried out in the Electron Microscopy Centre at The University of Western Australia, which is equipped with a

number of SEMs. For this thesis, only surface morphology analysis was of interest, and a Philips 505 scanning electron microscope was used.

Carbon & gold coated a-Si:H thin film samples deposited on c-Si substrates were used. They were mounted on top of pin-type SEM mounts, which were then loaded into the SEM specimen chamber. For imaging analysis the system used secondary electrons, which constitute a relatively low energy emission beam, suitable for surface viewing purposes. For most of the SEM micrographs presented in this study, samples were tilted at 60°, beam energy ranged between 15 and 30 keV, and the spot size was usually 50 to 100 nm.

6.1.8 Elastic Recoil Detection Analysis (ERDA) and Rutherford Backscattering (RBS) Measurements

The elastic recoil detection of protons by MeV He ions was used in this work to profile hydrogen in a-Si:H thin films. Additionally, Rutherford backscattering (RBS) was also simultaneously used in some cases to determine film thickness more accurately. Figure 6.8 below shows the schematic diagram of the ERDA and RBS geometries used for the hydrogen energy calibration, hydrogen profile and thickness measurements. ERDA and RBS measurements were made simultaneously on a 3 MV Van de Graaff accelerator, using a 2.4 MeV ^{4}He beam, with a current density of 0.5 $nA.mm^{-2}$. The ^{4}He beam was incident at 15° to the sample surface, with the ERDA measurements made at a recoil angle of 30°, and the RBS measurements at a scattering angle of 150°. A 100 μm surface barrier detector with a 9.5 μm mylar range foil was used to measure the energy (depth) distribution of the recoil protons. Hydrogen content calibrations were made using the polyimide material Kapton.

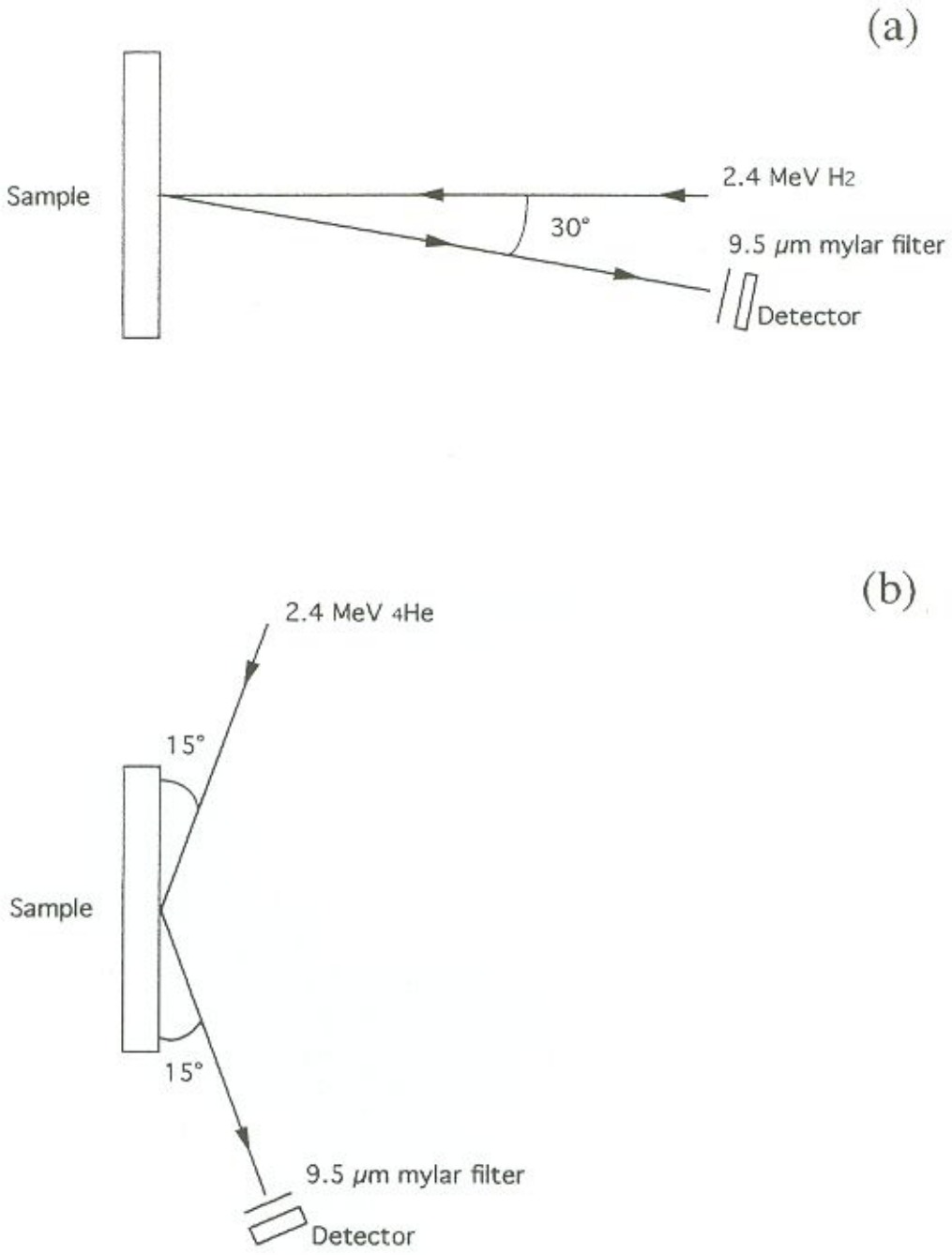

Figure 6.8: Schematic representation of the ERDA and RBS geometries, showing the (a) hydrogen energy calibration set up, and the (b) hydrogen profile measurements set up.

For the various experiments described in the forthcoming sections, ERDA (and in some cases RBS) measurements and infrared scans were always made on the same sample,

thus avoiding sample to sample variations. By measuring the infrared spectra of films before and after the ERDA measurements, we were satisfied that the ERDA measurement did not change the hydrogen content of the films. Also, Amato *et al.* [176] have shown that the choice of the substrate for ERDA measurements among c-Si, Corning glass or quartz does not play any role, so that the c-Si substrates used for FTIR spectroscopy were found suitable for both measurements.

By performing a series of complementary measurements with ERDA and RBS for a-Si:H films of different thicknesses it was possible to obtain an accurate depth scale for ERDA. After ERDA measurements, hydrogen profile simulations calculated with a RUMP-like [161] computer code were superimposed on the measured spectra. The computer code takes into account stopping powers of ions in target and foil, straggling, roughness and multiple scattering in the target and foil [154,160,162]. The program also allows hydrogen concentration profiles to be determined by fitting the measured and calculated spectra.

6.1.8.1 ERDA and RBS Data Analysis

The most common approach to analysis is to use computer codes to simulate measured spectra and through these to infer elemental distributions [151]. Since it is unusual that the constituent elements of a sample to be analysed are totally unknown, the simulation technique consists of making an educated guess at the composition and structure of a sample and calculating the resulting ERDA or RBS spectrum. This is then compared with the measured data and adjustments made to the input structure until the simulated and experimental spectra agree, using a least squares criterion. Particular attention is paid to the fits to step heights and to leading edge positions, as energy shifts can indicate the presence of surface layers (i.e. oxides or contaminants).

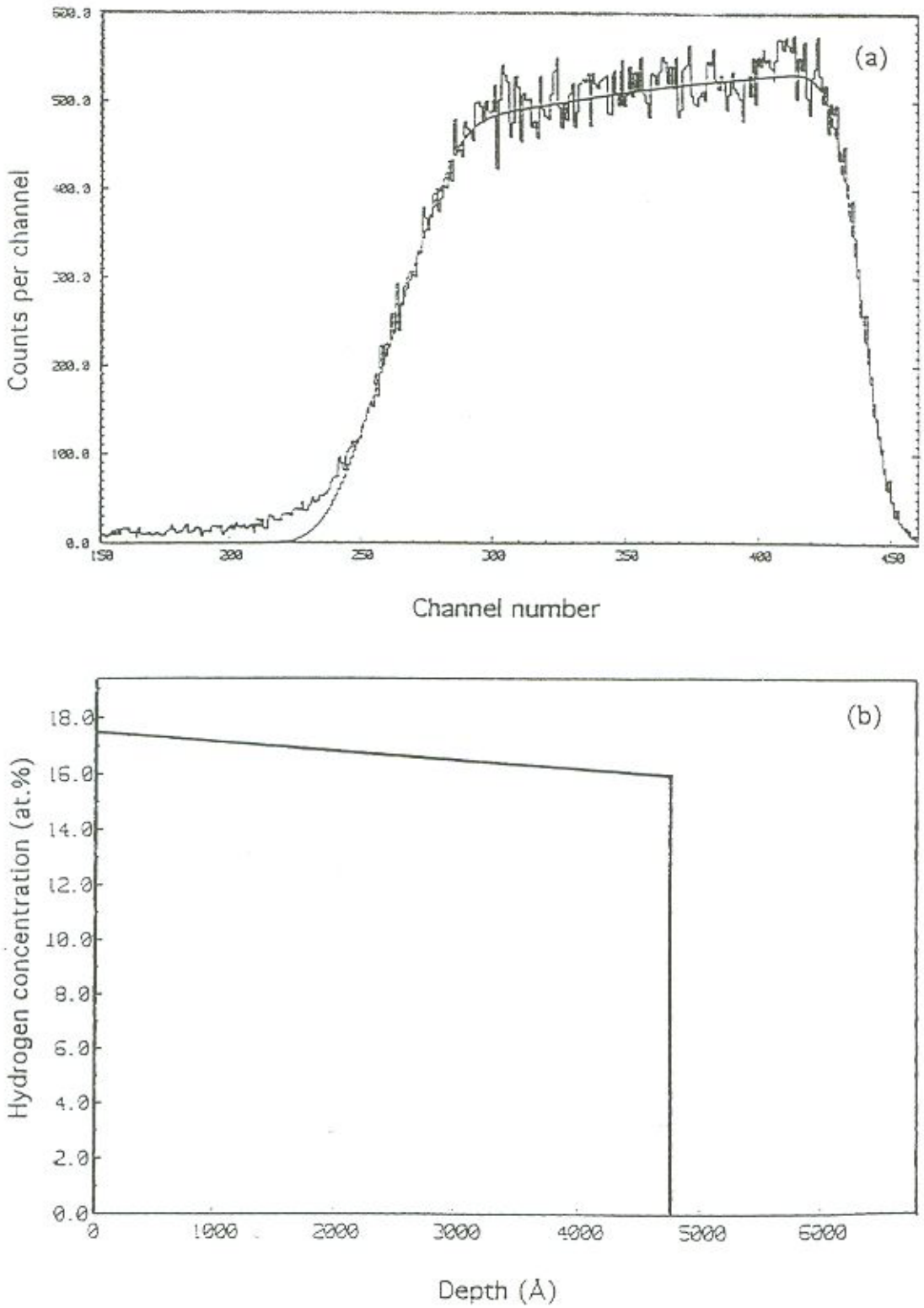

Figure 6.9: ERDA hydrogen depth profile, showing the measured (a - jagged line) and simulated (a - smooth line and b) hydrogen profiles of the same a-Si:H thin film. In (a), the right-hand edge corresponds to the film surface and the left-hand edge corresponds to the film-substrate interface.

The computer code contains tabulated stopping power data for all elements and either calculates Rutherford cross-sections for RBS or uses tabulated values for non-Rutherford or reaction cross-sections [151]. The effects of straggling in the sample and detector absorber foil, as well as the energy resolution of the detector system, are included in the calculations. Figure 6.9 above shows an example of measured and simulated ERDA spectra for an a-Si:H thin film.

6.1.9 Thermal Annealing

In some of the experiments to be further described, selected samples were subjected to thermal annealing in conjunction with FTIR, ERDA, RBS and SEM analysis. Thermal annealing was performed in resistance-type tubular furnaces at both the University of Western Australia using a quartz tube furnace, and at the Australian Nuclear Science and Technology Organisation (ANSTO, where all of the ERDA measurements and some of the FTIR spectra collection were also performed), using an alumina tube furnace. Samples were loaded onto a quartz boat which was then inserted into the furnace tube. In all cases, samples were loaded and unloaded from the furnace while at room temperature. Annealing temperatures as well as heating and cooling temperature ramps are specified for each of the experiments in the appropriate sections.

6.2 Commercial-Type a-Si Solar Modules

This section describes the materials and methods used in experiments involving commercially-available amorphous silicon solar cells and modules.

6.2.1 Light-Soaking of a-Si Solar Modules

Solar simulator systems offer a reliable and reproducible means of evaluating the performance of photovoltaic solar modules under simulated light at any time. These systems can reproduce a particular solar spectral distribution (usually AM 1.0 or AM 1.5) with an acceptable degree of accuracy. All light-soaking experiments described in this work were carried out under a Kratos/Schoeffel 2500 W Solar Simulator, calibrated to the AM 1.0 spectrum. This solar simulation system is based around a xenon short-arc lamp, which has been found to be the most reliable type of light source for this purpose, with a long life, extremely repeatable performance and steady output [177]. Control over spectral distribution is given by filtering of the xenon spectrum, which provides outputs closely following the accepted air mass standard. Figure 6.10 provides a rough comparison of the spectral distribution of the solar simulator versus the AM1.0 standard.

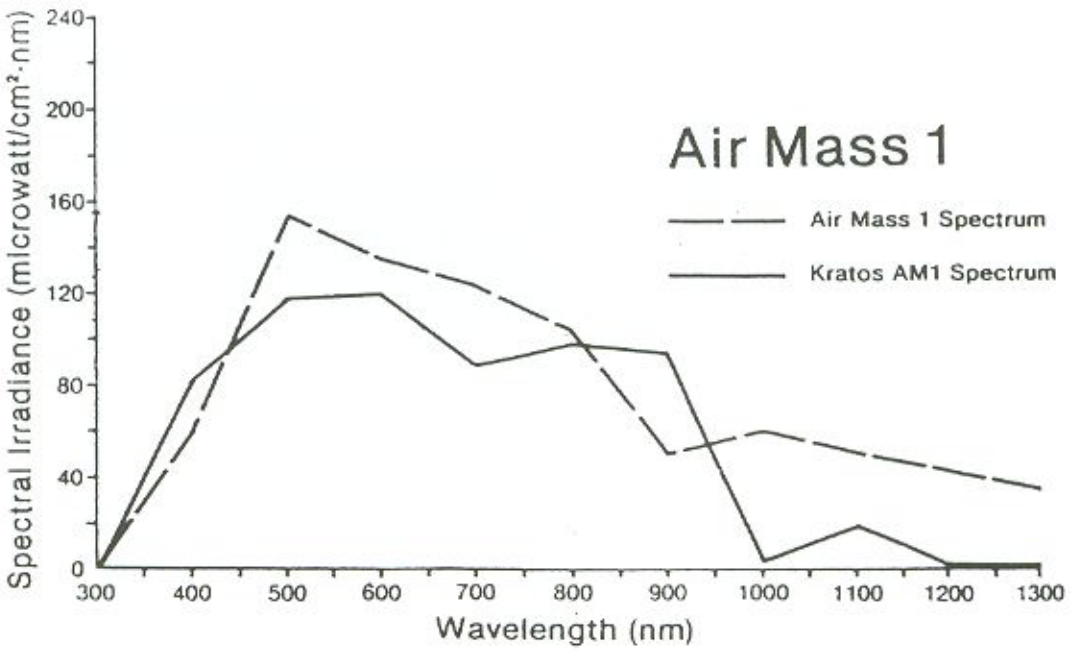

Figure 6.10: Comparative air mass spectra, showing the AM 1.0 standard spectrum (dashed line) and the filtered xenon spectrum (continuous line) of the Kratos solar simulator [177].

In this system configuration, light intensity is proportional to beam size and distance from subject, and an intensity of 1 Sun (100 $mW.cm^{-2}$) was chosen for the experiments described in this work. The intensity of the light source was set by means of a calibrated crystalline silicon solar cell. In order to simulate winter and summer solar cell operating temperatures, an attachment has been devised in which solar modules were attached to a water-cooled heat sink. The whole system was installed in a 3 x 3 m^2 closed, windowless room, with wind speed virtually nil. Operating solar cell temperatures were monitored by means of thermocouples attached either to the rear of solar modules (in the case of glass-substrate design models) or to the front surface of a "dummy" solar module of identical type to those used in the experiments (in the case of stainless steel-substrate design models). In this work, the terminology "operating solar cell temperature" was always used in comparative terms, *i.e.* solar modules with identical and identically placed temperature sensors were used in order to establish what the temperature differential between so-called "summer" and "winter" conditions was. Those temperatures did not necessarily correspond to those of the respective active photovoltaic layer (i-layer), even though these differences are believed to be small. Figure 6.11 shows a diagram of the solar simulator system including solar modules holders (either water-cooled or not), current-voltage (I-V) and temperature readout, and the calibrated c-Si reference cell.

All light-soaking experiments were carried out under open circuit conditions, which represent the worst-case scenario for stability studies. At open circuit all carriers must recombine within the cell, causing carrier densities to build up, increasing the number of recombinations which produce the dangling bonds believed to be responsible for the light-induced degradation effect. At the load point, the current flow out of the contacts reduces the net carrier density in the i-layer, slowing the rate of degradation by an order of magnitude or so [33].

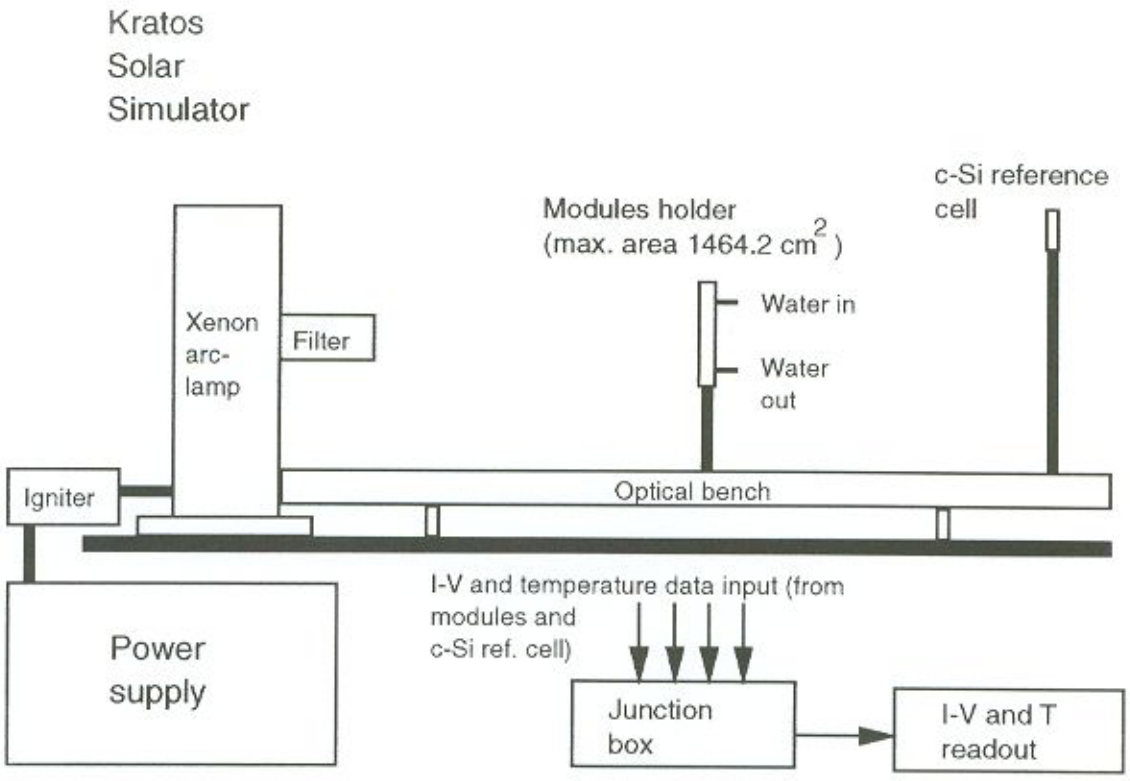

Figure 6.11: Diagrammatic representation of the xenon arc-lamp Kratos solar simulator system used for light-soaking of a-Si:H solar cells and modules.

6.2.2 Terrestrial Solar Spectral Content Measurements

Spectralradiometric measurements were used in this work to study the seasonal changes in the spectral content of sunlight in the response range of single-junction amorphous silicon solar cells (bandgap = 1.75 eV). Measurements of the terrestrial solar spectral content were made using an International Light model IL700 research radiometer readout unit with a high sensitivity IL780 spectroradiometer detector probe. This system allows measurements of absolute irradiance in units of $W.cm^{-2}.nm$. With this instrument, continuous measurements of light intensity can be made in the spectral band from 190 nm to 1100 nm with the appropriate detector. The particular system used

in this work was calibrated from 250 nm to 800 nm and could read spectral irradiance levels as low as 1 x 10^{-11} $W.cm^{-2}.nm$. An attached model S-20 photomultiplier was also used for short-wavelength measurements to increase sensitivity and readability at the very low light levels occurring in the near-UV region.

Due to scatter, it is possible for light of longer wavelengths to pass through the monochromator, thus introducing an error in the readings taken from 250 - 300 nm. In order to avoid this effect, a BLK270 blocking filter was used. In an interference system such as a grating monochromator, all wavelengths which are multiples of the fundamental will pass through. Sorting filters, which block the second order transmission, were also used in the 400 - 600 nm and 600 - 800 nm regions to block all but the primary wavelength.

Total solar spectral irradiance measurements were made on clear days at solar noon, at the rooftop facilities of the Solar Energy Research Group at the University of Western Australia (Perth, Australia, latitude: 31.9 °S, longitude: 115.8 °E, elevation: 19 m). All measurements were carried out over the region of 280 nm to 800 nm in steps of 10 nm.

Chapter 7

The Role of Substrate Temperature and In-Chamber Annealing in H-Si Bonding Configurations and H Content in a-Si:H Thin Films

7.1 Introduction

The identification and control of H-Si bonding configurations in a-Si:H thin films for solar cell applications is of both scientific and technological interest. In order to better understand and propose solutions to some mechanisms contributing to the light-induced degradation effect, it is essential that hydrogen in this material must be intensively investigated. The metastable defects which affect the stability of a-Si-based solar cells have been identified as possibly being caused by hydrogen, impurities, inhomogeneities (~ 20 Å scale) and strained bonds [178]. A great deal of research has been conducted in the elucidation of the role of hydrogen in these films since it is generally accepted that hydrogen content and structure play a major role in the Staebler-Wronski effect.

It is considered that an appropriate amount of hydrogen present in a specific bonding configuration within the amorphous silicon network is the key to the optimal electrical, optical and opto-electrical properties necessary for the production of high efficiency, high stability a-Si:H photovoltaics. In solar cell applications, which usually use the p-i-n structure configuration as described in section 3.2.1, intrinsic (i-type) amorphous silicon is the active layer where the photocarrier generation takes place. Not only

the H content of this layer, but also the way these H atoms are bonded to the structure, seems to affect markedly the cell's performance and stability. Control, therefore, of the hydrogen content (C_H) and hydrogen bonding configurations in intrinsic-type amorphous silicon thin films is an important aspect in solar cell technology.

In the reactive sputtering deposition process, C_H is basically governed by surface bombardment by hydrogen (*i.e.* the abundance of hydrogen reaching the deposition surface), and by the substrate temperature T_s (through physical and chemical processes which promote hydrogen removal), whereas the factors which control the bonding configuration distribution are still not clear. In this deposition method the hydrogen content can be independently adjusted by a change in T_s or by a change in the partial pressure of hydrogen gas introduced during deposition. Moreover, sputtering is expected to produce a different mix of active growth species as compared to the commonly used glow discharge decomposition of silane gas (*e.g.* PECVD process), and various differences might prove beneficial, particularly in the area of light-induced degradation which is commonly attributed to microstructural origins [179].

There has been renewed interest in sputter-deposited amorphous silicon [178-184]. A review of the literature [51,52,179,182,185-187] shows that in most cases the films produced by sputtering techniques presented a much higher SiH_2 than SiH bond density, as determined by the IR absorption peaks centred at about 2100 and 2000 cm^{-1} respectively, except when very high power densities [188] (~ 3 $W.cm^{-2}$), which cause a more energetic bombardment producing stress and increasing the deep gap states density [189], were used. In this chapter it will be shown that it is possible to improve the relative densities of SiH over SiH_2 bonds in sputter-deposited a-Si:H thin films at relatively low power densities. An in-chamber annealing post-deposition treatment has been devised to that purpose, and its effects

on the infrared absorption spectra, where a higher degree of control over H-Si bonding configurations has been achieved, will be demonstrated.

The optimal quality a-Si:H material prepared by the PECVD technique is usually obtained at a deposition temperature between 200 - 300 °C, which more or less fixes its optical energy gap at about 1.75 eV [190]. The reason why such deposition conditions result in low defect densities is explained by the thermal equilibrium model [34], in which the dangling bond-type defects are believed to equilibrate with weak Si-Si bonds via the diffusion of hydrogen. For solar cell applications, the bandgap of a-Si:H is usually broadened with carbon (a-$Si_{1-x}C_x$:H) and narrowed with germanium (a-$Si_{1-x}Ge_x$:H). However, incorporation of carbon or germanium atoms distorts the silicon network and it is therefore preferable to broaden the gap without alloying with these elements. This work presents a-Si:H films with a variety of H-Si bonding configurations (which is presumed to lead to a variety of defect density levels) prepared at various deposition temperatures and in-chamber annealing treatments. This resulted in optical energy gaps which can range from ~ 1.61 to 1.88 eV (as calculated from a hydrogen content range of ~ 7 - 21 at.% using the relations shown in [30]) for the best quality films as far as the bonding configuration distribution is concerned.

Most of the a-Si:H thin films presented in this thesis were less than 1 μm thick. Elastic recoil detection analysis (ERDA) and Rutherford backscattering (RBS) were used to check the hydrogen concentrations obtained by infrared methods (FTIR). This was done in order to check the validity of the correction proposed by Maley and Szafranek [147] for film thickness < 1 μm when using the widely employed Brodsky, Cardona and Cuomo [52] method.

7.2 Experimental Procedures

Amorphous silicon thin films were prepared in a RF reactive sputtering system, which was used to deposit intrinsic-type films only. The RF plasma was maintained by the 13.56 MHz RF generator which is connected to the lower "J" shaped electrode in a conventional vacuum system capable of providing initial pressures below 10^{-6} Torr in the 20 litre chamber. The 1 x 2 cm^2 (100) c-Si substrates were cleaned with three different organic solvents, distilled deionised (DD) water, ultrasonic bath and HF etched, as described in chapter 6, prior to being placed on the grounded upper electrode. Sodalime glass substrates were also cleaned and placed on the same substrate holder to provide samples for routine thickness measurements. The distance between electrodes (target-substrate distance) was 5 cm. Various sets of samples, each set typically consisting of three c-Si and one glass substrate, were co-deposited, and before each deposition run a base vacuum of 10^{-6} Torr or better was reached. Table 6.1 in section 6.1.3 describes the reaction conditions, which have been previously optimised in this laboratory [191], and table 7.1 below describes the different substrate temperatures (T_S), and the post-deposition in-chamber annealing treatment conditions used for the samples described in this chapter. Each sample corresponds to, and is representative of, a particular set of deposition/in-chamber annealing conditions.

For all samples presented here, except for sample 9 which was ~ 1 μm thick, film thickness varied in the range 0.35 - 0.50 μm. The deposition rate has been calculated from the deposition time, and was ~ 1 $Å.s^{-1}$ for the samples described in table 7.1. The desired substrate temperature was reached by means of a tungsten heating element, which was turned on some 4 to 6 hours prior to deposition, to allow for the set temperature to be reached in the evacuated reactor chamber. The in-chamber annealing treatment to which some samples were subjected, consisted, as soon as deposition was finished, in keeping the samples at a temperature (T_{ICA}) slightly below the deposition temperature (T_S) for 2 hours, in either vacuum, an atomic hydrogen

atmosphere produced by a hot tungsten filament (starting from the same Ar + H_2 atmosphere used during deposition), or a hydrogen plasma (the same Ar + H_2 deposition plasma). With the in-chamber annealing treatment we intended to promote structural relaxation and activate surface reactions, allowing hydrogen-silicon bonding configurations to rearrange and permit hydrogen in- and out-diffusion to and from the films.

Table 7.1: Deposition temperature (T_s) and in-chamber annealing (ICA) treatment conditions for a-Si:H thin film samples

Sample	T_s (°C)	In-chamber annealing conditions
1	170	not in-chamber annealed
2	215	atomic hydrogen, for 2 hours, at 180 °C
3	260	atomic hydrogen, for 2 hours, at 240 °C
4	260	not in-chamber annealed
5	285	vacuum, for 2 hours, at 215 °C
6	285	not in-chamber annealed
7	285	atomic hydrogen, for 2 hours, at 250 °C
8	285	vacuum, for 2 hours, at 230 °C
9	285	atomic hydrogen, for 2 hours, at 230 °C
10	300	hydrogen plasma, for 2 hours, at 285 °C
11	300	atomic hydrogen, for 2 hours, at 250 °C
12	300	hydrogen plasma, for 2 hours, at 285 °C plus atomic hydrogen, for 2 hours, at 250 °C
13	300	not in-chamber annealed

In order to check whether there would be any differences between performing the in-chamber annealing as described, and annealing the samples in the same way but after allowing them to cool to room temperature (thus allowing the random network to "freeze-in" and the hydrogen chemical potential to decrease before the in-chamber annealing treatment), we performed a further experiment. Samples 4 and 6 were annealed in atomic hydrogen under the same conditions and reactor chamber as those that, in the in-chamber annealing treatment, led to samples 3 and 9. Table 7.2 summarises these thermal annealing in hydrogen conditions.

Table 7.2: Thermal annealing conditions for samples 4 and 6, after being allowed to cool to room temperature inside the deposition chamber

Sample	Annealing conditions
4	atomic hydrogen, for 2 hours, at 240 °C
6	atomic hydrogen, for 2 hours, at 230 °C

Infrared spectra of all samples were measured according to the procedures described in section 6.1.6, in the range 4400 - 400 cm^{-1} immediately upon removal of the samples from the reactor. The hydrogen concentration (C_H) was determined from the integrated strength of the wagging band infrared peak centred at ~ 640 cm^{-1} using equations 5.1 to 5.3. In this work, the correction proposed by Maley and Szafranek [147] (equation 5.5) was applied whenever sample thickness was < 1μm. All peaks in the stretching, bending and wagging bands were deconvoluted and fitted into Gaussians using the Nelder-Mead optimisation program, and optimisation was carried out until no more improvements in the RMS deviation could be achieved (a curve fit was only considered

acceptable if RMS deviation was below 10% for a band region including three or more peaks and below 5% for a band region involving one or two peaks).

ERDA and RBS analyses were carried out at the Lucas Heights Research Laboratories (Australian Nuclear Science and Technology Organisation - ANSTO) in New South Wales as part of a project supported by the Australian Institute of Nuclear Science and Engineering (AINSE), entitled "Elastic Recoil Analysis on In-Chamber Annealed Hydrogenated Amorphous Silicon Thin Films". A number of samples deposited on c-Si substrates (*viz.* samples 2, 5, 6, 7, 8, and 9) was selected in order to check the validity of equation 5.5. The ERDA (hydrogen profile) and RBS (film thickness) measurements were made simultaneously on a 3 MV Van de Graaff accelerator, using a 2.4 MeV ^{4}He beam, with a current density of 0.5 nA/mm^2. The ^{4}He beam was incident at 15° to the sample surface, with the ERDA measurements made at a recoil angle of 30°, and the RBS measurements at a scattering angle of 150° as previously described (section 6.1.8). In order to eliminate sample to sample variations and making use of the nondestructive character of both FTIR and ERDA techniques, a number of single a-Si:H samples typical of each of the different deposition and in-chamber annealing conditions described for the selected samples was used.

The glass-substrate samples (typically 2 x 3 cm^2) were deposited using a metal mask showing a 1 x 2 cm^2 portion of the glass substrate. This design allowed room for the surfometer stylus to be displaced during the thickness measurements, which were also routinely carried out after each deposition run. While surfometer and RBS thickness measurements agreed well, with RBS measurements providing much more accurate results (with an estimated + or - 100 Å error), surfometer measurements provided a fast and inexpensive estimate of sample thickness and were the means ordinarily employed throughout this work.

7.3 Results and Discussion

7.3.1 Role of T_S and In-Chamber Annealing in H-Si Bonding Configurations and Hydrogen Concentration

In table 7.3 we present the total bonded hydrogen concentration for the samples described in table 7.1, after applying equation 5.5 to correct for film thickness as previously discussed. During deposition of a-Si:H, as growth proceeds and Si is bonded into the network, the different characteristics of Si and H become evident. Silicon forms a rigid, non-equilibrium structure, whereas hydrogen has a more mobile equilibrium structure [22], and can partially penetrate the silicon network as we will further show. The stable bonding configurations are the Si-H bonds and unstrained Si-Si bonds which are too strongly bonded to be broken by hydrogen, while highly strained Si-Si bonds have energies close enough to the chemical potential of H that they are broken and either reconstruct as Si-H bonds or into stronger Si-Si bonds [22]. In this sense, hydrogen scavenges the growing film of its weak strained bonds, resulting in a more ordered network. Hydrogen diffusion during growth is what dictates the process kinetics, which is thus highly temperature dependent.

The comparison of samples 1, 4, 6 and 13, none of which was in-chamber annealed, shows the strong influence of substrate temperature alone on the total bonded hydrogen content. This can be seen in samples 1 and 4 (T_S = 170 and 260 °C respectively), where a 90 °C temperature difference caused C_H to change by less than 2 at.%, while a more than twofold decrease occurred from sample 4 to 6 (T_S = 260 and 285 °C respectively) for a 25 °C temperature difference, and a further strong reduction in C_H took place from sample 6 to 13 (T_S = 285 and 300 °C respectively) for a 15 °C temperature difference. The higher the substrate temperature, the lower the amount of hydrogen incorporated into the amorphous

silicon network. Particularly noticeable is the strong temperature dependence of the hydrogen incorporation process.

Table 7.3: Total bonded hydrogen concentration (C_H) for a-Si:H samples. C_H has been calculated from the integrated intensity of the ~ 640 cm^{-1} wagging band infrared absorption peak and corrected for film thickness according to [147].

Sample	C_H (at.%)
1	20.9
2	17.8
3	15.3
4	19.2
5	9.3
6	7.3
7	17.6
8	6.7
9	10.9
10	16.3
11	5.7
12	5.4
13	4.6

Moreover, the infrared spectra of the stretching and bending bands for samples 1 and 4, shown in figure 7.1 and 7.2, indicate that the lower T_s sample presented a larger amount of higher hydrides (as indicated also by a larger ~ 2100 cm^{-1} IR peak), with occurrence

of polyhydride bonding configurations inferred from the presence of two peaks in the bending band. The presence of a doublet in the 840 - 895 cm^{-1} infrared region (as was the case for sample 1) is usually assigned to the presence of silicon polyhydrides ($(SiH_2)_n$ and SiH_3) in the films [192], whereas the presence of a single peak in that region (as was the case for sample 4) indicates the presence of silicon dihydrides (SiH_2) only. Since higher hydrides are associated with weakly bonded hydrogen (WBH) [193], higher deposition temperatures in the 170 - 260 °C range have produced a-Si:H films with a larger amount of tightly bonded hydrogen (TBH) atoms. The stretching bands shown in figure 7.1 corroborate this hypothesis since the ratio of mono-to-higher hydrides shown is increased for the higher T_s sample (sample 4).

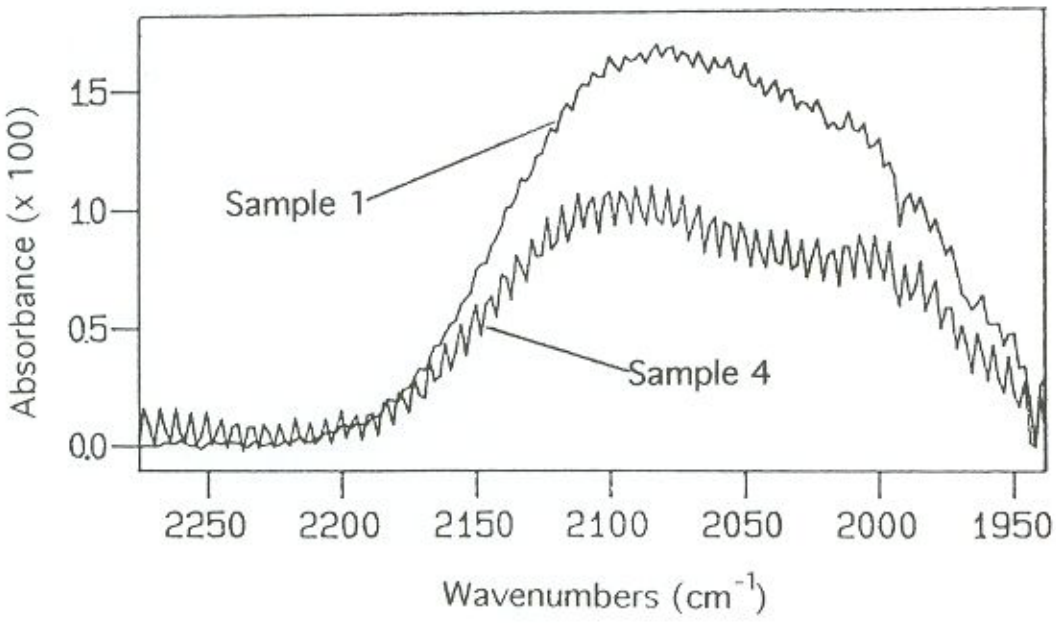

Figure 7.1: Stretching band region of the IR absorption spectra of samples 1 and 4, showing the ~ 2100 and ~ 2000 cm^{-1} peaks.

Samples 6 and 13, for which the substrate temperatures used were 285 and 300 °C respectively, presented a much smaller amount of hydrogen incorporation into each film's random structure. The relative amounts of higher hydrides as inferred from the

bending band peaks for these samples, however, were considerably higher than for samples 1 and 4. Therefore, deposition of samples at higher T_s alone (in order to achieve the desired 5 - 10 at.% usually found in high quality a-Si:H thin films for solar cell applications) was not found to be satisfactory as far as the incorporation of undesired higher hydrides is concerned.

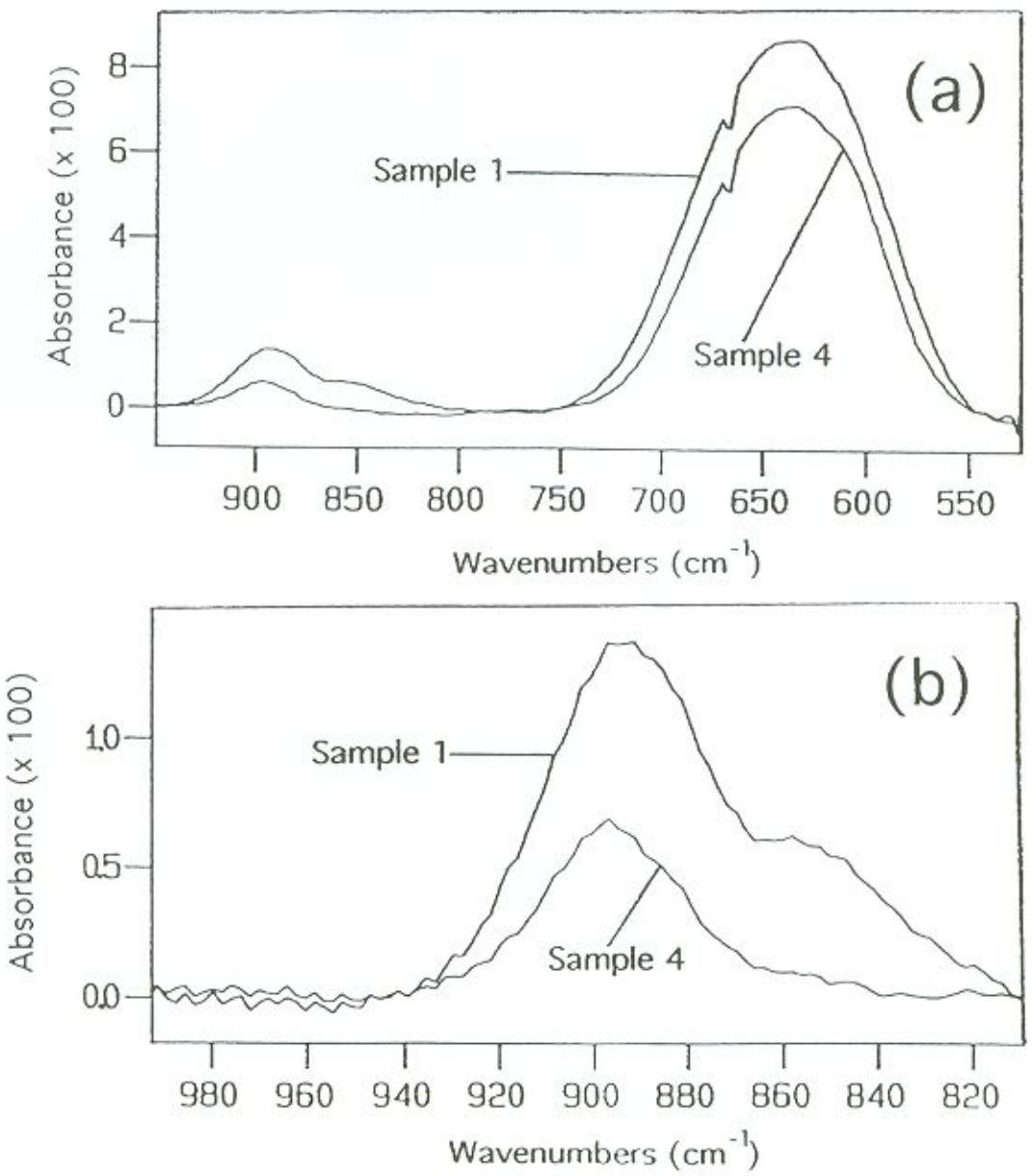

Figure 7.2: (a) Bending and wagging band regions of the IR absorption spectra of samples 1 and 4; (b) enlarged view showing the bending band region only.

We now turn to the analysis of the effects of our in-chamber annealing treatment on both the amount of bonded hydrogen and on the resulting H-Si bonding configurations in sputter-deposited amorphous silicon thin films.

We start by comparing samples 5, 6 and 8, which were all deposited at the same substrate temperature of 285 °C. Except for the in-chamber annealing (in vacuum) treatment to which samples 5 and 8 were subjected (for 2 hours at T_{ICA} of 215 and 230 °C respectively), all conditions were the same for these samples. However, if we take the hydrogen content of sample 6 (C_H = 7.3 at.%) as a starting point, in-chamber annealing in vacuum *increased* C_H for a T_{ICA} of 215 °C (sample 5, C_H = 9.3 at.%), but slightly *decreased* it for a T_{ICA} of 230 °C (sample 8, C_H = 6.7 at.%). We could speculate that the extra hydrogen present in sample 5, which was incorporated during the in-chamber annealing (in vacuum) treatment, was supplied by the surroundings, either the substrate (the c-Si chip) or the reactor chamber, or else, that this increase might have been caused by some trapped molecular hydrogen in the network (IR inactive) that could have formed H-Si bonds during the in-chamber annealing treatment, thus becoming IR active. We shall discuss this point further in chapters 9 and 10. In any case, again the role of temperature was substantial, with slight variations in the in-chamber annealing temperature causing opposite effects.

Differences between in-chamber annealing in vacuum at these slightly different temperatures did not only cause contrasting results in C_H; Si-H bonding configurations were also markedly different for samples 5 and 8. Figure 7.3 shows the deconvoluted and bandfitted stretching band absorption regions of samples 5, 6 and 8. While samples 5 and 6 presented a relatively more pronounced ~ 2100 cm^{-1} peak, indicating a higher proportion of either higher hydrides, or clustered monohydrides or both, and a small contribution from the ~ 2000 cm^{-1} peak (assigned to isolated monohydrides), sample 8 presented a higher contribution from the ~ 2000 cm^{-1} peak.

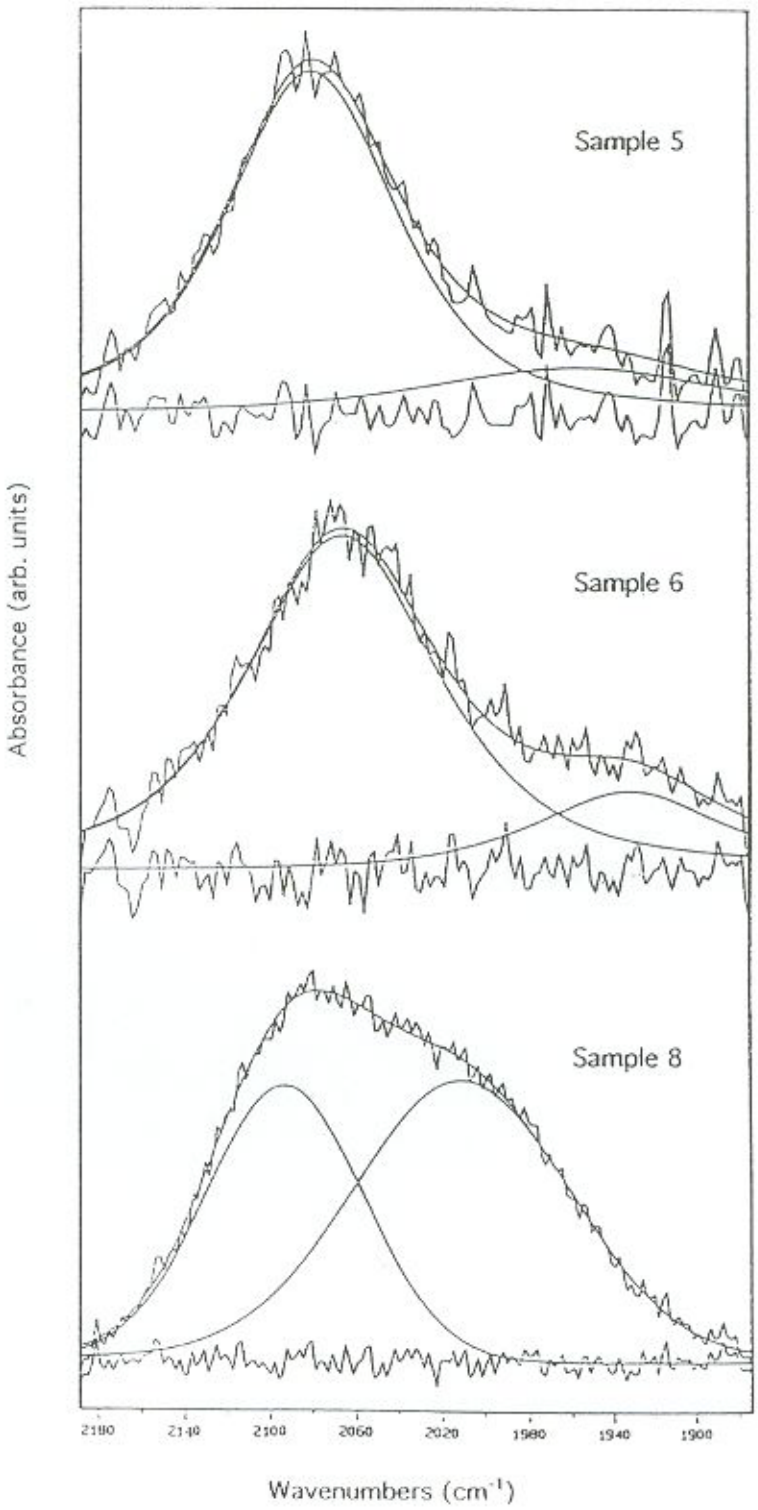

Figure 7.3: Deconvoluted and bandfitted stretching band absorption peaks of samples 5, 6, and 8, showing the original spectra (jagged sloping line), the estimated peaks and their sum (smooth line curves), and the difference (jagged horizontal line).

It should be noted here that although the original spectrum (jagged-line) might show a more pronounced shoulder for the ~ 2100 cm^{-1} peak for sample 8, the fitting of bands to that spectrum, whose sum is the continuous smooth line superimposed to the original spectrum, resulted in a higher integrated strength for the ~ 2000 cm^{-1} peak as shown. The RMS deviation for all bandfittings in figure 7.3 was smaller than 5%.

In summary, in-chamber annealing in vacuum at 215 °C of a sample deposited at 285 °C resulted in an increased hydrogen content and similar bonding configuration distribution with respect to a sample deposited under the same conditions but not in-chamber annealed.

On the other hand, in-chamber annealing in vacuum at 230 °C of a sample deposited under identical conditions resulted in a lower hydrogen content and an improved bonding configuration distribution. In the first case, in-chamber annealing in vacuum caused the incorporation of more hydrogen after deposition was completed, but the hydrogen-silicon bonds appear to be of the weak type (WBH) as determined by infrared spectroscopy, a feature that is generally regarded as an indication of poor quality for solar cell applications. In the second case, in-chamber annealing in vacuum apparently removed some of the undesired, weakly bonded hydrogen features, resulting in a higher proportion of isolated silicon monohydride groups.

We now discuss the results of samples 2, 3, 7, 9, 10, 11, and 12, all in-chamber annealed in hydrogen. We start by comparing samples prepared at a particular substrate temperature and not in-chamber annealed, with their in-chamber annealed (in hydrogen) counterpart. We compare sample 3, which was in-chamber annealed in hydrogen at 240 °C, and sample 4 which was not in-chamber annealed, both deposited at the same substrate temperature (T_s = 260 °C). We note that the in-chamber annealing treatment reduced the amount of bonded hydrogen from 19.2 to 15.3 at.% after deposition was completed. Furthermore, analysis of the stretching band peaks in figure 7.4, reveals that

the ~ 4 at.% hydrogen which was out-diffused from sample 3 during the in-chamber annealing treatment was of the weak type (WBH), since the ratio of mono-to-higher hydrides is considerably increased from sample 4 to 3. For the particular conditions described, in-chamber annealing in an atomic hydrogen atmosphere resulted in improved H-Si bonding configurations. The argument that the resulting bonding configurations could have resulted from a lower hydrogen concentration alone could be raised, but we will show later on in this chapter that C_H alone is not what determined the relative amounts of each H-Si bonding type in our a-Si:H thin films.

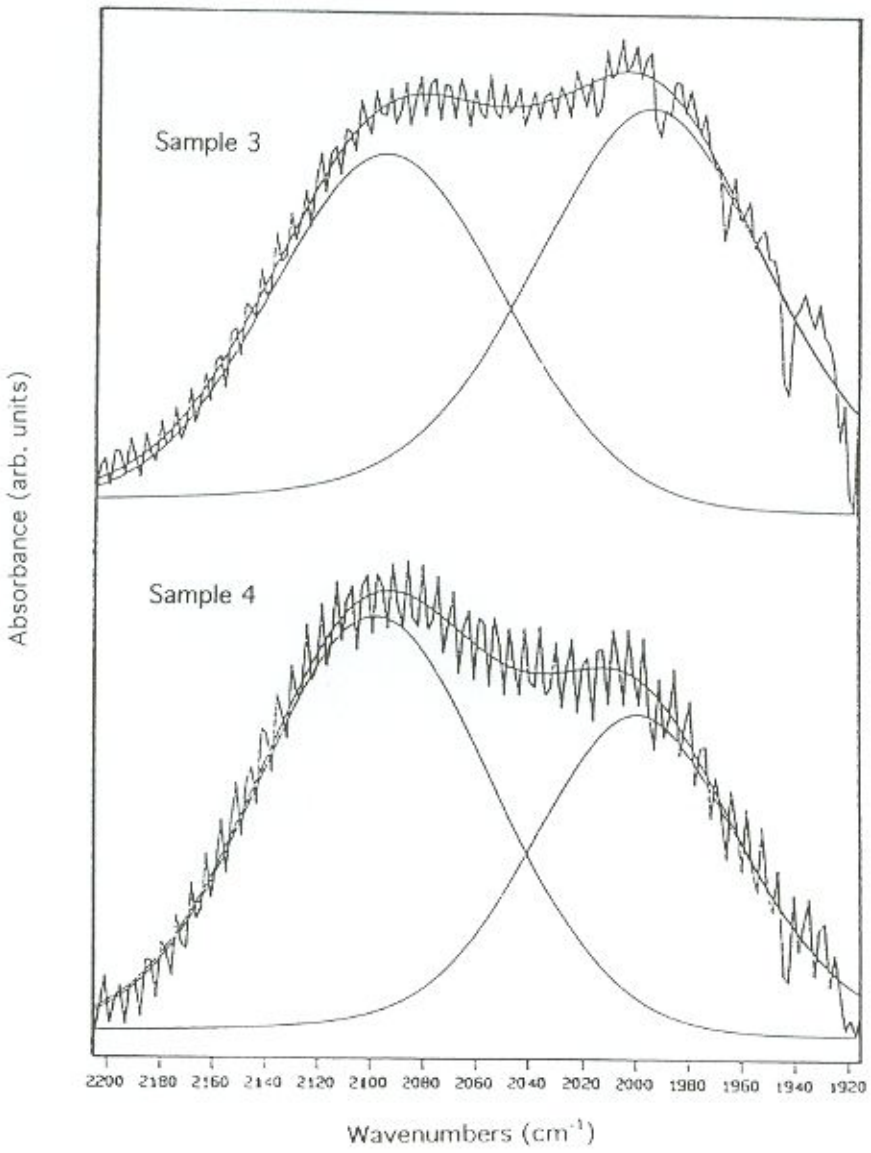

Figure 7.4: Deconvoluted and bandfitted stretching band absorption peaks of samples 3 and 4, showing the original spectra (jagged line), and the estimated peaks and their sum (smooth lines).

Let us now compare a set of samples deposited at the relatively higher substrate temperature of 285 °C. Samples 6 (not in-chamber annealed), 7 (in-chamber annealed at 250 °C), and 9 (in-chamber annealed at 230 °C) were all deposited at the same T_s; their total bonded hydrogen concentrations were 7.3, 17.6 and 10.9 at.% respectively. Here, the in-chamber annealing treatment increased C_H after film deposition was completed, but slight differences in in-chamber annealing temperatures caused a large variation in the amount of bonded hydrogen in those films. It appears that the rise in the hydrogen chemical potential at T_{ICA} = 250 °C was much more pronounced than at T_{ICA} = 230 °C, causing the amorphous network to rearrange, and allowing a much higher degree of hydrogen diffusion and incorporation. The more than two-fold increase in C_H from sample 6 to sample 7 is remarkable and points to extensive network reconstruction, which is confirmed in figure 7.5 which shows the stretching band peaks for samples 6, 7, and 9. The uneven distribution between the ~ 2000 and ~ 2100 cm^{-1} peaks in sample 6 gives place to a more balanced ratio in the case of sample 7.

It should be noted here that the spectra in this figure are not to scale, and that the absolute integrated intensity of the IR peaks for sample 7 is higher than that for sample 6 as expected from their considerably different hydrogen contents. In-chamber annealing in atomic hydrogen at 250 °C resulted in a better ratio of mono-to-higher hydrides; however, during the in-chamber annealing treatment, because both the stretching band infrared features showed considerable increases in absolute terms, both kinds of Si-H bonds were additionally formed and incorporated into the network.

Looking now at sample 9 we notice that a small decrease in the in-chamber annealing temperature caused a considerable reduction in the total bonded hydrogen content as compared to sample 7, *i.e.*, comparatively less hydrogen was diffused into the sample during the ICA treatment.

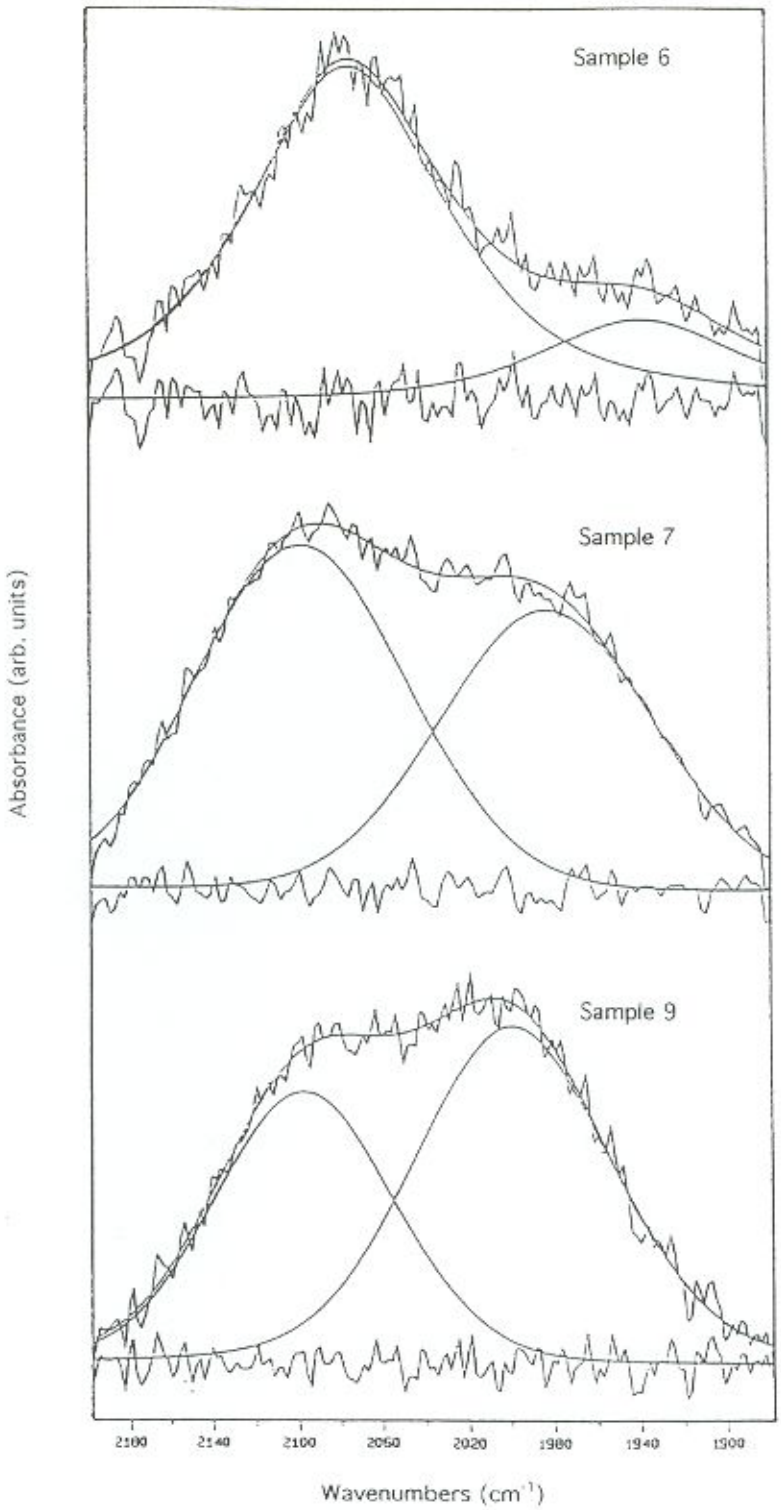

Figure 7.5: Deconvoluted and bandfitted stretching band absorption peaks of samples 6, 7, and 9, showing the original spectra (jagged sloping line), the estimated peaks and their sum (smooth line curves), and the difference (jagged horizontal line).

Moreover, at that temperature, as compared to the not-in-chamber annealed sample 6, more of the usually considered beneficial silicon monohydrides were incorporated into that film, as indicated by a relatively higher ~ 2000 cm^{-1} infrared peak. The ratio of mono-to-higher hydrides in that sample is remarkably changed from the original, not-in-chamber annealed sample 6 and was not caused by the elimination of weak H-Si bonds. Rather, it was caused by the incorporation, after deposition, of a higher proportion of silicon monohydrides. At a higher in-chamber annealing temperature (as was the case for sample 7), more hydrogen was incorporated into the sample, indicating that the balance between the competing effects of raising the hydrogen chemical potential (which increases the ability of H to be incorporated) and of hydrogen thermal effusion (which causes hydrogen out-diffusion) under those particular conditions favoured the former effect to a much higher degree. Let us go back to sample 3 before concluding the discussion involving samples 7 and 9. We note that sample 3 presented, for an in-chamber annealing temperature in between that of samples 7 and 9, a hydrogen bonding configuration distribution similar to that of sample 9, but a total C_H ~ 40 % higher than that of sample 9. This will lead to a slightly higher bandgap, for virtually the same improved bonding configuration structure, a particularly useful feature for multijunction a-Si solar cells.

Before continuing with higher T_s samples, let us compare samples 2 (T_s = 215 °C, ICA in hydrogen at 180 °C) and 7 (T_s = 285 °C, ICA in hydrogen at 250 °C). These two samples were deposited and in-chamber annealed at considerably different temperatures, yet their total bonded hydrogen concentrations were the same, around 17 at.%. From figure 7.6, however, we note that the way in which this hydrogen was bonded to silicon in each film differs markedly. Sample 2 shows a much higher concentration of higher hydrides, or weak H-Si (WBH) bonds. This sample was in-chamber annealed at a temperature slightly below the equilibrium temperature of a-Si:H, which is ~ 190 °C [194], and which resulted in no perceptible

improvement in the H-Si bonding distribution. The comparison of these two samples confirms our first observations that hydrogen-silicon bonding configuration distributions do not necessarily depend on or correspond to the total amount of bonded hydrogen. We will further comment on this aspect after analysing sample 10.

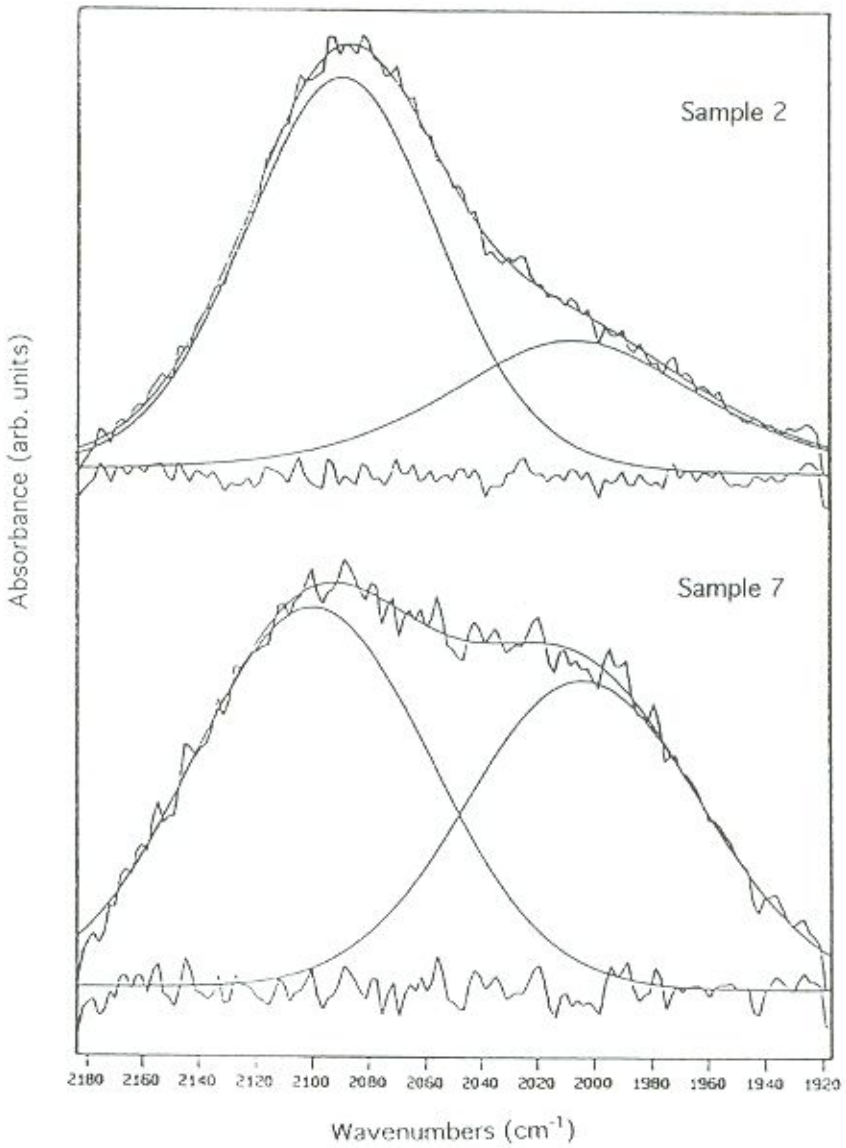

Figure 7.6: Deconvoluted and bandfitted stretching band absorption peaks of samples 2 and 7, showing the original spectra (jagged sloping line), the estimated peaks and their sum (smooth line curves), and the difference (jagged horizontal line).

We finally compare samples 10, 11, 12, and 13, all deposited at the same relatively higher substrate temperature of 300 °C. The first three samples were all in-chamber annealed in either a hydrogen plasma (sample 10, with T_{ICA} = 285 °C for 2 hours), atomic hydrogen (sample 11, with T_{ICA} = 250 °C for 2 hours), or both (sample 12, with T_{ICA} = 285 °C for 2 hours plus T_{ICA} = 250 °C for 2 hours, for the plasma and atomic H treatments respectively).

As can be seen in table 7.3, the total bonded hydrogen concentration for these samples varied over a wide range (4.6 to 16.3 at.%), and the analysis of C_H gives us further insight into the roles of substrate temperature and the in-chamber annealing treatment in the incorporation of H in the amorphous silicon network. Sample 13 was not in-chamber annealed, and from its very low hydrogen content of 4.6 at.% the effect of a higher T_s of 300 °C is evidenced. Moreover, even with a low C_H, the relative amount of loosely bound hydrogen was extremely high in comparison to the amount of isolated monohydrides, as can be noted in figure 7.7, which shows the stretching band peaks for samples 10 to 13. This again shows that H-Si bonding configuration distributions in our amorphous silicon films are not directly related to the total bonded hydrogen content.

Considering sample 10, when a film deposited under identical conditions as those for sample 13 was in-chamber annealed in a hydrogen plasma at 285 °C, a massive hydrogenation took place, with C_H increasing more than threefold. The bonding configuration distribution for this sample, however, presented approximately the same mono-to-higher hydrides ratio as that for the not-in-chamber annealed sample 13, with a very high proportion of the stretching band contribution lying in the ~ 2100 cm^{-1} peak as figure 7.7 shows. Sample 10 presented approximately the same C_H as that of samples 2 and 7, with the same undesirable stretching band shape as that of sample 2; sample 7, however, with T_s and T_{ICA} in between those of the other two, resulted in a much improved H-Si bonding configuration distribution.

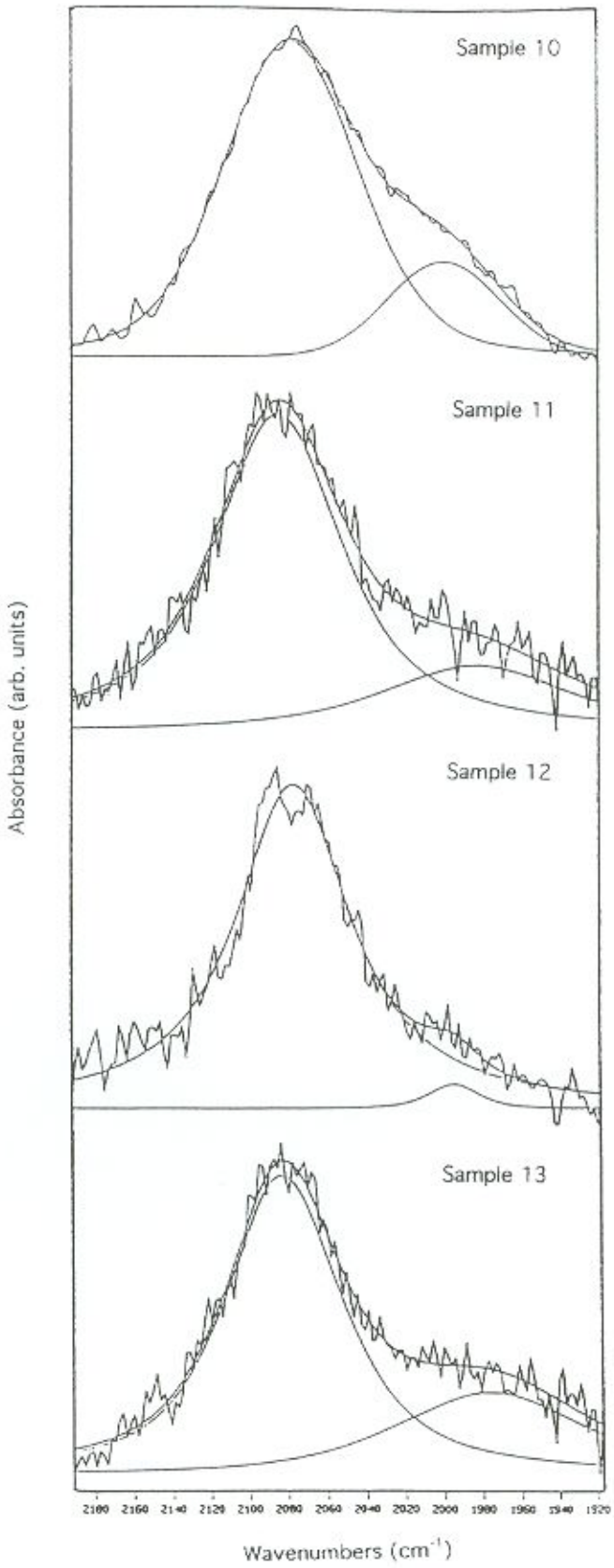

Figure 7.7: Deconvoluted and bandfitted stretching band absorption peaks of samples 10, 11, 12, and 13, showing the original spectra (jagged line), and the estimated peaks and their sum (smooth lines).

The marked effect of subtle variations in deposition and annealing temperatures in the 200 - 300 °C region is once again evidenced here.

For sample 11, which was in-chamber annealed in atomic hydrogen, hydrogen incorporation during this treatment resulted in a small increase in C_H in comparison to sample 13, but no improvement in the mono-to-higher hydrides ratio was observed; much to the contrary, the ~ 2000 cm^{-1} infrared peak is relatively smaller than that of samples 10 or 13. In comparing samples 11 and 13, it seems unlikely that the amount of tightly bonded hydrogen (TBH) would have decreased during the in-chamber annealing in hydrogen treatment as the infrared data indicate. Weakly bound hydrogen (WBH) would be expected to have evolved instead, and then also only if C_H had decreased, which was not the case, much to the contrary. This apparent contradiction can be satisfactorily explained if we consider the occurrence of monohydride clustering, a topic we will just briefly mention now and develop further in chapter 9. Clustered monohydrides are believed to vibrate at ~ 2100 cm^{-1}, as we mentioned in chapter 2 (section 2.3.1). We thus believe that in-chamber annealing under the conditions described for sample 11 increased C_H at the same time as it promoted, at that relatively high temperature, silicon monohydrides to cluster, thus shifting part of the integrated intensity from the ~ 2000 to the ~ 2100 cm^{-1} peak in the stretching bands of this sample.

For sample 12 we consecutively performed the in-chamber annealing treatments of both samples 10 and 11. The result was a total bonded hydrogen concentration of 5.4 at.%, that is, lower than the one resulting from any one of the treatments alone, and higher than a not-in-chamber annealed sample deposited at the same deposition temperature. From the analysis of samples 10, 11, and 13, we gather that the first ICA treatment has probably massively increased the low (< 5 at.%) C_H of sample 12, but the second ICA treatment has removed almost all of that post-deposition-incorporated hydrogen. That also confirms that most, if not all, of the hydrogen incorporated during the ICA in

hydrogen plasma treatment was loosely bound, since it was so readily evolved from the film during the ICA in atomic hydrogen treatment. Figure 7.7 corroborates this hypothesis, showing a stretching band for sample 12 in which the ~ 2000 cm^{-1} peak presents only a marginal contribution. It has been previously shown that exposure of device-quality a-Si:H to a H plasma results in both diffusion of hydrogen atoms into the film and interchange of atomic hydrogen between the film and the plasma [195]. Preparation of a-Si:H films at a deposition temperature of 300 °C in our sputtering system resulted, even when followed by the in-chamber annealing treatment shown to be beneficial at lower temperatures (*viz.* samples 3 and 9), in poor film quality as far as H-Si bonding configuration distributions are concerned. The marked differences in C_H observed for samples 10 to 13 indicate that large amounts of hydrogen atoms were loosely bound to the amorphous silicon network in those films.

We finally conclude our discussion about the in-chamber annealing treatment by commenting on the effects of annealing samples 4 and 6 in atomic hydrogen at conditions that would have led, had they been subjected to the in-chamber annealing treatment, to samples 3 and 9. Table 7.4 presents the total bonded hydrogen concentration for these samples, re-labelled as samples 4_{ANN} and 6_{ANN}. For sample 4_{ANN}, no significant changes were noticed in any of the H-related infrared peaks. That is, the in-chamber annealed structure of sample 3 was not achieved. The slight increase in C_H as compared to sample 4 is believed to be either an experimental artefact (an artificial increase of the I_{640} IR peak caused by increasing nonspecular scattering that might have occurred if the sample develops a rougher surface on annealing) or due to the conversion of some trapped molecular H_2 (infrared transparent) into infrared-active hydrogen.

For sample 6_{ANN}, however, some changes did occur. The total bonded hydrogen concentration doubled from sample 6 to sample 6_{ANN}, but almost all of this hydrogen was incorporated in the form of higher hydrides and/or clustered monohydrides, as can

be noticed from figure 7.8, which shows the stretching band region for sample 6_{ANN}. Comparing this figure with the stretching bands for sample 9 shown in figure 7.5, and from the results just shown for sample 4 -> 4_{ANN}, it is obvious that an important requirement of the in-chamber annealing is that the film should not be allowed to cool-down before the treatment. In-chamber annealing should be performed while the network is still not "frozen-in" and the hydrogen chemical potential is still high, in order to promote the desired H-Si bonding configuration reconstruction.

Table 7.4: Total bonded hydrogen concentration (C_H) for samples 4 and 6 (hereafter labelled 4_{ANN} and 6_{ANN}) after annealing in hydrogen under the conditions described in table 7.2.

Sample	C_H (at.%)
4_{ANN}	20.1
6_{ANN}	15.2

In the series of samples presented in this chapter, the in-chamber annealing treatment caused the total bonded hydrogen concentration, depending on the particular deposition and ICA temperatures, to either increase or decrease. In some cases this increase/decrease was accompanied by an improvement of the mono-to-higher hydrides ratio; in other cases this ratio was not affected or was even slightly degraded. Lucovsky *et al.* [196] demonstrated that sputtering and PECVD offer advantages over other glow discharge processes in the control of polyhydride formation in a-Si:H films. They claimed, however, that polyhydride formation is not controlled by the substrate temperature or any other single process variable, but that the determining factor is

the total bonded hydrogen content. Our results clearly show that, at least for the reactive sputtering technique under the particular conditions here described, polyhydride concentration in a-Si:H films can vary over a wide range for the same amount of bonded hydrogen concentration.

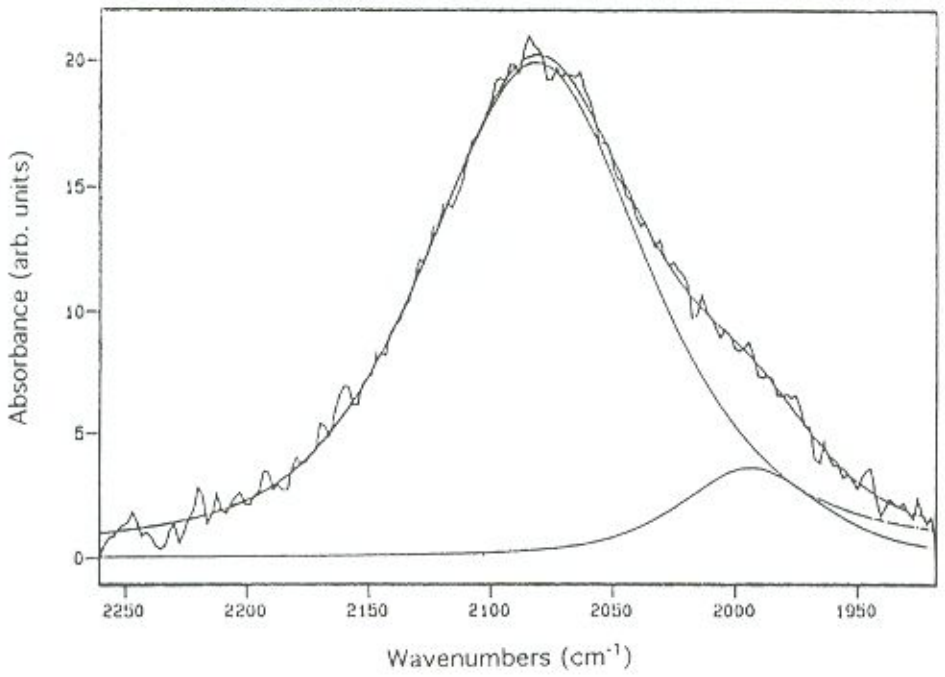

Figure 7.8: Deconvoluted and bandfitted stretching band absorption peaks of sample 6_{ANN}, showing the original spectrum (jagged line), and the estimated peaks and their sum (smooth lines).

A novel preparation technique termed "chemical annealing" (CA) has been proposed by Shirai *et al.* [197,198]. In this technique, the deposition of a very thin layer (a few tens of Å thick) of a-Si:H and the treatment of its surface with active species such as atomic hydrogen or excited inert gas (Ar or He) were alternately repeated until the desired film thickness was achieved. They suggested that the silicon network in the growing surface was reconstructed by the release of hydrogen during the CA treatment, which resulted in a more rigid structure. In the course of our studies we have used the in-chamber annealing treatment, which is a post-deposition treatment, and obtained a variety of

results. Our interpretation is that the combined (and competing) effects of an increased hydrogen chemical potential (as in our ICA treatment) and the promotion of hydrogen effusion from the films (caused by the increasing temperatures used in our work) can cause both hydrogen release and incorporation from/into the amorphous network. The overall picture that emerges from our investigation is that temperature is what determines which effect will be dominant. Moreover, the temperature range in which one or the other effect dominates seems to be very small.

7.3.2 Hydrogen Concentration: An Infrared and Elastic Recoil Analysis

Table 7.5 shows the hydrogen concentrations as estimated by FTIR using the method described in [52], and the ERDA profiles (surface and interface C_H), as well as the corrected (C_{Hcorr}) values, as proposed by Maley and Szafranek and described in chapter 5 for film thickness < 1 μm. Except for sample 9, which was thicker than 1 μm and for which FTIR and ERDA results agreed well (within 10%), all the other hydrogen concentration estimates by the infrared technique were overestimated, and the correction proposed in [147] brought the values to within the range estimated by the ERDA measurements.

To our knowledge, all the estimates of the proportionality constant for the wagging band peak (A_{640} or A_{wag}) to date have resulted from relating infrared absorbance, which detects infrared active hydrogen (H-Si bonds) only, to the total hydrogen content measured independently by techniques like ERDA and nuclear reaction analysis (NRA), which account for both infrared active and inactive hydrogen (molecular H_2). Discrepancies between C_H obtained via FTIR analysis (even for film thicknesses larger than 1 μm) and ERDA or NRA can be due in part to different amounts of molecular

hydrogen in the a-Si:H films produced by different reactors and techniques. Our results are in good agreement with the correction proposed by Maley and Szafranek [147] for infrared data analysis when film thickness is less than ~ 1 μm, and the scatter in the C_H data is within the typical resolution of the methods.

Table 7.5 Hydrogen concentration C_H, as determined by the FTIR and ERDA techniques, and the corrected C_{Hcorr} as suggested in [147]. All hydrogen concentrations are in at.%.

Sample	C_H(FTIR)	C_H(ERDA)	C_{Hcorr}
2	24.9	8-21	17.8
5	13.0	9-11	9.3
6	10.4	7-9	7.3
7	25.6	16-17	17.6
8	9.7	7-8.5	6.7
9	10.9	5.5-13	not applicable

7.4 Conclusions

In this chapter we have presented a series of i-type a-Si:H thin films deposited under similar deposition conditions, except for the deposition temperature and an alternative in-chamber annealing treatment we have proposed. Total bonded hydrogen concentrations varied over a wide range (4.6 to 20.9 at.%) over a deposition temperature (T_s) range of 170 - 300 °C and an in-chamber annealing temperature (T_{ICA}) range of 180 - 285 °C. More importantly, the H-Si bonding

configuration distributions were markedly changed with this *in situ* in-chamber annealing treatment, and some control and optimisation over the resultant structures was achieved. The lower hydrogen concentrations (as well as lower spin densities as reported by [199]) resulting from higher deposition temperatures have been explained by assuming that at higher T_s the growing film is better thermally annealed, thereby reducing the density of dangling bonds and consequently the concentration of hydrogen bonding sites [199]. The a-Si:H system has also been described as a Si structure in which hydrogen can diffuse relatively easily [200,201]. Hydrogen in this structure is believed to be distributed in two phases: a phase of isolated monohydrides diluted in the bulk and a loosely bound phase essentially contained in clusters of monohydride and dihydride [72]. These hydrogen clusters can be pictured as microvoids whose internal walls are decorated by H atoms [202].

By exposing a-Si:H thin films to chemically active hydrogen atoms and ions at temperatures above the equilibrium temperature of a-Si:H (*ca.* 190 °C [194]), we attempted to anneal the structure into a more relaxed configuration by means of hydrogen motion through the lattice, aiming at reducing the number of potential defect creation sites in the amorphous network. The high mobility of the resulting atomic H in the in-chamber annealing technique led to significant bonding rearrangements in the amorphous network, allowing a reasonable degree of control over H-Si bonding configurations in these sputter-deposited a-Si:H thin films. Liang, Maley and Abelson [184] have recently reported on improved stability of a-Si:H films grown by a sputtering process at high (320 - 440 °C) substrate temperatures. They believe that the improvement of stability comes from the combined effect of less hydrogen incorporation and a better amorphous network. We believe that with our in-chamber annealing treatment the same level of optimisation can be achieved using lower deposition and in-chamber annealing temperatures.

Temperature has been shown in this chapter to have a strong effect not only on the total bonded hydrogen concentration, but also on the way this hydrogen was bonded to silicon in the amorphous network. Higher temperatures influence the structural details of the a-Si:H network, through greater adatom mobility and bulk relaxation [184]. Nevin *et al.* [203] found a reduction in the light-induced degradation for plasma-treated films. Their films were plasma-treated at 70 and 340 °C and in both cases C_H was reduced as compared to non-treated films. In their treatment, however, samples were allowed to cool to room temperature and even unloaded from the deposition reactor before the plasma treatment, so that the silicon network at the time of plasma treatment would have undergone a significantly different relaxation path as compared to samples prepared using our in-chamber annealing treatment. Moreover, plasma treating a-Si:H thin films usually results in some degree of plasma etching and the associated plasma damage, which was not assessed in their work. We will further comment on this aspect in chapter 9. Asensi *et al.* [204] have found that solar cells in which the mono-to-higher hydrides ratio was increased presented a remarkably lower degradation after long-term illumination. In their cells, the intrinsic layer was deposited by a glow discharge technique at higher temperatures (~ 350 °C) to achieve the improved H-Si bonding configurations, and it is expected that the in-chamber annealing treatment in sputter-deposited films would lead to similar or even further improvements in that direction, with a higher flexibility over the resultant C_H.

Toneva *et al.* [44] have found that a certain amount of dihydride bonds is needed in order to relax the internal strains in the amorphous silicon network. Moderately high deposition temperatures (T_S) of 260 - 285 °C and slightly lower in-chamber annealing temperatures (T_{ICA}) of 230 - 240 °C resulted in the total bonded hydrogen concentrations of 10 - 15 at.% usually found in device-quality a-Si:H for solar cell applications. Moreover, these conditions also resulted in the improved bonding configuration distributions mentioned, translated by a higher ratio of mono-to-higher hydrides in the stretching band infrared peaks. Among the many models on the

Staebler-Wronski effect, the bonded hydrogen configurations appear very important in determining the ultimate stability of the many possible silicon-hydrogen arrangements. Control, therefore, over H-Si bonding configurations in a-Si:H thin films might offer alternatives by which the light-induced degradation problem in this photovoltaic material can be mitigated.

Chapter 8

Surface Morphology, Strain Relief and Microstructure on Thermal Annealing in a-Si:H Films

8.1 Introduction

In recent years the role of hydrogen in a-Si:H thin films has been extensively investigated, and it is well known that H acts as a Si-Si bond strain reliever as well as a dangling bond terminator in the amorphous silicon network. It saturates undercoordinated silicon atoms, thus lowering the density of these dangling bonds and producing a material of high electronic quality in the intrinsic form. This material can then be used as the active layer in thin film amorphous silicon p-i-n solar cells among other devices. The defect passivation effect of H is also what allows n- and p-type doping in a-Si:H to become effective [26].

In order to characterise the role of hydrogen in a-Si:H, infrared analyses and annealing studies were found to be useful, since a range of annealing temperatures can be systematically used in a single sample, providing information on a sequence of hydrogen evolution steps and bonding configuration changes as annealing temperatures are increased. Oxygen and nitrogen contamination, either during or after deposition, or both, can also be systematically determined. When annealed at temperatures (T_a) higher than the deposition temperatures (T_s), the material is subjected to extreme thermal conditions, which can affect the film's morphology.

Annealing can thus increase both the intrinsic compressive stress and also the extrinsic stress, due to hydrogen pressure rise in microvoids. This can produce fractures in the bulk material in areas where hydrogen accumulates and microvoids concentrate, originating larger voids which can be observed as blisters on the surface by scanning electron microscopy (SEM) [205]. A common feature of amorphous solids is the presence of voids or microscopic inhomogeneities in the disordered structure, and for amorphous semiconductors the characteristics of the voids are strongly dependent on the growth conditions [206]. The Staebler-Wronski effect has been described in Carlson's model [18] as being associated with metastable defect centres, assuming that holes (positive carriers) can be trapped near microvoids and can induce the motion of hydrogen on the internal surfaces of such voids. Infrared analysis has often been used to evaluate the presence of multivacancies and microvoids in a-Si:H material [146,207].

We have shown in chapter 7 how the *in situ* in-chamber annealing treatment can improve the H-Si bonding configuration distribution in sputter-deposited a-Si:H thin films. With the in-chamber annealing treatment it was possible to some extent, even when using lower power densities (~ 350 $mW.cm^{-2}$) during deposition, aimed at reducing the energetic bombardment which produces stress in the films, to shift the H-Si bonding configurations from multiply grouped polyhydrides (SiH_2, SiH_3, $(SiH_2)_n$) to isolated SiH sites. In this chapter we describe studies encompassing a wide range of annealing temperatures of samples deposited at different T_s, and also the use of FTIR spectroscopy and SEM microscopy to analyse the evolution in sample characteristics on annealing. The evolution of H-Si bonding configurations and total bonded hydrogen content at different annealing temperatures (200 - 600 °C) is presented, and the evolution in film's surface morphology on annealing is correlated with the motion and content of hydrogen in the amorphous network.

8.2 Experimental Procedures

Substrate cleaning plays an important role in the adhesion, morphology and structure of a-Si:H grown on crystalline silicon by sputtering techniques [169]. The cleaning procedures used in this work, described in chapter 6, were carefully chosen so as to eliminate this from the possible factors on which film adhesion depends. Details of sample preparation have been described in previous sections; apart from deposition temperature (T_s) and the in-chamber annealing treatment, which are shown in table 8.1, all samples were sputter-deposited under the same conditions. Sample thickness ranged between 0.5 and 0.7 μm. After deposition, immediately upon removal from the reactor, infrared absorption spectra were taken of the samples in the as-deposited state.

Table 8.1. Deposition temperature (T_s) and in-chamber annealing (ICA) treatment conditions for a-Si:H thin film samples

Sample	T_s (°C)	In-chamber annealing conditions
14	270	not in-chamber annealed
15	262	atomic hydrogen, for 2 hours, at 240 °C
16	170	not in-chamber annealed

The analysis of infrared absorption spectra allows one to determine the bonded hydrogen content from the integrated intensity of the wagging band. Information can also be obtained about the H bonding configurations from the intensities of the stretching and bending bands that occur in the 2000 - 2100 cm^{-1} and 800 - 900 cm^{-1} regions respectively. Furthermore, the IR spectrum can also be used to detect and

quantify oxygen and nitrogen, which present infrared absorption bands located in the 700 - 1200 cm^{-1} region. In this chapter all the hydrogen- nitrogen- and oxygen-related infrared peaks have been deconvoluted and bandfitted, and their integrated intensities will be presented and discussed in connection with morphological aspects. Furthermore, the amount of hydrogen bonded in some sort of microstructure was estimated from the integrated intensities of the IR-stretching modes centred at ~ 2000 cm^{-1} (monohydride bonding configuration, I_{2000}) and ~ 2100 cm^{-1} (polyhydride bonding and clustered monohydrides on the internal surface of microvoids, I_{2100}). This was assessed in terms of the parameter R [146] previously defined in chapter 5 (equation 5.4).

After infrared absorption spectra collection, samples were taken to the scanning electron microscope (SEM) for surface morphology analysis, before the annealing of films at higher temperatures. Samples were then thermal annealed in a tubular-type, resistance furnace, always for 2 hours in air, at 200, 300, 400, 500, and 600 °C (heating rate of approximately 20 $°C.min^{-1}$), and after each annealing treatment allowed to cool slowly (at approximately 2 $°C.min^{-1}$) to room temperature before infrared spectra were taken again. The surface morphology of the samples was observed before and after each annealing temperature step.

8.3 Results and Discussion

Tables 8.2, 8.3, and 8.4 show, from the deconvolution of peaks occurring in the 500 - 700 cm^{-1}, 700 - 1200 cm^{-1} and 1900 - 2200 cm^{-1} regions respectively, the integrated intensities for the hydrogen-, nitrogen- and oxygen-related peaks.

From table 8.2 the amount of chemically bonded hydrogen appears to have increased at first, during the initial steps of thermal annealing at lower temperatures, and after that, at higher annealing temperatures, it progressively decreased as expected. Boyce *et al.*

[208] have found that a small amount of molecular H_2 can be trapped in voids in the a-Si matrix. This can be responsible for the increase in the integrated absorption under the ~ 640 cm^{-1} peak on annealing at moderate temperatures, as some IR inactive trapped hydrogen becomes IR active. The amounts, however, should be orders of magnitude smaller than those in table 8.2. Das *et al.* [209] found that the overall increase in the IR absorption peaks is an artefact, because the film surface becomes rougher with annealing, thus increasing nonspecular scattering. Should void-trapped molecular H_2 be the reason for this increase in absorption, the hydrogen evolved at these moderate temperatures, *i.e.* up to around 300 °C, is not IR active in the as-deposited state, and hence probably not chemically bonded to the a-Si lattice. We note here that for sample 15, which was in-chamber annealed and presented a lower as-deposited hydrogen content, hydrogen was apparently more tightly bonded, since after annealing at 400 °C the ~ 640 cm^{-1} peak for that sample presented the highest integrated intensity compared to the other two at the same annealing temperature. That sample retained almost 90 % of its initial hydrogen content after successive 2 hour annealing steps up to 400 °C, thus indicating the occurrence of a much more tightly bonded hydrogen in that in-chamber annealed film.

The featureless, as-deposited surface morphology of samples 14 and 15 can be seen in figure 8.1(a). Apart from some debris, resulting from sample cutting, the surface is smooth and defect-free, no blisters or peeling-off were noticed in such samples (samples 14 and 15 presented identical initial surface morphology, with figure 8.1(a) corresponding to sample 14). Sample 16 (figure 8.1(b)), however, showed a severely damaged as-deposited surface, leaving portions of the substrate exposed. These holes are believed to have been produced by an accumulation of gaseous hydrogen at the film-substrate interface, which probably caused an explosive release once the yield stress was reached [55]. Microvoids in a-Si:H filled with molecular hydrogen under high pressure are often cited in the literature [41,205], and are correlated with the low-temperature peaks in thermal desorption spectroscopy spectra.

Table 8.2: Integrated intensities (I_{640} in cm^{-1}) for the wagging band infrared peak and the estimated total bonded hydrogen content (C_{Hcorr} in at.%, corrected for film thickness as suggested in [147]).

Sample	T_a (°C)	I_{640}	C_{Hcorr}
14	as dep *	769	20.1
14	200	874	22.9
14	300	878	23.0
14	400	381	10.0
14	500	187	4.9
14	600	63	1.6
15	as dep *	521	13.6
15	200	675	17.7
15	300	572	15.0
15	400	456	11.9
15	500	190	5.0
15	600	56	1.5
16	as dep *	850	20.4
16	200	690	16.6
16	300	736	17.7
16	400	447	10.7
16	500	293	7.0
16	600	78	1.9

*as dep = sample in the as-deposited state

(a)

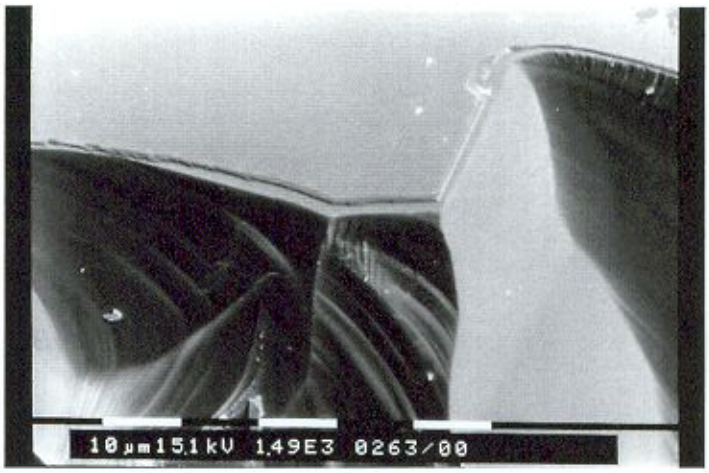

(b)

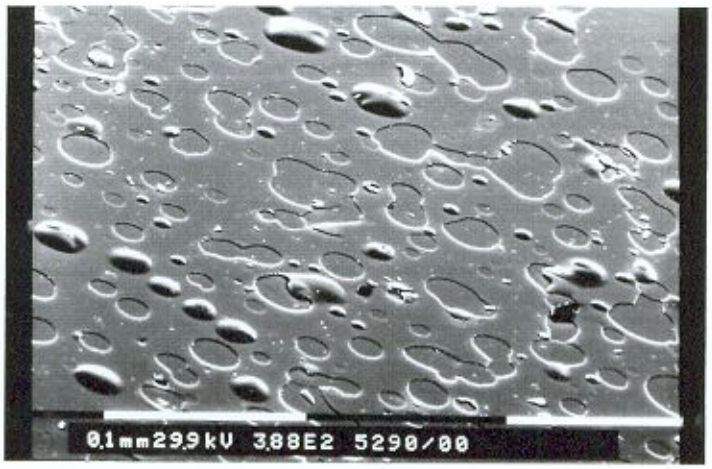

Figure 8.1: SEM photographs of as-deposited surface morphology of a-Si:H grown on c-Si substrates: (a) sample 14 (sample 15 presented the same featureless surface morphology), space bar equal to 10 µm; (b) sample 16, space bar 100 µm. Tilted at 60° in relation to the surface of sample.

Figures 8.2(a), 8.2(b), and 8.2(c) show samples 14, 15, and 16 respectively after the annealing treatment at 300 °C. Comparing figures 8.2(a) and 8.2(c) it is observed that

for sample 14 the holes resulting from annealing have roughly the same diameter as the ones in sample 16, covering, however, a smaller area. This can be related to the sample's lower initial hydrogen content, leading to less accumulation sites at the film-substrate interface being formed. A comparison between figures 8.1(b) and 8.2(c) reveals that apparently no change in surface morphology occurred for sample 16 from the as-deposited to the 300 °C annealed state, which sends us back to table 8.2, where we note that sample 16 was the only one for which the I_{640} infrared peak decreased between these two states. Both trapped molecular hydrogen and increases in nonspecular scattering might thus have caused the initial increase in the IR absorption peaks for samples 14 and 15, since the increase of the I_{640} peak for these samples under the particular annealing conditions described was accompanied by surface roughening. Figure 8.2(b) shows the surface of sample 15, the in-chamber annealed sample, after the same annealing treatment at 300 °C. Compared to figures 8.2(a) and 8.2(c), hole diameter for this sample is much smaller and can be related to the sample's lower initial hydrogen content from an alloy composition point of view. The yield stress for samples 14 and 16 is, therefore, apparently the same and we believe that hole concentration might be related to the concentration of gaseous hydrogen available at the film-substrate interface, while hole diameter might be related to alloy composition, resulting in different yield stress, which depends on the film's H-Si mix. For sample 15, yield stress seems to be lower, thus being reached with the accumulation of less gaseous hydrogen resulting in smaller holes popping off the sample. According to Windischmann [210] it is generally observed that if deposition conditions favour low mobility of the condensing atoms in sputter deposition, a porous, void-rich microstructure is produced. This may occur when deposition is performed at low homologous temperature (*i.e.* $T_s / T_m < 0.2$, where T_s is the absolute deposition temperature and T_m is the film's melting temperature). For our samples $T_s / T_m \sim 0.32$ for sample 14, ~ 0.31 for sample 15 and ~ 0.26 for sample 16, and the accumulation of gaseous hydrogen in voids is thus favoured for sample 16.

(a)

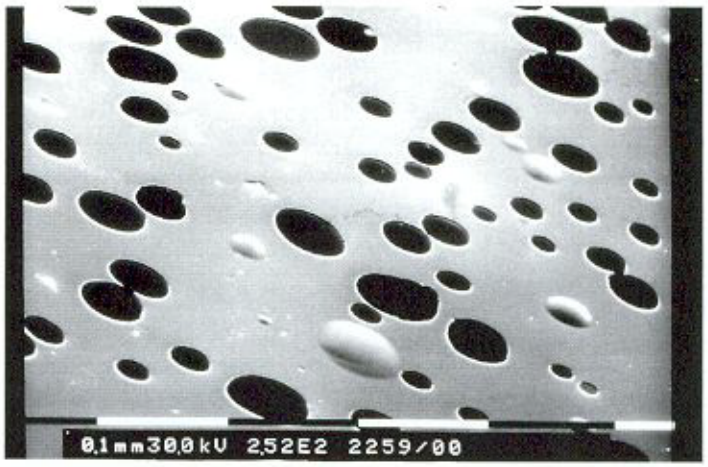

(b)

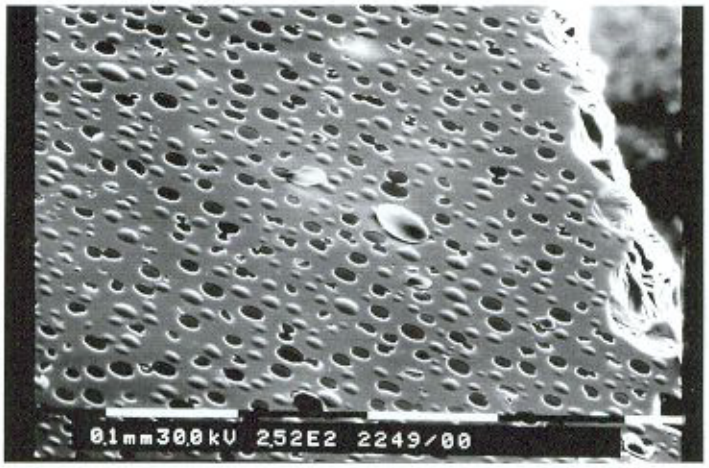

(c)

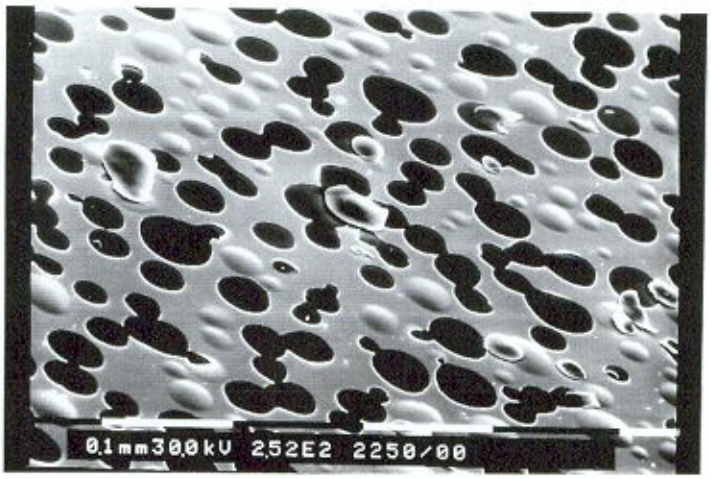

Figure 8.2: SEM photographs of samples annealed at 300 °C: (a) sample 14; (b) sample 15; and (c) sample 16. Space bars equal to 100 μm in all cases. Tilted at 60° in relation to the surface of sample.

We now turn to the analysis of the bending and stretching absorption bands and comment on nitrogen and oxygen contamination in our samples. The analysis of the 700 - 1200 cm^{-1} infrared spectral region, shown in table 8.3, indicates that the typical IR peak occurring at ~ 790 cm^{-1}, usually assigned to nitrogen contamination, was not detected in our samples in the present study. From the oxygen-related IR peaks we note that oxygen changed bonding configurations and partially evolved at low annealing temperatures for samples where $T_a < T_s$, while it increased right from the first annealing step for sample 16, for which $T_a > T_s$. Pronounced oxygenation seems to have occurred after hydrogen evolved and sample surfaces roughened, and in the first stages of annealing was less pronounced for samples with the least initial hydrogen concentration, in agreement with results by Biegelsen *et al.* [211]. The in-chamber annealed sample 15 showed the lowest degree of oxygen contamination up to annealing temperatures close to T_s. Films prepared at low T_s / T_m are porous and prone to forming oxides because of a large internal surface area [210].

Table 8.4 shows the integrated intensity of the H-Si stretching bands. As previously mentioned, it is generally accepted for the stretching mode absorption of monohydride species that isolated SiH vibrates at ~ 2000 cm^{-1}, the frequency shifting to near 2100 cm^{-1} as the number of other SiH bonds nearby increases [59]. This model is strengthened by the presence in some cases of stretching modes near 2100 cm^{-1}, which have no corresponding bending modes in the 845 - 890 cm^{-1} region. At annealing temperatures up to 300 °C, most of the changes in I_{2000} and I_{2100} are believed to be due to network reconstruction (*i.e.* monohydride clustering and/or bond switching), since hydrogen evolution below that temperature is usually not pronounced. At annealing temperatures higher than 300 °C, however, table 8.4 indicates that loosely bound hydrogen evolved from all samples.

Table 8.3: Integrated intensities (I in cm^{-1}) for peaks occurring in the 700 - 1200 cm^{-1} IR region. I_{845} and I_{890}; I_{790}; and I_{750}, I_{980} and I_{1080} correspond respectively to hydrogen bending modes, nitrogen stretching mode and oxygen stretching modes.

Sample	T_a (°C)	I_{845}	I_{890}	I_{790}	I_{750}	I_{980}	I_{1080}
14	as dep*	nd	26	nd	nd	99	4
14	200	nd	30	nd	nd	59	12
14	300	nd	22	nd	nd	94	23
14	400	nd	1	nd	nd	43	26
14	500	5	nd	nd	nd	24	72
14	600	nd	nd	nd	nd	nd	244
15	as dep*	nd	25	nd	nd	52	2
15	200	nd	26	nd	nd	42	3
15	300	nd	18	nd	nd	65	14
15	400	nd	3	nd	nd	62	22
15	500	nd	2	nd	nd	24	64
15	600	nd	nd	nd	nd	nd	205
16	as dep*	nd	26	nd	nd	64	2
16	200	nd	23	nd	nd	67	2
16	300	nd	21	nd	nd	95	11
16	400	nd	16	nd	nd	119	41
16	500	8	nd	nd	nd	34	70
16	600	nd	nd	nd	nd	nd	267

*as dep = sample in the as-deposited state, nd= not detected

Table 8.4: Integrated intensities (I in cm^{-1}) and the parameter R (eq. 5.4) for peaks occurring in the 1900 - 2200 cm^{-1} IR region

Sample	T_a (°C)	I_{2000}	I_{2100}	Parameter R
14	as dep*	146	138	0.49
14	200	126	143	0.53
14	300	90	177	0.66
14	400	35	92	0.72
14	500	19	55	0.74
14	600	11	29	0.73
15	as dep*	121	121	0.50
15	200	97	148	0.60
15	300	84	143	0.63
15	400	37	84	0.69
15	500	47	62	0.57
15	600	24	41	0.63
16	as dep*	88	157	0.64
16	200	87	159	0.65
16	300	97	139	0.59
16	400	38	62	0.62
16	500	23	50	0.68
16	600	21	43	0.67

*as dep = sample in the as-deposited state

This was particularly pronounced from samples 14 and 16 (not in-chamber annealed), in good agreement with the evolution of I_{640} shown in table 8.2 which also shows a more pronounced H effusion from 300 to 400 °C for those samples. Sample 15 showed the smallest drop in the ~ 2000 and 2100 cm^{-1} peaks, in accordance with the hypothesis that hydrogen in that sample was more tightly bonded.

We finally discuss the results of the stretching band peaks in terms of the increase in the parameter R, which has been suggested as being proportional to that fraction of hydrogen bonded in some sort of microstructure (multivacancies, small voids, *etc.*), leading to a larger density deficiency [146]. Samples 14 and 15 showed the same as-deposited R, considerably lower than the one for sample 16, and are believed therefore to present a lower void fraction. After the thermal annealing treatment at 300 °C, however, R started to increase steadily for sample 14, and more or less so for sample 15, and remained fairly constant, with only small variations (within the estimated accuracy of the method) for sample 16. The behaviour of R agrees well with the SEM analysis in which sample 16, with a large as-deposited R value, presented severe surface damage in the form of blisters (figure 8.1(b)). Samples 14 and 15, with lower initial R values and a smooth as-deposited morphology, started to show increases in R to values comparable to the ones for sample 16 only when annealing temperatures resulting in surface damage were reached.

8.4 Conclusions

The effects of substrate temperature and in-chamber annealing on the level of stress and surface morphology, as well as the total silicon-bonded hydrogen content and bonding configuration (microstructure) evolution upon thermal annealing, have been investigated for a-Si:H thin films deposited by reactive sputtering. Infrared analysis of samples in the as-deposited state and after successive thermal annealing treatments at

temperatures ranging from 200 to 600 °C revealed that in-chamber annealed samples are less susceptible to oxygen contamination, and hydrogen appears to be more tightly bonded.

Scanning electron microscope images of the a-Si:H films revealed that surface damage occurred for samples with the highest hydrogen concentration (grown at the lowest T_S) even in the as-deposited state, before subjecting them to any thermal annealing treatment. This indicates the deleterious effects of excessive initial hydrogen concentration in those samples. Thin films with a lower initial hydrogen content presented surface damage (under the annealing conditions presented here) only after annealing temperatures of 300 °C were reached. We believe that to be due to the fact that lower T_S-deposited samples are more stressed both because lower temperatures allow less strain relief during and immediately after deposition, and also because of the higher, perhaps excessive, hydrogen content resulting from lower deposition temperatures.

Chapter 9

Bond Switching, Si-H Cluster Formation and H Effusion on Thermal Annealing in a-Si:H Thin Films

9.1 Introduction

In the search for a more stable hydrogenated amorphous silicon material, where the light-induced degradation problem present in a-Si solar cells could be avoided or minimised, considerable efforts have been made in understanding the behaviour of hydrogen in the amorphous network and the role it plays in metastability [15,178,212]. Although the microscopic mechanism of light-induced metastable changes is not thoroughly understood, hydrogen motion is apparently involved in the formation of light-induced defects [16-18]. As hydrogen diffuses it can change the bonding configurations of the silicon network. Thus, a detailed knowledge of Si-H bond switching, clustering and evolution is of fundamental interest if a more stable amorphous silicon material is to eventuate.

It has been suggested [213] that the thermal equilibration of the electronic properties and the metastable effects in amorphous silicon must be accompanied by more or less extensive structural rearrangements, and that such structural equilibration could be associated with the silicon network or the hydrogen bonding, being thus directly related to the motion of these atoms. On the other hand, from their recent observations Roca i Cabarrocas *et al.* [214] concluded that neither the hydrogen nor the impurity (oxygen

and nitrogen) content are key parameters in the metastability of a-Si:H, suggesting that it may be the type of film microstructure and in particular the mobility of hydrogen in the network that control the effect.

In this chapter a comparative study of a-Si:H thin films deposited at similar conditions but subjected to different *in situ* in-chamber annealing treatments was undertaken. Some contrasting differences in the behaviour of hydrogen motion in the amorphous material for different films were noticed. Bond switching and monohydride clustering seem to have occurred, upon thermal annealing in the range 200 to 600 °C, in varying degrees depending on the sample's deposition conditions and thermal history. Hydrogen in the loosely bound phase can effuse from the film through a percolating network of microvoids at annealing temperatures above 300 °C [72,215,216]. At temperatures below those at which hydrogen effusion starts, however, significant rearrangements in H-Si bonding configurations can take place. Moreover, for amorphous silicon films with varying bonded hydrogen contents and structures, it is reasonable to expect bonding configurations and microstructure to rearrange in different ways. In fact, Shinar *et al.* [217] have found for a-Si:H presenting a variety of microstructures, that in some cases migration of Si-bonded hydrogen to the internal surfaces of the film can occur, and recombination to molecular H_2 can take place, which then escapes through the largely interconnected voids.

9.2 Experimental procedures

Details of sample preparation were generally the same as previously described. Most of the samples used were actually either the same or from the same deposition run as the ones used in former chapters (in which case sample number has been retained in this chapter). We note that for all samples co-deposited during a single run, infrared spectra were identical and each sample was representative of that particular set. Table 9.1

shows, for each of the samples to be discussed here, the substrate temperature (T_s) and the in-chamber annealing treatment conditions when applicable. Here again, making use of the nondestructive nature of both ERDA and FTIR techniques, all measurements described and results assigned to a particular sample were performed on a single specimen. Sample thickness was typically < 0.5 μm, lying in the thickness range used in thin film solar cells.

Table 9.1: Deposition temperature (T_s) and in-chamber annealing (ICA) treatment conditions for a-Si:H thin film samples.

Sample	T_s (°C)	In-chamber annealing conditions
5	285	vacuum, for 2 hours, at 215 °C
6	285	not in-chamber annealed
7	285	atomic hydrogen, for 2 hours, at 250 °C
17	215	not in-chamber annealed
10	300	hydrogen plasma, for 2 hours, at 285 °C
11	300	atomic hydrogen, for 2 hours, at 250 °C
12	300	hydrogen plasma, for 2 hours, at 285 °C plus atomic hydrogen, for 2 hours, at 250°C
13	300	not in-chamber annealed

After deposition, and in some cases in-chamber annealing, samples 5, 6, 7, and 17 only were annealed for 2 hours at temperatures ranging from 200 to 600 °C at 100 °C steps. Heating and cooling rates of 10 and 2 °C.min^{-1} respectively were chosen to minimise

surface damage. Before and after each annealing step, ERDA measurements were made and FTIR spectra were taken from all samples presented.

ERDA measurements were made using the same configuration previously described, in the 3 MV Van de Graaff accelerator and related facilities at the Lucas Heights Research Laboratories, using a 2.4 MeV ^4He beam and a current density of 0.5 nA/mm^2. Hydrogen profiles of each of the films of table 9.1 and for each of the annealing steps for samples 5, 6, 7, and 17 were obtained. Film thickness was measured using the RBS technique, which was performed simultaneously with the ERDA measurements.

FTIR spectra in the 4400 - 400 cm^{-1} region were obtained with a BioRad FTS-40 FTIR spectrometer, equipped with a liquid nitrogen-cooled cadmium mercury telluride (CMT) detector attached to a Digilab 3200 data station system. This equipment was also present at the Lucas Heights Research Laboratories facilities, allowing for the whole experiment to be carried out in the same place and in a few days. Scan parameters used were the same as routinely used at the Solar Energy Research Group facilities at the University of Western Australia. Despite some differences in noise and background moisture features, the spectra of samples in the as-deposited state presented the same features and intensities, irrespective of whether they had been collected at one or the other laboratory. The total bonded hydrogen content (C_H) was estimated from the integrated intensity of the ~ 640 cm^{-1} wagging band infrared peak as described in previous chapters. C_H was adjusted using the appropriate correction for film thickness earlier discussed, since all films were less than 1 μm thick.

Thermal annealing treatments were carried out in an alumina-tube-type resistance furnace also available for this project at the Lucas Heights Research Laboratories. Samples were loaded into a quartz boat which was then inserted inside the alumina tube which constituted the furnace chamber.

9.3 Results and Discussion

Table 9.2 presents the total bonded hydrogen content (C_H) corrected for film thickness, as well as the film thickness as determined by the RBS technique for samples 5, 6, 7, and 17. For sample 17, which presented the highest amount of bonded hydrogen, FTIR and ERDA estimates of C_H did not agree well. $C_{H\text{-}FTIR}$ was 26.2 at.%, whereas $C_{H\text{-}ERDA}$ ranged between 20 - 24 at.%. For a-Si:H films deposited in our sputtering system with hydrogen contents higher than ~ 20 at.%, we suspect that the infrared peaks might have been artificially increased by increasing nonspecular scattering [209]. We thus consider this artefact to be a possible reason for the deviation between FTIR and ERDA hydrogen estimates in the case of sample 17. In any case, the infrared-determined C_H does appear to have been overestimated, because comparing sample 17 to sample 1, presented in chapter 7 (table 7.3, and for which $C_{H\text{-}FTIR}$ was 20.9 at.%), neither of which was in-chamber annealed, we would expect sample 1 to have a higher hydrogen concentration than sample 17, since it was deposited at a lower substrate temperature of 170 °C.

Table 9.2: Total bonded hydrogen concentration (C_H, corrected for film thickness) and film thickness for a-Si:H samples.

Sample	C_H (at.%)	Thickness (Å)
5	9.3	4526
6	7.3	4243
7	17.6	3768
17	26.2	4463

9.3.1 Hydrogen Effusion During Growth and the Resultant Hydrogen Depth Profile

The ability to tailor the hydrogen content in a-Si:H films by means of changes in deposition temperature (*i.e.* film growth at higher T_S in order to obtain a lower C_H), can have a strong effect in the film's hydrogen distribution profile. Figure 9.1 illustrates this effect, showing the as-deposited ERDA hydrogen depth profiles for samples 5, 6, 7, and 17. The comparison of samples 5, 6, and 7, all deposited at 285 °C, reveals that deposition at this relatively high substrate temperature resulted in a very steep hydrogen profile for the not-in-chamber annealed sample 6. It also indicates that a very strong hydrogen effusion from the bulk must have taken place during deposition at that temperature. Sample 5, in-chamber annealed in vacuum, showed a more homogeneous hydrogen distribution throughout the film thickness; and for sample 6, in-chamber annealed in hydrogen, the hydrogen depth profile presented the most homogeneous distribution of them all. From that figure it is evident that the in-chamber annealing treatment, even in vacuum, allows hydrogen to be incorporated into the bulk of the amorphous silicon film after deposition is completed, completely changing and homogenising the hydrogen distribution profile.

Sample 17, however, which was not in-chamber annealed and was deposited at a lower substrate temperature of 215 °C, presented a much more homogeneous hydrogen distribution profile, comparable to the profiles of samples 5 and 7. The lower deposition temperature resulted in a much higher hydrogen content in that film, approximately three times that of sample 6. From the comparison between these two samples (6 and 17) it is apparent that the higher deposition temperature caused the strong hydrogen evolution which resulted in the profile shown for sample 6. It should be noted that for sample 17 the profile is also sloped towards the film surface, indicating that even for that lower deposition temperature some hydrogen evolution from the bulk must have taken place during deposition.

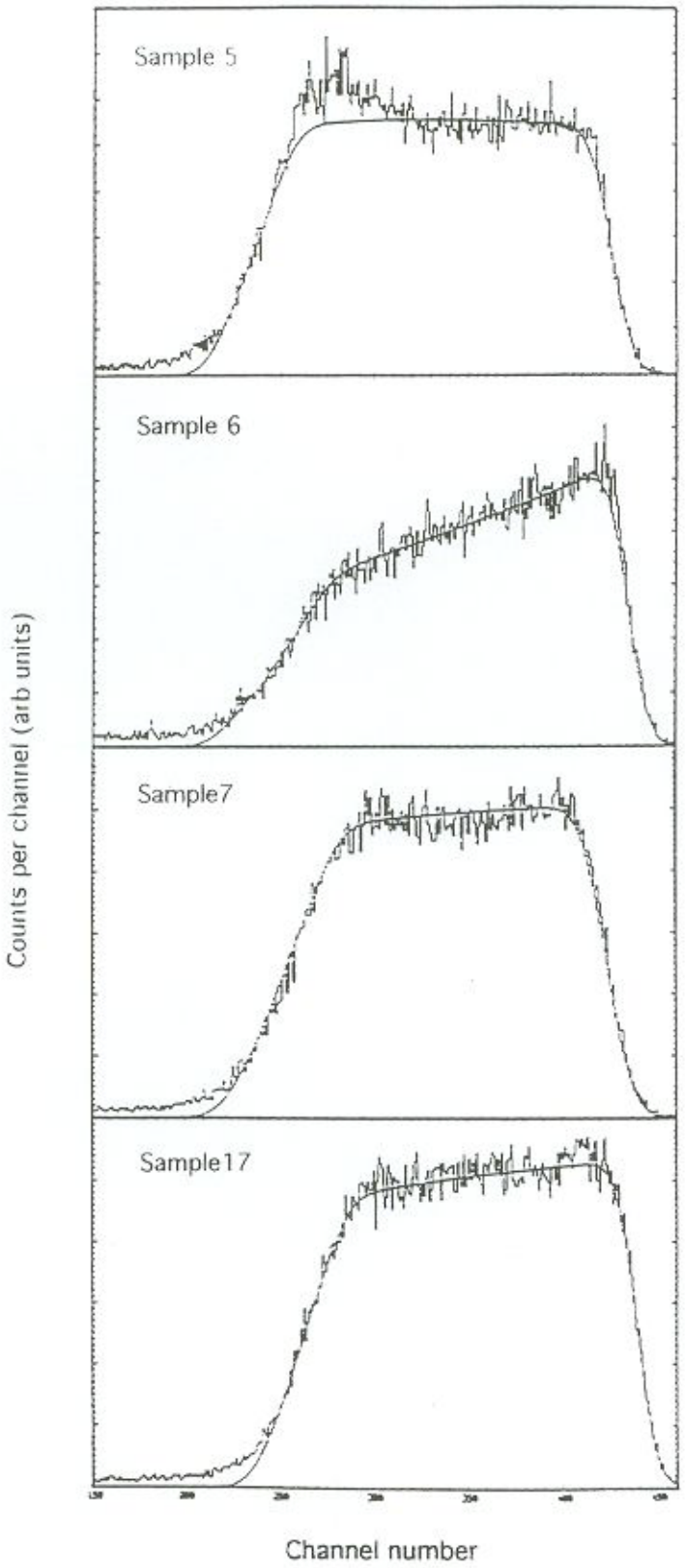

Figure 9.1: Measured (jagged line) and simulated (smooth line) ERDA hydrogen depth profiles of samples 5, 6, 7, and 17. The right-hand edge corresponds to the film's surface. Vertical axes not to scale.

Even though samples 5, 6, and 7 were deposited under identical conditions apart from the alternative just-after-deposition in-chamber annealing treatment, film thickness for sample 7 is between ~ 12 - 17 % smaller than for the other two. In-chamber annealing in hydrogen thus resulted in a more dense structure as well as in a more homogeneous hydrogen depth profile for the particular conditions described.

Let us briefly go back to samples 10 - 13 of chapter 7. Figure 9.2 shows the ERDA hydrogen depth profiles for those samples, all deposited at 300 °C. Here again the hydrogen profile of a not-in-chamber annealed sample (sample 13) was very steep, indicating that hydrogen evolution from the bulk has probably occurred during film growth at that high temperature. In-chamber annealing in atomic hydrogen (sample 11) levelled-off (as well as increased, as discussed in chapter 7) the hydrogen distribution throughout the film thickness. The effect of in-chamber annealing in a hydrogen plasma can be seen in the ERDA profile of sample 10. The resultant hydrogen distribution for that sample presented a maximum at approximately the middle of the film thickness, indicating the concomitant hydrogen incorporation caused by the increased hydrogen chemical potential, and the effusion promoted by the particularly high in-chamber annealing temperature of 285 °C. For sample 12, which was in-chamber annealed in a hydrogen plasma immediately followed by in-chamber annealing in atomic hydrogen, the resultant hydrogen profile was again steeper than for sample 11, pointing to the effects of plasma etching and plasma damage previously mentioned. It looks like the slight difference in C_H between samples 11 and 12 (5.7 and 5.4 at.% respectively) is due to the out-diffusion, during the in-chamber annealing in atomic hydrogen treatment, of a large quantity of loosely bound hydrogen incorporated during the in-chamber annealing in hydrogen plasma (sample 10) treatment. A single in-chamber annealing treatment in atomic hydrogen thus seems to result in the most homogeneous and tightly bonded hydrogen distribution for our sputtered a-Si:H films.

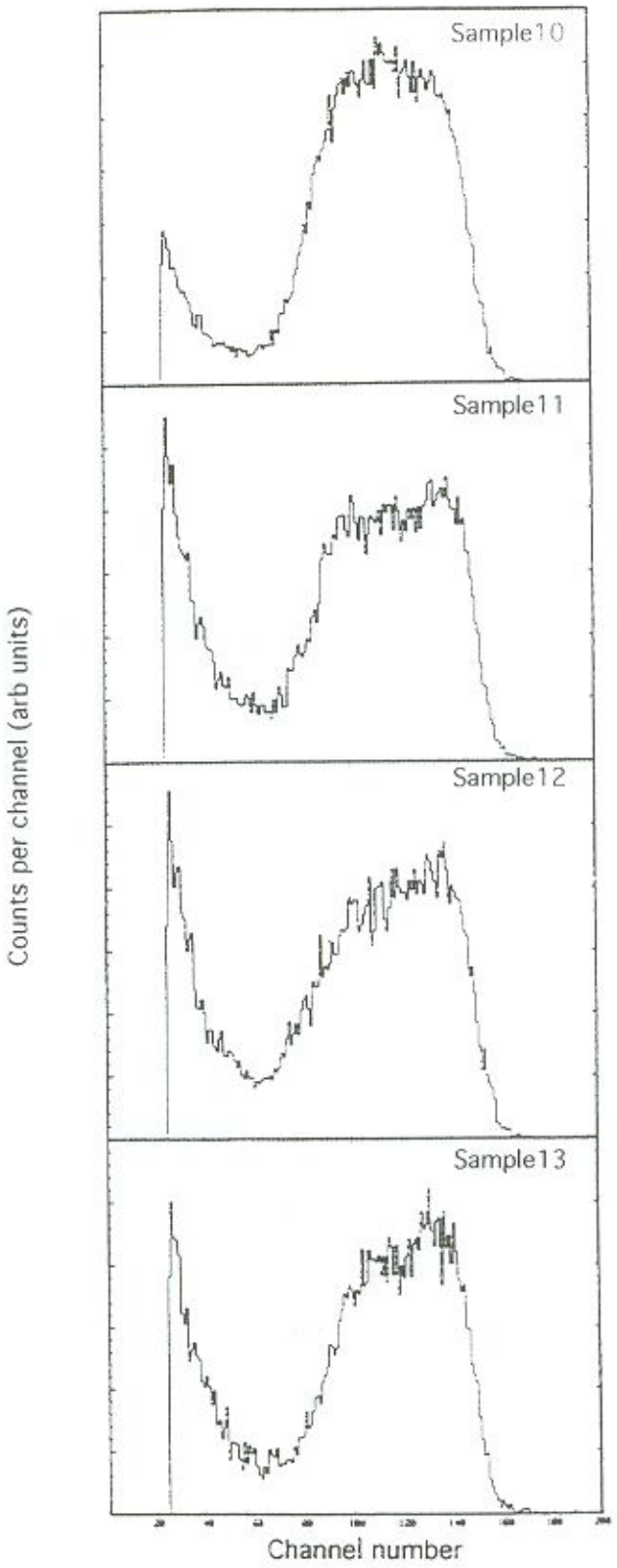

Figure 9.2: ERDA hydrogen depth profiles of samples 10, 11, 12, and 13. The right-hand edge corresponds to the film's surface. Vertical axes not to scale.

In-chamber annealing in atomic H after in-chamber annealing in H plasma resulted in approximately the same amount of H incorporation as that obtained with in-chamber annealing in atomic H alone. The H distribution profile, however, shows how dissimilar these two films were.

9.3.2 Hydrogen Motion and Network Reconstruction on Thermal Annealing

Figure 9.3 shows the ERDA hydrogen depth profiles for samples 5, 6, 7, and 17. Each graph shows 6 curves, corresponding to the hydrogen profile measured at the different annealing temperatures. The topmost curve corresponds to the as-deposited state, and the bottom curve to the 600 °C anneal. For all samples the profiles show that up to ~ 300 °C annealing, only very small amounts of hydrogen effused. In all cases some narrowing of the profiles, which indicates that film thickness suffered a reduction on annealing, can be observed even when comparing the as-deposited state with annealing at temperatures as low as 200 °C. Yang *et al.* [218] have found that the thickness of a-Si:H films was reduced by 220 Å from an initial thickness of 1200 Å when films were annealed in N_2 at 615 °C. They found that film thickness reduction starts at the very early stages of annealing, being almost completed within 30 minutes, and that reduction of film thickness could not be the result of crystallisation (which started only after 5 hours at that temperature in their experiments). They believe that it is more likely to be accompanied by hydrogen effusion, due to the annihilation of microvoids which are originally incorporated in the as-deposited films.

Yi *et al.* [219] showed that in a-Si:H, microcrystallisation starts at temperatures around 600 °C, and that the anneal time only has a small effect on crystallisation, compared to the more critical effect of temperature. In our samples hydrogen started to evolve in considerable quantities only when temperatures of ~ 400 °C were reached; however,

some narrowing of the profiles can be noticed even at lower annealing temperatures, especially noticeable for sample 17 (fig. 9.3d). For higher temperatures the narrowing is more prominent and the mechanism proposed by Yang might explain the results, but below 300 °C, even without considerable hydrogen effusion, some void annihilation and/or network densification might have taken place. If that is the case, then bond switching and/or monohydride clustering are probably involved in the densification process. Reimer, Vaughan and Knights [58] showed by nuclear magnetic resonance (NMR) studies that on annealing, hydrogen in the less clustered domain (predominantly monohydride) diffuses internally prior to evolution, confirming the occurrence of monohydride clustering on annealing. The absence of extensive low temperature effusion in our samples indicates that it might take place by diffusion of hydrogen atoms through the bulk, suggesting the absence or low concentration of interconnected voids [220]. Another interesting feature of figure 9.3 is the steep hydrogen profile of sample 6 (fig. 9.3b), for which the ERDA profile shows that hydrogen content at the substrate-film interface is about 2/3 of that on the film surface. As previously discussed, this points to a strong hydrogen effusion from the bulk which has probably taken place during the deposition of that sample, and indicates that the H-Si bonds then formed were predominantly of the weak type [193].

The analysis of figure 9.3 leads to further interpretations as to hydrogen evolution on annealing at higher ($\geq$ 400 °C) temperatures and H-Si bond strength. Sample 6 and sample 17, neither of which was in-chamber annealed, and which presented the lowest and highest C_H respectively, were the ones for which hydrogen evolution was the strongest. After thermal annealing at 600 °C, the remaining total hydrogen content for those samples (bottom curves in figure 9.3 a to d) was considerably lower than that of the in-chamber annealed samples. Sample 7, in-chamber annealed in atomic hydrogen, presented the highest remaining H content of them all, indicating that hydrogen in that film was more tightly bonded than in the others. In relative terms, sample 17 presented the largest amount of loosely bound hydrogen.

Figure 9.3: ERDA hydrogen depth profiles of samples 5, 6, 7, and 17 (a, b, c, and d respectively). Each graph shows 6 curves, corresponding to the hydrogen profile measured after annealing at different temperatures. The topmost curve corresponds to the as-deposited state, and the bottom curve to 600 °C. The right-hand side of the spectra corresponds to the film surface, and the left-hand side to the film-substrate interface.

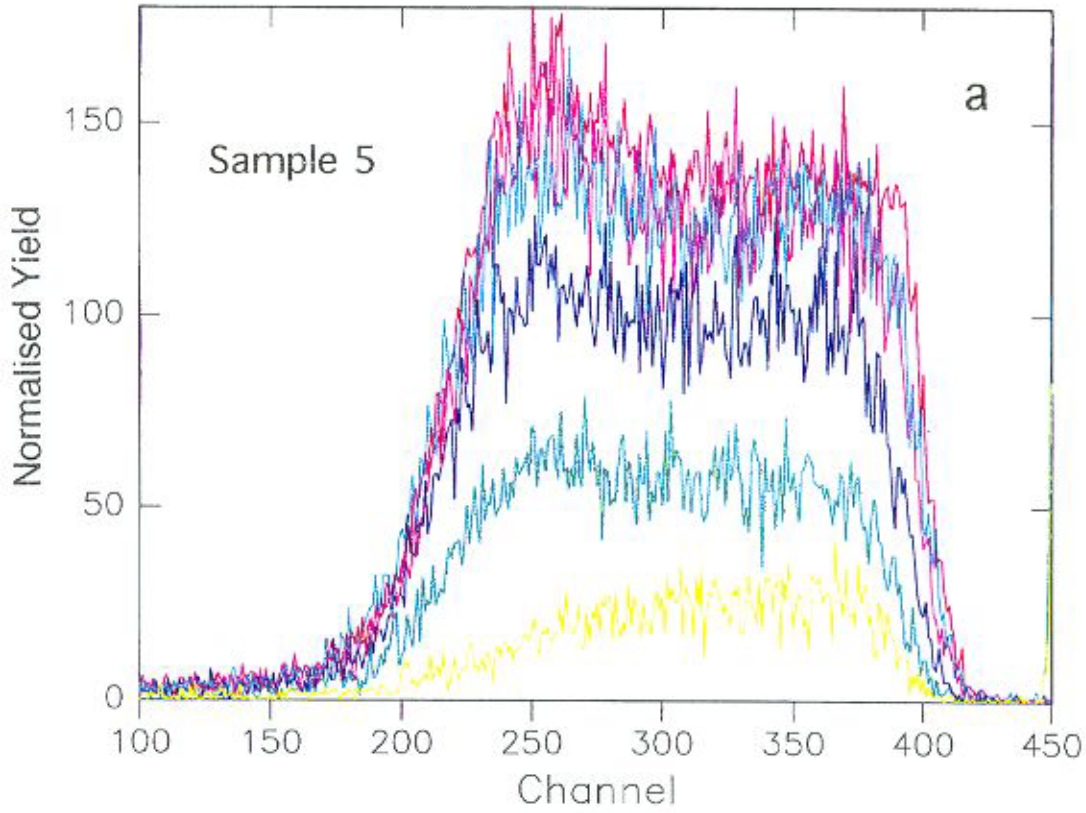
a
Sample 5
Normalised Yield
150
100
50
0
100
150
200
250
300
350
400
450
Channel

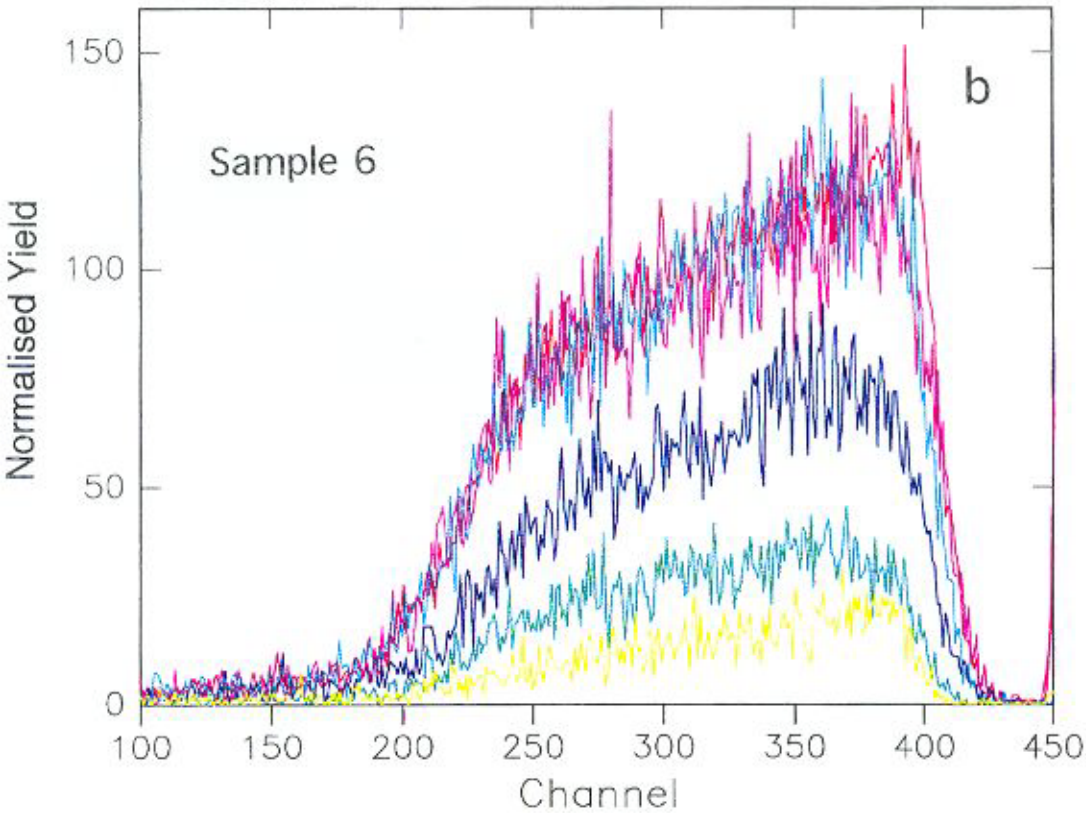
b
Sample 6
Normalised Yield
150
100
50
0
100
150
200
250
300
350
400
450
Channel

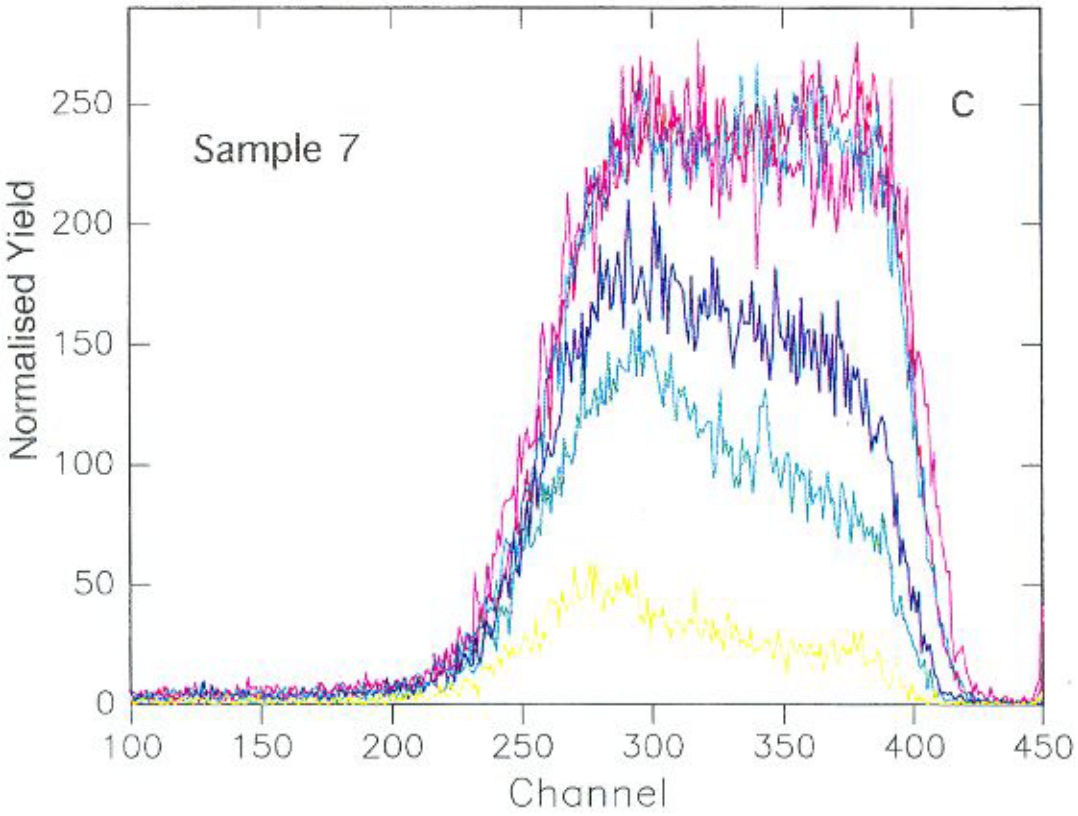
Sample 7
c
Normalised Yield
250
200
150
100
50
0
100
150
200
250
300
350
400
450
Channel

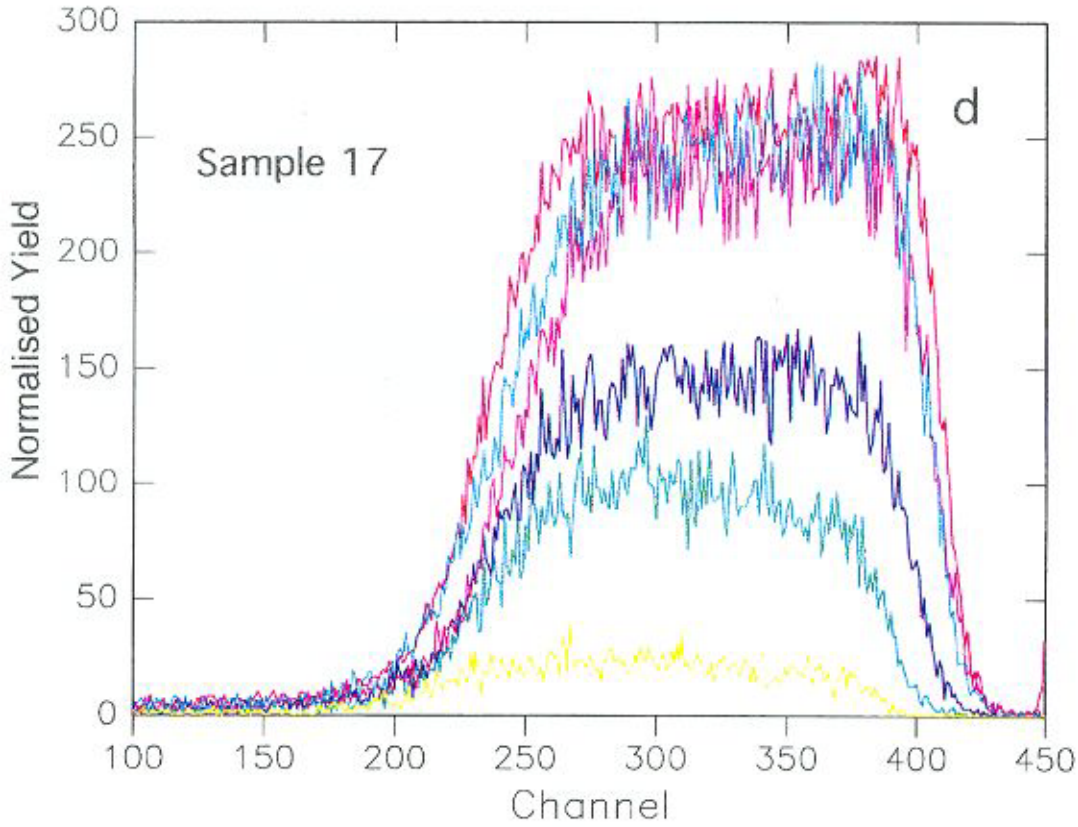
Sample 17
d
Normalised Yield
300
250
200
150
100
50
0
100
150
200
250
300
350
400
450
Channel

Figure 9.3 indicates that the amount of tightly bonded hydrogen (TBH) depends on the sample preparation conditions, irrespective of the total hydrogen amount. Our results indicate that hydrogen incorporation does not necessarily follow the path of first producing strong H-Si bonds, and then, as the network saturates with hydrogen, producing weaker H-Si bondings. Moreover, they also show that hydrogen is so mobile in the amorphous network, that network reconstruction can take place with treatments like in-chamber annealing in atomic hydrogen and result in post-deposition tighter H-Si bonds.

Thermal annealing of a-Si:H films at 100 °C steps showed some interesting IR spectra features, especially up to 300 °C, which we now discuss in detail. Figures 9.4, 9.5 and 9.6 and table 9.3 present the normalised results of the infrared wagging (~ 640 cm^{-1}), stretching (~ 2100 and ~ 2000 cm^{-1}) and bending (~ 845 and ~ 890, or ~ 875 cm^{-1}) modes. In sample 5 the ~ 2100 cm^{-1} peak (figure 9.5), which is usually assigned to either higher hydride vibrations (SiH_2, $(SiH_2)_n$, SiH_3), or to clustered monohydrides $(SiH)_n$ [55,59], or both, slightly increased before starting to decrease as would be expected. Sample 5 was in-chamber annealed in vacuum for 2 hours at 215 °C. Because higher hydrides are assigned to weak H-Si bonds they would be the first to be expected to evolve from the film on annealing. Since the ~ 640 cm^{-1} peak (figure 9.4) decreased some 10 % during the first annealing step and was then fairly constant up to 400 °C, we infer that only a very small amount of bonded hydrogen effused from the network up to that temperature. On the other hand, the ~ 2000 cm^{-1} peak (figure 9.6) decreased from the beginning, indicating a high degree of monohydride clustering and/or bond switching (conversion of mono to higher hydrides). The bending band (table 9.3), which presented one peak only (at ~ 875 cm^{-1} indicating the presence of SiH_2 [56]), decreased from the first annealing step. From the overall changes in infrared peaks we conclude that silicon dihydrides were present in large quantities from the as-deposited state in that sample, and that all the effusion that took place up to 400 °C must have been due to that SiH_2. The increase in the ~ 2100 cm^{-1} peak we

conclude to have been due to clustering of monohydrides, since both the ~ 2000 cm^{-1} and ~ 875 cm^{-1} peak decreased from the very first annealing step. At 400 °C the ~ 2000 cm^{-1} peak was not detected any more, but it reappeared after annealing at 500 °C and increased after annealing at 600 °C. We believe that at those higher annealing temperatures the clustered monohydride bonds started to effuse, with the remaining SiH units then vibrating at ~ 2000 cm^{-1}. This hypothesis is corroborated by the massive decrease in the ~ 2100 cm^{-1} peak from 400 to 500 °C.

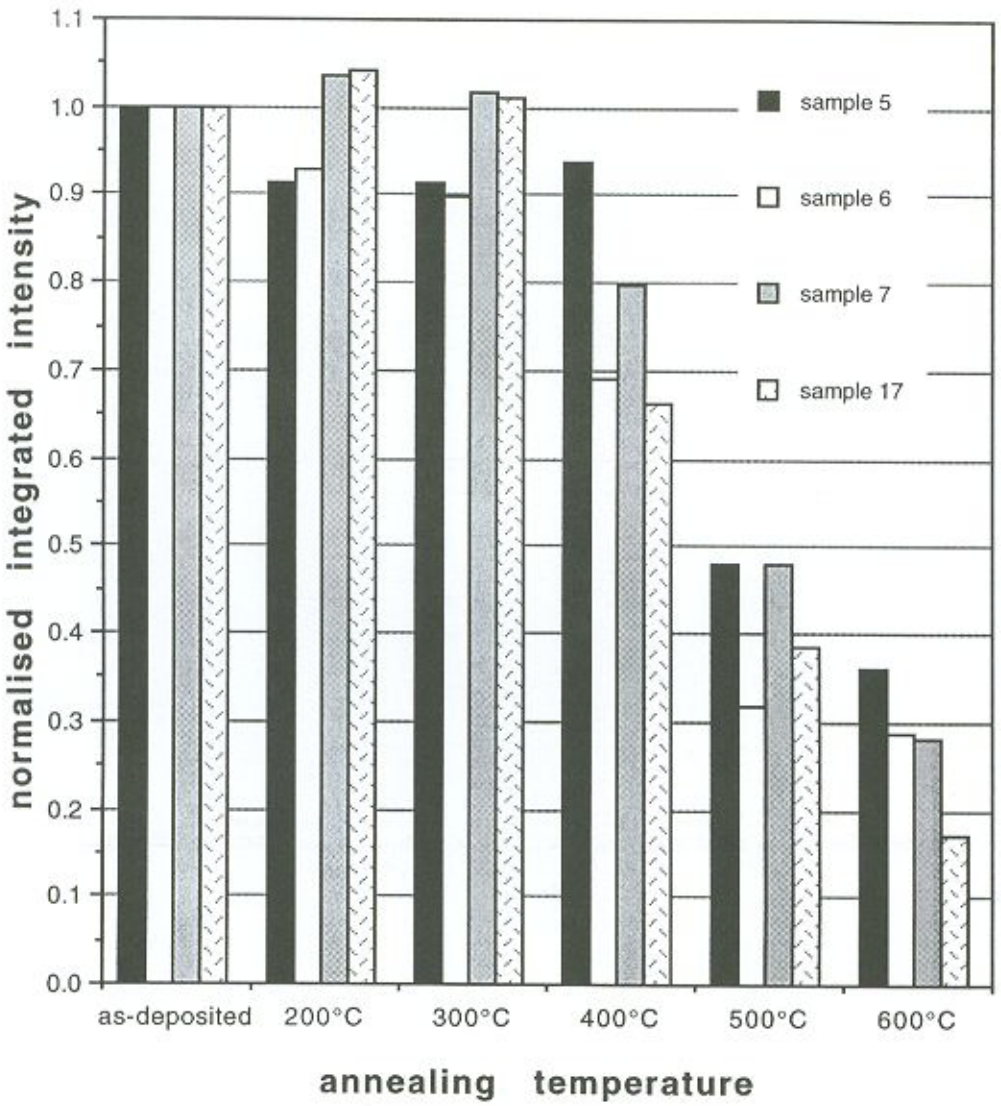

Figure 9.4: Evolution of the integrated intensities of the ~ 640 cm^{-1} infrared peaks of samples 5, 6, 7, and 17 on thermal annealing at increasing temperatures up to 600 °C. Intensities normalised to the as-deposited values.

Sample 6, which was deposited at the same temperature as samples 5 and 7, but was not in-chamber annealed, showed the lowest bonded hydrogen content of all the samples studied. The ~ 640 cm^{-1} peak (figure 9.4) showed only a small degree of hydrogen effusion up to ~ 300 °C. In the stretching band, since the ~ 2000 cm^{-1} peak (figure 9.6) suffered a strong reduction after annealing at 200 °C, while the ~ 2100 cm^{-1} peak (figure 9.5) decreased only marginally, we conclude that some monohydride clustering might have occurred, along with some minor effusion of hydrogen from the sample.

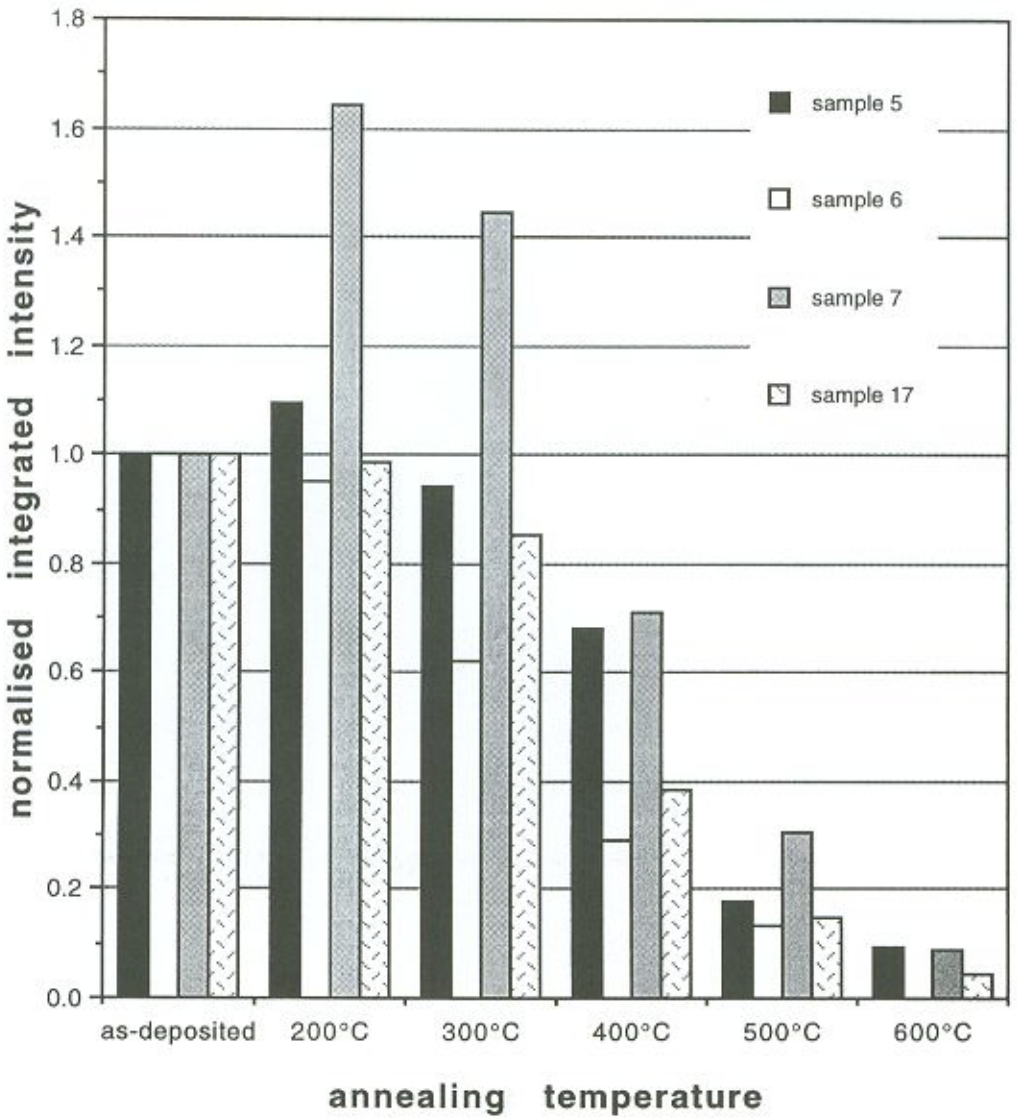

Figure 9.5: Evolution of the integrated intensities of the ~ 2100 cm^{-1} infrared peaks of samples 5, 6, 7, and 17 on thermal annealing at increasing temperatures up to 600 °C. Intensities normalised to the as-deposited values.

At higher annealing temperatures the ~ 2000 cm^{-1} peak eventually disappeared, which corroborates the possibility of monohydride clustering. The bending band presented one peak only, at ~ 875 cm^{-1}, and its behaviour upon annealing was similar to that of sample 5.

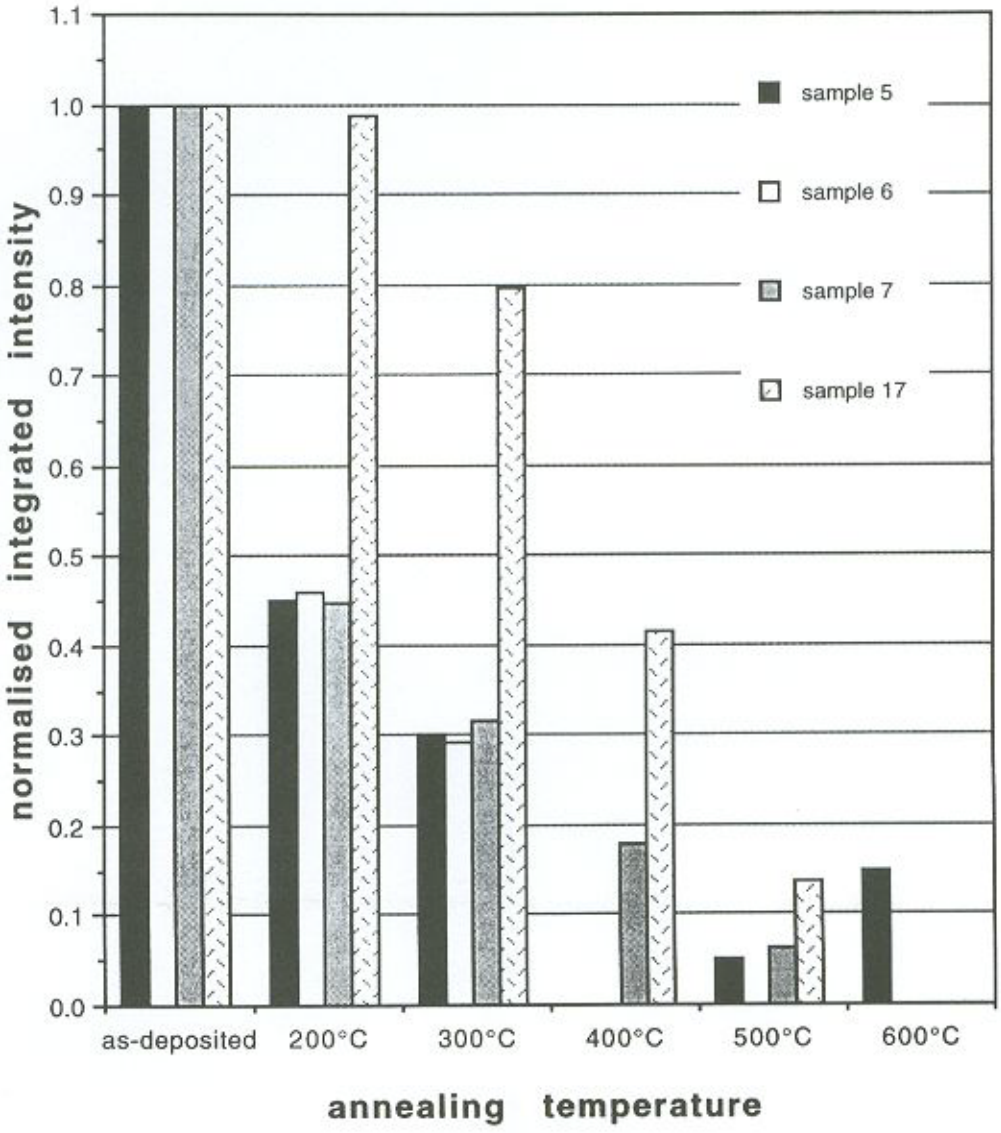

Figure 9.6: Evolution of the integrated intensities of the ~ 2000 cm^{-1} infrared peaks of samples 5, 6, 7, and 17 on thermal annealing at increasing temperatures up to 600 °C. Intensities normalised to the as-deposited values.

In sample 7, subjected to the atomic hydrogen *in situ* in-chamber annealing treatment prior to the thermal annealing steps to which all the samples were subjected simultaneously, we believe that considerable bond switching might have taken place. For that sample the ~ 2000 cm^{-1} peak (figure 9.6) showed a massive decrease from the first annealing step, indicating either monohydride clustering or bond switching of mono to higher hydrides, or both. The integrated intensity of the peak centred at ~ 640 cm^{-1} (figure 9.4) remained fairly constant, and only after annealing to 400 °C started to effuse hydrogen from the amorphous network. The bending band showed no detectable peak in the as-deposited state, from which we infer that no higher hydrides were present at that stage, being the ~ 2100 cm^{-1} peak in that case assigned exclusively to clustered monohydrides [59]. We note here that this was the only sample for which this peak was centred at exactly 2100 cm^{-1}, while for samples 5, 6 and 17 peak centre was respectively at 2084, 2084, and 2080 cm^{-1}. After annealing at 200 °C a massive bending band peak appeared, centred at 850 cm^{-1}, which supports the not less massive increase in the 2100 cm^{-1} peak (figure 9.5). It appears that in this case higher hydrides were formed through bond switching. Moreover, in the stretching band, a shift of the 2100 cm^{-1} peak to 2080 cm^{-1} after annealing corroborates the hypothesis that initially the 2100 cm^{-1} peak accounted exclusively to clustered monohydrides in that sample [56]. At higher temperatures, during annealing at 600 °C, monohydride clustering might have taken place to some extent, as indicated by the disappearance of the ~ 2000 cm^{-1} peak while the ~ 2100 cm^{-1} was still present. The ~ 640 cm^{-1} peak, however, seemed excessively high at that temperature, suggesting that nonspecular scattering might have artificially increased that peak's intensity [209].

Sample 17 showed a somewhat different behaviour. The slight increase observed in the ~ 640 cm^{-1} peak might be an experimental artefact, again caused by nonspecular scattering due to film surface roughening on annealing [209]. Alternatively or concurrently, an increase in the bonded hydrogen content resultant from some trapped molecular hydrogen (which is infrared transparent, but which might have reconstructed

into H-Si bonds on annealing, thus becoming infrared active) is also a possibility to consider. Both the ~ 2100 and ~ 2000 cm^{-1} peaks (figures 9.5 and 9.6 respectively) showed a very slight decrease up to 200 °C, and a more pronounced reduction from that temperature on, indicating that extensive monohydride clustering has probably not occurred at least up to 400 °C. C_H for that sample was more than twice that of sample 5.

Table 9.3: Integrated intensities (I_{BEND} in cm^{-1}) of the H-Si infrared bending mode peaks for samples 5, 6, 7, and 17 in the as-deposited state and after annealing at different temperatures (numbers in parenthesis denote peak centre wavenumber, in cm^{-1})

State	Sample 5	Sample 6	Sample 7	Sample 17
as-deposited	231(875)	235(876)	n.d.	16 (847)
				95 (894)
200°C anneal	186(876)	181(875)	403(850)	17 (847)
				85 (894)
300°C anneal	172(875)	165(873)	375(851)	21 (847)
				74 (893)
400°C anneal	161(873)	104(871)	313(854)	18 (847)
				35 (891)
500°C anneal	104(872)	74(872)	210(853)	36 (844)
				40 (892)
600°C anneal	77(880)	94(870)	151(849)	29 (839)
				26 (890)

n.d.: not detected

Nevertheless, the bending band peak intensities (with peaks at ~ 845 and ~ 895 cm^{-1}, indicating the presence of polymerised dihydrides $(SiH_2)_n$ [56]) were about half that of sample 5, and decreased from the first annealing step. From the differences in C_H and in the integrated intensities of the bending bands it could be inferred that sample 17 presented a relatively higher degree of clustered monohydrides than sample 5 in the as-deposited state. Since all infrared bands seemed to decrease in a similar fashion we conclude that neither bond switching nor extensive monohydride clustering took place in that sample up to 500 °C. At 600 °C higher hydrides should have effused and the absence of the ~ 2000 cm^{-1} peak and presence of a small peak at ~ 2100 cm^{-1} might be satisfactorily explained by the clustering of monohydrides, contrary to what appears to have been the case with sample 5.

In comparing samples 5, 6, and 7, which were all deposited under the same conditions (the only difference being the post-deposition *in situ* in-chamber annealing to which some were subjected), table 9.2 shows that C_H is notably different. From the difference in C_H between samples 5 and 6 it could be concluded that after deposition was completed, in-chamber annealing in vacuum under the particular conditions described increased the bonded hydrogen content of a sample deposited at 285 °C. We could speculate that this increase might have been caused by some trapped molecular hydrogen in the network (IR inactive) that could have formed H-Si bonds during the in-chamber annealing treatment, thus becoming IR active. The results of ERDA measurements however, which account for all types of H in the sample, confirm the same trend in hydrogen content as that of C_H determined from infrared measurements. Figures 9.3a and 9.3b would have to show very similar hydrogen profiles if that was the case. We thus conclude that the extra hydrogen present in sample 5, incorporated during the in-chamber annealing treatment, was probably supplied by surfaces in the surroundings, either the substrate (c-Si) or the reactor chamber. In contrast with some of our previous results, shown and discussed in chapter 7, for samples deposited and in-chamber annealed at slightly lower temperatures, in-chamber annealing under the

conditions described in table 9.1 lead to an increase in C_H after deposition was completed, as sample 7 shows. That sample was also deposited at 285 °C, but its resultant C_H after in-chamber annealing in H_2 + Ar amounted to about twice that of sample 5, and ~ 2.4 times that of sample 6. Minor temperature changes in the 250 - 300 °C range, therefore, can cause strong variations in C_H. Also noteworthy is the slight increase in the ~ 640 cm^{-1} peak after annealing at 200 °C showed by samples 7 and 17, which presented the highest C_H. As previously mentioned, this still remains a topic of discussion and further attempts to clarify this matter will be presented in chapter 10.

9.4 Conclusions

In this chapter it was shown that, for sputter-deposited a-Si:H thin films grown at relatively high deposition temperatures (T_S = 285 and 300 °C), the hydrogen distribution throughout the film thickness can result in a very steep profile. Strong hydrogen evolution from the bulk of the growing film is believed to have occurred at those higher temperatures, since hydrogen concentration at the film's surface was much higher than at the film-substrate interface. In-chamber annealing in atomic hydrogen compensated the uneven hydrogen profile, levelling it off, as well as resulted in a higher amount of tightly bonded hydrogen (TBH).

It was also shown that different post-deposition in-chamber annealing treatments affected not only the bonded hydrogen content and bonding configurations, but also the behaviour of hydrogen motion, and in/out-diffusion in a-Si:H thin films annealed at temperatures ranging between 200 - 400 °C. Bonded hydrogen has been shown to diffuse intensively, even at temperatures as low as 200 °C in a-Si:H, as previously reported by other authors [201]. Not in-chamber annealed, sputter-deposited thin films presented larger amounts of loosely bound hydrogen, irrespective of the initial total

hydrogen concentration. For those samples, hydrogen evolution on thermal annealing at higher temperatures was more pronounced than for in-chamber annealed samples. Film thickness reduction after annealing could be observed from ERDA hydrogen depth profiles for annealing temperatures as low as 200 °C for some samples. Bond switching and monohydride clustering were apparent from the analysis of the infrared spectroscopy results presented, and depended on sample deposition conditions and thermal treatment history. It was shown that TBH and WBH formation are not directly related to the total hydrogen content, and that even after deposition has been completed, TBH can still be incorporated into the amorphous network.

Chapter 10

Nonspecular Scattering on Thermal Annealing of a-Si:H Thin Films

10.1 Introduction

Infrared studies of the hydrogen content of amorphous silicon thin films subjected to thermal annealing treatments at temperatures around 300 °C, have shown that quite often the hydrogen-related infrared absorption peaks show an overall increase in the apparent absorption. As we have indicated in previous chapters, the reasons for the increase in integrated absorption under these H-Si bands have been speculated to be related to either or both of the following [185,187,209,221]:

(i) Some of the infrared transparent hydrogen (IR inactive species like trapped molecular H_2) possibly present in the samples becomes infrared active upon annealing, by means of H-H --> H-Si bond reconstruction

(ii) Because the film surface structure changes and becomes rougher on annealing, nonspecular scattering increases, in which case the increase in overall infrared absorbance might be an artefact

In this chapter we have undertaken a low temperature thermal annealing study of a-Si:H thin films in order to further investigate the causes for the increase in

infrared absorbance mentioned above. The evolution in hydrogen-related infrared peaks on annealing at temperatures of 200 and 300 °C was compared to the simultaneous evolution in total hydrogen concentration as measured by the elastic recoil detection analysis (ERDA) technique (integrated yield). The infrared technique (FTIR) cannot detect trapped molecular H_2, whereas the ERDA technique allows for the determination of the total hydrogen content, irrespective of bonding configuration or species. Thus, the assignment of the increase in IR absorbance on thermal annealing to either (i) or (ii) above might become clearer.

10.2 Experimental Procedures

Samples used in the experiment described in this chapter were from the same deposition runs as some of those used in previous chapters, namely samples 10, 11, 12, and 13. Table 10.1 shows details of substrate temperature (T_S) and the in-chamber annealing treatment conditions where applicable. As in previous chapters, both FTIR and ERDA measurements were performed on a single specimen, thus avoiding sample to sample variations.

After deposition, and in some cases in-chamber annealing (samples 10, 11, and 12), all samples were simultaneously annealed for 2 hours, first at 200 °C, and then at 300 °C. Thermal annealing treatments were carried out, with heating and cooling rates of 10 and 2 °C.min^{-1} respectively, chosen to minimise surface damage as described before. Before and after each annealing step, FTIR spectra were taken and ERDA measurements were made for all samples using the same procedures described in previous chapters.

Table 10.1: Deposition temperature (T_S) and in-chamber annealing (ICA) treatment conditions for a-Si:H thin film samples

Sample	T_S (°C)	In-chamber annealing conditions
10	300	hydrogen plasma, for 2 hours, at 285 °C
11	300	atomic hydrogen, for 2 hours, at 250 °C
12	300	hydrogen plasma, for 2 hours, at 285 °C plus atomic hydrogen, for 2 hours, at 250°C
13	300	not in-chamber annealed

10.3 Results and Discussion

Figures 10.1 and 10.2 show respectively the integrated intensity of the ~ 640 cm^{-1} wagging band infrared peak, and the integrated yield resulting from ERDA measurements for samples 10, 11, 12, and 13, for the as-deposited as well as after thermal annealing at 200 and 300 °C temperatures. In accordance with results presented in previous chapters for different samples, and also by other researchers [185,187,209,221], we observe in figure 1 that the ~ 640 cm^{-1} infrared peak in many cases showed an increase in integrated intensity on annealing. However, ERDA measurements shown in figure 2 do not support that trend; ERDA integrated yield always decreased with increasing annealing temperature, even when the respective infrared peak showed an increased integrated absorption (for sample 2, the 200 °C anneal ERDA result in figure 10.2 has been found to be in error and was therefore omitted).

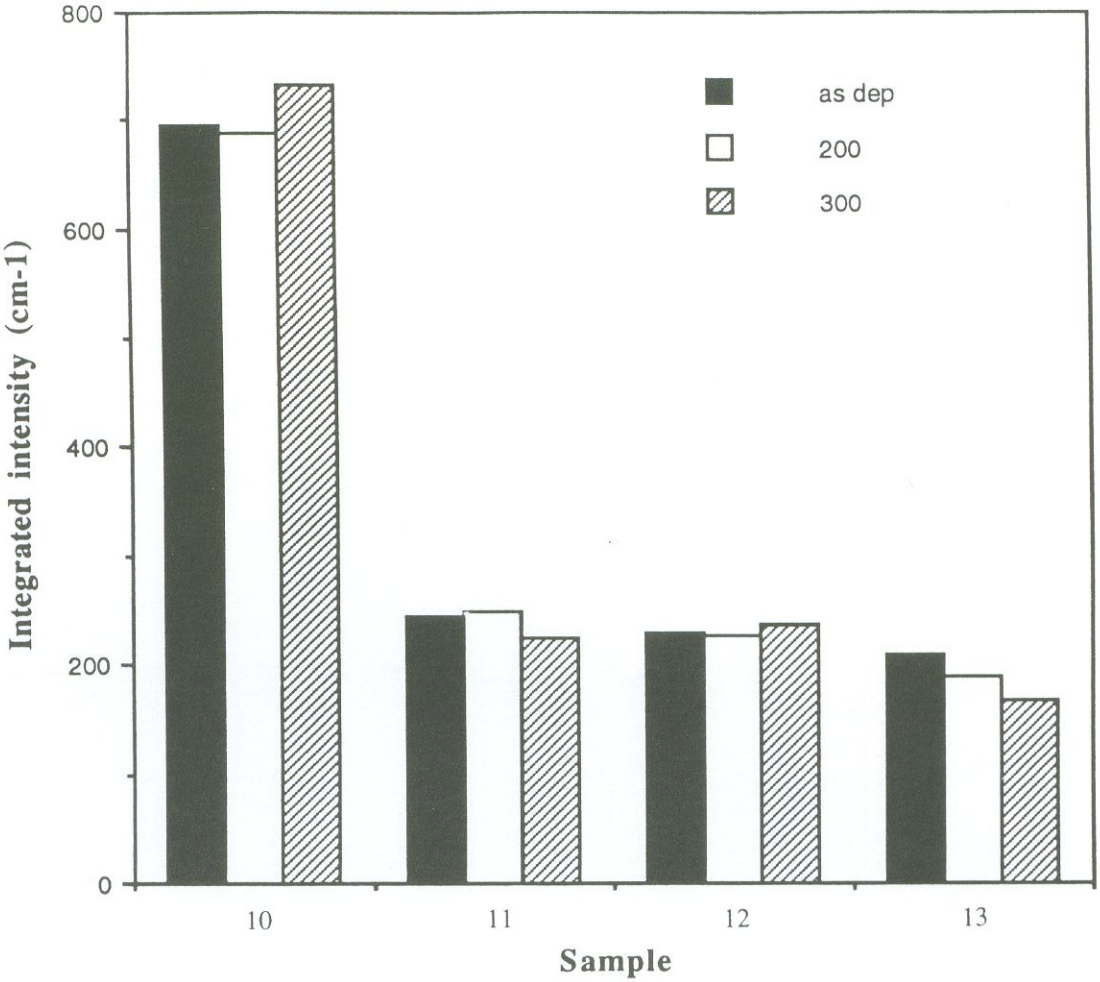

Figure 10.1: Integrated intensity of the ~ 640 cm^{-1} infrared peaks of samples 10, 11, 12, and 13 in the as-deposited state as well as after annealing at 200 and 300 °C.

Had the ERDA integrated yield remained constant on annealing, then the increased IR peaks of figure 1 could have been caused by either (i) or (ii) above, or both. Since ERDA integrated yields decreased on annealing for all samples and temperatures, the increase in IR absorption is not believed to have been caused by H-H --> H-Si bond reconstruction. Moreover, the ERDA yield decrease at those low temperatures (which in fact were lower than or equal to the deposition temperature, T_S) was probably due to hydrogen evolved which was not infrared active, and possibly not chemically bonded to the amorphous silicon network (most probably trapped molecular H_2). For

sample 13 both integrated infrared intensity and yield showed a decrease for all annealing steps.

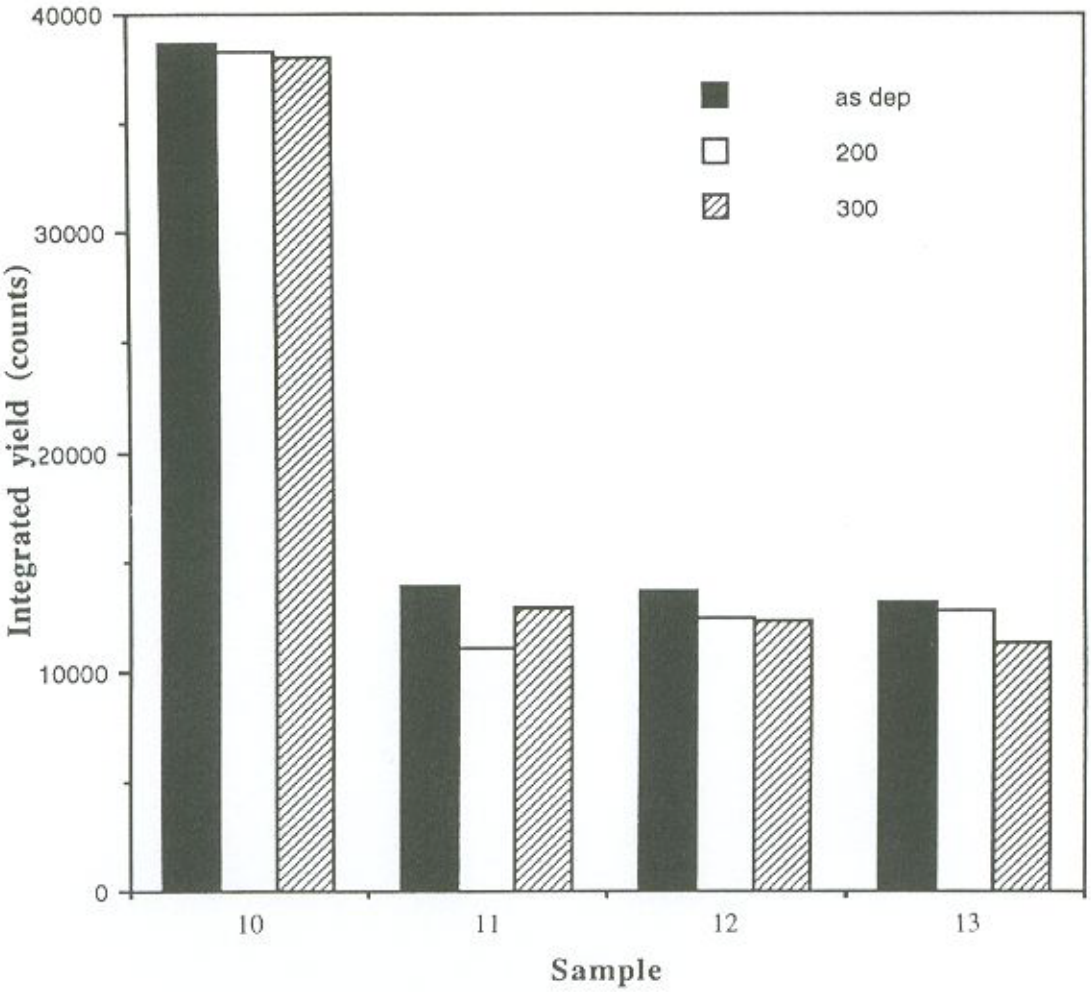

Figure 10.2: ERDA integrated yield for the total hydrogen content of samples 10, 11, 12, and 13 in the as-deposited state as well as after annealing at 200 and 300 °C (for sample 2, the 200 °C anneal ERDA result has been found to be in error and was thus omitted).

Even though that sample presented a low hydrogen concentration (C_H ~ 4.6 at.%), we believe that decrease to be due to a large amount of weakly bonded hydrogen (WBH) in that film (which was prepared under non-optimal conditions), as we have already mentioned in chapter 7.

10.4 Conclusions

We have carried out an experiment with the aim to better understand the causes for the overall increase in the H-Si infrared absorption peaks on annealing of a-Si:H films at low temperatures (200 and 300 °C).

Even though it is minor at those temperatures, our results point to a hydrogen content decrease (H out-diffusion) on annealing. We thus conclude that, at least for the particular set of conditions described in our work, the overall increase in the infrared absorption on annealing is probably an experimental artefact. Structural changes in film structure, more specifically surface roughening with thermal annealing, which leads to increased nonspecular scattering, appear to be responsible for the increased absorption. Our results indicate that the small amounts of hydrogen evolved from the amorphous silicon material at those relatively low temperature annealing treatments were probably mostly due to molecular H_2 trapped inside microvoids dispersed in the amorphous silicon network.

Chapter 11

Seasonal Output Variations in Amorphous Silicon Solar Cells

11.1 Introduction

Amorphous silicon is the fastest growing segment of the PV market. The total market for a-Si cells grew rapidly from 1980, when the first commercial a-Si solar cells were introduced by Sanyo powering a pocket calculator [4], a clever low light level, low power, indoor application in which amorphous silicon cells are most efficient. In the mid- to late-1980's walk lights, battery chargers and other low power applications were introduced, where cells were then exposed to outdoor or direct sunlight conditions. In the last few years utilities and research centres have been testing a-Si PV modules in grid-connected demonstration arrays, and for these high power outdoor applications, module efficiency is a matter of greatest concern. While for indoor, low power applications the Staebler-Wronski effect is of relatively little concern, the effect is a serious problem in outdoor applications, in the generation of kilo and megawatt power electricity.

An aspect of amorphous silicon PV operation which is characteristic of outdoor applications only is the so-called seasonal effect, which describes the output efficiency pattern in a long-time scale. As mentioned in chapter 3, output power decreases during the winter and recovers in summer time, with the maximal power ranging from 71 to

83% between the two seasons [124]. In recent years, these periodic variations in module efficiency in an annual basis have been frequently reported [20,115,123-125,222-234], although to the best of our knowledge no detailed study on all the possible causes has been reported. Most of the above cited publications merely report on the observation of a periodic efficiency pattern, which can be correlated with the evolution of the ambient temperature. This has led to the belief that a partial recovery of the Staebler-Wronski effect due to thermal annealing during summer months is the major cause of the increased efficiency.

Variations in the solar spectral distribution on a yearly basis are significant in the response range of amorphous silicon alloys and other higher bandgap materials. For PV devices using these materials, spectral effects should be considered more carefully, because their response range falls in the region of the solar spectrum where most changes between winter and summer occur, as we will further discuss in this chapter.

Peculiarities of the amorphous silicon solar cell contrast with some characteristics of the more traditional crystalline silicon PV technology. They have to be taken into account when a-Si solar cells are exposed outdoors and in the interpretation of the seasonal effect. The temperature coefficient in output power is in the order of -0.1 to -0.3 $\%.^{o}C^{-1}$ for amorphous, while it ranges from -0.5 to -0.8 $\%.^{o}C^{-1}$ for single crystal silicon solar cells [20], resulting in reduced power loss at high temperatures for the amorphous cells. Another important difference between a-Si and c-Si solar cells is in their spectral response. Being a function of the material's bandgap and also of its optical absorption coefficient, it is much narrower for amorphous silicon (ranging from ~ 360 to 780 nm for a single-junction device) than it is for the crystalline silicon solar cell (where it ranges between ~ 380 to 1180 nm). Finally, taking into account the Staebler-Wronski effect, which is only present in the amorphous silicon-type solar cell, all these factors combined contribute to the general picture for outdoor exposure being

that a-Si photovoltaics are more efficient during summer months, while it is in winter time that c-Si devices perform better.

11.2 Experimental Procedures

The experimental work described in this chapter consisted in light-soaking experiments, indoors under a solar simulator, of commercial-type amorphous silicon solar modules. Moreover, to quantify the variation during the year of the solar spectral distribution, we have measured the total solar spectral irradiance (Perth, Australia, lat: 31.9 °S, long: 115.8 °E, elevation: 19 m) in the response range of amorphous silicon solar cells, using a research spectroradiometer.

11.2.1 Light-Induced Degradation of a-Si Solar Modules at Different Operating Temperatures: The Seasonal Effect (I)

The purpose of this experiment was to study the influence that the operating cell temperature can have on the degradation behaviour of amorphous silicon solar cell modules. Winter and summer operating cell temperatures were simulated and their effect on the output parameters of solar modules was monitored. With that procedure it was intended to ascertain whether the seasonal variations in operating temperature that solar modules undergo during the year could be identified as the major contributor to the seasonal effect in amorphous silicon photovoltaics.

Two sets of commercially available single-junction p-i-n amorphous silicon solar modules, designated "winter" and "summer", were used to compare the evolution of the degradation in I-V parameters under light-soaking. Each set consisted of four 2 x 5.5 cm^2, eight-cell modules. The two sets were exposed simultaneously to the same

simulated AM 1.0 spectrum, while keeping them at different temperatures corresponding to winter and summer extreme operating cell temperatures, and monitoring their output parameters with exposure time. Modules were kept in an open-circuit condition (worst case load for stability performance studies) while under light-soaking, and measurements of the open circuit voltage (V_{oc}), short circuit current (I_{sc}), and cell temperature (T_{cell}) were made at hourly intervals.

The total exposure time was 200 hours under 1 SUN, AM 1.0 spectrum (200 $kWh.m^{-2}$). The illumination regime was 8 hours of light-soaking followed by 16 hours in the dark before the next 8 hours illumination period and so on. All light-soakings were made on a Kratos solar simulator calibrated to the AM 1.0 spectrum. The intensity of the light source was set by means of a calibrated crystalline silicon solar cell. No spectral effects were considered since all experiments were carried out under the same 1000 $W.m^{-2}$ simulated light intensity and all modules were mounted in the same plane, normal to the light beam. For the set of modules designated "winter", cell temperatures were kept around 20 °C at all times by means of a water-cooled heat sink to which the modules were attached. For the "summer" modules, cell temperatures reached up to 70 °C during light-soaking in the 3 x 3 m^2 closed room (wind speed virtually nil).

11.2.2 Determination of the Seasonal Terrestrial Solar Spectral Distribution in the Response Range of a-Si:H Solar Cells: The Seasonal Effect (II)

The purpose of this second experiment was to determine how important the differences (spectral shift) between winter and summer solar spectral distribution can be to the performance of a-Si solar modules deployed outdoors. Since amorphous silicon presents a narrower spectral response in comparison to crystalline silicon solar cells, it is believed

that seasonal shifts in the solar spectral distribution can affect much more the performance of the amorphous devices. It was thus intended to verify whether these seasonal changes in the solar spectral content could qualify as a major contributor to the seasonal effect in amorphous silicon photovoltaics.

To that effect, in order to better understand the match between solar cell spectral response and solar radiation spectral content, the measurement of the terrestrial solar spectral distribution in Perth, Australia, was made on typical days for the four seasons. A spectral radiometer was used to record the spectra as described in chapter 6. Our system was optimised for the visible range, and calibrated over the wavelength range of 250 nm to 800 nm, ideally matching the spectral response of commercial-type single-junction a-Si solar cells. All the solar spectra (southern hemisphere winter and summer solstices, and autumn and spring equinoxes) were taken over 280 to 800 nm in steps of 10 nm, and were recorded on clear days at solar noon.

11.3 Results and Discussion

We now present and discuss our results for commercial-type amorphous silicon solar modules, and the seasonal shifts in the incident spectra recorded for the four seasons in Perth, Australia. To further illustrate the discussion, we include some results obtained at Telecom Australia Research Laboratories' amorphous silicon outdoor testing facilities [235], which have been provided to us as raw data, with permission to publish.

Figures 11.1 and 11.2 present the normalised evolution of V_{oc} and I_{sc} for the sets "winter" and "summer" (average for 4 modules each). Figure 11.3 shows the evolution of cell temperature (T_{cell}) of the "summer" set and of the ambient temperature in the solar simulator room in a typical 10 hour run. For the "winter" set, cell

temperatures were kept around 20 °C all the time, corresponding to the horizontal axis of figure 11.3.

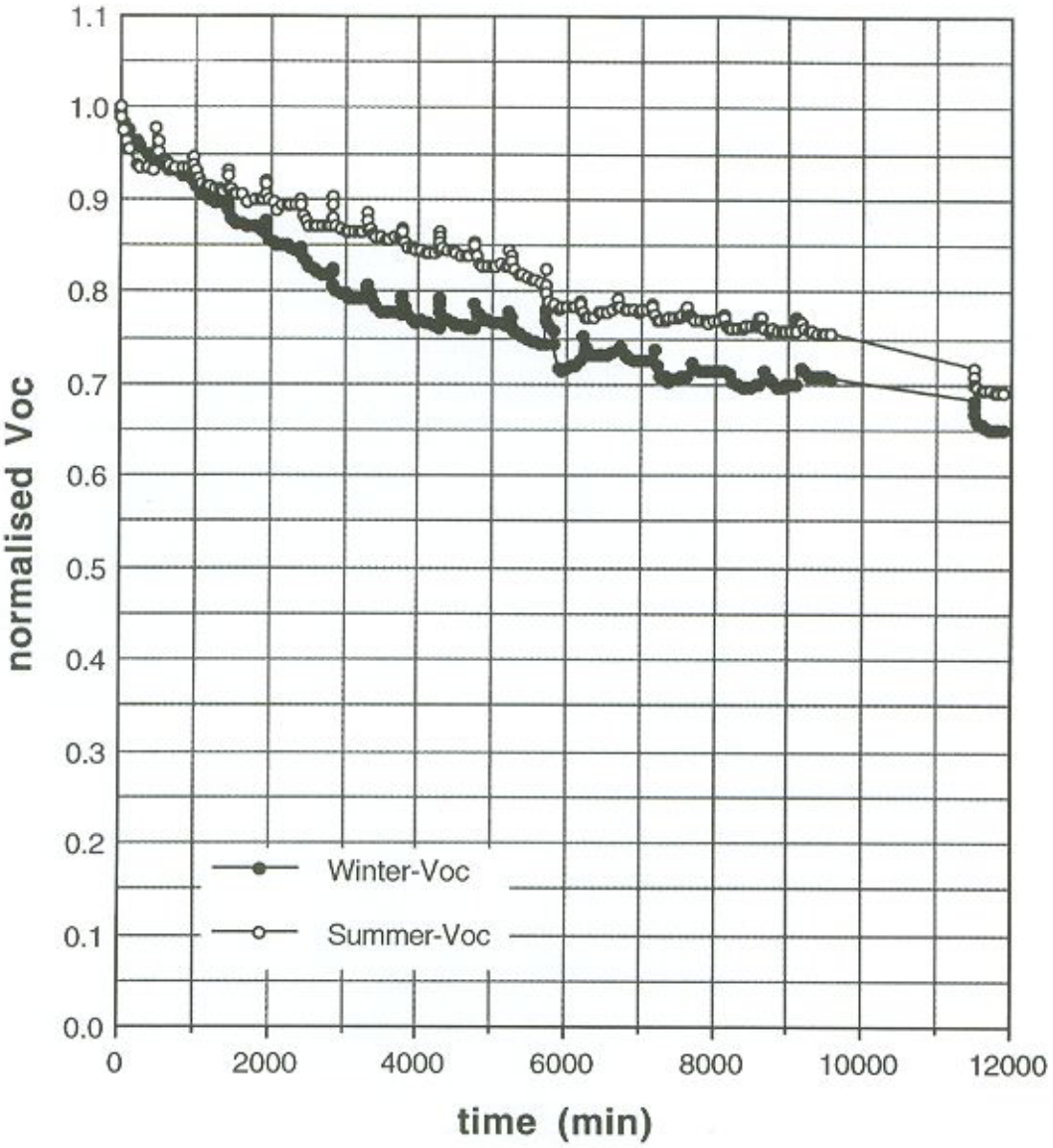

Figure 11.1: Normalised evolution of the open circuit voltage (V_{oc}) for the sets "winter" and "summer" for 200 hours light-soaking under simulated 100 mW.cm^{-2} AM 1.0 light (average for 4 modules each).

In general, and in accordance with other published results [236], the evolution of the parameters presented a sharper decrease during the first 50 kWh.m^{-2} (50 hours) and slowed down in a second period from 50 to 200 kWh.m^{-2}, when the efficiency gets closer

to a stabilised value. The open circuit voltage V_{oc} of sets "winter" and "summer" degraded to 68.3 % and 71.7 % of the original values respectively after the 200 hour exposure; the short circuit current I_{sc} values decreased to 61.8 % and 65.6 % for "winter" and "summer" respectively.

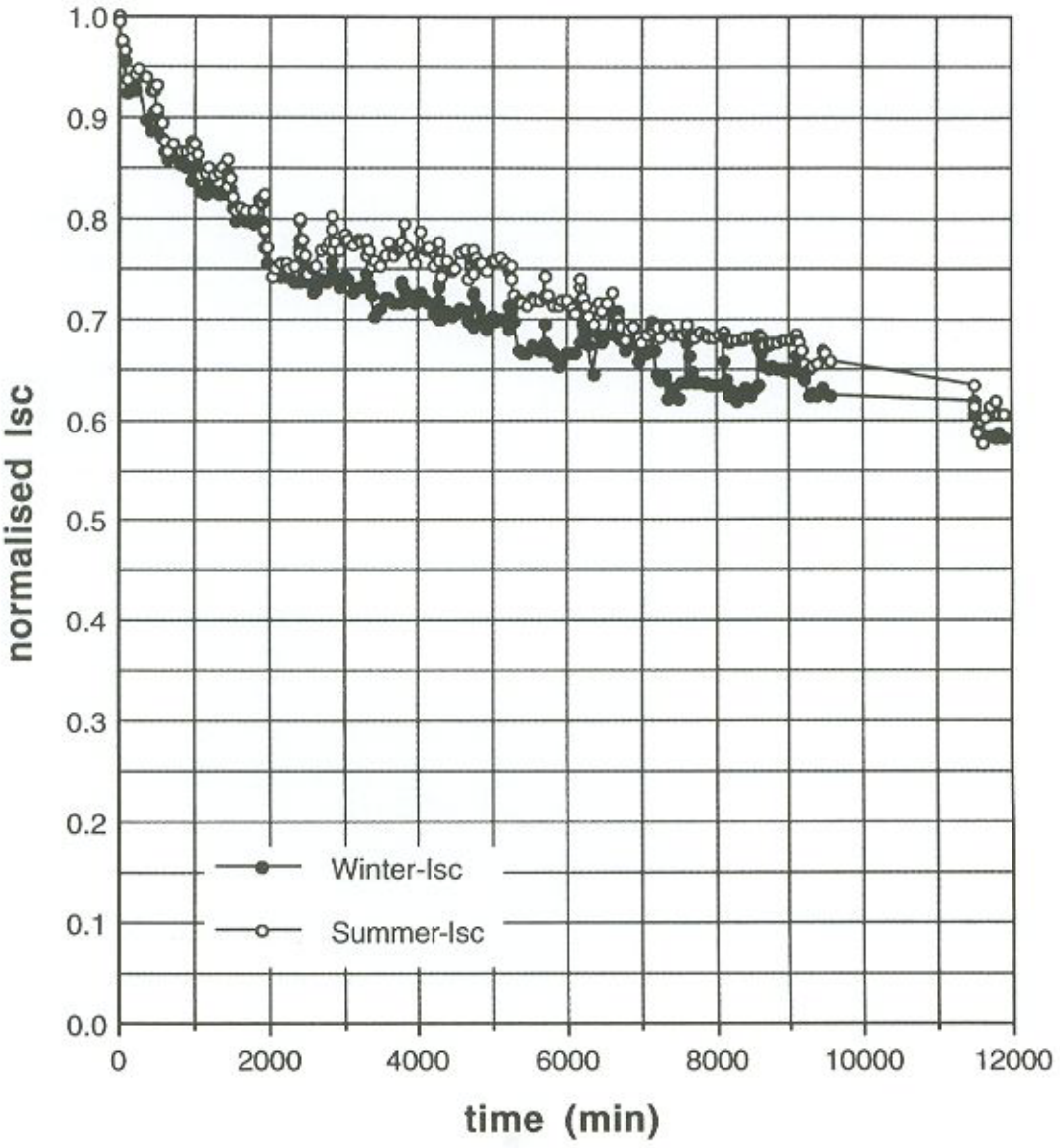

Figure 11.2: Normalised evolution of the short circuit current (I_{sc}) for the sets "winter" and "summer" for 200 hours light-soaking under simulated 100 $mW.cm^{-2}$ AM 1.0 light (average for 4 modules each).

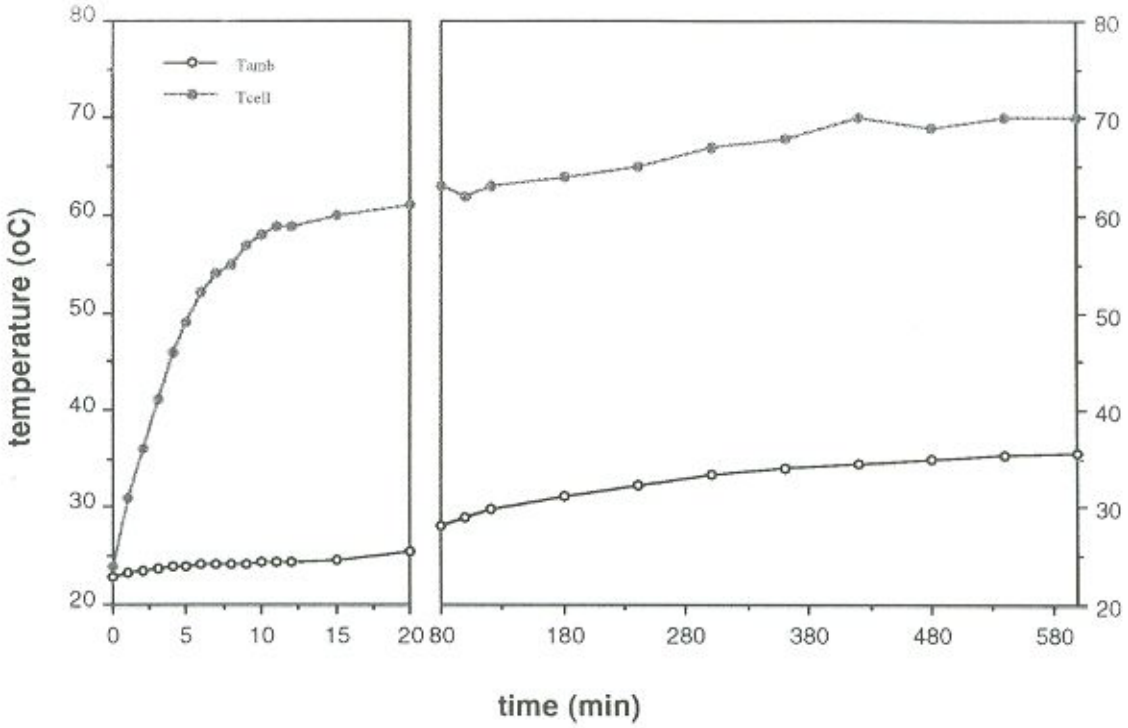

Figure 11.3: Evolution of cell and ambient temperatures for a 10 hours run in the solar simulator laboratory (Tcell corresponds to the "summer" set cell temperatures; Tamb to the ambient temperature. Cell temperature for the "winter" set corresponds to the horizontal axis).

Figures 11.4 and 11.5 are Telecom Australia's results for 0.49 m^2 surface area, commercial-type single junction modules exposed to about 1600 days outdoor illumination (data measured indoors, at 25 ^oC under a solar simulator). They show, for V_{oc} and I_{sc}, 1 to 2 % differences between winter and summer months, in good agreement with our relative values in the difference of the amount of degradation between modules exposed to winter and summer temperatures. The commercial modules used in our work, however, showed a much more pronounced degradation in absolute values, especially for V_{oc}. The 1 to 2% differences between summer and winter values of V_{oc} and I_{sc} of figure 11.4 result in differences in the maximal power (P_{max}) for the same period averaging ~ 4.5 %, as shown in figure 11.5 for modules deployed outdoors. Even though

the solar modules represented in figures 11.4 and 11.5 were exposed to outdoor conditions, I-V parameter measurements were made indoors, under a solar simulator, and are free from any spectral effects therefore. This result contrasts with the ones by Ragot *et al.* [124] who find 12 % differences for the same parameter. Their results, however, are for modules deployed and measured outdoors, so that spectral changes might be present in that case, being absent in the former as we have already mentioned. This latter point is made more important by the problems of research workers in trying to find a proper amorphous silicon reference cell which could be used to normalise I-V data from a-Si cells and modules operating outdoors. The lack of such a bona fide reference cell is a serious drawback since filtered crystalline silicon cells, which are currently used as such references, are far from ideal for normalising purposes in outdoor measurements. A serious limitation of the reference cell technique is that it requires a device with a spectral response reasonably well matched to that of the testing cell. Such reference cell is not available for a-Si devices due to the Staebler-Wronski effect. Not only does their integrated output decreases upon light exposure, but their spectral response is also shifted as light-induced degradation proceeds [237].

Day zero in figure 11.5 corresponds to 25/5/88, just before winter began in the southern hemisphere; P_{max} degraded some 14 % in the first 190 days and started to recover, on 1/12/88 (close to the southern hemisphere's summer solstice), up to a maximum of 2.6 % recovery, which occurred on 8/3/89 (day 287). After that, P_{max} periodically reached minima and maxima at the mid to end of winter and summer each year respectively, and it is interesting to note how the degradation rate declined (14 %, 7.4 %, 4.4 %, 5.1 %, 4.7 %) while the recovery rate increased (2.6 %, 3.2 %, 3.9 %, 3.5 %) with exposure time. This shows the strong initial intensity of the Staebler-Wronski effect, and the little recovery that summer temperatures can provide initially. Figure 11.5 also shows the evolution of the fill factor (FF) and the voltage at peak-power (V_{pp}) for the same period.

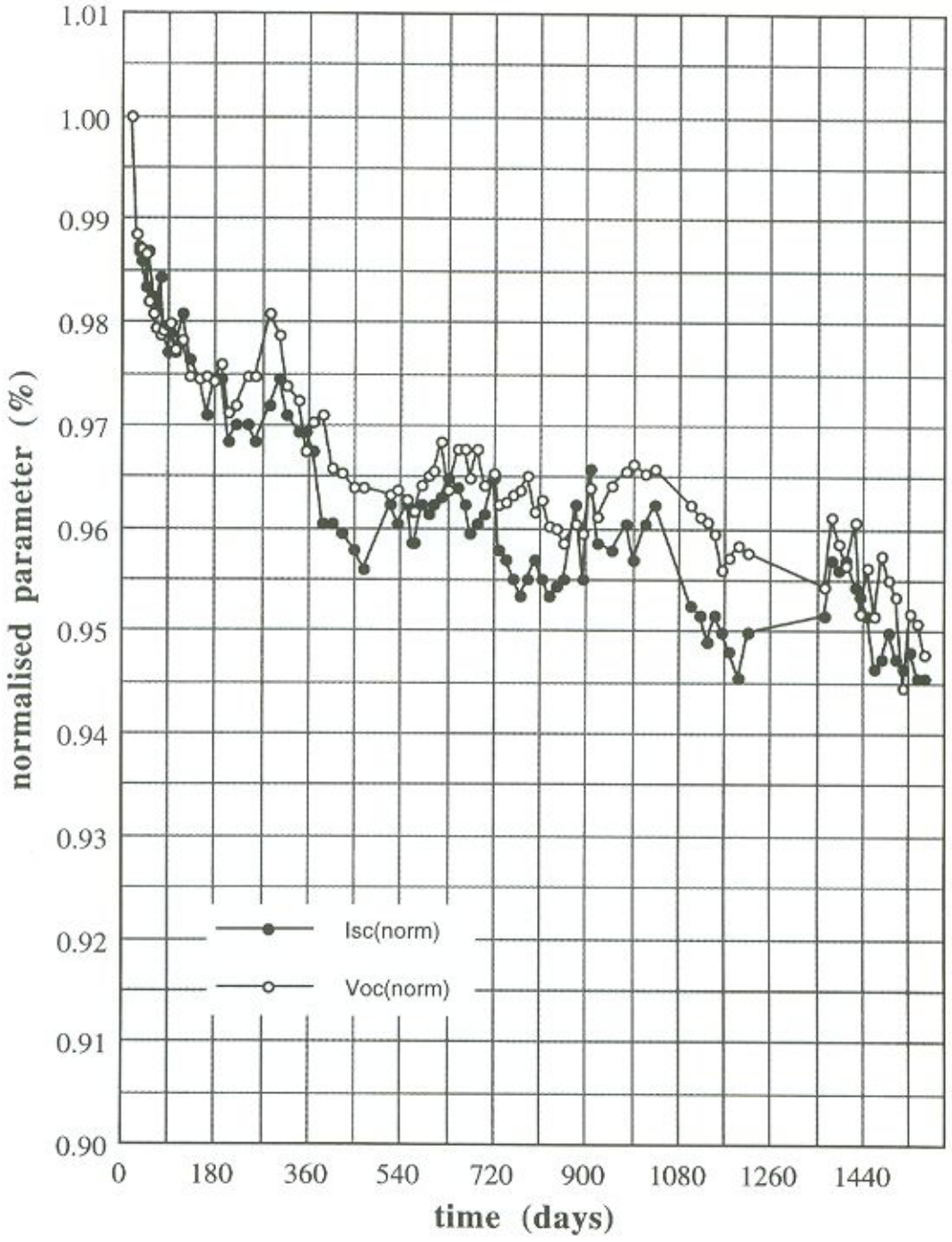

Figure 11.4: Normalised evolution of the open circuit voltage (V_{oc}) and short circuit current (I_{sc}) for Telecom Australia's outdoor testing facility site in eastern Australia. Modules were exposed outdoors, but I-V measurements were made indoors under a solar simulator [235].

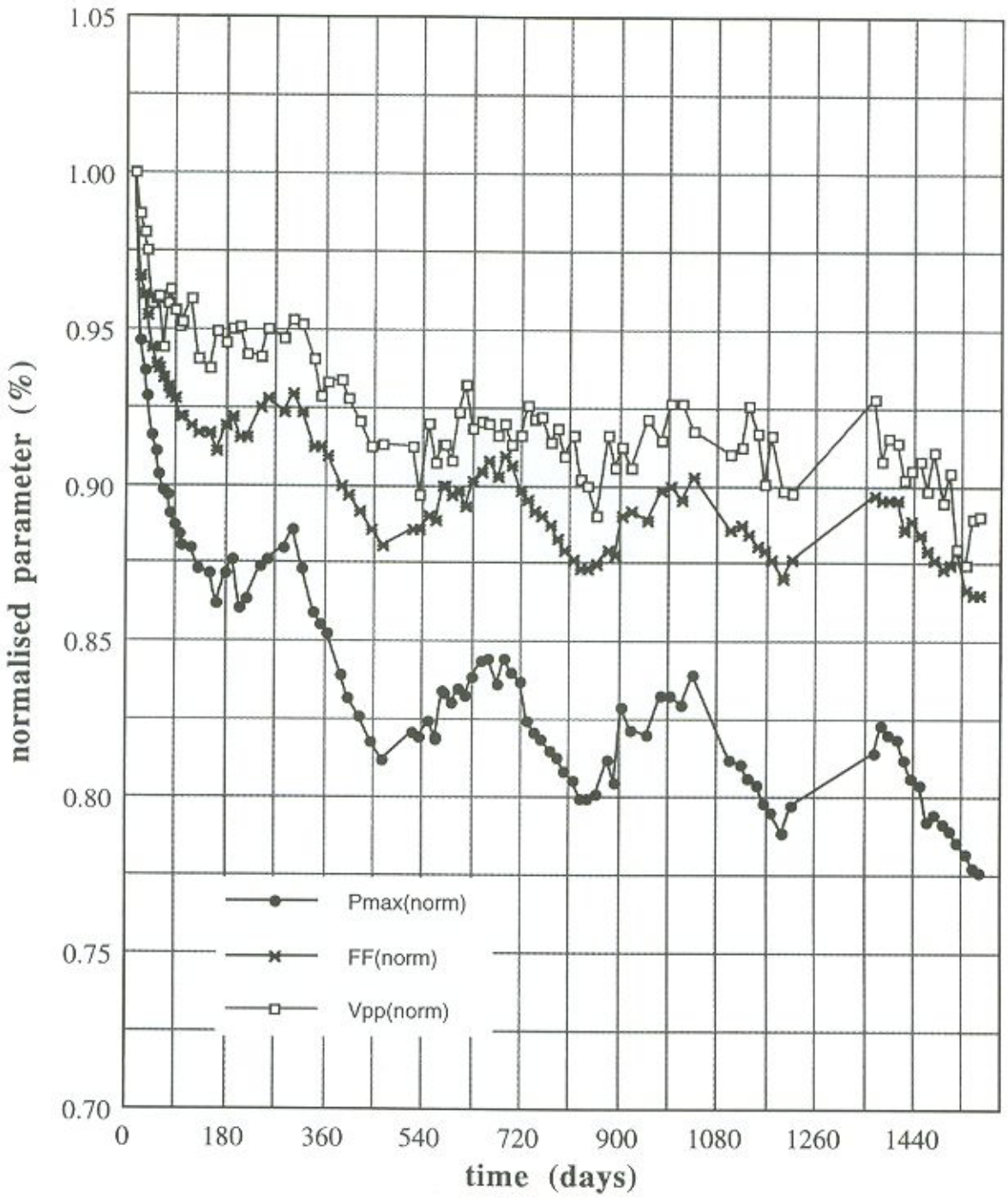

Figure 11.5: Normalised evolution of the maximal power (P_{max}), fill factor (FF), and voltage at peak-power (V_{pp}) for Telecom Australia's outdoor testing facility site in eastern Australia. Modules were exposed outdoors, but I-V measurements were made indoors under a solar simulator [235].

In our figures 11.1 and 11.2 the peaks after every 8 hour light-soak are probably due to both overnight annealing of the Staebler-Wronski effect and also to the lower cell temperatures, even for the "winter" set, at the beginning of every 8 hour illumination period (each such point corresponds to reading of I-V data 5 minutes after the beginning of every 8 hour light-soaking period). In figure 11.6 we plotted, for the "summer" set, the evolution during four consecutive days of the relative decays of V_{oc} and I_{sc} for the 20 first minutes each day. As the temperature increased with exposure time, V_{oc} decreased; the first point each day shows a recovery probably due to night-time annealing of the Staebler-Wronski effect and also because the cell temperature was still low (see minute 1 in figure 11.3). I_{sc}, in this same time scale, did not peak as V_{oc}; as the temperature increased with exposure time I_{sc} would tend to increase (I_{sc} presents a positive temperature coefficient), but the effect was probably counterbalanced by the Staebler-Wronski effect, which takes over as soon as light exposure begins. As pointed out by Delahoy *et al.* [238], easily annealed defects are rapidly restored once the cells are exposed to light again after a period in the dark. It can therefore be expected for modules operated outdoors that night-time annealing, while always present to some degree depending mainly on ambient temperature, does not in itself represent an increase in integrated energy output for the solar module.

The results shown in figures 11.1 and 11.2 are based in the temperature profile shown in figure 11.3, in an ambient with wind speed practically zero, incurring in a cell temperature difference between the "winter" and "summer" conditions of almost 50 °C. Real outdoor testing facility winter-summer cell temperature differences are usually lower, ranging for example between 25 °C in southern France [239] and 32 °C in eastern Australia [235], and are respectively 20 °C and 27 °C above ambient temperature at these sites at maximum. Furthermore, Luft *et al.* [240] have found that no discernible difference in output recovery could be observed when annealing 1000-hours light-soaked solar cells at 60 °C and then at 70 °C. The solar cell operating temperature of a module is determined mainly by the solar irradiance, but is also influenced by ambient temperature

and wind speed. Differences in the mean daily maximum temperatures between winter and summer (July and February) in Perth (Australia) do not exceed 12 °C on average; wind speeds, especially during summer months, can range from 11 to 30 km.h^{-1} on average [241].

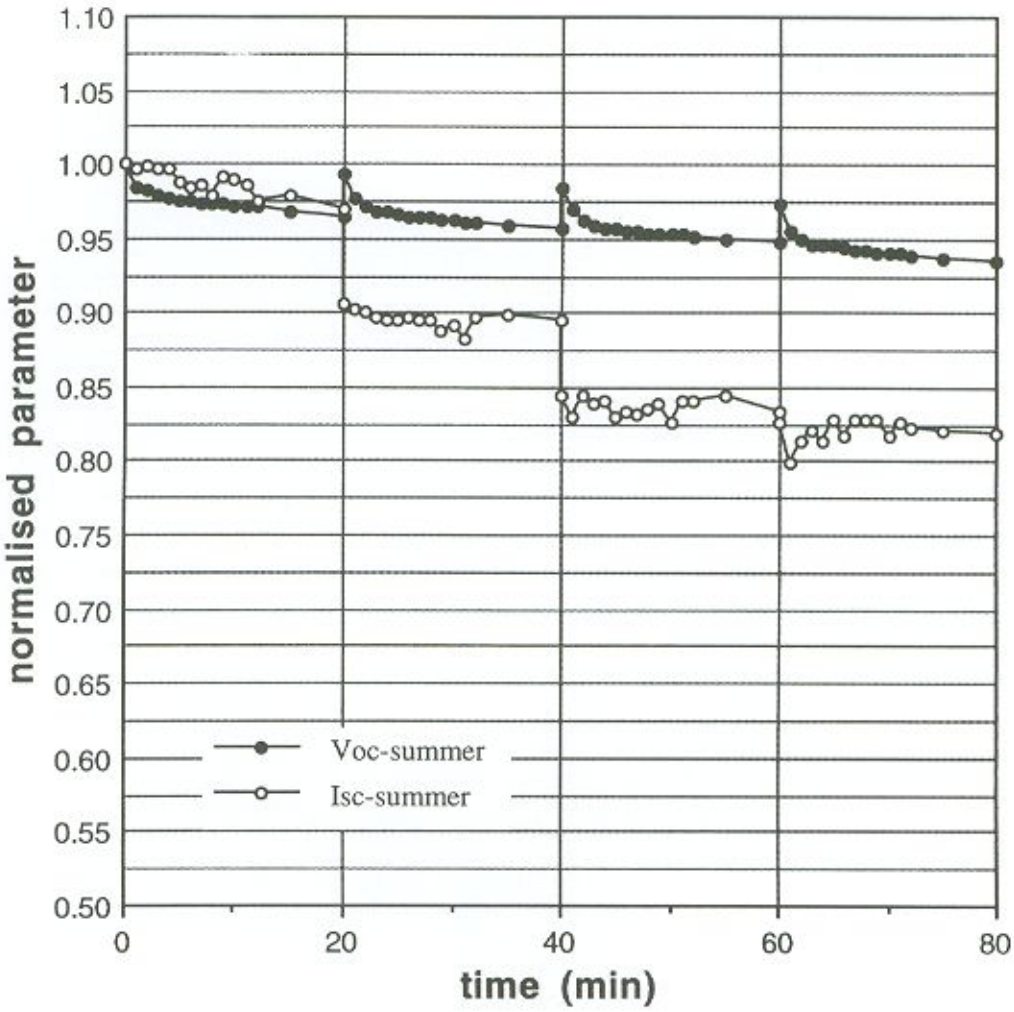

Figure 11.6: Normalised evolution, in a short-time scale, of the open circuit voltage (V_{oc}) and short circuit current (I_{sc}) for the set "summer". The ordinate (time scale) represents the first 20 minutes of four consecutive days of 8 hours light-soaking each.

Going back to a-Si material properties, Schneider *et al.* [132] found that for 20 and 30 minutes isochronous annealing of electron irradiated films (sputter and glow discharge deposited) no considerable recoveries in photoconductivity values (a measure of the

Staebler-Wronski effect) were noted before ~ 75 °C temperatures were reached, so that below those temperatures, although it occurs, annealing has very little recovering effects. In saturation experiments, a steady state is reached more quickly when the experiment is performed at elevated temperatures. The limiting value of the equilibrium defect density decreases as temperature is raised, although the rate of defect creation is insensitive to the temperature [22]. In any case, however, according to a model by Redfield and Bube [242], even when the sample temperature is as high as 70 °C, the thermal annealing effect is much smaller than the light-induced annealing term. Light-induced annealing in amorphous silicon solar cells may therefore be playing a role in the seasonal effect, although the effect has not been sufficiently quantified.

Differences in the annealing behaviour between defects produced by various creation mechanisms are due to differences in their annealing energy distribution, and easily annealed defects are rapidly restored by light-soaking. For this reason, over many light-soak/rest cycles, as is the case in modules operating in an outdoor environment, module efficiency is determined mainly by accumulated light-exposure time, regardless of the extent of interspersed annealing [238].

Local hydrogen motion may be involved in the annealing recovery of the light-induced defects. As was pointed out in chapter 3, and illustrated by figure 3.5 based on results by Hata and Wagner [122], if the annealing process which restores initial cell efficiencies involves bond breaking, it should be strongly temperature dependent. Annealing times are in the order of 1 hour at 150 °C and around 1000 hours at 50 °C in the dark to completely remove light-induced defects in amorphous silicon films. Thermal annealing of defects is a highly temperature dependent process as figure 3.5 indicates.

The relative radiation converted by an amorphous silicon solar cell has been shown by Wilson [243] to have a standard deviation (over the period of 2 years) of 4.7 %, and a difference between the extreme values (winter and summer) of 16 %. Figure 11.7

illustrates the reason for the large change in the fraction of irradiation converted by the amorphous cell. It clearly shows the effect of increasing midday air mass from summer to winter (AM 1.0 to AM ~ 1.4 [117]), due to increased zenith angles, resulting in a shift of the spectrum towards longer wavelengths. There is a remarkable shift to the red in the winter solstice, with a considerable difference occurring in the blue region, which causes a-Si:H cells, due to their spectral response, to drop in efficiency. For crystalline silicon solar cells, however, due to a wider spectral response, the change in conditions is negligible, as pointed out in figures 11.8 and 11.9. Not only does the a-Si cell respond better to slightly shorter wavelengths than the c-Si device, but, more importantly, it also presents a much higher optical absorption coefficient in the blue region of the spectrum. This makes the amorphous device a much "bluer" solar cell than its crystalline counterpart. Optical losses in solar cells depend on the match of the solar spectrum with the optical absorption coefficient of the active material, and are, therefore, strongly material-dependent.

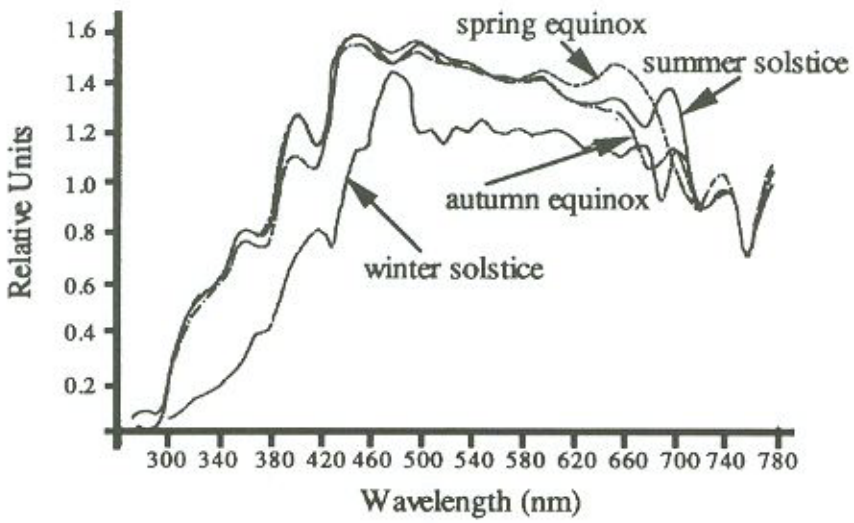

Figure 11.7: Seasonal evolution of the terrestrial solar spectrum distribution during one year in Perth, Australia, in the range of amorphous silicon solar cells spectral response. Measurements made at solar noon.

The solar spectral distribution of the irradiance that an a-Si PV module detects varies according to the module's orientation relative to the sun. Most of the times, especially in utility applications and other large outdoor testing facilities, arrays have a fixed tilt and orientation, which accounts for the lowered plan-of-array irradiance values during most part of the year as compared to tracking systems. Fixed tilt arrays are usually mounted with a surface slope equal to latitude, which provides the maximum annual energy availability. Outdoor I-V readings are usually normalised to standard testing conditions (STC) based on irradiance values collected by optically broad band sensors such as pyrheliometers or pyranometers (solarimeters), which do not present the spectral sensitivity that amorphous silicon and other higher bandgap materials present.

Let us compare two distinct radiation scenarios. Let one be, for example, a clear winter day (higher zenith angle, leading to a "redder" spectrum as compared to a clear summer day). Let the other be a partly cloudy summer day (in which the spectrum is "bluer" due to the precipitable water present in the air between the cloud droplets which absorb in the red end of the spectrum, and also because of the lower air mass values typical of summer months). While both might provide the same irradiance reading as measured by a solarimeter, this will lead to considerable error when normalising an amorphous silicon module I-V reading. That is because while the solarimeter might "see" them as equivalent irradiance values, the amorphous silicon cell will not. Spectral *content* is here the issue.

A correlation between the ratio of infrared to total insolation and amorphous silicon module efficiencies has been reported by Candelario *et al.* [244]. A correlation was also reported between ambient temperature and efficiency, which they related back to the module's sensitivity to IR insolation, since the ambient temperature influences the absolute humidity, which affects the proportion of IR in the incident solar spectrum. Humidity conditions, therefore, are important when total irradiance and efficiency data

are reported. Water vapour, as well as ozone amount, turbidity, *etc.*, affect spectral bands above certain wavelengths, which, depending on the device's spectral response, directly influence efficiency.

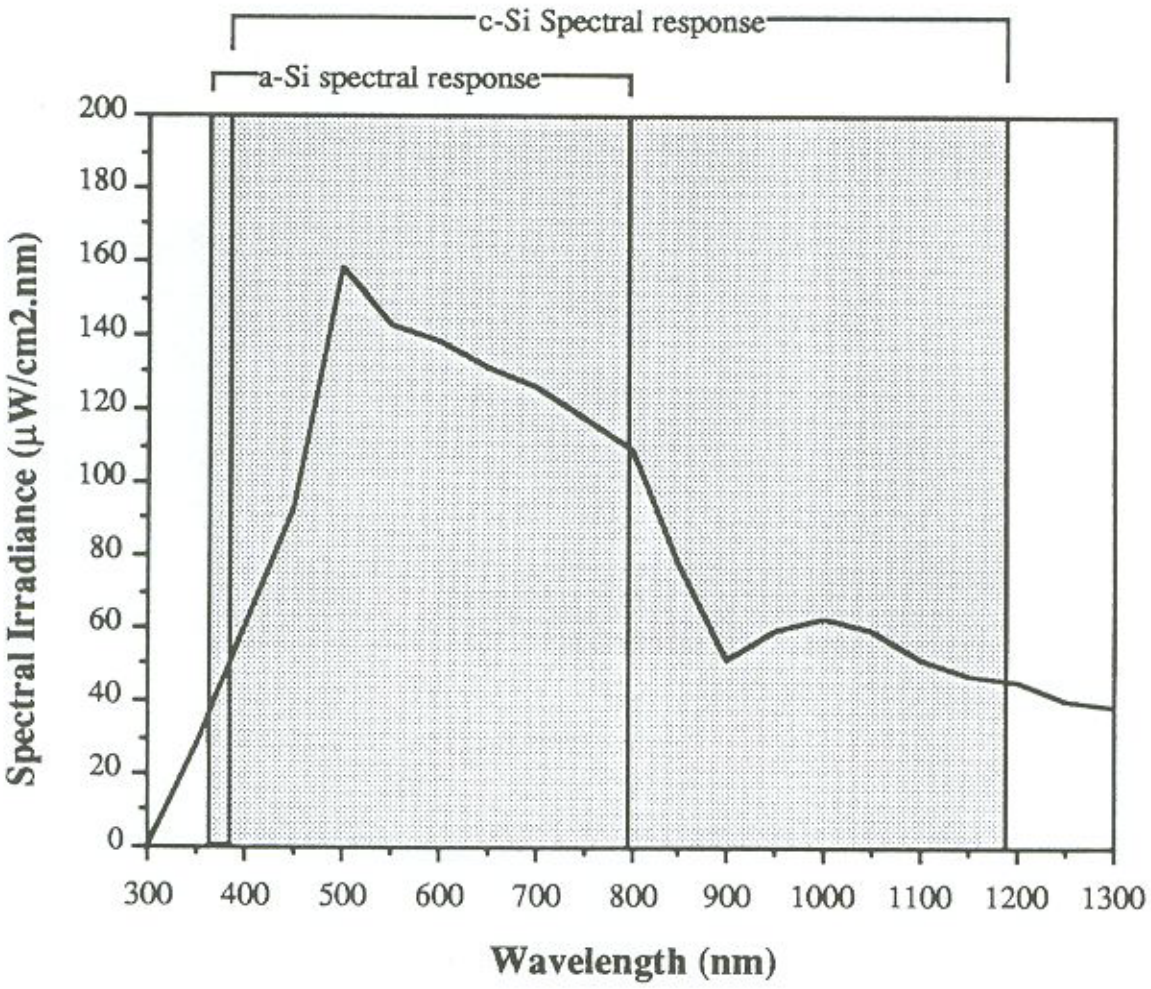

Figure 11.8: Spectral response regions of amorphous (single-junction) and crystalline silicon solar cells superimposed on a simplified AM 1.0 spectrum [177]. A shift of this spectral distribution towards longer wavelengths affects much more the efficiency of a-Si than that of c-Si devices.

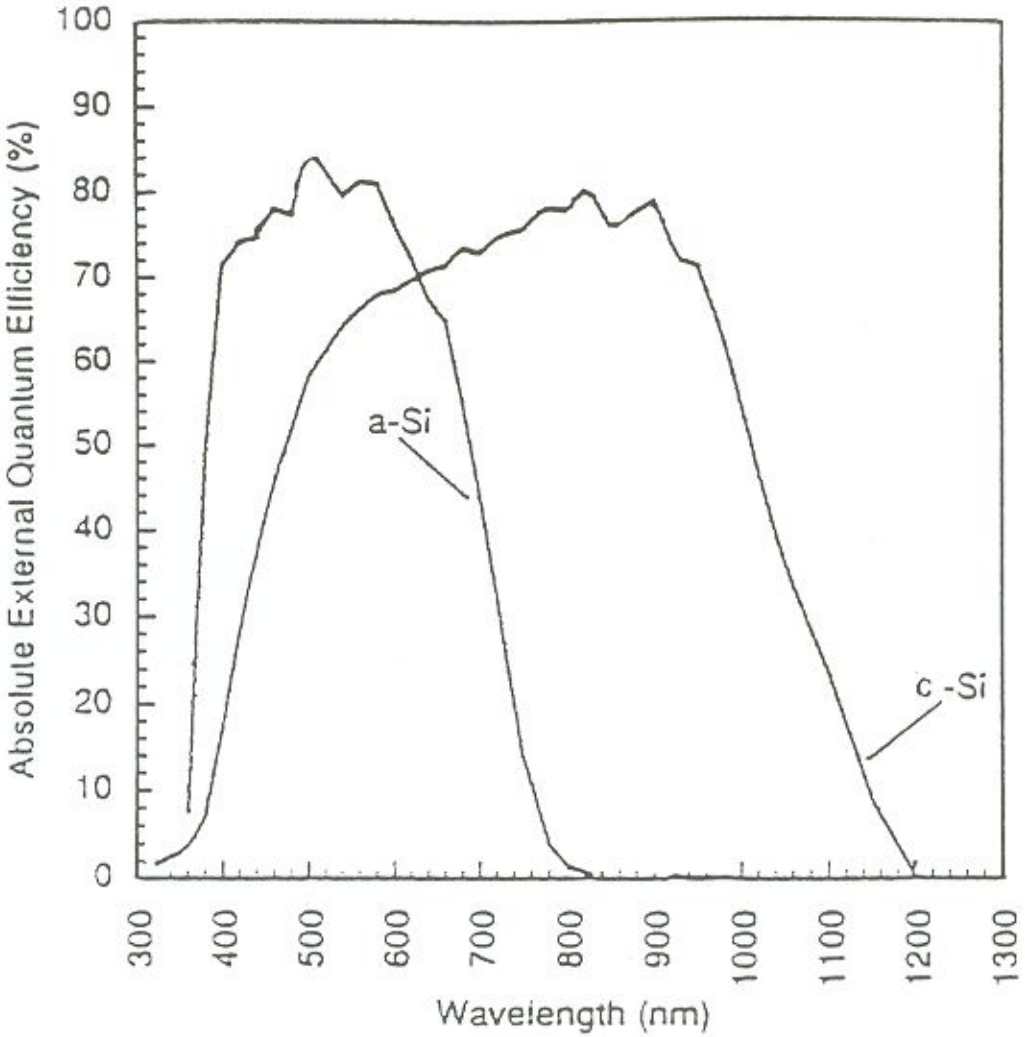

Figure 11.9: Measured quantum efficiencies for production single crystalline Si and a-Si:H (single-junction) solar cells [115].

11.4 Conclusions

The experimental results presented in this chapter indicate that the thermal annealing effect contributes to a lesser extent to the widely reported (more than 10 % variation in normalised power output) seasonal effects in amorphous silicon solar module outputs than generally believed. The fact that the evolution in cell efficiency can be correlated

with that of the ambient temperature is somewhat misleading. Thermal annealing is a highly temperature dependent process, and is not believed to be so prominent in the range of temperatures to which a-Si solar cells deployed outdoors are exposed. Researchers at the National Renewable Energy Laboratory - USA (NREL, formerly SERI) reported that there is some recovery in the power output upon annealing in the dark at temperatures up to 70 ^{o}C, but it ranges between 2 and 4 % [240]. The results we presented for Telecom Australia's modules are in excellent agreement with that. Spectral changes between winter and summer terrestrial insolation are remarkable, and are especially important for higher bandgap devices like a-Si:H, CdTe, and GaAs, which present a "bluer response" as shown in figure 11.9 and also 3.3 of chapter 3. For these materials, and more particularly for amorphous silicon, these spectral changes occur exactly in the wavelength range where their spectral response lies; and constitute, therefore, a major contributor to the seasonal efficiency variation. The use of solarimeter readings to normalise a-Si PV readings to reference spectra is far from ideal. Those instruments have a response which is independent of either wavelength or angle of incidence of the solar radiation, contrary to amorphous silicon solar cells, which are very sensitive, especially to radiation wavelength shifts. Together, these phenomena seem to add up and determine that, contrary to what happens with the crystalline silicon PV technology, amorphous silicon perform better in summer than in winter, in what we usually call the seasonal effect.

The relative performance of crystalline and amorphous Si devices outdoors, under realistic operation conditions can show marked differences from the ideal standard conditions under which these devices have their output usually rated. Ishikawa [245] has recently shown that a two-junction, same bandgap amorphous silicon module with a stabilised conversion efficiency of 7.5 % exhibited an average conversion efficiency of about 8 % when monitored throughout the day for several months outdoors. A crystalline silicon panel with an efficiency of 12 % exhibited an average conversion efficiency of about 10 % during the same period. The smaller conversion efficiencies

(as compared to the AM 1.5 efficiencies) resulted partly from the fact that the a-Si module made better use of the solar spectrum both early and late in the day [246]. Also influencing the results is the fact that the amorphous silicon panel exhibits better relative performance at elevated temperatures.

Chapter 12

Concluding Remarks and Scope for Future Work

12.1 Amorphous Silicon Thin Films

One of the main objectives of the work leading to this thesis was the investigation of amorphous silicon thin films regarding film deposition, characterisation, hydrogen-silicon bonding configurations and especially the effects of temperature on the amorphous network. Modification of the hydrogen-silicon bonding configurations and reduction of the number of weak bonds appears to be one of the most important targets in the attempts to minimise the Staebler-Wronski effect. The experiments described in chapters 7 to 10 aimed at improving the understanding of the role of hydrogen in the amorphous network and on how to control the way hydrogen atoms bond to silicon atoms in the random structure. We believe that the ability to introduce hydrogen controllably into amorphous silicon can have strong implications for a-Si:H stability, with important applications in a-Si:H materials research and device fabrication. We have been able to demonstrate in this study that with an in-chamber annealing treatment it is possible to obtain a higher degree of control over hydrogen incorporation into sputter-deposited amorphous silicon films.

Although increasing (the presumably undesired) higher hydride formation can be expected with increasing total hydrogen concentration from simple statistical considerations [199], our results have shown that hydrogen content alone is not what

determined the amount of higher hydrides in our a-Si:H films. Rather, our in-chamber annealing treatment has shown that a variety of H-Si bonding configurations can be obtained, irrespective of the hydrogen content. We believe that to be the result of different just-after-deposition relaxation conditions resulting from the various in-chamber annealing and substrate temperature conditions described in our experiments. The in-chamber annealing treatment we have proposed resulted in improved and more stable a-Si:H material as far as hydrogen-silicon bonding configurations are concerned.

In solar cell devices, multijunction designs should result in higher photovoltaic conversion efficiencies than their single-junction counterparts. Kuwano *et al.* [105] have shown that efficiencies of 21 % may be achieved in two terminal tandem cells, with 24 % being possible in a similar triple junction device. In these designs, one of the layers is presumed to be 1.7 eV bandgap a-Si:H. The need for both higher and lower bandgap high quality alloys for triple and tandem junction solar cells is at the present one of the greatest challenges facing the development of such devices. Changing the bandgap by depositing the intrinsic layer at different substrate temperatures is a routinely used strategy in commercial amorphous silicon production lines [247]. We have shown that with our in-chamber annealing treatment higher (lower) bandgap material can be achieved without the need to use the lower (higher) substrate temperatures that lead to non-optimal H-Si bonding configurations. It is known from previous work [72,215,216] that, below 300 °C, the rapid effusion of the loosely bound hydrogen out of the film is not likely to occur, and that the proportion of that hydrogen phase is large when the substrate temperature during film deposition is low. More severe Staebler-Wronski degradation occurs in those films where the hydrogen concentration (C_H) may be as high as 20 at.% than in films deposited at higher temperatures [72]. In-chamber annealed films can be deposited at higher temperatures (T_s ~ 260 °C), with reduced amounts of the loosely bound hydrogen, and high hydrogen concentrations. A higher ability to tailor C_H, and consequently the

bandgap, was thus achieved. Moreover, with the in-chamber annealing treatment it was possible in principle to obtain a structurally optimised amorphous silicon alloy with an energy gap similar to that of a-SiGe:H, without the need to incorporate Ge and its associated disadvantages, and using relatively low processing temperatures. In summary, in-chamber annealing of a-Si:H showed many advantages as a post-deposition treatment, allowing a higher degree of control over hydrogen-silicon bonding configurations and total bonded hydrogen concentration in sputter-deposited amorphous silicon thin films. Furthermore, our thermal annealing studies revealed that in-chamber annealed amorphous silicon films are less susceptible to oxygen contamination.

When amorphous silicon is grown without being in-chamber annealed, inhomogeneous hydrogen distribution profiles often result. This we believe to be caused by the evolution of loosely bound hydrogen from the bulk of the growing film. Inhomogeneous hydrogen profiles can be prevented by in-chamber annealing the sample just after deposition and before allowing the material to cool down to room temperature.

In all cases presented in this work, irrespective of the total hydrogen concentration, infrared data analysis indicated that amorphous silicon which was not in-chamber annealed presented larger relative amounts of loosely bound hydrogen. Hydrogen evolution on thermal annealing at higher temperatures for such samples was more pronounced than for samples subjected to that treatment, as indicated by ERDA results. Film thickness reduction after thermal annealing and intensive bond switching and monohydride clustering were also observed, again being more pronounced for not in-chamber annealed films.

It was shown that tightly bonded hydrogen and weakly bonded hydrogen formation are not directly related to the total hydrogen content, and that even after deposition has

been completed, tightly bonded hydrogen can still be incorporated into the amorphous network.

The overall increase in the apparent infrared absorption often observed in amorphous silicon films subjected to thermal annealing at temperatures around 300 °C we concluded to be an experimental artefact. We believe that surface roughening with thermal annealing, which leads to increased nonspecular scattering, is responsible for the increased absorption.

In our work we used a sputtering technique to deposit amorphous silicon; in sputtering techniques the amount of incorporated hydrogen (C_H) can also be varied by varying the partial pressure of H_2, although the substrate temperature (T_s) is a much more effective parameter for that effect. When a-Si:H is fabricated by the RF plasma enhanced chemical vapour deposition (PECVD) method, hydrogen content is most effectively controlled by the substrate temperature during deposition. Wide-gap a-Si:H films with a large amount of hydrogen are usually obtained at the low T_s of $\leq$ 100 °C. Lowering T_s, however, often results in poor film properties [87]. Hydrogen atoms can also be incorporated into a-Si:H after film deposition by exposing the film to a hydrogen plasma [87], but plasma damage effects have then to be avoided, which is not a trivial task. Lately, hydrogen dilution is being used in glow discharge processes, where the feedstock gas silane (SiH_4) presents a fixed Si:H ratio, to improve cell performance [248]. The use of in-chamber annealing in connection with glow discharge processes (*e.g.* PECVD) therefore represents scope for future work.

Because narrow bandgap amorphous silicon alloys are of technological interest for use as a bottom layer in multijunction, a-Si based solar cells, deposition of a-SiGe:H in conjunction with the in-chamber annealing treatment has also scope for future work. In the deposition of Si alloys containing Ge, higher deposition temperatures are required, which increase hydrogen out-diffusion and degrade film quality. In-chamber annealing

of a-SiGe:H alloys might therefore prove beneficial in the control of the hydrogen content and bonding configurations.

In the course of our studies on a-Si:H films, we have found that temperature can have a strong effect not only on the total bonded hydrogen concentration, but also on the way this hydrogen was bonded to silicon in the amorphous network. Furthermore, small temperature differences (in the less than 50 °C range) can have strong effects on hydrogen incorporation and on the resultant H-Si bonding configurations in the random structure, both during deposition (T_s) and in the in-chamber annealing treatment (T_{ICA}).

In most of the models on the Staebler-Wronski effect, the bonded hydrogen configurations appear to be very important in determining the number of sites at which stable silicon dangling bonds can be created. Investigation of the role of microstructure, hydrogen bonding and impurities on the stability of amorphous silicon materials deposited under different conditions continues, and will help us to have a better understanding of the issues involved in the degradation phenomena of this scientifically and technologically important material.

In summary, this study has shown the tremendous value to be obtained through annealing of hydrogenated amorphous silicon films in the presence of hydrogen immediately after film formation. The treatment is very sensitive to the annealing temperature used but, when carried out under the prescribed conditions, it allows independent control of the hydrogen concentration in the samples and of the quality of the bonding structures. It has been shown that the optimum hydrogen-silicon structure incorporates strongly bound, dispersed, monohydrides (SiH), as distinct from higher or polyhydrides, clusters of monohydrides, or inclusions of hydrogen molecules. The optimised structures result in a high quality semiconductor material which is also

resistant to oxygen contamination and should therefore be less susceptible to light-induced (Staebler-Wronsky) degradation, leading to more stable solar cells.

12.2 Commercial-type a-Si Solar Modules

The work described in chapter 11 of this thesis involved amorphous silicon solar module devices and their output degradation behaviour, as well as terrestrial spectral content measurements. It aimed at the investigation of temperature and spectral content effects on the seasonal performance trends particular to the amorphous silicon technology.

An experiment was carried out, where amorphous silicon solar cell devices were subjected to light-soaking under the same standard spectrum, at temperatures corresponding to extreme summer and winter operating temperatures. We have observed some degree of thermal annealing-recovery in the performance of a-Si solar modules exposed to summer temperatures as compared to winter temperatures when spectral effects were not present. However, the overall performance differences usually reported in the literature (where temperature, spectral and other possible contributory effects might be present) amount to more than twice the differences observed in our studies for temperature effects.

The seasonal spectral variations in solar radiation reaching the earth's surface were also monitored for typical days for the four seasons and have shown, on a qualitative basis, a marked shift in the wavelength region in which amorphous silicon solar cells respond.

The overall picture that emerges from this study is that temperature effects, *i.e.* the thermal annealing effect, even though present, is not the major contributor to the

seasonal changes in device performance widely reported in the literature for many different testing sites around the globe. Rather, spectral effects appear to have a much stronger influence in the seasonal effect in amorphous silicon. In this work we have been able to show, on a qualitative basis, that summer and winter spectra reaching Perth, Australia, are considerably different, especially in a spectral region close to the a-Si device response peak. Based on these results is that we strongly believe that seasonal spectral content shifts are the dominant cause for the seasonal effect in amorphous silicon photovoltaics.

Quantifying the contribution of the seasonal shifts in the solar spectral distribution at different sites has also scope for future work. It might also reveal the existence of further contributory causes to the seasonal effect not yet identified. Furthermore, it has been established [249] that the temperature at which amorphous silicon solar cells are first light-soaked, rather than the final operating temperature, is what will determine the stabilised output. The degradation pattern might thus be quite different for a-Si devices which are first exposed outdoors in summer or in winter at the same site, and also from warm to cold climate sites. Investigation of this aspect might shed more light into the effects of temperature in amorphous silicon solar cells.

References

1. Carlson, D.E. *Markets, Manufacturing and Technical Progress in Amorphous Silicon Photovoltaics in the U.S.* in *22nd IEEE Photov. Spec. Conf.* 1991. Las Vegas, USA: IEEE. p. 1207.

2. Chittick, R.C., J.H. Alexander, and H.F. Sterling, *The Preparation and Properties of Amorphous Silicon.* J. Electrochem. Soc., 1969, **116**(1), p. 77.

3. Carlson, D.E. and C.R. Wronski, *Amorphous Silicon Solar Cell.* Appl. Phys. Lett., 1976, **28**(11), p. 671.

4. Kuwano, Y., T. Imai, M. Ohnishi, and S. Nakano. *A Horizontal Cascade Type Amorphous Si Photovoltaic Cell Module.* in *14th IEEE Photov. Spec. Conf.* 1980. San Diego, USA: IEEE. p. 1408.

5. Ovshinsky, S.R., *News Release: ECD Receives $8 Million Photovoltaic Manufacturing Technology Cost-Sharing Contract from DOE*, Energy Conversion Devices, INC. 1992

6. Zanatta, A.R. and I. Chambouleyron. *Nitrogen Doping in a-Ge:H Films.* in *11th European Photovol. Solar Energy Conf.* 1992. Montreux, Switzerland: Harwood Academic Publishers. p. 629.

7. Guha, S., J. Yang, A. Banerjee, T. Glatfelder, K. Hoffman, and X. Xu. *High Efficiency Multijunction Amorphous Silicon Alloy-Based Solar Cells and Modules.* in *12th NREL PV Program Review Meeting*. 1993. Denver, USA: p. 1.

8. Carlson, D.E. and S. Wagner, *Amorphous Silicon Photovoltaic Systems,* in *Renewable Energy - Sources for Fuels and Electricity,* T.B. Johansson, *et al.*, Editors. 1993, Island Press: Washington, USA. p. 403.

9. Staebler, D.L. and C.R. Wronski, *Reversible Conductivity Changes in Discharge-Produced Amorphous Si.* Appl. Phys. Lett., 1977, **31**(4), p. 292.

10. Jones, G.J., H.N. Post, and M.G. Thomas. *Terrestrial Photovoltaic Power Technology.* in *19th IEEE Photov. Spec. Conf.* 1987. New Orleans, USA: IEEE. p. 25.

11. Ovshinsky, S.R., *The Material Basis of Efficiency and Stability in Amorphous Photovoltaics.* Sol. Energy Mater. and Solar Cells, 1994, **32**, p. 443.

12. Müller, G., G. Krötz, S. Kalbitzer, and G.N. Greaves, *Reversible and Irreversible Structural Changes in Amorphous Silicon.* Philos. Mag. B, 1994, **69**(2), p. 177.

13. Street, R.A., J. Kakalios, C.C. Tsai, and T.M. Hayes, *Thermal-Equilibrium Processes in Amorphous Silicon.* Phys. Rev. B, 1987, **35**(3), p. 1316.

14. Catalano, A., *Solar Cells Made of Amorphous and Microcrystalline Semiconductors,* in *Amorphous & Microcrystalline Semiconductor Devices - Optoelectronic Devices,* J. Kanicki, Editor. 1991, Artech House: Norwood, USA. p. 458.

15. Wronski, C.R., N. Maley, T.M. Peterson, J.R. Abelson, M.B. Bennett, P.K. Bhat, R. Biswas, V.L. Dalal, A.E. Delahoy, S.J. Fonash, C.M. Fortmann, S. Guha, W. Luft, T. McMahon, D. Redfield, P.C. Taylor, and S. Wagner. *Findings and Plans of the Stable Materials Advisory Research Team.* in *11th European Photovol. Solar Energy Conf.* 1992. Montreux, Switzerland: Harwood Academic Publishers. p. 72.

16. Wynveen, A., J. Fan, J. Kakalios, and J. Shinar. *Studies of Light Soaking Stability in rf Sputter-Deposited a-Si:H.* in *AIP Conference.* 1991. Denver, USA: American Institute of Physics. p. 241.

17. Jackson, W.B. and J. Kakalios, *Evidence for Hydrogen Motion in Annealing of Light-Induced Metastable Defects in Hydrogenated Amorphous Silicon.* Phys. Rev. B, 1988, **37**(2), p. 1020.

18. Carlson, D.E., *Hydrogenated Microvoids and Light-Induced Degradation of Amorphous Silicon Solar Cells.* Appl. Phys. A, 1986, **41**, p. 305.

19. Lin, W., H. Tsai, S. Lee, W. Sah, and W. Tzeng, *Identification of Infrared Absorption Peaks of Amorphous Silicon-Carbon Alloy by Thermal Annealing.* Appl. Phys. Lett., 1987, **51**(25), p. 2112.

20. Jennings, C. *PV Module Performance at PG&E.* in *20th IEEE Photov. Spec. Conf.* 1988. Las Vegas, USA: IEEE. p. 1225.

21. Chittick, R.C. and H.F. Sterling, *Glow Discharge Deposition of Amorphous Semiconductors: The Early Years,* in *Tetrahedrally Bonded Amorphous Semiconductors,* D. Adler and H. Fritzsche, Editors. 1985, Plenum Press: New York. p. 1.

22. Street, R.A., *Hydrogenated Amorphous Silicon.* First ed. Cambridge Solid States Science Series, eds. R.W. Cahn, E.A. Davis, and I.M. Ward. 1991, Cambridge, Great Britain: Cambridge University Press. 417.

23. Spear, W.E. *Localized States in Amorphous Semiconductors* in *Proc. Int. Conf. on Amorphous and Liquid Semiconductors.* 1974. London: Taylor and Francis. p. 1.

24. LeComber, P.G. and W.E. Spear, *Electronic Transport in Amorphous Silicon Films.* Phys. Rev. Lett., 1970, **25**(8), p. 509.

25. Spear, W.E., R.J. Loveland, and A. Al-Sharbaty, *The Temperature Dependence of Photoconductivity in a-Si.* J. Non-Cryst. Solids, 1974, **15**, p. 410.

26. Spear, W.E. and P.G. LeComber, *Substitutional Doping of Amorphous Silicon.* Solid State Commun., 1975, **17**, p. 1193.

27. Lewis, A.J., G.A.N. Connel, W. Paul, J.R. Pawlik, and R.J. Temkin. *Hydrogen Incorporation in Amorphous Germanium.* in *Tetrahedrally Bonded Amorphous Semiconductors.* 1974. Yorktown Heights, USA: American Institute of Physics. p. 27.

28. Fritzsche, H. *Localized States and Doping in Amorphous Semiconductors.* in *Proc. 7th Int. Conf. on Amorphous and Liquid Semiconductors.* 1977. Edinburgh: CICL. p. 3.

29. Zhao, S. and S. Hunklinger, *Optical Absorption and Density of States in Band Gap of Hydrogenated a-Si Films.* Sol. Energy Mater., 1982, **6**, p. 233.

30. Matsuda, A., M. Matsumura, S. Yamasaki, H. Yamamoto, T. Imura, H. Okushi, S. Iizima, and K. Tanaka, *Boron Doping of Hydrogenated Silicon Thin Films.* Jpn. J. Appl. Phys., 1981, **20**(3), p. L183.

31. Albers, M.L., *A Study of Deposition Conditions and Hydrogen Motion in R.F. Sputtered Hydrogenated Amorphous Silicon*1987, Iowa State University:

32. Cody, G. D., T. Tiedje, B. Abeles, T. D. Moustakas, B. Brooks, and Y. Goldstein, *Disorder and the Optical Absorption Edge of Hydrogenated Amorphous Silicon.* J. de Physique-Colloque C4, 1981, **10**(42), p. 301.

33. Smith, Z.E., *Amorphous Silicon for Solar Cell Applications: Defect Generation, Annealing, and Equilibrium*, PhD Thesis, Princeton University, 1987.

34. Street, R.A., *Hydrogen Chemical Potential and Structure of a-Si:H.* Phys. Rev. B, 1991, **43**(3), p. 2454.

35. Chopra, K.L. and D.S. R., *Thin Film Solar Cells.* 1983, New York, USA: Plenum Press. 607.

36. Weil, R., I. Abdulhalim, R. Beserman, M. Janai, and B. Pratt, *Comparison of Strain in Glow Discharge a-Si:F and a-Si:H.* J. Non-Cryst. Solids, 1985, **77 & 78**, p. 261.

37. Das, D., H. Shirai, J. Hanna, and I. Shimizu, *Narrow Band-Gap a-Si:H with Improved Minority Carrier-Transport Prepared by Chemical Annealing.* Jpn. J. Appl. Phys., 1991, **30**(2B), p. L239.

38. Williamson, D.L., A.H. Mahan, B.P. Nelson, and R.S. Crandal, *The Observation of Microvoids in Device Quality Hydrogenated Amorphous Silicon.* J. Non-Cryst. Solids, 1989, **114**, p. 226.

39. Uchida, Y., *DC Glow Discharge,* in *Semiconductors and Semimetals,* J.I. Pankove, Editor. 1984, Academic Press: New York. p. 41.

40. Hishikawa, Y., K. Ninomiya, E. Maruyama, S. Kuroda, A. Terakawa, K. Sayama, H. Tarui, M. Sasaki, S. Tsuda, and S. Nakano. *Approaches for Stable Multi-Junction a-Si Solar Cells.* in *1st World Conf. on Photovol. Energy Conversion.* 1994. Hawaii, USA, in press.

41. Roca i Cabarrocas, P., Z. Djebbour, J.P. Kleider, C. Longeaud, D. Mencaraglia, J. Sib, M.L. Thèye, G. Sardin, and J.P. Stoquert, *Hydrogen, Microstructure and Defect Density in Hydrogenated Amorphous Silicon.* J. Phys. I France, 1992, **2**, p. 1979.

42. Beldi, N., J. Sib, L. Chahed, T. Smail, T. Mohammed-Brahim, Z. Djebbour, J.P. Kleider, C. Longeaud, and D. Mencaraglia, *Optimisation of the Hydrogen Content in a-Si:H Deposited at High Rate by DC Magnetron Sputtering.* J. Non-Cryst. Solids, 1993, **164-166**, p. 309.

43. Zellama, K., J.H. von Bardeleben, V. Quiller, Y. Bouizem, P. Sládek, M.L. Theye, and P. Roca i Cabarrocas, *Experimental Study of the Disorder and Defects in Undoped a-Si:H as a Function of Annealing and Hydrogen Evolution.* J. Non-Cryst. Solids, 1993, **164-166**, p. 285.

44. Toneva, A., P. Danesh, L. Vassilev, and V. Kudoyarova, *Correlation Between Short-Range Order and Hydrogen Bonding in Hydrogenated Amorphous Silicon Obtained by Homogeneous Chemical Vapour Deposition.* Philos. Mag. B, 1994, **70**(6), p. 1187.

45. Morin, P., C. Godet, B. Equer, and P. Roca i Cabarrocas. *Metastability under High-Intensity Light of Device Quality He-Diluted, H_2-Diluted and "Standard" a-Si:H: Not All a-Si:H are Created Equal.* in *12th European Photovol. Solar Energy Conf.* 1994. Amsterdam, The Netherlands: Harwood Academic Publishers, in press.

46. Wagner, S., X. Xu, X.R. Li, D.S. Shen, M. Isomura, M. Bennett, A.E. Delahoy, X. Li, J.K. Arch, J. Nique, and S.J. Fonash. *Performance and Modeling of Amorphous Silicon Solar Cells Soaked at High Light Intensity.* in *22nd IEEE Photov. Spec. Conf.* 1991. Las Vegas, USA: IEEE. p. 1307.

47. Lucovsky, G., *Chemical Effects on the Frequencies of Si-H Vibrations in Amorphous Solids.* Solid State Commun., 1979, **29**, p. 571.

48. Paul, W., *Dissent from the Dihydride Model of the Vibrational Spectra of Amorphous Silicon-Hydrogen Alloys.* Solid State Commun., 1980, **34**, p. 283.

49. Socrates, G., *Infrared Characteristic Group Frequencies*. Second ed. ed. G. Socrates. 1994, Middlesex, UK: John Wiley & Sons. 250.

50. Zanzucchi, P.J., *The Vibrational Spectra of a-Si:H,* in *Semiconductors and Semimetals,* J.I. Pankove, Editor. 1984, Academic Press: New York. p. 113.

51. Freeman, E.C. and W. Paul, *Infrared Vibrational Spectra of RF-Sputtered Hydrogenated Amorphous Silicon.* Phys. Rev. B, 1978, **18**(8), p. 4287.

52. Brodsky, M.H., M. Cardona, and J.J. Cuomo, *Infrared and Raman Spectra of the Silicon-Hydrogen Bonds in Amorphous Silicon Prepared by Glow Discharge and Sputtering.* Phys. Rev. B, 1977, **16**(8), p. 3556.

53. John, P. and J.I.B. Wilson, *Structure and H Bonding in Device Quality a-Si:H,* in *Tetrahedrally Bonded Amorphous Semiconductors,* D. Adler and H. Fritzsche, Editors. 1985, Plenum Press: New York. p. 107.

54. Fritzsche, H., *Characterization of Glow-Discharge Deposited a-Si:H.* Sol. Energy Mater., 1980, **3**, p. 447.

55. Shanks, H., C.J. Fang, L. Ley, M. Cardona, F.J. Demond, and S. Kalbitzer, *Infrared Spectrum and Structure of Hydrogenated Amorphus Silicon.* phys. stat. sol. (b), 1980, **100**, p. 43.

56. Pollard, W.B. and G. Lucovsky, *Phonons in Polysilane Alloys.* Phys. Rev. B, 1982, **26**(6), p. 3172.

57. Wagner, H. and W. Beyer, *Reinterpretation of the Silicon-Hydrogen Stretch Frequencies in Amorphous Silicon.* Solid State Commun., 1983, **48**(7), p. 585.

58. Reimer, J.A., R.W. Vaughan, and J.C. Knights, *Proton-Magnetic-Resonance Studies of Microstructure in Plasma-Deposited Amorphous-Silicon-Hydrogen Films.* Phys. Rev. B, 1981, **24**(6), p. 3360.

59. Shanks, H.R., F.R. Jeffrey, and M.E. Lowry, *Bonding in Hydrogenated Amorphous Silicon.* Journal de Physique-Colloque C4, 1981,**10**(42), p. C4-773.

60. Street, R.A., *Hydrogen Diffusion in Amorphous Silicon.* Philos. Mag. B, 1987, **56**(3), p. 305.

61. Matsuda, A., S. Mashima, K. Hasezaki, A. Suzuki, and S. Yamasaki, *Preparation of Stable and Photoconductive Hydrogenated Amorphous Silicon from a Xe-Diluted Silane Plasma.* Appl. Phys. Lett., 1991, **58**(22), p. 2494.

62. Tsu, D.V. and G. Lucovsky, *Properties of the Si-H Bond-Stretching Absorption Band in a-Si:H Grown by Remote Plasma Enhanced CVD (RPECVD).* J. Non-Cryst. Solids, 1987, **97 & 98**, p. 839.

63. Zou, X., W. Zhang, H. Zhuang, and Z. Jin, *Ab Initio Calculation of Infrared and Raman Spectra for Hydrogenated Amorphous Silicon.* phys. stat. sol. (b), 1994, **184**, p. 553.

64. Lucovsky, G., R.J. Nemanich, and J.C. Knights, *Structural Interpretation of the Vibrational Spectra of a-Si:H Alloys.* Phys. Rev. B, 1979, **19**(4), p. 2064.

65. Isomura, M. and S. Wagner, *The Saturation of Light-Induced Defects in Hydrogenated Amorphous Silicon.* J. Non-Cryst. Solids, 1992, **141**, p. 204.

66. Abelson, J.R., *Plasma Deposition of Hydrogenated Amorphous Silicon: Studies of the Growth Surface.* Appl. Phys. A, 1993, **56**, p. 493.

67. Könenkamp, R. and E. Wild, *Relaxation Kinetics in Hydrogenated Amorphous Silicon.* Phys. Rev. B, 1990, **42**(9), p. 5887.

68. Park, H.R., J.Z. Liu, P. Roca i Cabarrocas, A. Maruyama, M. Isomura, S. Wagner, J.R. Abelson, and F. Finger. *Saturation Behavior of the Light-Induced Defect Density in Hydrogenated Amorphous Silicon*. in *21st IEEE Photov. Spec. Conf.* 1990. Florida, USA: IEEE. p. 1642.

69. Stutzmann, M., W.B. Jackson, and C.C. Tsai, *Light-Induced Metastable Defects in Hydrogenated Amorphous Silicon: A Systematic Study.* Phys. Rev. B, 1985, **32**(1), p. 23.

70. Caputo, D., G. de Cesare, F. Irrera, F. Palma, M.C. Rossi, G. Conte, G. Nobile, and G. Fameli, *A Systematic Investigation of the Role of Material Parameters in Metastability of Hydrogenated Amorphous Silicon.* J. Non-Cryst. Solids, 1994, **170**, p. 278.

71. Fortmann, C.M., R.M. Dawson, and C.R. Wronski, *Charge-Defect Equilibrium Description of Metastable Defect Concentrations.* J. Non-Cryst. Solids, 1991, **137 & 138**, p. 207.

72. Greim, O., J. Weber, Y. Baer, and U. Kroll, *Hydrogen Diffusion in a-Si:H Stimulated by Intense Illumination.* Phys. Rev. B, 1994, **50**(15), p. 10644.

73. Veprek, S., O. Ambacher, and M. Vanecek. *Photodegradation and Stability of a-Si Prepared at High Deposition Rates*. in *Mat. Res. Soc. Spring Meeting '92*. 1992. San Francisco, USA: Materials Research Society. p. 45.

74. Street, R.A., J. Kakalios, and T.M. Hayes, *Thermal Equilibration in Doped Amorphous Silicon.* Phys. Rev. B, 1986, **34**(4), p. 3030.

75. Smith, Z.E., S. Aljishi, D. Slobodin, V. Chu, S. Wagner, P.M. Lenahan, R.R. Arya, and M.S. Bennett, *Thermal-Equilibrium Defect Processes in Hydrogenated Amorphous Silicon.* Phys. Rev. Lett., 1986, **57**(19), p. 2450.

76. Füssel, W., R. Könenkamp, M. Schmidt, and H. Flietner. *Degradation Effects at Si/SiO_2 Interfaces Compared to those in a-Si.* in *11th European Photovol. Solar Energy Conf.* 1992. Montreux, Switzerland: Harwood Academic Publishers. p. 746.

77. Stutzmann, M., *Weak Bond-Dangling Bond Conversion in Amorphous Silicon.* Philos. Mag. B, 1987, **56**(1), p. 63.

78. Adler, D., *Defects in Amorphous Chalcogenides and Silicon.* Journal de Physique - Colloque C4, 1981, **10**(42), p. C4-3.

79. Redfield, D. and R.H. Bube, *Identification of Defects in Amorphous Silicon.* Phys. Rev. Lett., 1990, **65**(4), p. 464.

80. Stradins, P. and H. Fritzsche, *Photo-Induced Creation of Metastable Defects in a-Si:H at Low Temperatures and their Effect on the Photoconductivity.* Philos. Mag. B, 1994, **69**(1), p. 121.

81. Muramatsu, Y. and N. Yabumoto, *Hydrogen Abstraction from Hydrogenated Amorphous Silicon Surface by Hydrogen Atoms.* Appl. Phys. Lett., 1986, **49**(19), p. 1230.

82. Gallagher, A. and J. Scott, *Gas and Surface Processes Leading to Hydrogenated Amorphous Silicon Films.* Solar Cells, 1987, **21**, p. 147.

83. An, I., Y. Li, C.R. Wronski, and R.W. Collins. *Modification of a-Si:H by Thermally Generated Atomic Hydrogen: A Real Time Spectroscopic Ellipsometry Study of Si Bond Breaking.* in *Mat. Res. Soc. Spring Meeting '92.* 1992. San Francisco, USA: Materials Research Society. p. 27.

84. Hishikawa, Y., M. Isomura, S. Okamoto, H. Hashimoto, and S. Tsuda, *Effects of the i-Layer Properties and Impurity on the Performance of a-Si Solar Cells.* Sol. Energy Mater. and Solar Cells, 1994, **34**, p. 303.

85. Tanaka, H., N. Ishiguro, T. Miyashita, N. Yanagawa, M. Sadamoto, M. Koyama, Y. Ashida, and N. Fukuda, *Fabricating High Performance a-Si Solar Cells by Alternately Repeating Deposition and Hydrogen Plasma Treatment Method.* Sol. Energy Mater. and Solar Cells, 1994, **34**, p. 493.

86. Nishiwaki, H., M. Ohnishi, H. Haku, H. Dohjoh, K. Sayama, Y. Hishikawa, Y. Nakashima, K. Wakisaka, S. Tsuda, S. Nakano, Y. Kishi, and Y. Kuwano. *High Efficiency a-Si and a-Si:Alloy Solar Cells.* in *6th. Int. Photovoltaic Science and Engineering Conf.* 1992. New Delhi, India: Oxford & IBH Publishing, New Delhi. p. 469.

87. Okamoto, S., Y. Hishikawa, S. Tsuge, M. Sasaki, K. Ninomiya, M. Nishikuni, and S. Tsuda, *High-Quality Wide-Gap Hydrogenated Amorphous Silicon Fabricated Using Hydrogen Plasma Post-Treatment.* Jpn. J. Appl. Phys., 1994, **33**(1-4A), p. 1773.

88. Hishikawa, Y., S. Tsuge, N. Nakamura, S. Tsuda, S. Nakano, and Y. Kuwano, *Device-Quality Wide-Gap Hydrogenated Amorphous Silicon Films Deposited by Plasma Chemical Vapor Deposition at Low Substrate Temperatures.* J. Appl. Phys., 1991, **69**(1), p. 508.

89. Pankove, J.I., M.A. Lampert, and M.L. Tarng, *Hydrogenation and Dehydrogenation of Amorphous and Crystalline Silicon.* Appl. Phys. Lett, 1978, **32**(7), p. 439.

90. Kar, S., J.I. Pankove, and Y.S. Tsuo, *Remote Plasma Hydrogenation of Ion Beam Amorphized Silicon.* Appl. Phys. Lett, 1991, **59**(6), p. 718.

91. Nakamura, M., T. Ohno, K. Miyata, N. Konishi, and T. Suzuki, *Hydrogenation Kinetics and Defect Termination of Post-Plasma-Treated Chemical-Vapor-Deposited Amorphous Silicon Film.* J. Appl. Phys., 1989, **65**(8), p. 3061.

92. Conde, J.P., V. Chu, S. Tanaka, D.S. Shen, and S. Wagner. *Amorphous Silicon-Germanium Alloy Multilayers for Solar Cells.* in *20th IEEE Photov. Spec. Conf.* 1988. Las Vegas, USA: IEEE. p. 235.

93. Okamoto, H., Y. Nitta, T. Yamaguchi, and Y. Hamakawa, *Device Physics and Design of a-Si ITO/p-i-n Heteroface Solar Cells.* Solar Energy Materials, 1980, **2**, p. 313.

94. Hamakawa, Y., *Present Status of Solar Photovoltaic R&D Projects in Japan.* Surface Sci., 1979, **86**, p. 444.

95. Hamakawa, Y., *Recent Advances in Amorphous Silicon Solar Cells.* Solar Energy Materials, 1982, **8**, p. 101.

96. Carlson, D.E., *Amorphous Silicon Solar Cells.* IEEE Trans. on Electron Devices, 1977, **ED-24**(4), p. 449.

97. Okamoto, H., Y. Nitta, T. Adachi, and Y. Hamakawa, *Glow Discharge Produced Amorphous Silicon Solar Cells.* Surf. Sci., 1979, **86**, p. 486.

98. Uchida, Y., *Amorphous Silicon Solar Cells,* in *Amorphous Semiconductors,* Y. Hamakawa, Editor. 1984, North-Holland Publishing Company: Tokyo, Japan. p. 179.

99. Tabuchi, K., W.W. Wenas, M. Yoshino, A. Yamada, M. Konagai, and K. Takahashi. *Optimization of ZnO Films for Amorphous Silicon Solar Cells.* in *11th European Photovol. Solar Energy Conf.* 1992. Montreux, Switzerland: Harwood Academic Publishers. p. 529.

100. Hamakawa, Y. and H. Okamoto, *Amorphous Silicon Solar Cells,* in *Advances in Solar Energy - An Annual Review of Research and Development,* K.W. Böer, Editor. 1989, Plenum Press: New York, USA. p. 1.

101. Street, R.A., *Physics of a-Si:H p-i-n Devices.* J. Non-Cryst. Solids, 1993, **164-166**, p. 643.

102. Hamakawa, Y. and H. Okamoto, *Device Physics and Optimum Design of the Amorphous Silicon Solar Cells,* in *Amorphous Semiconductors - Technologies and Devices,* Y. Hamakawa, Editor. 1983, North-Holland Publishing Company: Tokyo, Japan. p. 182.

103. Fiorini, P., A. Mittiga, I. Chambouleyron, and F. Evangelisti. *Optimum Band Gap for Amorphous Silicon Based Solar Cells.* in *21st IEEE Photov. Spec. Conf.* 1990. Florida, USA: IEEE. p. 1526.

104. Dalal, V., R. Knox, and B. Moradi, *Measurements of Urbach Edge and Midgap States in Amorphous Silicon p-i-n Devices.* Sol. Energy Mater. and Solar Cells, 1993, **31**, p. 349.

105. Kuwano, Y., M. Ohnishi, H. Nishiwaki, S. Tsuda, T. Fukatsu, K. Enomoto, Y. Nakashima, and H. Tarui. *Multi-Gap Amorphous Si Solar Cells Prepared by the*

Consecutive, Separated Reaction Chamber Method. in *16th IEEE Photov. Spec. Conf.* 1982. New York, USA: IEEE. p. 1338.

106. Carlson, D.E., *Recent Developments in Amorphous Silicon Solar Cells.* Solar Energy Materials, 1980, **3**, p. 503.

107. Haruki, H., Y. Uchida, H. Sakai, and M. Nishiura, *Analysis of Conversion Efficiency of Large Area a-Si:H Solar Cells.* Jpn. J. Appl. Phys. (Suppl.), 1982, **21-1**, p. 283.

108. Yukimoto, Y., *Multi-Layered and Stacked Solar Cells,* in *Amorphous Semiconductor Technologies and Devices,* Y. Hamakawa, Editor. 1983, North-Holland Publishing Co.: Tokyo, Japan. p. 228.

109. Bennett, M., J. Newton, C. Poplawski, and K. Rajan. *Impact of Defects on the Performance of High Efficiency 12" x 13" a-Si Based Triple Junction Modules.* in *22nd IEEE Photov. Spec. Conf.* 1991. Las Vegas, USA: IEEE. p. 1281.

110. Arya, R.R., A. Catalano, M. Bennett, J. Newton, B. Fieselman, L. Yang, M. Li, and R. D'Aiello. *Triple Junction, Triple Bandgap, a-Si:H Alloy Based Devices for Stable Performance.* in *11th European Photovol. Solar Energy Conf.* 1992. Montreux, Switzerland: Harwood Academic Publishers. p. 199.

111. Izu, M. and S. Ovshinsky, *Roll-to-Roll Plasma Deposition Machine for the Production of Tandem Amorphous Silicon Alloy Solar Cells.* Thin Solid Films, 1984, **119**, p. 55.

112. Carts, Y.A., *Amorphous Solar Cells Last Longer, are More Efficient.* Laser Focus World, 1994, **30**(4), p. 20.

113. Green, M.A., *Solar Cells - Operating Principles, Technology, and System Applications*. First ed. Prentice-Hall Series in Solid State Physical Electronics, ed. N. Holonyak Jr. 1982, Sydney, Australia: Prentice-Hall, Inc. 274.

114. Möller, H.J., *Semiconductors for Solar Cells*. First ed. The Artech House Optoelectronics Library, eds. B. Culshaw, A. Rogers, andH. Taylor. 1993, Norwood, USA: Artech House, Inc. 343.

115. Nann, S. and K. Emery, *Spectral Effects on PV-Device Rating.* Sol. Energy Mater. and Solar Cells, 1992, **27**, p. 189.

116. Duffie, J.A. and W.A. Beckman, *Solar Engineering of Thermal Processes.* Second ed. 1991, Madison, USA: John Wiley & Sons, Inc. 919.

117. Jennings, C. *Outdoor Versus Rated Photovoltaic Module Performance.* in *19th IEEE Photov. Spec. Conf.* 1987. New Orleans, USA: IEEE. p. 1257.

118. Dalal, V.L. and G. Baldwin. *Design Considerations for Stable Amorphous Silicon and Silicon-Germanium Solar Cells.* in *22nd IEEE Photov. Spec. Conf.* 1991. Las Vegas, USA: IEEE. p. 1363.

119. Camani, M., D. Chianese, and S. Rezzonico. *Long-Term Behaviour of Monocrystalline and of Amorphous Modules in the Medium-Size Grid Connected PV Plant Tiso.* in *11th European Photovol. Solar Energy Conf.* 1992. Montreux, Switzerland: Harwood Academic Publishers. p. 1235.

120. Sakai, H., *Status of Amorphous Silicon Solar Cell Technologies in Japan.* Sol. Energy Mater. and Solar Cells, 1994, **34**, p. 9.

121. Takahisa, K., K. Nakamura, S. Nakazawa, Y. Sugiyama, J. Nose, S. Igari, and T. Hiruma, *Long-Term Reliability of Amorphous Silicon Solar Cells.* Sol. Energy Mater. and Solar Cells, 1994, **34**, p. 485.

122. Hata, N. and S. Wagner, *A Comprehensive Defect Model for Amorphous Silicon.* J. Appl. Phys., 1992, **72**(7), p. 2857.

123. Costa, H.S., P. Ragot, and D. Desmettre, *Evaluation of Amorphous Silicon Module Outdoor Performance.* Sol. Energy Mater. and Solar Cells, 1992, **27**, p. 59.

124. Ragot, P., H.S. Costa, and D. Desmettre. *Higher Efficiency New Generation Amorphous Silicon PV Modules*. in *11th European Photovol. Solar Energy Conf.* 1992. Montreux, Switzerland: Harwood Academic Publishers. p. 553.

125. Jennings, C., C. Whitaker, and D. Sumner, *Thin Film PV Performance at PG&E.* Solar Cells, 1990, **28**, p. 145.

126. Mrig, L. and W.B. Berry. *Stability, Performance and Trend Modeling of Amorphous Silicon Photovoltaic Modules*. in *Mat. Res. Soc. Symp. Proc.* 1989. Materials Research Society. p. 453.

127. Hata, N. and A. Matsuda, *Difference in Light-Induced Annealing Behavior of Deposition- and Light-Induced Defects in Hydrogenated Amorphous Silicon.* Appl. Phys. Lett., 1993, **63**(14), p. 1948.

128. Fujikake, S., H. Ota, M. Ohsawa, T. Hama, Y. Ichikawa, and H. Sakai, *Light-Induced Recovery of a-Si Solar Cells.* Sol. Energy Mater. and Solar Cells, 1994, **34**, p. 449.

129. de O. Graeff, C.F., R. Buhleier, and M. Stutzmann, *Light-Induced Annealing of Metastable Defects in Hydrogenated Amorphous Silicon.* Appl. Phys. Lett., 1993, **62**(23), p. 3001.

130. Hata, N. and A. Matsuda, *Difference Between Deposition- and Light-Induced Defects in a-Si:H Studied by Light-Induced Annealing Experiments.* J. Non-Cryst. Solids, 1993, **164-166**, p. 187.

131. Moustakas, T.D., *Sputtering,* in *Semiconductors and Semimetals,* J.I. Pankove, Editor. 1984, Academic Press: New York. p. 55.

132. Schneider, U., J. Sopka, B. Schröder, and H. Oechsner. *Some Aspects on the Saturation Level and the Origin of Metastable Defects in a-Si:H*. in *20th IEEE Photov. Spec. Conf.* 1988. Las Vegas, USA: IEEE. p. 346.

133. Matsuda, A. and N. Hata, *Deposition Process and Growth Mechanism,* in *Glow-Discharge Hydrogenated Amorphous Silicon,* K. Tanaka, Editor. 1989, KTK Scientific Publishers: Tokyo, Japan. p. 9.

134. Abelson, J.R., L. Mandrell, and J.R. Doyle, *Hydrogen Release Kinetics During Reactive Magnetron Sputter Deposition of a-Si:H: An Isotope Labeling Study.* J. Appl. Phys., 1994, **76**(3), p. 1856.

135. Beldi, N., J. Sib, L. Chahed, T. Smail, T. Mohammed-Brahim, Z. Djebbour, J. P. Kleider, C. Longeaud, D. Mencaraglia, *Optimisation of the Hydrogen Content in a-Si:H Deposited at High Rate by DC Magnetron Sputtering*. J. Non-Cryst. Solids, 1991, **164-166**, p. 309.

136. Ababou, N., N. Beldi, and T. M-Brahim, *Hydrogen Analysis in Hydrogenated Amorphous Silicon Thin Films Produced by DC Reactive Magnetron Sputtering.* Materials Chemistry and Physics, 1993, **33**, p. 221.

137. Roca i Cabarrocas, P., *Towards High Deposition Rates of a-Si:H: The Limiting Factors.* J. Non-Cryst. Solids, 1993, **164-166**, p. 37.

138. Sun, Y., R. Nishitani, and T. Miyasato, *Study of Sputtering Mechanism of Silicon with Hydrogen Plasma Controlled by Magnetic Field.* Jpn. J. Appl. Phys., 1994, **33**, p. L263.

139. Stutzmann, M., D.K. Biegelsen, and R.A. Street, *Detailed Investigation of Doping in Hydrogenated Amorphous Silicon and Germanium.* Phys. Rev. B, 1987, **35**(11), p. 5666.

140. Nebel, C.E., R.A. Street, W.B. Jackson, and N.M. Johnson, *Kinetics of Metastability in Doped Hydrogenated Amorphous Silicon.* Philos. Mag. B, 1994, **69**(2), p. 291.

141. Griffiths, P.R. and J.A. de Haseth, *Fourier Transform Infrared Spectrometry.* first ed. Chemical Analysis, eds. P.J. Elving, J.D. Winefordner, andI.M. Kolthoff. 1986, New York, USA: John Wiley & Sons, Inc. 656.

142. Michelson, A.A., *Visibility of Interference-Fringes in the Focus of a Telescope.* Philos. Mag., 1891, **31**(5), p. 256.

143. Fang, C.J., K.J. Gruntz, L. Ley, M. Cardona, F.J. Demond, G. Müller, and S. Kalbitzer, *The Hydrogen Content of a-Ge:H and a-Si:H as Determined by IR Spectroscopy, Gas Evolution and Nuclear Reaction Techniques.* J. Non-Cryst. Solids, 1980, **35 & 36**, p. 255.

144. Cardona, M., *Vibrational Spectra of Hydrogen in Silicon and Germanium.* Phys. Status Solidi (b), 1983, **118**, p. 463.

145. Langford, A.A., M.L. Fleet, B.P. Nelson, W.A. Lanford, and N. Maley, *Infrared Absorption Strenght and Hydrogen Content of Hydrogenated Amorphous Silicon.* Phys. Rev. B, 1992, **45**(23), p. 13367.

146. Bhattacharya, E. and A.H. Mahan, *Microstructure and The Light-Induced Metastability in Hydrogenated Amorphous Silicon.* Appl. Phys. Lett., 1988, **52**(19), p. 1587.

147. Maley, N. and I. Szafranek. *Systematic Errors in the Analysis of the Infrared Transmission Data of Hydrogenated Amorphous Silicon.* in *Mat. Res. Soc. Symp. Proc.* 1990. Materials Research Society. p. 663.

148. Maley, N., *Critical Investigation of the Infrared-Transmission-Data Analysis of Hydrogenated Amorphous Silicon Alloys.* Phys. Rev. B, 1992, **46**(4), p. 2078.

149. Hasegawa, S. and Y. Imai, *Thickness Dependence of Electrical and Optical Properties and ESR in Undoped a-Si:H.* Philos. Mag. B, 1982, **46**(3), p. 239.

150. Maley, N., *Interference-Free Determination of the Absorption Coefficient of Amorphous Silicon Thin Films.* Jpn. J. Appl. Phys., 1992, **31**(3), p. 768.

151. Earwaker, L.G., *Rutherford Backscattering and Nuclear Reaction Analysis.* Vacuum, 1994, **45**(6/7), p. 783.

152. See for example, Nucl. Instrum. Methods, 1978, **149**.

153. Doyle, B.L. and P.S. Peercy, *Technique for Profiling ^{1}H with 2.5 MeV Van de Graaff Accelerators.* Appl. Phys. Lett., 1979, **34**(11), p. 811.

154. Hoffman, A., D.A. Cohen, A. Crial, D. Haneman, and H. Jafr. *Hydrogen Measurements by Elastic Recoil Analysis.* in *NTA Conference*. 1991. p. 114.

155. Changgeng, L., W. Yongqiang, Y. Shengsheng, J. Hui, and Z. Zhihao, *Study on the Hydrogen Depth Profiles in Amorphous Silicon Films by Elastic Recoil Detection.* Vacuum, 1993, **4**(11/12), p. 1193.

156. L'Ecuyer, J., C. Brassard, C. Cardinal, J. Chabbal, L. Deschênes, B. Terreault, J.G. Martel, and R. St.-Jacques, *An Accurate and Sensitive Method for the Determination of the Depth Distribution of Light Elements in Heavy Materials.* J. Appl. Phys., 1976, **47**(1), p. 381.

157. Deconnick, G., *Introduction to Radioanalytical Physics*. Nuclear Methods Monographs 1, 1978, Budapest, Hungary: Elsevier Science. 242.

158. Turos, A. and O. Meyer, *Depth Profiling of Hydrogen by Detection of Recoiled Protons.* Nucl. Instrum. Methods in Phys. Res. B, 1984, **4**, p. 92.

159. Dytlewski, N., *Private Communication,* 1995.

160. Kótai, E., *Computer Methods for Analysis and Simulation of RBS and ERDA Spectra.* Nucl. Instrum. Methods in Phys. Res. B, 1994. **85**, p. 588.

161. Doolittle, L.R., *Algorithms for the Rapid Simulation of Rutherford Backscattering Spectra.* Nucl. Instrum. Methods in Phys. Res. B, 1985, **9**, p. 344.

162. Blanpain, B., P. Revesz, L.R. Doolittle, K.H. Purser, and J.W. Mayer, *The Use of the 3.05 MeV Oxygen Resonance for ^{4}He Backscattering Near-Surface Analysis of Oxygen-Containing High Z Compounds.* Nucl. Instrum. Methods in Phys. Res. B, 1988, **34**, p. 459.

163. Vizkelethy, G., *Simulation and Evaluation of Nuclear Reaction Spectra.* Nucl. Instrum. Methods in Phys. Res. B, 1990, **45**, p. 1.

164. Saarilahti, J. and E. Rauhala, *Interactive Personal-Computer Data Analysis of Ion Backscattering Spectra.* Nucl. Instrum. Methods in Phys. Res. B, 1992, **64**, p. 734.

165. Kelley, J. and C.P. Comeau, *Light Measurement: Many Ways.* Photonics Spectra, 1983. **March 1983**: p. 52.

166. Langford, A.A., M.L. Fleet, and A.H. Mahan, *Correction for Multiple Reflections in Infrared Spectra of Amorphous Silicon.* Solar Cells, 1989, **27**, p. 373.

167. Stutzmann, M., *Role of Mechanical Stress in the Light-Induced Degradation of Hydrogenated Amorphous Silicon.* Appl. Phys. Lett., 1985, **47**(1), p. 21.

168. Paduschek, P., C. Höpfl, and H. Mithlehner, *Hydrogen-Related Mechanical Stress in Amorphous Silicon and Plasma-Deposited Silicon Nitride.* Thin Solid Films, 1983, **110**, p. 291.

169. Yang, S. and J.R. Abelson, *Amorphous Silicon Alloys on c-Si: Influence of Substrate Cleaning and Ion Bombardment on Film Adhesion and Microstructure.* J. Vac. Sci. Technol. A, 1993, **11**(4), p. 1327.

170. Tsuo, Y.S., E.B. Smith, X.J. Deng, Y. Xu, and S.K. Deb, *Ion-Beam-Hydrogenation of Amorphous Silicon.* Solar Cells, 1988, **24**, p. 249.

171. Rüther, R. and J. Livingstone. *In-Chamber Annealing of Amorphous Silicon Thin Films for Solar Cell Fabrication.* in *30th Annual Conf. of the Australian and New Zealand Solar Energy Society.* 1992. Darwin, Australia: ANZSES. p. 301.

172. Rüther, R. and J. Livingstone, *The Role of Substrate Temperature and In-Chamber Annealing in H-Si Bonding Configurations in Sputtered a-Si:H.* Thin Solid Films, 1993, **226**(1), p. 59.

173. Tomellini, S.A., D.D. Saperstein, J.M. Stevenson, G.M. Smith, H.B. Woodruff, and P.F. Seelig, *Automated Interpretation of Infrared Spectra with an Instrument Based Minicomputer.* Anal. Chem., 1981, **53**, p. 2367.

174. Esen, R. and H. Kavak, *Spectrum Digitizing and Conditioning for the Infrared Library of Amorphous Silicon Alloys.* J. Chem. Inf. Comput. Sci., 1994, **34**, p. 1158.

175. BioRad, *Bandfit - User Software notes* 1990, BioRad - Digilab Division.

176. Amato, G., G. Della Mea, F. Fizzotti, C. Manfredotti, R. Marchisio, and A. Paccagnella, *Hydrogen Bonding in Amorphous Silicon with Use of Low Pressure Chemical Vapor Deposition Technique.* Phys. Rev. B, 1991, **43**(8), p. 6627.

177. Kratos/Schoeffel, *Kratos/Schoeffel Solar Simulator System Manual,* 1979.

178. Wronski, C.R. *Instabilities in a-Si:H Solar Cells: Materials and Device Issues.* in *21st IEEE Photov. Spec. Conf.* 1990. Florida, USA: IEEE. p. 1487.

179. Pinarbasi, M., N. Maley, A. Myers, and J.R. Abelson, *Hydrogenated Amorphous Silicon Films Deposited by Reactive Sputtering: The Electronic Properties, Hydrogen Bonding and Microstructure.* Thin Solid Films, 1989, **171**, p. 217.

180. von Roedern, B. *Can We Improve the Stability of Amorphous Silicon Based Solar Cells Through the Use of "More Stable" i-Layer Materials?* in *10th European Photovol. Solar Energy Conf.* 1991. Lisbon, Portugal: Kluwer Academic Publishers. p. 1197.

181. Polyakov, O.V. and A.M. Badalian, *Defects in a-Si:H Related to Dangling Bonds.* phys. stat. sol. (b), 1994, **185**, p. K1.

182. Wakagi, M., K. Ogata, and A. Nakano, *Structural Study of a-Si and a-Si:H Films by EXAFS and Raman-Scattering Spectroscopy.* Phys. Rev. B, 1994, **50**(15), p. 10666.

183. Yang, Y.H., M. Katiyar, G.F. Feng, N. Maley, and J.R. Abelson, *Subsurface Hydrogenated Amorphous Silicon to μc-Hydrogenated Silicon Transformation During Magnetron Sputter Deposition Determined by Spectroscopic Ellipsometry.* Appl. Phys. Lett., 1994, **65**(14), p. 1769.

184. Liang, Y.H., N. Maley, and J.R. Abelson, *The Improved Stability of Hydrogenated Amorphous Silicon Films Grown by Reactive Magnetron Sputtering at High Substrate Temperature.* J. Appl. Phys., 1994, **75**(7), p. 3704.

185. Talukder, G., J.C.L. Cornish, P. Jennings, G.T. Hefter, B.W. Clare, and J. Livingstone, *Effects of Annealing on Infrared and Thermal Effusion Spectra of Sputtered a-Si:H Alloys.* J. Appl. Phys., 1992, **71**(1), p. 403.

186. Demichelis, F., C.F. Pirri, E. Tresso, T. Stapinski, L. Boarino, and P. Rava. *A Comparison Between Fluorinated and Hydrogenated Amorphous Silicon Carbide Prepared by Reactive Sputtering.* in *10th European Photovol. Solar Energy Conf.* 1991. Lisbon, Portugal: Kluwer Academic Publishers. p. 121.

187. Talukder, G., *A Study of Sputtered a-Si:H by Thermal Effusion and Infrared Spectroscopy*, PhD Thesis, Murdoch University, 1992.

188. Jeffrey, F.R., H.R. Shanks, and G.C. Danielson, *The Effect of Hydrogen Content on the Properties of Reatively Sputtered Amorphous Si-H.* J. Non-Cryst. Solids, 1980, **35 & 36**, p. 261.

189. Amaral, A., L. Rodrigues, L. Guimarães, R. Martins, D. Mencaraglia, Z. Djebbour, J.P. Kleider, and C. Longeaud. *Influence of the RF Power Density on the Electrical Properties of Glow-Discharge Amorphous Silicon.* in *10th European Photovol. Solar Energy Conf.* 1991. Lisbon, Portugal: Kluwer Academic Publishers. p. 368.

190. Ganguly, G., H. Nishio, and A. Matsuda, *Reduction of the Defect Density in Hydrogenated Amorphous Silicon by Thermally Energized Growth Precursors.* Appl. Phys. Lett, 1994, **64**(26), p. 3581.

191. Cheah, S.H., *Amorphous Silicon Devices*, MSc Thesis, The University of Western Australia, 1987.

192. Basrour, S., J.C. Bruyere, E. Bustarret, C. Godet, J.P. Stoquert, and G. Sardin. *Study of Hydrogen Configurations by Infrared Spectroscopy, Effusion and Nuclear Analisys in a-$Si_xGe_yH_z$ alloys.* in *9th European Photovol. Solar Energy Conf.* 1989. Freiburg, Germany: Kluwer Academic Publishers. p. 1010.

193. Sardin, G. and J.L. Morenza, *Unifying Model of Thermal and Light-Induced Degradations of a-Si:H.* Sol. Energy Mater., 1990, **20**, p. 189.

194. Xu, X., A. Morimoto, M. Kumeda, and T. Shimizu, *Thermal Equilibrium Process in Undoped Hydrogenated Amorphous Silicon and Silicon-Carbon Alloy Films.* Appl. Phys. Lett., 1988, **52**(8), p. 622.

195. Santos, P.V. and W.B. Jackson, *Trap-Limited Hydrogen Diffusion in a-Si:H.* Phys. Rev. B, 1992, **46**(8), p. 4595.

196. Lucovsky, G., B.N. Davidson, G.N. Parsons, and C. Wang, *Incorporation of Polyhydride Bonding Groups Into Thin Films of Hydrogenated Amorphous Silicon (a-Si:H).* J. Non-Cryst. Solids, 1989, **114**, p. 154.

197. Shirai, H., D. Das, J. Hanna, and I. Shimizu, *A Novel Preparation Technique for Preparing Hydrogenated Amorphous Silicon with a more Rigid and Stable Si Network.* Appl. Phys. Lett., 1991, **59**(9), p. 1096.

198. Shirai, H., J. Hanna, and I. Shimizu. *Very Stable a-Si:H Prepared by "Chemical Annealing".* in *AIP Conference*. 1991. Denver, USA: American Institute of Physics. p. 203.

199. Albers, M.L., J. Shinar, and H.R. Shanks, *A Study of Plasma-Film Interactions in He/H_2, Ar/H_2, and Xe/H_2 Radio Frequency Sputtered a-Si:H.* J. Appl. Phys., 1988, **64**(4), p. 1859.

200. Street, R.A., *Hydrogen Diffusion and Thermal Equilibrium of Electronic States in a-Si:H,* in *Amorphous Silicon Semiconductors - Pure and Hydrogenated,* A. Maclam, *et al.*, Editors. 1987, Material Research Society: Pittsburgh, USA. p. 13.

201. Street, R.A. and K. Winer, *Defect Equilibria in Undoped a-Si:H.* Phys. Rev. B, 1989, **40**(9), p. 6243.

202. Gleason, K.K., M.A. Petrich, and J.A. Reimer, *Hydrogen Microstructure in Amorphous Hydrogenated Silicon.* Phys. Rev. B, 1987, **36**(6), p. 3259.

203. Nevin, W.A., H. Yamagishi, and Y. Tawada, *Improvement of the Stability of Hydrogenated Amorphous Silicon by Hydrogen Plasma Treatment.* Jpn. J. Appl. Phys., 1994, **33**(1-9A), p. 4829.

204. Asensi, J.M., J. Bertomeu, J. Andreu, J. Puigdollers, and J.L. Morenza. *Influence of Deposition Temperature on the Stability of a-Si:H Solar Cells.* in *10th European Photovol. Solar Energy Conf.* 1991. Lisbon, Portugal: Kluwer Academic Publishers. p. 151.

205. Roch, C. and J.C. Delgado, *Correlation Between Hydrogen Thermal Evolution and Morphology in Glow Discharge Deposited a-Si:H Films.* Thin Solid Films, 1992, **221**, p. 17.

206. Biswas, R., I. Kwon, A.M. Bouchard, C.M. Soukoulis, and G.S. Grest, *Intense Small Wave-Vector Scattering from Voids in Amorphous Silicon: A Theoretical Simulation.* Phys. Rev. B, 1989, **39**(8), p. 5101.

207. Mahan, A.H., J. Carapella, B.P. Nelson, and R.S. Crandall, *Deposition of Device Quality, Low H Content Amorphous Silicon.* J. Appl. Phys., 1991, **69**(9), p. 6728.

208. Boyce, J.B., M. Stutzmann, and S.E. Ready, *Molecular Hydrogen in Amorphous Si: NMR Studies.* J. Non-Cryst. Solids, 1985, **77 & 78**, p. 265.

209. Das, S.R., S. Charbonneau, D.F. Williams, J.B. Webb, J.R. MacDonald, D.R. Polk, S. Zukotynski, and J. Perz, *The Relation Between Microstruscture and Hydrogen Content and Evolution for Hydrogenated Amorphous Silicon films Prepared by Magnetron Sputtering.* Can. J. Phys., 1985, **63**, p. 852.

210. Windischmann, H., *Intrinsic Stress in Sputter-Deposited Thin Films.* Critical Reviews in Solid State and Materials Sciences, 1992, **17**(6), p. 547.

211. Biegelsen, D.K., R.A. Street, C.C. Tsai, and J.C. Knights, *Hydrogen Evolution and Defect Creation in Amorphous Si:H Alloys.* Phys. Rev. B, 1979, **20**(12), p. 4839.

212. Wronski, C.R. and N. Maley. *Research on the Stability of a-Si:H Based Solar Cells by SMART.* in *AIP Conference.* 1991. Denver, USA: American Institute of Physics. p. 11.

213. Street, R.A., *The Origin of Metastable States in a-Si:H.* Solar Cells, 1988, **24**, p. 211.

214. Roca i Cabarrocas, P., J. Merten, C. Godet, B. Equer, Y. Bouizem, P. Sládek, M.L. Thèye, D. Mencaraglia, Z. Djebbour, J. Sib, J.P. Kleider, C. Longeaud, R. Meaudre, and M. Meaudre. *Metastability Studies in a-Si:H Films Deposited from Pure*

Silane and Silane-Helium Mixtures. in *11th European Photovol. Solar Energy Conf.* 1992. Montreux, Switzerland: Harwood Academic Publishers. p. 184.

215. Tang, X., J. Weber, Y. Baer, and F. Finger, *Dispersive Diffusion of Hydrogen in a-Si:H : Influence of the Film Deposition Temperature.* Phys. Rev. B, 1990, **41**(11), p. 7945.

216. Tang, X., J. Weber, Y. Baer, and F. Finger, *Hydrogen Diffusion in a-Si:H.* Solid State Commun., 1990, **74**(3), p. 171.

217. Shinar, J., H. Jia, R. Shinar, Y. Chen, and D.L. Williamson, *Microvoid, Si, H, and Al Dynamics in a-Si:H/Al_2O_3/Al Structures: A Small-Angle X-Ray-Scattering and Infrared-Absorption Study.* Phys. Rev. B, 1994, **50**(11), p. 7358.

218. Yang, Y., J. Shin, R. Hsieh, and J. Gan, *Film Thickness Reduction of Thermally Annealed Hydrogenated Amorphous Silicon Prepared with Plasma-Enhanced Chemical Vapor Deposition.* Appl. Phys. Lett., 1994, **64**(12), p. 1567.

219. Yi, J., R. Wallace, J. Palmer, and W.A. Anderson, *Thin Film Amorphous and Microcrystalline Si for Solar Cells.* Sol. Energy Mater. and Solar Cells, 1994, **33**, p. 145.

220. Heintze, M., K. Eberhardt, O. Tress, and G.H. Bauer, *Infrared Spectroscopy During Hydrogen Effusion of a-Si:H, a-SiGe:H and a-Ge:H.* J. Non-Cryst. Solids, 1991, **137 & 138**, p. 49.

221. Talukder, G., J.C.L. Cornish, P. Jennings, G.T. Hefter, M. Jain, J.L. Robins, and J. Livingstone, *Annealing Effects on Hydrogen, Oxygen and Nitrogen Bonding in Sputtered a-Si Network.* Thin Solid Films, 1993, **223**, p. 167.

222. D'Aiello, R.V., E.N. Twesme, and D.A. Fagnan. *Performance of Solarex/Philadelphia Electric Co. Amorphous Silicon PV Test Site*. in *20th IEEE Photov. Spec. Conf.* 1988. Las Vegas, USA: IEEE. p. 1092.

223. Pratt, R.G. and J. Burdick. *Performance of a 4kW Amorphous Silicon Alloy Photovoltaic Array at Oakland Community College, Auburn Hills, Michigan*. in *20th IEEE Photov. Spec. Conf.* 1988. Las Vegas, USA: IEEE. p. 1272.

224. Mrig, L., S. Rummel, D. Waddington, and R. DeBlasio. *Outdoor Stability Performance of Single and Tandem Amorphous Silicon Modules*. in *20th IEEE Photov. Spec. Conf.* 1988. Las Vegas, USA: IEEE. p. 1221.

225. Takigawa, K., H. Kobayashi, and Y. Takeda. *A Field Evaluation of Power Efficiency Degradation on Amorphous PV Modules*. in *4th International Photovoltaic Science & Engineering Conference*. 1989. Sydney, Australia: p. 777.

226. Jennings, C. *Thin Film Silicon Photovoltaic Module Performance Assessment*. in *AIP Conference Proceedings*. 1987. Palo Alto, USA: American Institute of Physics. p. 334.

227. Mrig, L. *Outdoor Stability Performance of Thin Film Photovoltaic Modules at SERI*. in *24th Intersociety Energy Conv. Engg. Conf.* 1989. IEEE. p. 761.

228. Ragot, P., A. Chenevas-Paule, H.S. Costa, D. Desmettre, E. Rossi, H. Ossenbrink, and R. van Steenwinkel. *Analysis of Performance Evolution of Amorphous Silicon Modules by Experimentation in Indoor and Outdoor Conditions*. in *10th European Photovol. Solar Energy Conf.* 1991. Lisbon, Portugal: Kluwer Academic Publishers. p. 403.

229. Ragot, P., R. Berre, and D. Desmettre. *Results of Field Testing of Amorphous Silicon Modules and Arrays*. in *9th European Photovol. Solar Energy Conf.* 1989. Freiburg, Germany: Kluwer Academic Publishers. p. 1028.

230. Berry, W.B. and M.J. Hahn. *Light-Induced Defect Influence on a-Si:H Field Test Performance*. in *10th European Photovol. Solar Energy Conf.* 1991. Lisbon, Portugal: Kluwer Academic Publishers. p. 387.

231. Chianese, D., M. Camani, P. Ceppi, and D. Iacobucci. *TISO: 4 kW Experimental Amorphous Silicon PV Power Plant*. in *10th European Photovol. Solar Energy Conf.* 1991. Lisbon, Portugal: Kluwer Academic Publishers. p. 755.

232. Atmaram, G.H., B. Marion, and C. Herig. *Performance and Reliability of a 15kWp Amorphous Silicon Photovoltaic System*. in *21st IEEE Photov. Spec. Conf.* 1990. Florida, USA: IEEE. p. 821.

233. Atmaram, G.H., B. Marion, and C. Herig. *Three Years Performance and Reliability of a 15 kWp Amorphous Silicon Photovoltaic System*. in *22nd IEEE Photov. Spec. Conf.* 1991. Las Vegas, USA: IEEE. p. 600.

234. Luft, W., B. Stafford, and B. von Roedern. *Stabilized Module Performance as a Goal for the Photovoltaic Amorphous Silicon Program in the United States*. in *AIP Conference*. 1991. Denver, USA: American Institute of Physics. p. 3.

235. Muirhead, I., *Private Communication,* 1992.

236. Chenlo, F. and N. Vela. *Analysis of Different Commercial Technologies a-Si Submodules: Characterization and Short-Time Outdoor Degradation Test*. in *10th European Photovol. Solar Energy Conf.* 1991. Lisbon, Portugal: Kluwer Academic Publishers. p. 408.

237. Costa, H.S., *Contribution a L'Etude des Generateurs Photovoltaiques au Silicium Amorphe: Characterisation Electrique, Energetique et Evolution dans le Temps*, PhD Thesis, Universite D'Aix-Marseille, 1992.

238. Delahoy, A.E., T. Tonon, J.A. Cambridge, M. Johnson, L. Michalski, and F.J. Kampas. *Light-Soaking Studies on Amorphous Silicon Photovoltaic Devices and Modules*. in *8th European Photovol. Solar Energy Conf.* 1988. Florence, Italy: Kluwer Academic Publishers. p. 646.

239. Ragot, P., *Private Communication,* 1992.

240. Luft, W., B. von Roedern, B. Stafford, D. Waddington, and L. Mrig. *Controlled Light-Soaking Experiment for Amorphous Silicon Modules*. in *22nd IEEE Photov. Spec. Conf.* 1991. Las Vegas, USA: IEEE. p. 1393.

241. Bureau of Meteorology, *Ambient Temperature and Wind Speed for 4 Western Australian Sites*, Western Australia Section-Bureau of Meteorology, 1992.

242. Redfield, D. and R.H. Bube, *Reinterpretation of Degradation Kinetics of Amorphous Silicon.* Appl. Phys. Lett., 1989, **54**(11), p. 1037.

243. Wilson, H.R. *Effect of Solar Spectral Variation on Solar Cell Short Circuit Current: Results of Long-Term Continuous Measurements*. in *7th European Photovol. Solar Energy Conf.* 1986. Sevilla, Spain: Kluwer Academic Publishers. p. 309.

244. Candelario, T.R., S.L. Hester, T.U. Townsend, and D.J. Shipman. *PVUSA - Performance, Experience, and Cost.* in *22nd IEEE Photov. Spec. Conf.* 1991. Las Vegas, USA: IEEE. p. 493.

245. Ishikawa, Y. *Fabrication Technology for Large-Area a-Si Solar Cells.* in *7th Intl. Photov. Sci. & Eng. Conf.* 1993. p. 37.

246. Carlson, D.E., *The Commercialization of Amorphous Silicon-Based Photovoltaics.* Optoelectronics - Devices and Technologies, 1994, **9**(3), p. 307.

247. Guha, S., J. Yang, A. Banerjee, T. Glatfelter, K. Hoffman, S.R. Ovshinsly, M. Izu, H.C. Ovshinsky, and X. Deng. *Amorphous Silicon Alloy Photovoltaic Technology - From R&D to Production.* in *Mat. Res. Soc. Symp. Proc.* 1994. Materials Research Society. p. 645.

248. Yang, J., A. Banerjee, T. Glatfelter, K. Hoffman, X. Xu, and S. Guha. *Progress in Triple-Junction Amorphous Silicon-Based Alloy Solar Cells and Modules using Hydrogen Dilution.* in *1st World Conf. on Photovol. Energy Conversion.* 1994. Hawaii, USA: p. in press.

249. von Roedern, B., *Private Communication,* 1995.

Publications Arising from this and Related Work

1. **Rüther R.** & Livingstone J., *In-Chamber Annealing of Amorphous Silicon Thin Films for Solar Cell Fabrication*, in J. Singh & S. Chandra (Ed.), 30th Annual Conf. of the Australian and New Zealand Solar Energy Society, (pp. 301-306), Darwin, Australia, 1992.

2. **Rüther R.** & Livingstone J., *Light-Induced Effects on In-Chamber Annealed Amorphous Silicon for Solar Cell s*, in J. Singh & S. Chandra (Ed.), 30th Annual Conf. of the Australian and New Zealand Solar Energy Society, (pp. 500-505), Darwin, Australia, 1992.

3. **Rüther R.** & Livingstone J., *The Role of Substrate Temperature and In-Chamber Annealing on H-Si Bonding Configurations in Sputtered a-Si:H*, Thin Solid Films **226** (1), 1993, 59-64.

4. **Rüther R.** & Livingstone J., *Aspects of the Seasonal Effects on Amorphous Silicon Solar Modules,* in Pálfy, M. (Ed.), ISES Solar World Congress, (pp. 243-248), Budapest, Hungary, 1993.

5. **Rüther R.** & Livingstone J., *Results of Seasonal Temperatures on Light-Induced a-Si Thin Film Characteristics,* in Pálfy, M. (Ed.), ISES Solar World Congress, (pp. 167-172), Budapest, Hungary, 1993.

6. **Rüther R.** & Livingstone J., *Amorphous and Crystalline Silicon Solar Modules: Choice of Technologies,* in T. Pryor (Ed.), 31st Annual Conf. of the Australian and New Zealand Solar Energy Society, (pp. 548-554), Fremantle, Australia, 1993.

7. **Rüther R.** & Livingstone J., *Seasonal Variations in Amorphous Silicon Solar Module Outputs and Thin Film Characteristics,* Solar Energy Materials and Solar Cells **36** (1), 1994, 29-43.

8. **Rüther R.** & Livingstone J., *Hydrogenated Amorphous Silicon: Hydrogen Content, Bonding Configurations and Morphology in Sputter-Deposited, In-Chamber Annealed Thin Films,* Thin Solid Films **251** (1), 1994, 30-35.

9. **Rüther R.**, Livingstone J., Dytlewski N. & Cohen, D., *Hydrogen Incorporation in Sputter-Deposited, In-Chamber Annealed Amorphous Silicon Thin Films: An Infrared and Elastic Recoil Analysis*, physica status solidi **145** (1), 1994, K37-42.

10. **Rüther R.** & Livingstone J., *Amorphous Silicon for Solar Cell Applications: Hydrogen-Related Stability Considerations,* in Prasad, D. K. (Ed.), 32nd Annual Conf. of the Australian and New Zealand Solar Energy Society, (pp. 270-274), Sydney, Australia, 1994.

11. **Rüther R.** & Livingstone J., *Temperature and Light Intensity Effects on Amorphous Silicon Solar Cell Modules* in Prasad, D. K. (Ed.), 32nd Annual Conf. of the Australian and New Zealand Solar Energy Society, (pp. 499-503), Sydney, Australia, 1994.

12. **Rüther R.,** Livingstone J., Dytlewski N. & Cohen, D., *Bond Switching, Si-H Cluster Formation and Hydrogen Effusion upon Thermal Annealing in Hydrogenated Amorphous Silicon Thin Films*, Thin Solid Films **in press**.

13. **Rüther R.,** Livingstone J., Dytlewski N. & Cohen, D., *Improved Hydrogen Depth Profiles with In-Chamber Annealing of Hydrogenated Amorphous Silicon Thin Films,* Journal of Applied Physics **in press**.

14. **Rüther R.** & Livingstone J., *An Infrared Study of Si-H Cluster Formation in a-Si:H Thin Films* , Infrared Physics and Technology **in press**.